Technische Universität München
TUM School of Natural Sciences

Development of Radiohybrid PSMA Ligands for the Endoradiotherapy of Prostate Cancer

Sebastian Fischer

Vollständiger Abdruck der von der TUM School of Natural Sciences der Technischen Universität München zur Erlangung eines

Doktors der Naturwissenschaften (Dr. rer. nat.)

genehmigten Dissertation.

Vorsitzende: **Prof. Dr. Angela Casini**

Prüfer*innen der Dissertation:

1. Prof. Dr. Susanne Kossatz
2. apl. Prof. Dr. Matthias Eiber

Die Dissertation wurde am 24.01.2023 bei der Technischen Universität München eingereicht und durch die TUM School of Natural Sciences am 04.04.2023 angenommen.

TABLE OF CONTENTS

ZUSAMMENFASSUNG

Im Laufe der letzten beiden Jahrzehnte wurde eine Fülle an prostataspezifischen Membranantigen (PSMA)-gerichteten Radioliganden zur Bildgebung und Behandlung von Prostatakrebs als eine der häufigsten Krebsarten weltweit entwickelt. Darunter wurde [^{177}Lu]Lu-PSMA-617 als bislang einziger PSMA-Ligand von der FDA zur Endoradiotherapie zugelassen, wobei klinische Ergebnisse insbesondere das rote Knochenmark und die Nieren als dosislimitierende Organe hervorheben. Für die entsprechende Patientenselektion und Therapiekontrolle wird derzeit die Applikation von [^{68}Ga]Ga-PSMA-11 als diagnostischer Ligand empfohlen. Demgegenüber würde die Verwendung von pharmakokinetisch identischen Verbindungen zur Therapie und Diagnostik (Theranostik) genauere, patientenspezifische Dosimetrieberechnungen als Grundlage einer personalisierten Therapie erlauben. Daher war das primäre Ziel dieser Arbeit, einen PSMA-Liganden mit einer theranostischen Anwendbarkeit und einem verbesserten Distributionsprofil durch optimierte Tumor/Blut- und Tumor/Nieren-Verhältnisse zu entwickeln. Als theranostische Leitstruktur diente Lu-rhPSMA-7.3, abgeleitet von dem aktuell klinisch untersuchten Liganden Ga-rhPSMA-7.3. Dessen radiohybrides Design umfasst einen Chelator zur Komplexierung von (Radio)Metallen und einen Silizium-basierten Fluoridakzeptor (SiFA) zur ^{18}F-Markierung. Dies ermöglicht den Zugang zu einem Paar von chemisch identischen Liganden, die mit zwei verschiedenen Nukliden orthogonal markiert werden können. Dieses Merkmal als Voraussetzung für einen echten theranostischen Ansatz in Kombination mit der bisherigen klinischen Performance von Ga-rhPSMA-7.3 zeichnet dieses Ligandengerüst als vielversprechende Plattform aus.

Zur Optimierung der Tumor/Hintergrund-Verhältnisse wurden verschiedene Strategien verfolgt: 1) die Insertion von metabolisch-instabilen Linkern zur Senkung der PSMA-vermittelten Nierenretention; 2) die Reduktion der Nettoladung zur Verringerung der renalen, tubulären Reabsorption; 3) die Modulation der Bindung zum humanen Serumalbumin (HSA) als Schlüsselparameter zur Regulierung der Plasmahalbwertszeit und Ganzkörper-Clearance. Das letztgenannte Thema umschließt mehrere Ansätze, wie das Design von verzweigten Linkerkonstrukten für die austauschbare Verknüpfung von diversen HSA-Bindern. Auch konnte die HSA-Affinität durch funktionelle Gruppen in direkter Nähe zur SiFA-Einheit – als inhärenter HSA-Binder der Leitstruktur – manipuliert werden. Schließlich wurde eine neue SiFA-Einheit entwickelt, um die Limitation durch eine hohe HSA-Bindung und ausgeprägte Lipophilie direkt anzugehen.

Untersuchte *in vitro*-Parameter waren Targetaffinität (IC_{50}) und Internalisierung in PSMA$^+$ LNCaP-Zellen mit ([^{125}I]I-BA)KuE entsprechend als Kompetitor und Referenz, Hydrophilie gemessen als *n*-Octanol/PBS-Verteilungskoeffizient ($logD_{pH\ 7.4}$) und HSA-Bindung. Letztere wurde sowohl *via* Hochleistungsaffinitätschromatographie (HPAC) an einer mit HSA-beschichteten HPLC-Säule als auch per Albumin-vermittelter Größenausschlusschromatographie (AMSEC) mit einer HSA-Lösung als mobile Phase untersucht.

Während durch das Einfügen von Linkersequenzen mit dem Ziel einer metabolischen Instabilität zumeist angemessene *in vitro*-Eigenschaften bewahrt wurden und eine Metabolisierung anhand von Blut-, Urin- und Nierenproben von CB17-SCID-Mäusen veranschaulicht werden konnte, wurde kein Nutzen für das Tumor/Nieren-Verhältnis im Vergleich zur Leitstruktur gefunden. Die Reduktion der Nettoladung innerhalb der Leitstruktur war teilweise erfolgreich mit der größten Verbesserung durch eine Substitution einer Carbonsäure durch ein Amin in Nähe zur HSA-bindenden SiFA-Einheit (Tumor/Nieren-Verhältnis: [^{177}Lu]Lu-RNC-6: 5.94 ± 1.27 vs. [^{177}Lu]Lu-rhPSMA-7.3: 1.24 ± 0.29). Jedoch wurde trotz der einhergehenden Senkung der HSA-Bindung *in vitro* eine leichte Verringerung der Tumor/Blut- und Tumor/Leber-Verhältnisse beobachtet und als Konsequenz eines Hydrophilieverlustes bewertet (–2.88 ± 0.06 vs. −4.12 ± 0.11). Die Modulation der HSA-Bindung durch verzweigte Linkerkonstrukte mit zusätzlichen, terminalen HSA-Bindern offenbarte Hürden. So ergaben sich umständliche Synthesen mit unvollständigen Kopplungsschritten bei sich wiederholenden Peptidsequenzen und hochlipophile Verbindungen als Resultat eines stark exponierten, lipophilen HSA-Binders ($\log D_{pH\ 7.4}$: –2.1 bis –2.5). Außerdem wurde während des Projektes klar, dass eine höhere HSA-Bindung für eine verbesserte Tumorbelieferung im Konflikt mit verringerten Tumor/Hintergrund-Verhältnissen steht. Auch wirkt die SiFA-Einheit selbst als inhärenter HSA-Binder, durch den die HSA-Bindung der Leitstruktur bereits ein Optimum übersteigt.

Die Identifikation der SiFA-Einheit der Leitstruktur (4-(Di-*tert*-butylfluorosilyl)benzoyl, (4-SiFA)Bz) als verantwortliches Motiv für eine exzessive HSA-Bindung und Lipophilie ermutigte zur Entwicklung und Charakterisierung der neuen SiFA-Einheit (5-Di-*tert*-butylfluorosilyl)isophtaloyl, (5-SiFA)Ip). Die strukturelle Erweiterung selbst gewährleistet eine effiziente Steigerung der Hydrophilie oder kann als Konjugationsstelle genutzt werden, um weitere Modifikationen einfach über eine modulare und praktische Synthese einzubringen. An Modellpeptiden und PSMA-Liganden untersuchte *in vitro*-Eigenschaften demonstrieren deutlich, dass die neuartige SiFA-Einheit ein effizientes Werkzeug zur Modulierung der HSA-Bindung und Hydrophilie über einen weiten Wertebereich für individuelle pharmakokinetische Anforderungen darstellt. Jedoch zeigte die neue SiFA-Einheit insbesondere als zweifach konjugierter Baustein eine gesteigerte Reaktivität. Im Vergleich mit der (4-SiFA)Bz-Einheit äußerte sich dies in einem überlegenen radiochemischen Umsatz in der ^{18}F-Markierung der (5-SiFA)Ip-Einheit auf Kosten einer unterlegenen *in vitro*- und *in vivo*-Stabilität. Folglich besitzt der PSMA-Ligand [^{18}F]^{nat}Lu-MSM-6 mit einer verbrückenden (5-SiFA)Ip-Einheit zwar eine schnelle Ganzkörper-Clearance aber auch den Nachteil einer sechsfach gesteigerten Knochenaufnahme verglichen mit [^{18}F]^{nat}Ga-rhPSMA-7.3 eine Stunde nach Injektion (2.43 ± 0.58 %ID/g vs. 0.38 ± 0.32 %ID/g). Dennoch zeigte das ^{177}Lu-markierte Gegenstück, [^{177}Lu]Lu-MSM-6, 24 h nach Injektion eine überaus vorteilhafte Pharmakokinetik mit einem zweifach verbesserten Tumor/Blut-Verhältnis verglichen mit [^{177}Lu]Lu-PSMA-617 und einem sogar 6.5-fach höheren Tumor/Nierenverhältnis im Gegensatz zur Leitstruktur [^{177}Lu]Lu-rhPSMA-7.3.

Zusammenfassend stellt der Gebrauch der neuartigen (5-SiFA)Ip-Einheit ein wertvolles Werkzeug zur Optimierung der Pharmakokinetik von SiFA-beinhaltenden Radiopharmaka dar, wenngleich weitere Bemühungen zur Stabilisierung der Si–F-Bindung erstrebenswert sind. Nichtsdestoweniger resultierten hier beschriebene Optimierungen in dem Radioliganden [^{177}Lu]Lu-MSM-6 als vielversprechenden Kandidaten zur klinischen Translation für eine therapeutische Anwendung.

ABSTRACT

Over the last two decades, a plethora of prostate-specific membrane antigen (PSMA)-targeting radioligands for the imaging and treatment of prostate cancer, as one of the most common cancer entities worldwide, was developed. As one of these ligands, [^{177}Lu]Lu-PSMA-617 was the so far only FDA-approved compound for endoradiotherapy with clinical results indicating the red bone marrow as well as the kidneys as dose-limiting organs. For the corresponding patient selection and therapy control, [^{68}Ga]Ga-PSMA-11 is recommended as diagnostic ligand. Opposingly, the use of compounds with identical pharmacokinetics for the therapeutic and diagnostic (theranostic) application would allow for more precise, patient-specific dosimetry calculations as a basis for personalized therapy. Thus, the primary objective of this work was the development of a PSMA ligand with a theranostic applicability and an improved distribution profile of optimized tumor-to-blood and tumor-to-kidney ratios. Lu-rhPSMA-7.3 served as a theranostic lead structure derived from Ga-rhPSMA-7.3 which is a ligand under current clinical investigations. Its radiohybrid design comprises of a chelator for (radio)metal chelation and a silicon-based fluoride acceptor (SiFA) for ^{18}F-labeling. This gives access to a pair of chemically identical ligands capable of orthogonal labeling reactions with two different nuclides. This feature as a prerequisite for a truly theranostic approach in combination with the so far clinical performance of Ga-rhPSMA-7.3 render this ligand scaffold as a promising platform.

To optimize tumor-to-background ratios, various strategies were pursued: 1) the use of metabolically instable linkers to decrease PSMA-mediated kidney retention; 2) the reduction of the net charge to decrease renal tubular reabsorption; 3) the modulation of human serum albumin (HSA) binding as key parameter for the regulation of plasma half-life and whole-body clearance. The latter topic includes several approaches like the design of a branching linker construct for the exchangeable attachment of various HSA binders. In addition, the HSA affinity could be manipulated by functional groups in direct proximity to the SiFA moiety as inherent HSA binder of the lead structure. Finally, a novel SiFA moiety was developed to directly face the limitation caused by strong HSA binding and pronounced lipophilicity.

Determined *in vitro* parameters were target affinity (IC_{50}) and internalization into PSMA$^+$ LNCaP cells using ([^{125}I]I-BA)KuE as competitor and reference, respectively, hydrophilicity measured as *n*-octanol/PBS partition coefficient ($logD_{pH\ 7.4}$) and HSA binding. The latter parameter was examined by high-performance affinity chromatography (HPAC) on an HSA-coated HPLC column as well as with albumin-mediated size exclusion chromatography (AMSEC) applying a solution of HSA as mobile phase.

While the inserted linker sequences aiming for metabolic instability mostly preserved reasonable *in vitro* properties and metabolization could be exemplified in blood, urine and kidney samples of CB-17 SCID mice, no benefit for the tumor-to-kidney ratio was found compared to the lead structure.

The reduction of the lead compound's net charge was partially successful with the best improvement for the alteration of a carboxylic acid to an amine in proximity to the HSA-binding SiFA entity (tumor-to-kidney ratio: [^{177}Lu]Lu-RNC-6: 5.94 ± 1.27 vs. [^{177}Lu]Lu-rhPSMA-7.3: 1.24 ± 0.29). However, despite the concomitantly reduced HSA binding *in vitro*, a slight decrease of the tumor-to-blood and tumor-to-liver ratios was observed and assessed as a consequence of a loss in hydrophilicity (–2.88 ± 0.06 vs. –4.12 ± 0.11).

The modulation of HSA binding by branching linker constructs with an additional, terminal HSA binder turned out to lead to hurdles. The outcome was an overelaborated synthesis with incomplete coupling steps of repeated peptide sequences and highly lipophilic compounds as a result of the strongly exposed, lipophilic HSA binder ($logD_{pH\ 7.4}$: –2.1 to –2.5). Moreover, during the course of this project it became evident that higher HSA binding aiming for improved tumor delivery is in conflict with inferior tumor-to-background ratios. Additionally, the SiFA entity itself acts as inherent HSA binder causing an HSA binding of the lead structure which is already above a sweet spot.

Identifying the SiFA entity in the lead structure (4-(di-*tert*-butylfluorosilyl)benzoyl, (4-SiFA)Bz) as a responsible motif for an excessive HSA binding and lipophilicity encouraged the development and characterization of the novel SiFA entity (5-di-*tert*-butylfluorosilyl)isophtaloyl, (5-SiFA)Ip). The structural extension itself ensures an efficient boost in hydrophilicity or can be used as conjugation site for further modifiers readily attached in a modular and convenient synthesis. *In vitro* properties examined on model peptides as well as PSMA ligands clearly demonstrate the novel SiFA entity as an effective tool in modulating HSA binding and hydrophilicity over a broad range towards individual pharmacokinetic requirements. However, the novel SiFA entity – especially if used as di-conjugated building block – exhibited an enhanced reactivity. In comparison to the (4-SiFA)Bz moiety, it turned out that a superior radiochemical conversion in the ^{18}F-labeling of the (5-SiFA)Ip came at the cost of an inferior stability *in vitro* and *in vivo*. Consequently, the PSMA ligand [^{18}F]^{nat}Lu-MSM-6 with a bridging (5-SiFA)Ip entity indeed possessed a promising fast whole-body clearance but also the drawback of a six-fold increased bone uptake compared to [^{18}F]^{nat}Ga-rhPSMA-7.3 at 1 h p.i. (2.43 ± 0.58 %ID/g vs. 0.38 ± 0.32 %ID/g). Nevertheless, the ^{177}Lu-labeled counterpart [^{177}Lu]Lu-MSM-6 showed highly favorable pharmacokinetics 24 h post injection with a two-fold improved tumor-to-blood ratio compared with [^{177}Lu]Lu-PSMA-617 and even a 6.5-fold higher tumor-to-kidney ratio opposed to the lead structure [^{177}Lu]Lu-rhPSMA-7.3.

In conclusion, the use of the novel (5-SiFA)Ip entity constitutes a valuable tool in optimizing the pharmacokinetics of SiFA-bearing radiopharmaceuticals albeit further efforts in the stabilization of the Si–F bond is desirable. Nonetheless, the herein presented optimizations resulted in the radioligand [^{177}Lu]Lu-MSM-6 being a promising candidate for clinical translation into a therapeutic application.

I. INTRODUCTION

1. Prostate Cancer (PCa)

1.1. Epidemiology

Worldwide, cancer is one of the leading causes of death. According to data of the World Health Organization (WHO) about the year 2019, cancer was the first or second leading cause of premature deaths (age <70 years) in more than 60% of all countries (*1*). Based on these mortality rates a correlation was found with the respective Human Development Indices (HDI). A raising HDI was mostly accompanied by a declining proportion of deaths related to cardiovascular diseases while the proportion of cancer-related deaths increased (*2*). In 2020, a total number of 19.3 million new cancer cases and 9.96 million cancer-related deaths were estimated by the WHO. Based on demographic changes, *Sung et al.* extrapolated the number of new cases reported in 2020. An increase by 47% in 2040 is expected not yet considering potential alterations in risk factors (*1*). Among all cancer entities for both sexes in 2020, prostate cancer (PCa) revealed the fourth most frequent incidence with 1.4 million new cases (7.3% of all new cancer cases) and was associated with about 375 000 deaths (3.8% of all cancer-related deaths). Respective data obtained by the GLOBOCAN 2020 database are visualized in **Figure 1** (*3*).

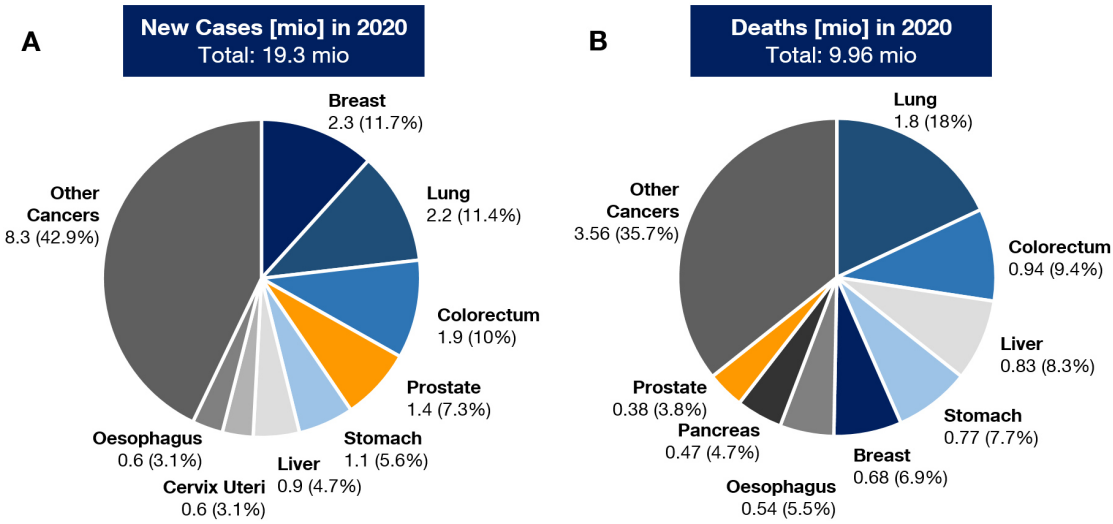

Figure 1: Statistics depicted in absolute numbers in million (and % of total) regarding both sexes and all ages in the year 2020; **A:** new cancer cases; **B:** cancer-related deaths; adapted from the GLOBOCAN 2020 database (*3*).

Commonly accepted, epidemiologically derived risk factors for developing PCa are age (higher risk for older men), race (especially African ancestry) and the occurrence in family. Furthermore, lifestyle-associated factors like diet, obesity, diabetes and physical activity are discussed to potentially influence the incidence or progression of disease (*4-7*). In an international comparison of incidence, drastic deviations are listed with higher numbers for Northern America, Europe and Oceania. Besides the aforementioned factors, again a correlation of a high HDI with a high age-

standardized incidence rate (ASIR) and a low age-standardized mortality rate (ASMR) becomes evident. *Wang et al.* mentioned the usage of prostate specific antigen (PSA)-screening to potentially affect the ASIR by overdetection but also to support the detection of PCa in an early stage and thus, decreasing the ASMR (*7*). In general, it is estimated that the total number of cancer cases worldwide will increase while prostate cancer belongs to the most common cancer entities.

1.2. Diagnosis and Staging

To encounter the risk for patients of developing non-curable cancer one might estimate the implementation of screenings for early detection of malignancies as desirable. In the case of PCa, the aforementioned screening of PSA as a serum marker is recommended by the German 'Leitlinienprogramm Onkologie' based on the results of a study with a cohort of >21 000 men and a median follow-up of 23 years. The examination should be offered to men at an age of ≥45 years after the discussion of advantages and limitations of the predictive value. Depending on the life expectancy (only if >10 years) of a patient and the determined PSA value (<1; 1–2; >2 ng/mL) different intervals (1; 2 or 4 years, respectively) of repeated PSA examinations are advised (*8,9*).
However, the usefulness of this method as a public screening is judged as a controversial topic balancing potential overdetection and overtreatment against desired reduced mortality. Indeed, clinical trials confirmed a more frequent diagnosis of PCa using PSA screening versus the control group. Furthermore, a higher proportion of localized disease opposed to advanced PCa was found in the intervention group. If this screening also affects the cancer-specific mortality cannot as easily be assessed with diverging results in different trials (*10*).
In the past, following former recommendations of the US Preventive Services Task Force (USPSTF) a decline in the use of PSA testing was associated with a rising rate of advanced disease at diagnosis potentially increasing cancer-specific mortality. Subsequently, this encouraged a re-introduction of the USPSTF recommendation for screenings at least for a restricted patient group (*11-14*).
In addition to PSA testing, the digital rectal examination (DRE) can be conducted for early detection. In suspicion of PCa-positive patients based on elevated initial PSA levels (≥4 ng/mL), noteworthy increases in PSA level over time or the finding of palpable tumors by DRE results are verified by needle biopsy and subsequent histopathological assessment (*9*). A combination of systematic and multiparametric magnetic resonance imaging (mpMRI)-targeted biopsy currently reveals the highest detection rates and is recommended as initial biopsy technique (*9,15*). The evaluation of the biopsy probe refers to a grading system commonly known as Gleason score assessing the histological morphology (well-/poor-differentiated) of both the most common pattern and the pattern with least differentiation (*16*). The former grading system ranging from 1 to 10 was updated by the International Society of Urological Pathology (ISUP) in 2014 to a scale

from 1 to 5 with some adoptions (*17*). Both scales display an increasingly aggressive disease for higher grading.

Results of the DRE, PSA testing and Gleason score/ISUP grade classify a patient as PCa positive or negative and deliver further information on the stage of the disease and the risk group. Depending on the risk group, different imaging modalities as MRI, computed tomography (CT), bone scintigraphy and prostate-specific membrane antigen positron emission tomography (PSMA PET) are considered to determine the presence of metastases (*9*).

The obtained data are used for disease classifications. Guidelines advice to use the UICC TNM classification and risk group classification of the European Association of Urology (EAU) based on D'Amico's classification system (*9,14*). The former classification describes the staging by the presence and extent of the primary tumor (T0–T4 with substages a–c), the infiltration in regional lymph nodes (N0, N1) and the presence of distant metastases (M0, M1) with some additional subgroups (*18*). The latter system divides patients with localized to locally advanced prostate cancer into groups of low, intermediate and high risk of biochemical recurrence after local treatment considering PSA level, Gleason score/ISUP grade and primary tumor stage (**Table 1**) (*14,19,20*).

Table 1: EAU risk groups for biochemical recurrence of localised and locally advanced prostate cancer; GS = Gleason score; adapted from the EAU-EANM-ESTRO-ESUR-SIOG Guidelines on Prostate Cancer 2020 (*21*).

Low-Risk	Intermediate-Risk	High-Risk	
PSA ≤10 ng/mL	PSA 10–20 ng/mL	PSA >20 ng/mL	any PSA
and GS <7	or GS <7	or GS <7	any GS <7
(ISUP grade 1)	(ISUP grade 2/3)	(ISUP grade 4/5)	(any ISUP grade)
and cT1–2a	or cT2b	or cT2c	cT3–4, or cN+
(localized)	(localized)	(localized)	(locally advanced)

On the basis of a precise disease staging, the patient's health status with respect to comorbidities and the patient's preference the question of treatment options is assessed (*9*).

1.3. Treatment Options

A common statement with regard to PCa is that more men die *with* rather than *because of* PCa. Autopsy studies present a clear age-related prevalence with positive findings for more than one-third aged >80 years and even over one-half for men >90 years (*22*). As the probability for PCa diagnosis increases with age, life expectancy and comorbidities are important factors to be considered besides the cancer-related risk group.

Thus, evaluating the individual benefits two rather passive strategies can be suggested avoiding overtreatment. For low-risk patients with local PCa the possibility of 'active surveillance' opposed to invasive treatment or radiotherapy should be assessed (*9*). In a prospective study with a patient cohort of 993 men selected for active surveillance, the long-term follow-up after 15 years revealed a cause-specific survival rate of 94.3% while 55% of patients remained untreated and still on

surveillance (*23*). This constitutes an example reflecting the common consensus that in frequent cases the cancer-specific survival rate stays unaltered no matter of attending to active surveillance or interventional forms of therapy (*9,24*). However, active surveillance was clearly correlated with higher rates of disease progression compared to surgery as well as radiotherapy (*25*). Moreover, the patient's preference should also be taken into account as active surveillance holds a psychological burden. Interviews of patients attending active surveillance indicated a subsequent choice of curative treatment in up to 10% of men without clinical necessity but because of cancer-related anxiety (*9,26*).

The second rather passive strategy is known as 'watchful waiting'. Opposed to active surveillance exhibiting a curative intention with active treatment only when clinically required, watchful waiting is rated as a more individual, palliative approach for frail patients receiving a symptomatic treatment (*14*).

As a first-line treatment of local PCa in all EAU risk groups the complete surgical resection of the prostate (radical prostatectomy) and in adaptation to the respective risk group also the dissection of pelvic lymph nodes is advised as monotherapy. External beam radiation therapy (EBRT) is offered as an alternative. For low-risk local PCa the implantation of radioactive seeds (brachytherapy) is also a listed option (*9,14*). Whereas radical prostatectomy can lead to erectile dysfunction and urinary incontinence (*27*), radiation therapies are associated with potential gastrointestinal or urogenital toxicities as well as a certain risk of developing second malignancies (*14,28,29*).

For the treatment of locally advanced PCa, radical prostatectomy with pelvic lymph node dissection (PLND) or EBRT with adjuvant androgen deprivation therapy (ADT) are recommended (*9,14*). As prostate cancer typically shows androgen-dependent growth, reduction of androgen levels by androgen receptor pathway inhibitors (ARPI) or removal of testicles (orchiectomy) aims for decelerated progression in adjuvant or palliative applications (*9,30,31*). In the case of clinical recurrence determined by PSA level, the respective hitherto not used option can be applied as salvage therapy (*9*).

Metastatic PCa is divided into metastatic hormone-sensitive PCa (mHSPC) and metastatic castration-resistant PCa (mCRPC) (*9*). Both forms of disease are judged as incurable with a 5-year relative survival rate of about 32% for patients with distant metastases (reported for men in the US, all races, 2012–2018) (*32*). Thus, respective therapies are conducted with palliative intent. While mHSPC patients are offered ADT with an optional adjuvant chemotherapy with docetaxel, mCRPC patients might receive a shift in drug choice to 'new hormonal agents' (second-line ARPI) for ADT in combination with docetaxel or cabazitaxel and optionally steroids (*9*).

Patients showing a well overall health status albeit further disease progression at exhaustion of all recommended treatment options may receive PSMA-targeted radioligand therapy (PRLT) with ^{177}Lu-labeled compounds (*9,33*). The therapeutic use of Lutetium Lu 177 vipivotide tetraxetan

(PLUVICTO™, formerly known as [^{177}Lu]Lu-PSMA-617) as radiopharmaceutical was most recently (March 2022) approved by the US Food and Drug Administration (FDA) (*34,35*). More insights into clinical results of PSMA-targeted imaging agents and ligands for endoradiotherapy will be presented below. But at first, information about PSMA as drug target and its binding pocket as structural setting for radioligand design are described within the next chapter.

2. Prostate-Specific Membrane Antigen (PSMA)

2.1. Expression and Function in Benign and Malign Tissue

The prostate-specific membrane antigen (PSMA, EC 3.4.17.21) is a transmembrane glycoprotein with an enzymatically active extracellular domain acting as a zinc-dependent metallopeptidase (*36*). According to the context, different names are common in the literature and refer to the same protein. In its function as glutamate carboxypeptidase II (GCP II) it is described to recognize two physiological substrates, namely the neurotransmitter *N*-acetyl-L-aspartyl-L-glutamate (NAAG) and poly-γ-glutamyl folate (*37-40*). Consequently, also applied terms are *N*-acetylated α-linked acidic dipeptidase I (NAALADase I) and folate hydrolase I (FOLH 1) more closely corresponding to its substrates.

The expression found in brain and its activity in the cleavage of NAAG to *N*-acetyl-L-aspartate and L-glutamate gained interest in the past as potential drug target against neurological disorders (*41,42*). The expression at the brush border membrane in the small intestine is assumed to play a crucial role in folate uptake by converting the poly-γ-glutamyl folate from nutrition into essential folate recognized by transport systems (*40,43*). Furthermore, physiological PSMA expression was detected in healthy prostate epithelium, proximal tubules of the kidney and in salivary glands besides some more weakly-expressing tissues (*44-46*).

In the last two decades, PSMA has gained considerable importance as a drug target for PCa imaging and therapy (*47*). *In vitro* results suggest that PSMA could facilitate carcinogenesis by supporting folate uptake and might even be involved in invasiveness of cancer cells (*48,49*). Additionally, the observed cell migration and adhesion of PSMA expressing cells to bone marrow matrix indicated a potential involvement of PSMA in the frequent formation of bone metastases in PCa (*50*). Compared with healthy prostatic epithelium the expression of PSMA was observed to be clearly upregulated in primary prostate tumors as well as in metastatic prostate cancer (*44,51-54*). Furthermore, expression levels seem to correlate with malignity determined by Gleason score and increased intratumoral angiogenesis (*52,55*). Indeed, PSMA revealed a regulatory effect on angiogenesis by modulating integrin signal transduction (*56*).

Perner et al. not only demonstrated a significant overexpression of PSMA in localized prostate adenocarcinoma, lymph node metastases and hormone refractory distant metastases opposed to benign prostate tissue but also impressively illustrated high PSMA expression as predictive for higher incidences of PSA recurrence (**Figure 2**) (*57*).

A study of *Minner et al.* investigated a total of 1700 prostate cancers including subgroups of different tumor stages, Gleason scores and PSA levels. Their immunohistochemical findings for PSMA expression were positive in >90% of cancers within each subgroup and almost 95% within the whole data set (*58*).

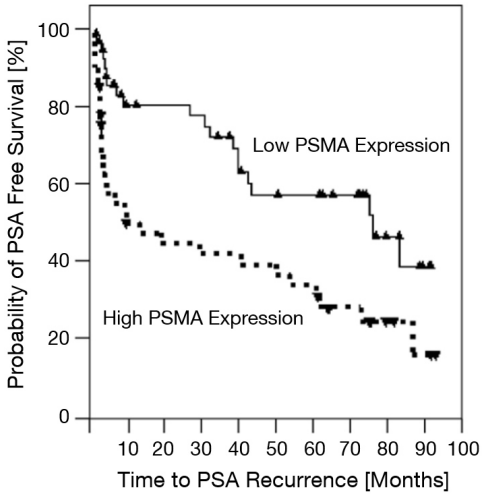

Figure 2: Kaplan-Meier survival curves illustrating an increased rate of PSA recurrence for patients with high PSMA expression; adapted from *Perner et al.* (*57*).

These histological findings together with a simple addressability as a cell surface protein clearly indicate the potential as a valuable biomarker in PCa. Consequently, scientists were encouraged to develop and optimize PSMA-targeted compounds. A structural basis is described hereafter.

2.2. Structural Insights as a Basis for Radioligand Design

PSMA is reported to comprise of a 750 amino acid sequence with an *N*-terminal intracellular region of 19 amino acids, a single transmembrane portion of 24 amino acids and the main part of 707 amino acids in the extracellular region (*43,59*). The full-length protein encompasses 10 *N*-glycosylation sites with major importance in folding, secretion and enzymatic activity (*60*). Offering a possible accumulation mechanism for drugs on a subcellular level, PSMA undergoes constitutive and antibody-induced internalization *via* clathrin-coated pits with an up to 3-fold increased internalization in the presence of an anti-PSMA antibody (*61,62*). Internalization is mediated by the cytoplasmic tail, in particular the terminal MXXXL motif, in interaction with the adaptor protein-2 (AP-2) and is further affected by the actin cross-linking protein filamin A (*62,63*).

The first crystal structure of the extracellular part was published in 2005 by *Davis et al.* and depicted the C_2-symmetric homodimer at a resolution of 3.5 Å (*64*). Later on, results were corrected by *Mesters et al.* revealing a different binding mode of the substrate NAAG at higher resolution (**Figure 3**, top) (*36*). The S1' pocket is characterized for bearing a highly specific 'glutarate sensor' forming attractive interactions by a network of hydrogen bonds and salt bridges to the *C*-terminal glutamate by participation of the amino acids Arg210, Asn275, Tyr552 and the more flexibly positioned amino acids Lys699 and Tyr700 indicating an induced-fit mechanism. The negatively charged aspartate sidechain is proposed to be attracted by the predominantly positively charged arginine patch formed by Arg463, Arg534 and Arg536 in the S1 pocket (*36*).

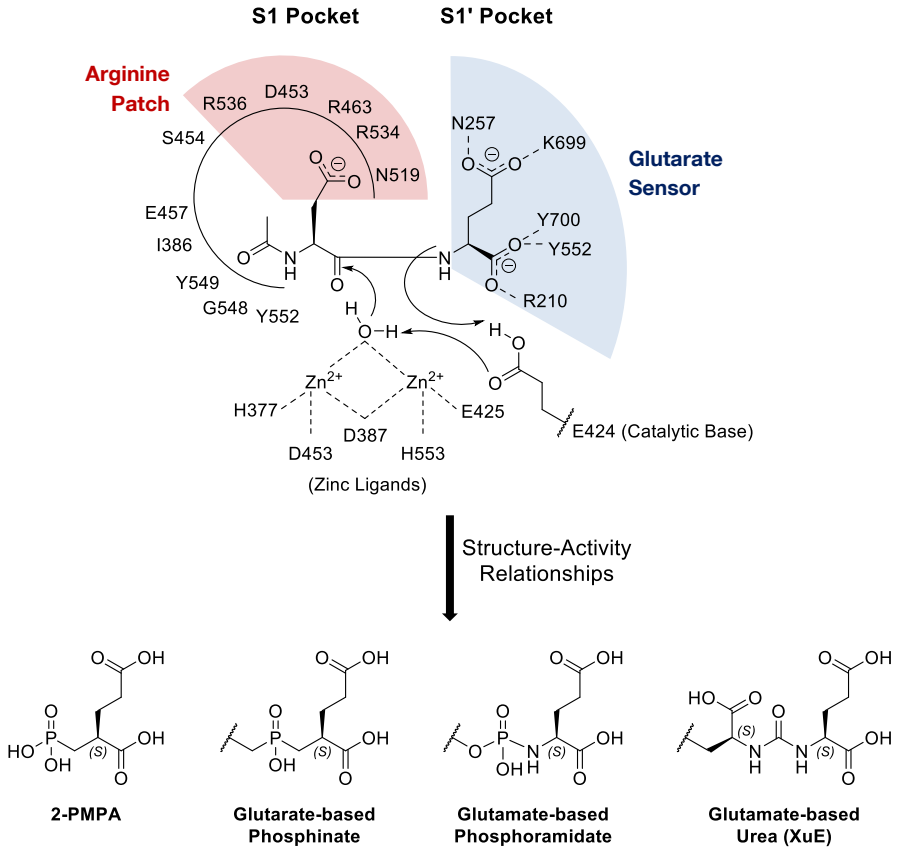

Figure 3: Top: interactions and mechanism of hydrolysis of the physiological substrate NAAG in the catalytic center of PSMA as proposed from the crystal structure with the arginine patch and the glutarate sensor highlighted in red and blue, respectively; adapted from *Mesters et al.* (*36*); **Bottom:** structure-activity relationships elucidated 2-(phosphonomethyl)pentanedioic acid (2-PMPA), phosphinates, phosphoramidates and ureas as highly affine binding motifs (*47*).

Not surprisingly, the glutarate entity is highly conserved in its binding mode and thus, anchored in the development of PSMA ligands with nanomolar affinity (*47,65*). To prevent enzymatic hydrolysis and simultaneously aim for attractive interactions with the binuclear zinc site, a few functional groups (**Figure 3**, bottom) were incorporated bridging amino acids in P1' and P1 position with the urea motif being the most common in PSMA inhibitors (*47*). Besides the depicted binding motifs, data of thiol- and hydroxamate-based motifs are also available. However, these classes display a subordinate role due to limited affinity (*66-68*).

While the combination of a glutamate or glutamate-like entity and a zinc-binding motif count as the minimum requirement for high affinity, the arginine patch in the S1 pocket and the distant remote arene-binding site located more closely to the protein surface are frequently addressed features in optimized ligand design (*65,69*).

Within the arginine patch, only Arg534 is found in an invariant position whereas Arg463 and Arg536 both can adopt two conformations. P1 carboxylates present in the Asp sidechain in NAAG or the α-carboxylate of amino acid X in urea-based binding motifs 'XuE' are likely to be attracted by the arginine patch fixing Arg536 in a binding position. Depending on the exact ligand structure, this binding mode can be accompanied by a shift of Arg436 opening the hydrophobic 'S1 accessory

pocket' enclosed by the five amino acid sidechains of Glu457, Arg463, Asp465, Arg534 and Arg536 (*65*). This 8.5 Å × 7 Å sized pocket is described to interact with aromatic moieties in suitable position. In this context, DCIBzL, also known as I-BA-KuE or MIP-1097, is one ligand perfectly fitting into the S1 accessory pocket (**Figure 4A**) (*65*). This is reflected by a remarkable affinity (K_i = 0.7 nM) (*70*).

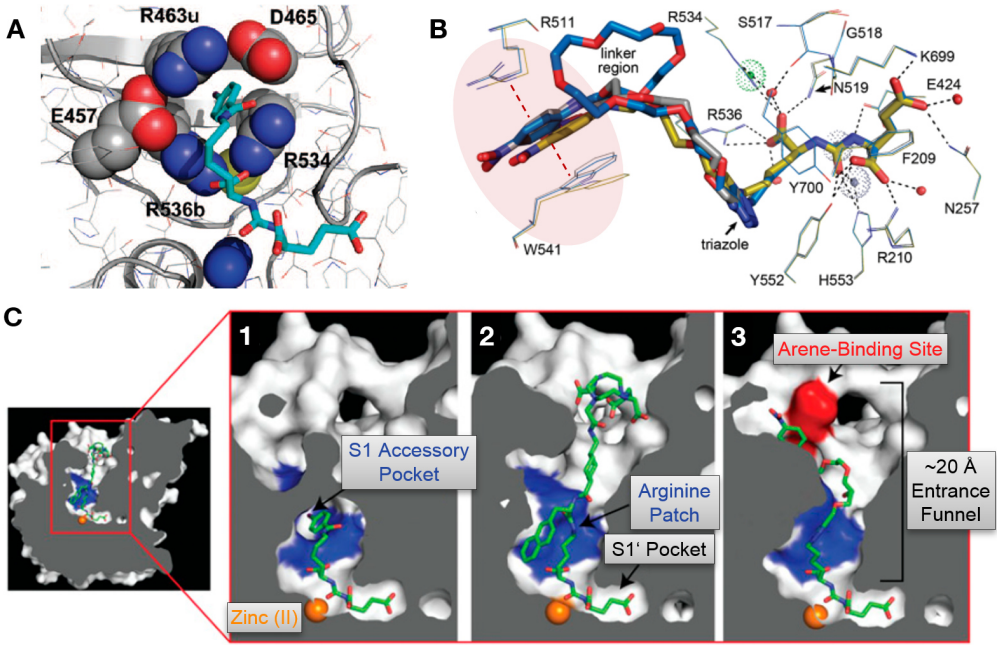

Figure 4: Structural features of the PSMA binding cavity comprised of **A:** the arginine patch with the possibility to form the S1 accessory pocket as depicted for the binding of DCIBzL, adapted from *Barinka et al.* (*65*); **B:** superposition of dinitrophenyl (DNP)-linker-KuE ligands (ARM-P2/-P4/-P8) with the DNP entity fixed at the remote arene-binding site (R511 and W541), adapted from *Zhang et al* (*69*); **C:** cross-sections of PSMA indicating the location of the S1' pocket, the binuclear zinc active site and the S1 pocket composed of the arginine patch/S1 accessory pocket, entrance funnel and (remote) arene-binding site within the binding cavity, depicted ligand conformations refer to 1) DCIBzL, 2) PSMA-617 and 3) ARM-P4, adapted from *Kopka et al.* (*71*).

Insights into the aforementioned remote arene-binding site were given by *Zhang et al*. (*69*). Their group investigated a series of KuE-based PSMA ligands connected to a dinitrophenyl (DNP) entity by PEG linkers with varied lengths. Affinity determinations revealed a trend indicating an attractive interaction of the DNP entity in a certain distance to the KuE binding motif. The assumption of a remote arene-binding site was confirmed by the superposition of crystal structures depicted in **Figure 4B**. For each of the three derivatives the orientation of the DNP entity was in close proximity to Arg511 and Trp541 indicating π-cation and π-stacking interactions. Moreover, alterations of the attached aromatic moiety and subsequent investigations showed a correlation of electron-poor aromatic rings (lower calculated LUMO energies) leading to higher PSMA affinities (*69*).

Importantly, the entrance lid to the inner binding cavity can form a closed conformation as determined for DCIBzL and visualized in **Figure 4C1**. However, for a ligand bound to the active site a simultaneous attractive interaction with the arene-biding site requires the conformation of an open entrance lid (**Figure 4C3**). This fact might limit the development of ligands addressing both subpockets, the accessory pocket and the arene-binding site (*69,71*).

Based on these structural insights a lot of PSMA-targeted radioligands were designed and further optimized corresponding to pharmacological needs. In the next chapter, so far published results of clinical trials of several ligands aiming for PCa imaging and/or therapy are presented.

3. Clinical Relevance of PSMA-Targeted Radioligands

3.1. Agents for Imaging

In this chapter, FDA-approved PSMA-targeted imaging agents as well as promising clinical candidates are presented. Respective structures are depicted in **Figure 5**.

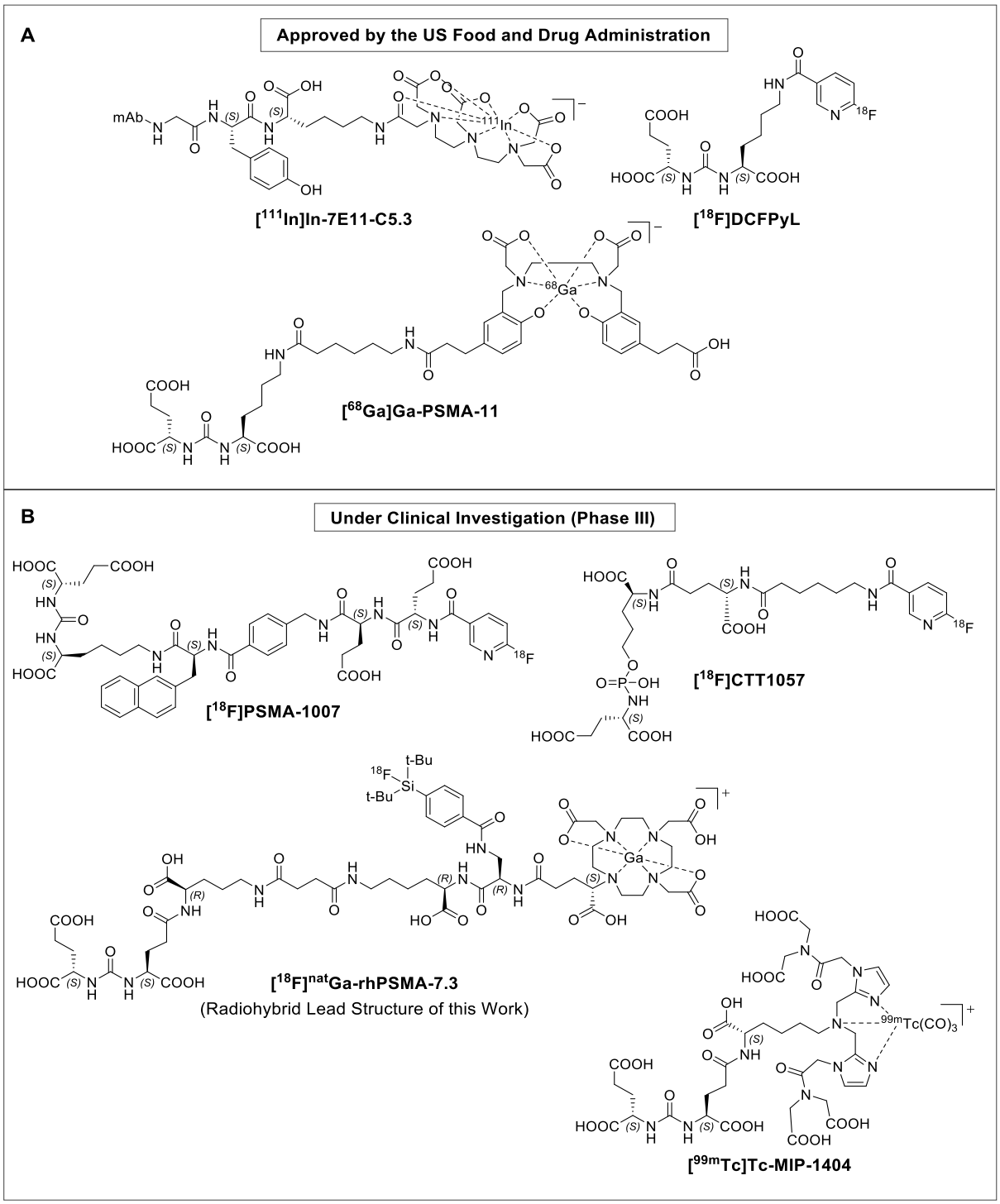

Figure 5: Structures of **A:** the FDA-approved agents [^{111}In]In-7E11-C5.3 (only the conjugation side of the chelator for labeling depicted, mAb = monoclonal antibody) for immunoscintigraphy, [^{68}Ga]Ga-PSMA-11 and [^{18}F]DCFPyL for PET imaging; **B:** clinical candidates in phase III studies [^{18}F]PSMA-1007, [^{18}F]CTT1075 and [^{18}F]^{nat}Ga-rhPSMA-7.3 for PET imaging as well as [^{99m}Tc]Tc-MIP-1404 for SPECT imaging (*72-78*).

All these ligands share the same principle of action. Their inherent PSMA-binding motif as part of the targeting vector is responsible for their accumulation in tumor tissue with up-regulated PSMA expression. The distribution of a radioligand is then retraced utilizing the attached radioactive label. Depending on the type of emitted particles during radioactive decay, different types of imaging modalities can be used for particle detection (positron emission tomography (PET): β^+-emission; single-photon emission computed tomography (SPECT): γ-emission) (*79*).

[^{111}In]In-7E11-C5.3 ([^{111}In]In-CYT-356, Indium In 111 Capromab Pendetide, Prostascint®)

The ^{111}In-labled, murine monoclonal antibody was characterized for the recognition of an intracellular epitope of PSMA (MWNLLH) (*80*). Thus, PSMA-mediated binding is limited to prostate cancer cells undergoing apoptosis or necrosis (*81*). Nevertheless, [^{111}In]In-7E11-C5.3 was already approved by the FDA as imaging agent for immunoscintigraphy in 1996 briefly after the discovery of PSMA as potential tumor marker (*82*). Obviously, for an antibody opposed to a small molecule ligand, the comparably slow pharmacokinetics (respective urinary excretion for [^{111}In]In-7E11-C5.3 and [^{68}Ga]Ga-PSMA-11: 10% at 72 h p.i. vs 14% at 2 h p.i.) are accompanied by some drawbacks like higher absorbed doses for the total body ([^{111}In]In-7E11-C5.3: 27 mGy/185 MBq vs. [^{68}Ga]Ga-PSMA-11: 3.7 mGy/259 MBq) and late image acquisition ([^{111}In]In-7E11-C5.3: 72–120 h p.i. vs. [^{68}Ga]Ga-PSMA-11: 50–100 min p.i.) (*73,75*). Nevertheless, in a group of presurgical patients (n = 152) sensitivity, specificity, positive predictive value (PPV) and negative predictive value (NPV) were determined as 62%, 72%, 62% and 72%, respectively (*75*).

[^{68}Ga]Ga-PSMA-11 (Gallium Ga 68 Gozetotide, (ILLUCCIX®/LOCAMETZ®)

[^{68}Ga]Ga-PSMA-11 was the first PSMA-targeted PET tracer approved by the FDA (December 2020) (*83*). Numerous clinical trials investigated its diagnostic accuracy in PCa patients. The FDA approval was based on two clinical prospective phase III trials (*73*). The PSMA PreRP trial (NCT02919111) focused on the evaluation of [^{68}Ga]Ga-PSMA-11 prior to subsequent radical prostatectomy and pelvic lymph node dissection (PLND) in an intermediate to high-risk patient cohort with biopsy-proven PCa. Meanwhile, more data are available by including two further trials (NCT03368547, NCT02611882). The most recent respective review by *Hope et al.* summarizes results of patients (n = 277) who received [^{68}Ga]Ga-PSMA-11 PET imaging scans for primary staging. Findings were validated by histopathology and revealed a sensitivity, specificity, PPV and NPV for pelvic nodal metastases of 40%, 95%, 75% and 81%, respectively (*84*).

The second study offering the basis for approval could clearly demonstrate a correlation of biochemical recurrence indicated by PSA level with positive findings in PET scans (NCT02940262 and NCT02918357) (*85*). A total of 635 patients was enrolled prior to radical prostatectomy, radiation therapy or both. In this cohort with a median PSA level of 2.1 ng/mL an overall detection rate of 75% was observed (*85*). In the cohort of 628 evaluable patients a dramatic increased

portion of positive PET scans was observed for patients with higher PSA levels (≥2 ng/mL: 91% vs. <0.5 ng/mL: 36%) (*73*). Furthermore, a significant advantage of [^{68}Ga]Ga-PSMA-11 over the competing [^{18}F]-fluciclovine in localizing early biochemical recurrence could be demonstrated (*86*). Currently, [^{68}Ga]Ga-PSMA-11 is also indicated for patient selection considering PRLT with Lutetium Lu 177 vipivotide tetraxetan ([^{177}Lu]Lu-PSMA-617) (*87,88*). Possibly, the PSMA-11 scaffold might also find its application as [^{18}F]AlF-labeled tracer following the clinical comparison of a phase III study (NCT03911310).

[^{18}F]DCFPyL (Piflufolastat F-18, PYLARIFY®)

Only a few months after the FDA approval of [^{68}Ga]Ga-PSMA-11 the second PSMA-targeted PET tracer [^{18}F]DCFPyL followed (May 2021) (*89*). One might suppose that the ^{18}F-labeled tracer providing a PET scan with higher resolution would have an impact on the clinical assessment (mean range of β^+ in H_2O [mm]: ^{68}Ga = 2.24 vs. ^{18}F = 0.64 mm) (*90*). However, the OSPREY trial (NCT02981368) investigating biopsy-proven PCa patients (n = 252) prior to radical prostatectomy and PLND exhibited quite comparable results for sensitivity, specificity, PPV and NPV for pelvic nodal metastases of 40.3%, 97.9%, 86.7% and 83.2%, respectively (*72,91*). Moreover, in a group of 199 evaluable patients the portion of positive PET scans in correlation with the determined PSA level resulted in a similar pattern in respect to [^{68}Ga]Ga-PSMA-11 (≥ 2 ng/mL: 90% vs. <0.5 ng/mL: 35%) in the CONDOR trial (NCT03739684) (*72,92*).

Further Imaging Agents under Clinical Investigations

Several other promising ^{18}F-labeled PSMA PET tracers are currently under clinical investigations in phase III studies, for example [^{18}F]PSMA-1007 structurally derived from the mainly therapeutically used PSMA-617 (NCT04102553, NCT04644822, NCT04742361, NCT04794777, NCT05079828) (*93,94*), [^{18}F]CTT1057 as one representative with the rarely incorporated phosphoramidate-based binding motif (*95*) characterized for its (pseudo-)irreversible target binding (NCT04838626, NCT04838613) and [^{18}F]^{nat}Ga-rhPSM-7.3 exploiting a novel radiohybrid concept by the structural combination of DOTAGA for the complexation of (radio)metal cations and an additional silicon-based fluoride acceptor (SiFA) for facilitated ^{18}F-fluorinations with high molar activities under mild conditions (*76*). The latter was previously developed by our group and is now tested for its applicability as tracer for newly diagnosed PCa (LIGHTHOUSE, NCT04186819, n = 356 patients) as well as for the recurrent stage (SPOTLIGHT, NCT04186845, n = 391 patients). First results of the SPOTLIGHT trial were recently reported and revealed a higher detection rate in correlation with PSA-level compared with the previously approved ligands [^{68}Ga]Ga-PSMA-11 and [^{18}F]DCFPyL (5> PSA ≥2 ng/mL: 96%; <0.5 ng/mL: 64%) emphasizing the potential of an ensuing approval (*96*).

A candidate as imaging agent for SPECT is [^{99m}Tc]Tc-MIP-1404 (Technetium Tc 99m Trofolastat). The clinical phase III trial prospect-AS (NCT02615067) investigates the sensitivity and specificity

in 531 enrolled participants with biopsy proven low-grade PCa (Gleason score ≤ 3 + 4). A prior phase II study (NCT01667536) demonstrated a sensitivity of 50% and specificity of 87% in a patient cohort (n = 105) with intermediate- to high-grade PCa before radical prostatectomy and PLND (*97*).

In summary, the first FDA-approved PSMA-targeted imaging agents are available and further promising candidates are in the pipeline. Data demonstrate PSMA-targeted imaging as a valuable opportunity for the detection and localization of metastases in PCa patients facilitating the staging of the disease and thus, support the clinical decision-making.

3.2. Agents for Endoradiotherapy

As described for imaging agents, the PSMA binding motif within radioligands is utilized for target-mediated activity accumulation in PSMA-positive tissues. However, one major difference between diagnostic and therapeutic compounds constitutes the applied radionuclide. In contrast to diagnostic compounds, the α- or β^--particles emitted by radionuclides applied in endoradiotherapy exhibit a distinctly higher linear energy transfer (LET). This increases the probability of cytotoxic events, like DNA double-strand breaks, in proximity to radioligand accumulation. As a consequence, apoptosis of target-expressing tumor cells is provoked (*79*).

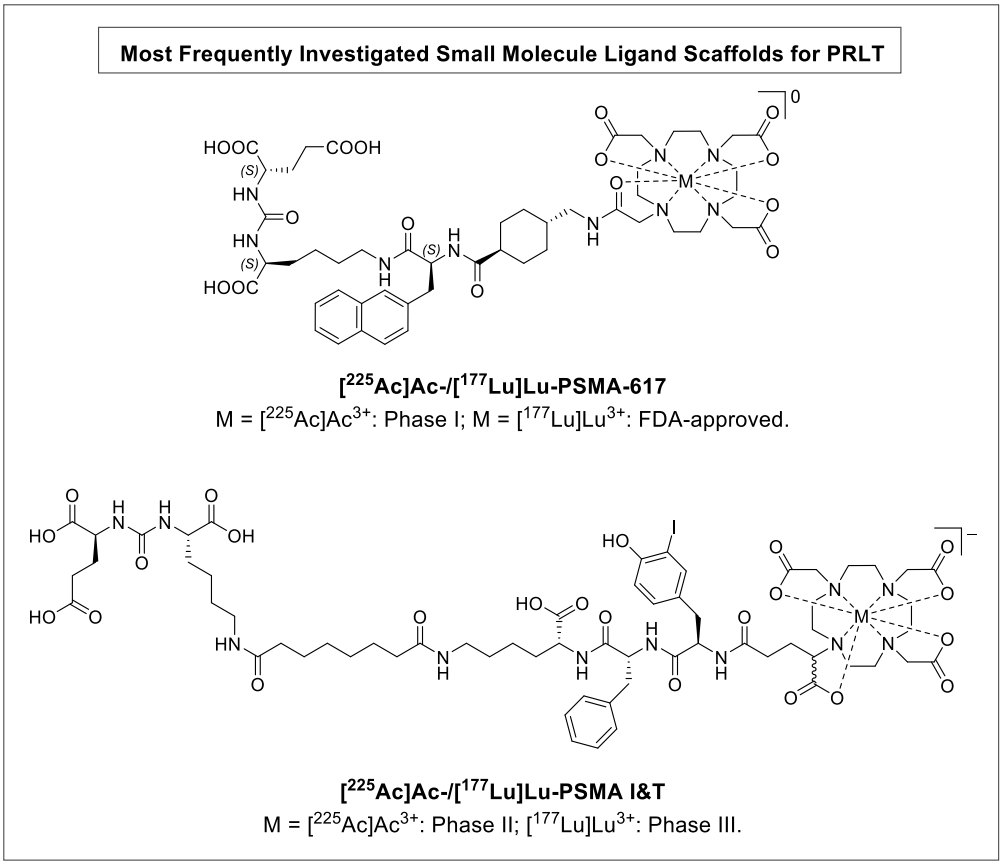

Figure 6: Structures of the FDA-approved therapeutic agent [^{177}Lu]Lu-PSMA-617, its ^{225}Ac-labeled counterpart under clinical investigation as well as the clinical candidates [^{177}Lu]Lu-PSMA I&T and [^{225}Ac]Ac-PSMA I&T (*98,99*).

The two PSMA-targeted therapeutic agents with most available clinical data are the FDA-approved [^{177}Lu]Lu-PSMA-617 and [^{177}Lu]Lu-PSMA I&T (clinical phase III). Both respective chelators within the peptide scaffolds alternatively offer the opportunity for ^{225}Ac-labeling. The corresponding ^{225}Ac-compounds are currently under clinical investigation as well (**Figure 6**).

[^{177}Lu]Lu-PSMA-617 (Lutetium Lu 177 vipivotide tetraxetan, PLUVICTO™)

So far, [^{177}Lu]Lu-PSMA-617 is the only PSMA-targeted agent with an FDA-approval (March 2022) for a therapeutic application (*34*). Based on results of the clinical phase III trial VISION (NCT03511664, n = 831 patients) the indication of the radiopharmaceutical is currently limited to PSMA-positive mCRPC patients after prior ADT with at minimum one androgen receptor pathway inhibitor (ARPI) and taxane-based chemotherapy (*88,100*). The trial compared the benefit of an additional treatment with [^{177}Lu]Lu-PSMA-617 (median number of cycles: 5, median cumulative dose: 37.5 GBq, n = 551 patients) and the best standard of care (BSoC) opposed to the BSoC alone (n = 280 patients). Indeed, comparing the intervention group with the control group the imaging-based progression-free survival (8.7 months vs. 3.4 months) as well as the overall survival (15.3 months vs. 11.3 months) were clearly prolonged (*100*). The most common adverse events in the intervention group vs. control group regarding all grades were fatigue (43.1% vs. 22.9%), xerostomia (38.8% vs. 0.5%) and nausea (35.3% vs. 16.6%) albeit rarely of grade ≥3 (*100*). Occurrences of severe toxicities of grade 3 to 5 in the intervention group vs. the control group explicitly listed in the prescribing information (*88*) and as part of the safety topics of interest in the trial-related publication by *Sartor et al.* are myelosuppression (23.4% vs. 6.8%) and renal toxicity (3.4% vs. 2.9%) (*100*).

As a consequence of the overall favorable clinical performance, several further studies currently focus on the applicability of [^{177}Lu]Lu-PSMA-617 in the treatment of PCa-positive patients in earlier clinical settings. In the phase III trial PSMAfore (NCT04689828) the efficacy of [^{177}Lu]Lu-PSMA-617 in combination with first-line ADT opposed to ADT with a second-line ARPI is tested in taxane-naïve mCRPC patients (n = 450) supported by BSoC in both groups (*101*).

The PSMAddition trial (phase III, NCT04720157) will compare the use of PRLT plus BSoC vs. BSoC alone including ADT as part of BSoC in both groups. In this study, about 1126 metastasized hormone-sensitive prostate cancer (mHSPC) patients without or minimal prior ADT shell be examined (*102*).

Following a study update in the BULLSEYE trial (phase II, NCT04443062) the use of [^{177}Lu]Lu-PSMA-617 instead of the former [^{177}Lu]Lu-PSMA I&T is investigated in comparison to ADT in a small patient cohort (n = 58) even in an oligo-metastatic hormone-sensitive stage (*103*). Many more trials about [^{177}Lu]Lu-PSMA-617 are registered at the moment. An overview is provided by *Keam et al.* (*104*).

[^{225}Ac]Ac-PSMA-617

A shift in the applied radioisotope from the β^--emitting lutetium-177 to the α-emitting actinium-225 might have beneficial effects in PRLT. β^--particles are characterized by a comparably longer range in tissue (670 µm for lutetium-177 (*105*)) resulting in a crossfire effect useful in the treatment of malignant tissues with heterogeneous target expression but at the cost of a proportionally higher radiation burden for healthy tissue. In contrast, α-particles exhibit a shorter range (47–85 µm for actinium-225 (*106*)) in tissue and a high linear energy transfer (LET) potentially leading to a more target-specific dose delivery and an improved biological effectiveness against target-expressing cells (*107,108*).

Despite the favorable dosimetry and proven efficacy of [^{177}Lu]Lu-PSMA-617 (*100,109*), diffuse red marrow infiltration has been considered as contraindication due to possibly relevant hematotoxicity (*110*). Inspired by results of targeted α-radiation therapy (TAT) with [^{213}Bi]Bi-DOTATOC, *Kratochwil et al.* investigated the potential of [^{225}Ac]Ac-PSMA-617 to reduce hematologic toxicity in patients with diffuse red marrow infiltration as well as to perhaps overcome radioresistance to β^--particle emitters. Both questions were addressed in the treatment of corresponding patients **A** and **B** as an initial experience. Respective [^{68}Ga]Ga-PSMA-11 PET/CT scans performed for (re-)staging (**Figure 7**) highlight an encouraging imaging response corroborated by a significant PSA decline *(110)*.

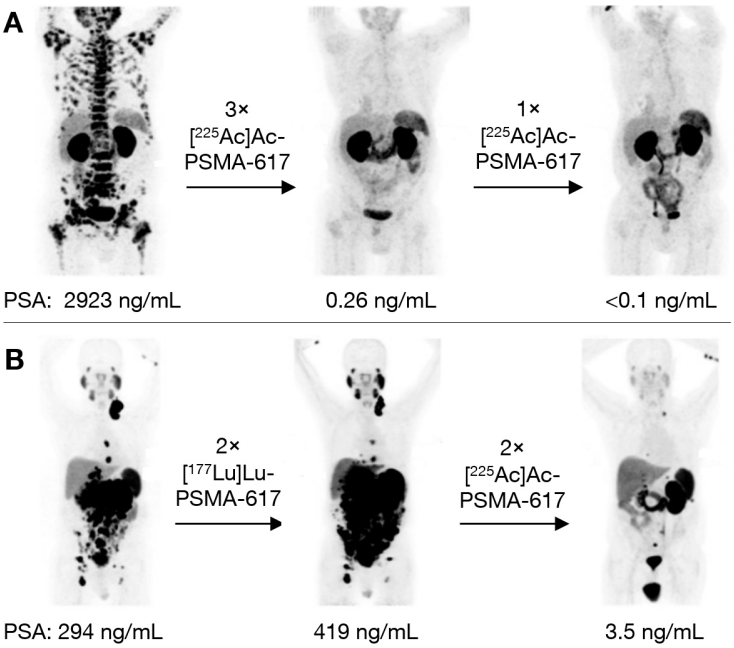

Figure 7: [^{68}Ga]Ga-PSMA PET/CT scans of patient **A:** staging before PRLT (left), restaging 2 months after 3rd cycle (middle) and 2 months after 4th cycle (right) of [^{225}Ac]Ac-PSMA-617; and patient **B:** staging before PRLT (left), restaging 2 months after 2 cycles of [^{177}Lu]Lu-PSMA-617 (middle) and restaging after 2 cycles of [^{225}Ac]Ac-PSMA-617 (right); scan after 3rd cycle (PSA <0.1 ng/mL) of [^{225}Ac]Ac-PSMA-617 not shown; adapted from *Kratochwil et al.* (*110*).

A systematic review on clinical data about [^{225}Ac]Ac-PSMA-617 TAT in end-stage mCRPC patients (n = 141 patients of 3 studies) is provided by *Ballal et al*. A median progression-free survival of 12 months was reported in the three included studies. The median overall survival was 17 months as determined in two of the three studies (n = 101 patients). The most common side effects were xerostomia (grade 1–2: 63%) and fatigue (grade 1–2: 45%). Only few severe hematological toxicities of grade 3 occurred (anemia: 6%; leukopenia: 2%, thrombocytopenia: 1%) as well as rare nephrotoxicity of grade ≥3 (5%) (*111-114*). Thus, the so far available data suggest a superior performance of the ^{225}Ac-labeled ligand regarding efficacy and hematological toxicity.

More information will be collected by the AcTION study (phase I, n = 60, NCT04597411). This dose escalation study is currently investigating [^{225}Ac]Ac-PSMA-617 in mCRPC patients with three different prior treatment regimens (chemotherapy and ADT with a second-line ARPI vs. first-line ADT vs. PRLT with [^{177}Lu]Lu-PSMA-617 or -PSMA I&T).

[^{177}Lu]Lu-PSMA I&T ([^{177}Lu]Lu-PNT2002)

[^{177}Lu]Lu-PSMA I&T was previously developed by our group (*99,115*). Most recently, a comparison with [^{177}Lu]Lu-PSMA-617 was published regarding their clinical performance in a cohort of 138 mCRPC patients. Results indicate a faster pharmacokinetic profile for [^{177}Lu]Lu-PSMA I&T with a higher initial tumor uptake but a faster whole-body clearance including a shorter tumor half-live and leading to a comparable mean absorbed tumor dose. Interestingly, despite the faster pharmacokinetics a slightly increased absorbed kidney dose was observed for [^{177}Lu]Lu-PSMA I&T (*116*).

Currently, two clinical phase III studies in a recruiting status are registered in the ClinicalTrials.gov database. In the SPLASH trial (NCT04647526) the benefit of PRLT vs. ADT with abiraterone or enzalutamide is tested in chemotherapy-naïve mCRPC patients after prior second-line ADT (n = 415). In the other phase III trial (NCT05204927, also referred to as ECLIPSE trial by the sponsor) mCRPC patients (n = 400) will either receive PRLT or standard of care ADT (abiraterone with prednisone or enzalutamide).

[^{225}Ac]Ac-PSMA I&T

Analogously to PSMA-617, the shift of the radioisotope from lutetium-177 to actinium-225 was also examined with the ligand PSMA I&T. *Zacherl et al.* previously reported first results of TAT with [^{225}Ac]Ac-PSMA I&T in a small cohort of 14 mCRPC patients who predominantly received exhaustive prior treatment with second-line ADT, chemotherapy as well as ^{177}Lu-PRLT. As expected, hematological toxicities and xerostomia partially occurred while a PSA decline of ≥50% was observed in half of the cohort (*117*). The investigation of the efficacy of [^{225}Ac]Ac-PSMA I&T in mCRPC patients will be extended by the phase II TATCIST trial (NCT05219500, n = 100 patients).

Further Clinical Candidates for PRLT

In **Figure 8**, structures of four more candidates currently under clinical investigation are depicted. The monoclonal antibody (mAb) J591 was first developed in the year 1997 and was characterized for the binding of an extracellular epitope of PSMA (*118*). Since then, several clinical studies examined the applicability as [^{177}Lu]Lu-DOTA-conjugate in PRLT (e.g. phase II, n = 47: NCT00195039; phase II, n = 55: NCT00859781). Interestingly, the antibody does not only exhibit expected slower distribution kinetics and longer tumor retention compared to small molecule ligands but also displays a lower uptake in organs with physiological PSMA expression, namely in lacrimal and salivary glands as well as in kidneys. An impressive dose-dependent overall survival of up to 42.3 months in the high-dose cohort of mCRPC patients was observed. However, the slow pharmacokinetics render widespread myelosuppression as a dose-limiting factor with frequently occurring grade ≥3 hematotoxicities (*119,120*). Thus, more recent studies focus on the ^{225}Ac-labeled antibody potentially showing reduced myelosuppression while maintaining or even enhancing the efficacy (PRLT, phase I/II, n = 105: NCT04506567; PRLT + immunotherapy, phase I/II, n = 76: NCT04946370).

Optimizing the pharmacokinetics to find a sweet spot outbalancing efficacy against the risk of myelosuppression, some groups developed small molecule PSMA ligands decorated with entities binding to human serum albumin (HSA) (*121,122*). This way, the altered affinity of the ligands towards HSA as most abundant plasma protein can be exploited to modulate the blood clearance (*123*). Examples for PSMA ligands modified with entities known for their strong HSA binding are [^{177}Lu]Lu-EB-PSMA-617 (modified with a truncated Evans Blue entity) and [^{177}Lu]Lu-CTT1403 (modified with a 4-(*p*-iodophenyl)butyric acyl entity) (*121,122*). Both ligands are situated in clinical phase I studies at the moment (NCT03780075, n = 50; and NCT03822871, n = 40, respectively).

Besides [^{18}F]^{nat}Ga-rhPSMA-7.3, which is currently investigated for its diagnostic performance, [^{177}Lu]Lu-rhPSMA-10.1 is another member of the radiohybrid family developed for PRLT by our group. Herein, the radiohybrid unit comprises of DOTA as chelator for complexation of (radio)metal cations and – analogously to rhPSMA-7.3 – a SiFA group for mild and fast ^{18}F-labelings, both connected *via* a trifunctional linker. Thus, a theranostic approach is possible utilizing only Lu-rhPSMA-10.1 either radiolabeled with lutetium-177 for therapy or fluorine-18 for PET imaging. However, in the latest phase I/II study (NCT05413850, n = 150) validating the anti-tumor activity of [^{177}Lu]Lu-rhPSMA-10.1 in 150 mCRPC patients, their lesions will be verified as PSMA-positive by [^{18}F]^{nat}Ga-rhPSMA-7.3 PET imaging as part of the recruitment process.

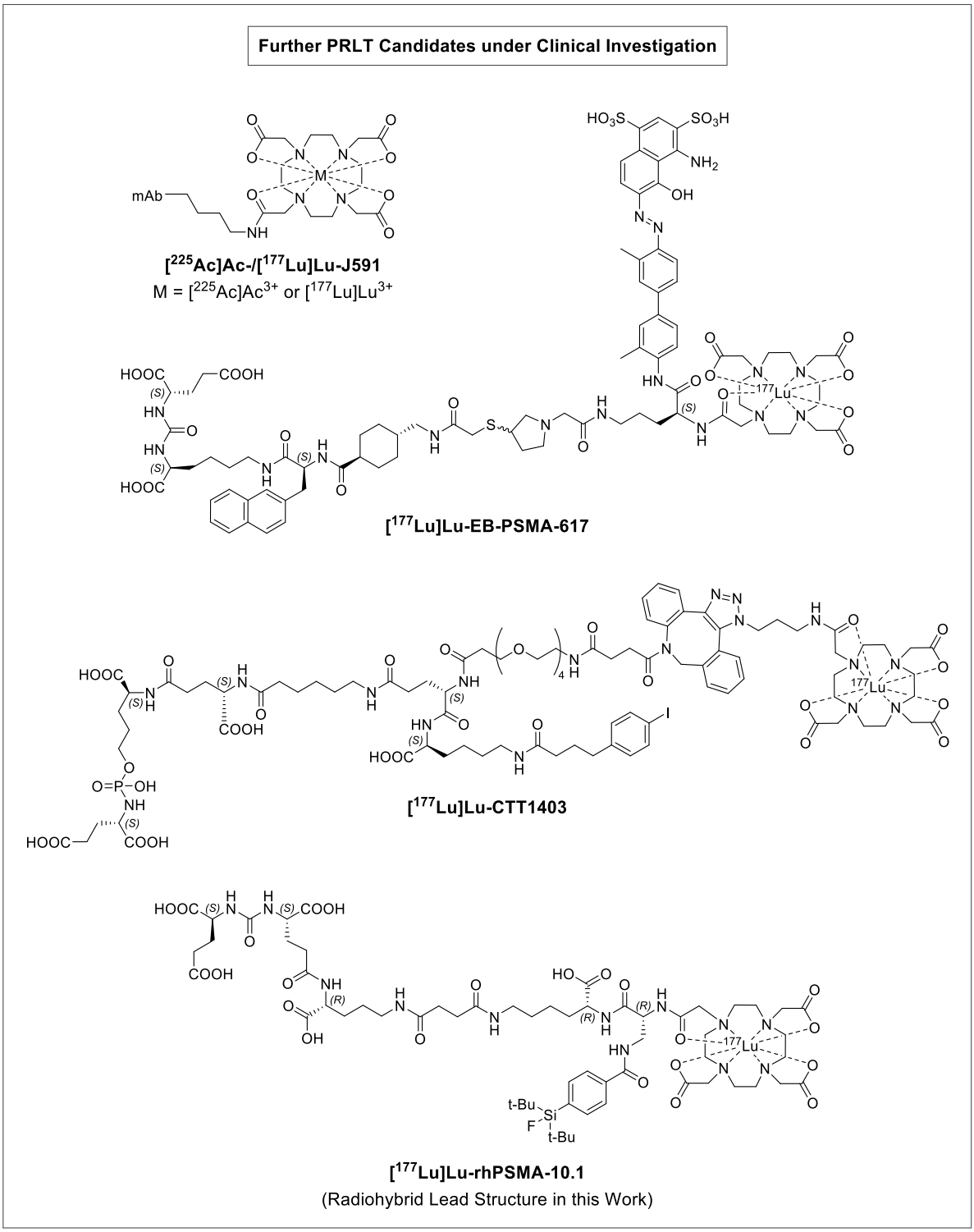

Figure 8: Structures of further clinical candidates under investigation for therapeutic application in PRLT: the monoclonal antibody [^{225}Ac]Ac-/[^{177}Lu]Lu-J591 (only conjugation side of the chelator for labeling depicted, mAb = monoclonal antibody), the 'truncated Evans Blue'-modified [^{177}Lu]Lu-EB-PSMA-617, [^{177}Lu]Lu-CTT1403 with the phosphoramidate-based binding motif and the 4-(*p*-iodophenyl)butyric acid as albumin binder and the radiohybrid compound [^{177}Lu]Lu-rhPSMA-10.1 suitable for orthogonal ^{18}F- or ^{225}Ac-/^{177}Lu-labeling (*121,122,124,125*).

In conclusion, as the first FDA-approved radiopharmaceutical [^{177}Lu]Lu-PSMA-617 displays the gold standard for PRLT up to date with most important limitations arising from myelosuppression and renal toxicity. On the other hand, previous clinical results of antibody-mediated PRLT hint for

a comparably superior efficacy as indicated by a significant prolonged overall survival but at the cost of more frequent and severe myelosuppression. Consequently, a modulation towards a blood clearance allowing for an optimized efficacy as well as minor hematologic toxicities is desirable. First small molecule-based candidates with intentionally prolonged plasma half-lives entered a clinical stage investigating a potential pharmacokinetic sweet spot. An alternative approach to boost the efficacy of fast-clearing compounds accompanied by a dose reduction for non-target tissue might constitute the shift of the radioactive label to an α-particle emitting isotope like actinium-225. Independently, the radiohybrid concept realized in rhPSMA compounds combining a chelator with a SiFA entity offers a unique theranostic approach described more closely in the next chapter.

4. Silicon-based Fluoride Acceptors in the Radiohybrid Concept

4.1. Truly Theranostic Ligand Design

In the past, predominantly two different radiopharmaceuticals were required for respective diagnostic and therapeutic purposes. This is exemplified by a recommended patient selection and therapy control using [^{68}Ga]Ga-PSMA-11 for PET imaging in PRLT with [^{177}Lu]Lu-PSMA-617 (*88*). Although declared as theranostic agent, even the labeling of PSMA I&T necessitates the use of two different radiometals for imaging (e.g. gallium-68) and therapy (e.g. lutetium-177) ending up in a pair of ligands with chemically different properties (*99*). However, the chemical properties of a compound directly affect its pharmacokinetics. Thus, results of dosimetry calculations obtained for the diagnostic ligand cannot directly be translated into the performance of a different therapeutic compound. In contrast, the radiohybrid concept as introduced by *Wurzer et al.* is allowing for a truly theranostic approach with a pair of chemically identical twins. This is accomplished by the combination of two entities within one ligand structure: 1) a chelator for (radio)metal complexation (e.g. Lu) and 2) a silicon-based fluoride acceptor (SiFA) suitable for ^{18}F-labeling *via* an isotopic exchange reaction (*126*). This concept is visualized in **Figure 9.**

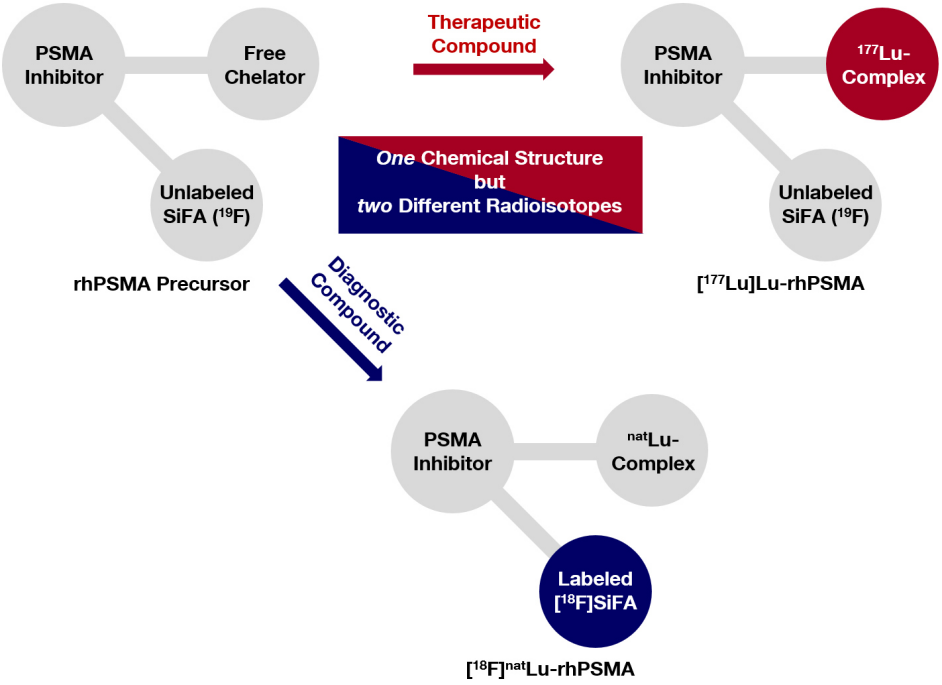

Figure 9: Illustration of the radiohybrid concept using a chelator and a SiFA group as orthogonal labeling entities for a truly theranostic approach; adapted from *Wurzer et al.* (*126*).

Such radiohybrid compounds offer the unique opportunity of utilizing one pair of differently labeled radiopharmaceuticals but with the same pharmacokinetics and distribution profile for initial staging, therapy and therapy control. With this tool in hand, there is a great potential for precise patient-specific dosimetry calculations representing one step closer to personalized medicine.

Having this theranostic concept in mind, two questions were met in the radiohybrid design by *Wurzer et al.* – which nuclides should be chosen and which labeling strategies should be applied? While DOTA and DOTAGA allow for a flexible labeling compatibility with the commonly used therapeutic radiometal ions, the diagnostic nuclide should exhibit favorable radiopharmaceutical properties and should be easily installed *via* an orthogonal, efficient labeling strategy. Background information supporting the chosen design are provided in the next chapter.

4.2. Fluorine-18: Properties and Labeling Strategies

Fluorine-18 is an attractive radioisotope for PET imaging with a high positron decay ratio (97%) and a comparably low positron energy (maximum: 0.635 MeV). The latter leads to a short tissue range until subsequent annihilation (maximum: <2.4 mm; mean: 0.64 mm). This small spatial offset between the origin of decay and the annihilation event is one important parameter for high image resolution. Furthermore, the half-life of 110 min is within a reasonable range for clinical patient management and dosimetry (*90,127,128*). Opposed to the competing PET nuclide gallium-68 received by ^{68}Ge/^{68}Ga-generator in limited quantities, a good availability of high activities is provided by the production of aqueous [^{18}F]fluoride solutions in onsite or nearby cyclotron facilities *via* the nuclear reaction ^{18}O(*p,n*)^{18}F (*128,129*).

These favorable radiopharmaceutical properties encouraged investigations regarding facile and efficient ^{18}F-labeling procedures. *Piron et al*. most recently published an overview about methods applied in the design of PSMA ligands focusing on fluorinations *via* carbon–, aluminum– and silicon–fluoride bond formation (*76*).

Common synthesis routes for the ^{18}F-labeling of (hetero)arene entities as prosthetic group in peptide ligands are based on the use of their respective trimethylammonium-substituted precursors. Classically, their labeling routes involve at least two reaction steps by either: 1) indirect labeling by fluorination of the prosthetic group prior to the subsequent coupling to the targeting vector or: 2) the direct labeling of a protected precursor *via* an attached prosthetic group and a following deprotection step. In general, such routes can lead to time-consuming multi-step procedures requiring high precursor amounts, harsh reaction conditions, elevated temperatures and eventually high-performance liquid chromatography (HPLC) purification resulting in moderate radiochemical yields and molar activities (*76*). Well-known examples in the context of PSMA ligands are [^{18}F]DCFPyL and [^{18}F]CTT1057 (*76,130-132*). However, for some ligands multiple procedures are published and ambitious optimizations occasionally lead to simplified routes with only one step and improved radiochemical yields as reflected by [^{18}F]PSMA-1007 (*133*).

A different, more kit-like approach with similarity to Ga-chelation displays the complexation of [^{18}F]AlF^{2+} under simple reaction conditions ([^{18}F]fluoride, $AlCl_3$, ~pH 4 e.g. by NaOAc, EtOH, chelating agent) by applying either open chain (e.g. HBED-CC) or cyclic chelators (e.g. NOTA). Though, a pentadentate chelation (N_3O_2 donor set) of the [^{18}F]AlF^{2+}-ion is clearly preferred with

respect to stability (*134*). Thus, it is comprehensible that *Lütje et al.* observed a strong formulation-dependent stability and found an increased bone uptake in biodistributions comparing [^{18}F]AlF-PSMA-11 with [^{68}Ga]Ga-PSMA-11 (5.0 ± 0.6%ID/g vs. 0.1 ± 0.0%ID/g) (*135*). Therefore, in favor of stability NOTA exhibits a superior suitability for [^{18}F]AlF^{2+}-chelation. However, the use of cyclic chelators requires higher temperatures (>100 °C) and impedes the application for heat-sensitive biomolecules. Consequently, efforts have been made to increase the rigidity of open chain chelators to preserve high conversions at mild temperatures while optimizing the stability. So far, the chelator (±)-H_3RESCA displays an interesting candidate for a mild and fast labeling (*136*).

Currently, a few PSMA ligands were labeled *via* the AlF-method (*76,134*). The NOTA-bearing [^{18}F]Bi-PSMA displays one example for a feasible upscaled automated one-step synthesis with a high non-decay corrected radiochemical yield of 43.2 ± 6.0% in an overall synthesis time of 30 min (reaction at 105 °C for 15 min) and a remarkable molar activity of 78–230 GBq/µmol (*76,137*). However, as the AlF-method belongs to the metal-based approaches and requires chelators sharing structural similarity with DOTA and DOTAGA intended for the chelation of therapeutic nuclides in our radiohybrid concept, the optimization for orthogonal reaction conditions is expected to become an issue.

Instead, the decision was made to install a silicon-based fluoride acceptor as a prosthetic group. The first [^{18}F]F–Si compound tested *in vivo* was [^{18}F]fluorotrimethylsilane in 1985 by *Rosenthal et al.* observing rapid defluorination by hydrolysis. Nevertheless, the facile labeling was emphasized to indicate a radiopharmaceutical utility and already back then, it was hypothesized to achieve an increased stability by steric hindrance (*138*). This idea was resumed by *Schirrmacher et al.* comparing stabilities of [^{18}F]fluorosilanes with different bulky substituents (trend of stability: Ph_3SiF << *t*$BuPh_2SiF$ < *t*Bu_2PhSiF). Their best candidate was further functionalized at the phenyl moiety for conjugation to an octreotate derivative. This ligand was ^{18}F-labeled following two different routes either applying a dry $^{18}F^-$/Kryptofix 2.2.2./K^+ solution in acetonitrile at rt for 10–15 min or even directly commercially available $^{18}F^-$/[^{18}O]H_2O with a need for heating to 95 °C for 30 min. Both methods demonstrated the feasibility of fast and convenient labeling procedures and cartridge-based purification for SiFA compounds resulting in molar activities of 3–5 GBq/µmol on a laboratory scale (*139*). Later on, extensive studies were undertaken by *Höhne et al.* investigating the influence of different functional groups on hydrolytic half-lives *in vitro*. Additionally, they could proof a stability with no detectable degradation of a SiFA-conjugated bombesin analog after 2 h at 37 °C in PBS as well as in mouse plasma *(140)*.

Whereas this new class of labeling synthons with access to a convenient, simple and efficient labeling procedure was determined to potentially exhibit a sufficient stability for *in vivo* applications, the bulky lipophilic silane substituents display a challenge in terms of pharmacokinetic performance. This is well illustrated in the development of the SiFA*lin*-modified

TATE published by *Niedermoser et al.* (*141*). The investigators tried to outbalance the lipophilicity of the SiFA building block by the introduction of a sugar moiety at the linker in between the pharmacophore and the prosthetic group. However, further steps were required to induce a shift from the dominating hepatobiliary to a renal excretion and to enhance tumor-to-background ratios. This was accomplished by two additional carboxylic acids in the linker region and the substitution of the SiFA moiety to the related SiFA*lin* entity ($SiFAN^+Br^-$, first developed by *Kostikov et al.* (*142*)) carrying a positively charged tetraalkylammonium ion as conjugation side at the phenyl substituent (*141*). The drastic effect on the pharmacokinetics is depicted in **Figure 10**.

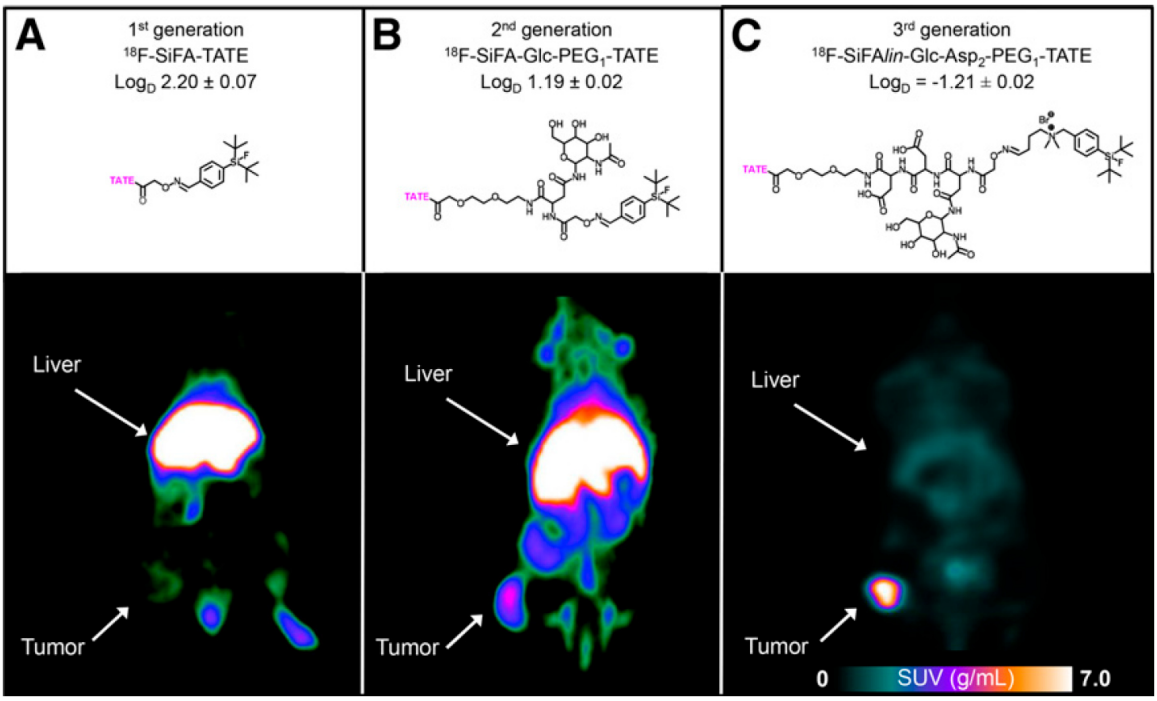

Figure 10: Development steps of SiFA-modified somatostatin analogs and the respective impact on the biodistribution in AR42J tumor-bearing mice visualized in PET images (figure by *Niedermoser et al.* (*141*)).

The translation of the novel SiFA approach into a radiohybrid PSMA ligand with a predominantly renal excretion by *Wurzer et al*. required less effort regarding hydrophilic modifiers. Utilizing a hydrophilic chelator as part of the radiohybrid concept in combination with a PSMA ligand including the highly polar standard binding motif X-urea-Glu seems like a perfectly suited prerequisite for the technology transfer. Even though the implementation of the SiFA entity was accompanied by a remarkably strong HSA binding and a slower blood clearance compared to [^{18}F]DCFPyL and [^{18}F]PSMA-1007 as a reference, the biodistribution revealed a high tumor targeting potential, a low kidney retention and no elevated bone uptake indicating a sufficient stability of the ^{18}F-labeled SiFA compound (*126*). As a consequence of the promising *in vivo* performance of [^{18}F]^{nat}Ga-rhPSMA-7 containing a mixture of four isomers, a direct preclinical comparison was strived for to elucidate the best candidate for clinical translation. For optimal comparability, biodistribution studies with the isomeric mixture were conducted. Subsequently, the mixture was extracted from organs of interest and the proportion of each isomer in the

respective extracts was determined by radio-HPLC. Finally, [^{18}F]^{nat}Ga-rhPSMA-7.3 was proposed as isomer of choice exhibiting a favorable compromise with a desirable high tumor accumulation and moderate uptakes in blood, kidney and liver samples (*77*).

To ensure the availability for clinical application, an optimized automated synthesis was established based on the experience of >200 routine productions with [^{18}F]^{nat}Ga-rhPSMA-7 and [^{18}F]^{nat}Ga-rhPSMA-7.3. The whole automated production was completed in approximately 16 min. The reaction time of 5 min at rt using activities of 89 ± 14 GBq and a precursor amount of 150 nmol resulted in an average radiochemical yield of 49.2 ± 8.6% and an excellent molar activity of 291 ± 62 GBq/µmol (*143*).

In conclusion, the facile labeling of SiFA compounds under mild conditions with high radiochemical yields and molar activities as well as simple cartridge-based purification renders this labeling strategy as highly advantageous. The feasibility of an orthogonal use of SiFA-based prosthetic groups with a chelator for (radio)metal complexation as basis for the radiohybrid concept was proven by the investigation of the diagnostic pair [^{18}F]^{nat}Ga-rhPSMA-7.3 and [^{68}Ga]Ga-rhPSMA-7.3 (*126*).
The present know-how regarding the labeling strategy as well as the promising pharmaceutical experience with the diagnostic compound [^{18}F]^{nat}Ga-rhPSMA-7.3 ranging from *in vitro* experiments to a clinical level create a solid foundation as a lead structure for the development of a radiohybrid PSMA-targeted ligand optimized for the endoradiotherapy of prostate cancer.

5. Objectives

The radiohybrid concept as introduced by *Wurzer et al.* combines the use of a silicon-based fluoride acceptor as prosthetic group for a mild, convenient and efficient ^{18}F-labeling with a chelator for (radio)metal complexation within one compound. This unique approach previously resulted in the invention of the diagnostic twins [^{18}F]^{nat}Ga-rhPSMA-7.3 and [^{68}Ga]Ga-rhPSMA-7.3 for PET imaging of PSMA-positive prostate cancer. These diagnostic twins support two labeling options for the adaptation to clinical needs with respect to facility-specific conditions. Furthermore, this structural concept can be extended by the substitution with another (radio)metal (e.g. lutetium) suitable for endoradiotherapy and hence, offering a truly theranostic approach (*77,126*).

Motivated by the promising performance of the so far purely diagnostically applied compound [^{18}F]^{nat}Ga-rhPSMA-7.3 in clinical trials (NCT04186819, NCT04186845) (*96*), our primary objective in this work was the development of a radiohybrid PSMA ligand exhibiting a pharmacokinetic profile explicitly optimized for a therapeutic application. For this purpose, we chose the respective lutetium complex of rhPSMA-7.3 as lead structure. Depending on the nuclide selection, this approach is allowing for imaging with the ^{18}F-labeled compound or radiotherapy with the respective ^{177}Lu-complex while using the very same target vector.

To maximize the efficacy of PSMA-targeted radioligand therapy (PRLT) while minimizing adverse events in treated PCa patients, a fast distribution and high tumor-to-background ratio, especially for radiation-sensitive organs, are desirable. Currently, [^{177}Lu]Lu-PSMA-617 is the only FDA-approved radiopharmaceutical for PRLT in mCRPC patients and can thus be assessed as gold-standard (*34*). According to partially occurring myelosuppression and nephrotoxicity as severe side effects, the ligand's blood and kidney retention are rated as dose-limiting factors (*100*). Assuming a certain comparability of the performance of [^{177}Lu]Lu-PSMA-617 with [^{177}Lu]Lu-rhPSMA-7.3, we explored several strategies in this project to improve the tumor-to-blood and tumor-to-kidney ratios. **Figure 11** presents the structure of the lead compound rhPSMA-7.3 as lutetium complex as well as an overview of structural sites that we modified in order to optimize pharmacokinetics for a therapeutic use.

1. Metabolic Instability (MI ligands, **chapter III.1**): As PSMA expression is found in healthy proximal tubules in the kidneys (*44-46*), the kidney retention of PSMA ligands is partially caused by target-specific interactions. Thus, we investigated the insertion of peptide sequences – previously reported as metabolically instable – in between the PSMA-binding motif and the radioactive label. With this approach, we aimed for a cleavage of the ligands by enzymes mainly expressed in the kidneys to decrease renal, PSMA-mediated activity retention.

2. Branched Linker Constructs (BLC Ligands, **chapter III.2**): HSA binding is known to be one main parameter to influence the blood clearance kinetics and thus, has a direct impact on tumor-to-organ ratios (*122,144-147*). To facilitate the optimization of HSA binding, we designed and

investigated a scaffold allowing for a modular attachment of an HSA binding entity in a distant position to the PSMA binding motif. For this purpose, we inserted various additional linkers into the lead structure branching off the main peptide chain.

3. Reduced Net Charge (RNC Ligands, **chapter III.3**): Publications hint for the involvement of charged groups in renal tubular reabsorption mechanisms (*145,148-150*). Furthermore, the manipulation of a compound's HSA binding by the charge of functional groups in structural vicinity to the main HSA binding entity was demonstrated (*146*). Consequently, we studied the alteration of three carboxylic acids in the lead structure to optimize the blood clearance and kidney retention.

4. Modified SiFA Moieties (Model Peptides (MPs) and MSM Ligands, **chapter III.4**): As the SiFA moiety contained in the lead structure exhibits a strong HSA binding and limits the desired hydrophilicity of radiohybrid ligands *(125,126,141)*, we developed and evaluated a novel SiFA moiety in model peptides as well as in PSMA ligands. We designed this building block as readily modifiable to provide a simple approach for the adaptation of hydrophilicity and HSA binding of a compound corresponding to the required pharmacokinetic needs.

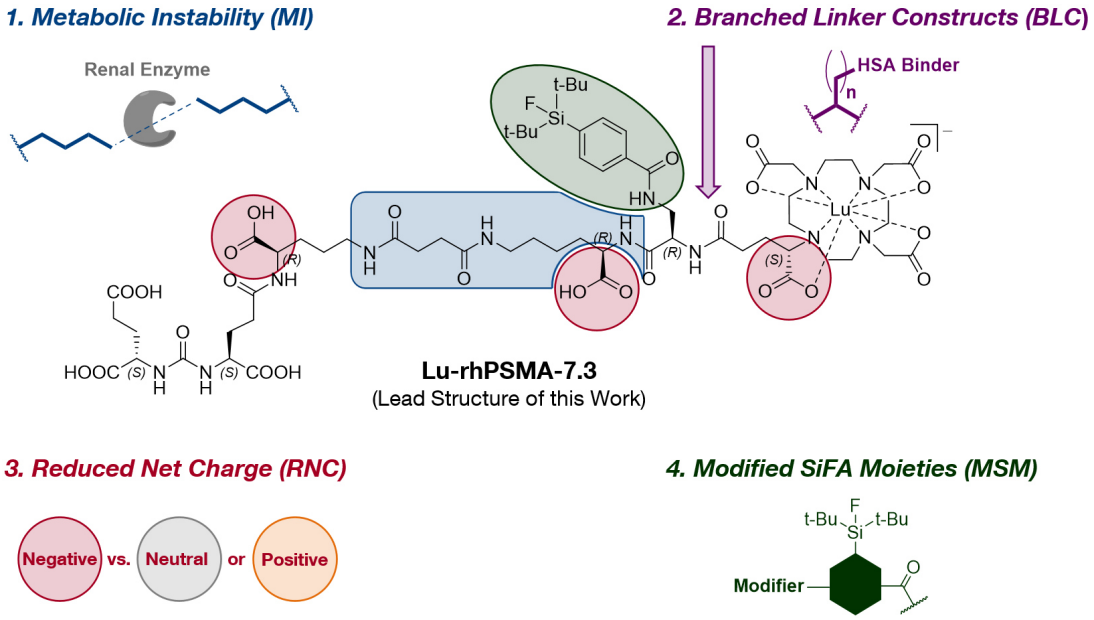

Figure 11: Overview of approaches investigated in this work and respective modification sites within the lead structure Lu-rhPSMA-7.3 aiming for an optimized blood clearance and a reduced kidney uptake.

To select the most promising compounds for subsequent animal experiments (biodistribution and µSPECT/CT imaging in tumor-bearing mice, metabolite analysis), we examined the fundamental *in vitro* properties as PSMA affinity and internalization into PSMA-expressing LNCaP cells, hydrophilicity ($logD_{pH\ 7.4}$) and HSA binding. To characterize a novel SiFA building block as prosthetic group for ^{18}F-labeling more closely, we conducted extended studies focusing on reactivity (radiochemical conversion/yield) and stability of the [^{18}F]F–Si bond within a set of model peptides.

II. MATERIAL AND METHODS

1. General Information

Chemicals: The protected amino acid analogs were purchased from Bachem (*Bubendorf, Switzerland*), Carbolution Chemicals (*St. Ingbert, Germany*) or Iris Biotech (*Marktredwitz, Germany*). The 2-chlorotritylchloride (2-CTC) resin was obtained from Sigma-Aldrich (*Steinheim, Germany*). Chematech (*Dijon, France*) delivered the chelators DOTA, DOTAGA and derivatives thereof. All necessary solvents and other organic reagents were purchased from either, Alfa Aesar *(Karlsruhe, Germany),* Sigma-Aldrich *(Steinheim, Germany),* Fluorochem *(Hadfield, United Kingdom)* or VWR *(Darmstadt, Germany*).

Devices for Synthesis: Solid phase synthesis of the peptides was carried out by manual operation using an Intelli-Mixer syringe shaker *(Neolab, Heidelberg, Germany).* pH values were measured with a SevenEasy pH-meter (*Mettler Toledo, Gießen, Germany*).

HPLC/ESI-MS: Analytical and preparative reversed-phase high-performance chromatography (RP-HPLC) was performed using Shimadzu gradient systems (*Shimadzu, Neufahrn, Germany*), each equipped with an SPD-20A UV/Vis detector (220 nm). A MultoKrom 100 C18 (150 × 4.6 mm, 5 µm particle size) column (*CS Chromatographie Service, Langerwehe, Germany*) was used for analytical measurements at a flow rate of 1 mL/min. Both specific gradients and the corresponding retention times t_R with capacity factor K' (**Equation 1**) are cited in the text.

$$K' = \frac{t_R - t_0}{t_0} \quad (1)$$

K´ = capacity factor; t_R = retention time [min]; t_0 = column dead time [min].

Preparative RP-HPLC purification was done with a MultoKrom 100 C18 (250 × 20 mm, 5 µm particle size) column (*CS Chromatographie Service, Langerwehe, Germany*) at a constant flow rate of 10 mL/min. Analytical and preparative radio-RP-HPLC was performed using a MultoKrom 100 C18 (150 × 4.6 mm,5 µm particle size) column or Multokrom 100 C18 (125 × 4.6 mm, 5 µm particle size) column *(CS Chromatographie Service, Langerwehe, Germany).* Radioactivity was detected through connection of the outlet of the UV-photometer to a HERM LB 500 NaI detector (*Berthold Technologies, Bad Wildbad, Germany*) or for the purpose of metabolite analysis to a Flowstar^2 LB 514 (*Berthold Technologies, Bad Wildbad, Germany*). Electrospray ionization-mass spectra for characterization of the substances were acquired on an expression^L CMS mass spectrometer *(Advion, Harlow, United Kingdom).*

RP-HPFC: Reversed-phase high-performance flash chromatography (RP-HPFC) was performed on a Biotage® SP HPFC System (*Biotage, Charlottesville, VA USA*) using Biotage SNAP cartridges (KP-C18-HS, 12 g). Eluents for all HPLC operations were water (solvent A) and MeCN (solvent B), both containing 0.1% trifluoroacetic acid.

NMR: Nuclear magnetic resonance (NMR) spectra were recorded on a Bruker (*Billerica, United States*) AVHD-300, AVHD-400 or AVHD-500 spectrometer at 298 K. Chemical shifts are given in δ-values [ppm] and are referenced to the residual proton signal of the used deuterated solvent. In cases of no solvent signal, e.g. for ^{19}F or ^{29}Si NMR spectra, the shifts are calibrated to the internal standards $CFCl_3$ and tetramethylsilane, respectively. Coupling constants (*J*) are reported in Hertz (Hz). Multiplicities were expressed as standard abbreviations: s – singlet, d – doublet, t – triplet, q – quartet, m – multiplet.

Analysis of Radioactive Samples: Activity quantification was performed using a 2480 WIZARD^2 automatic γ-counter (*PerkinElmer, Waltham, United States*) or a CRCR-55tR dose calibrator (*Mirion Technologies, Ramsey, NJ, USA*). Radio-thin layer chromatography (TLC) was carried out with a Scan-RAM detector (*LabLogic Systems, Sheffield, United Kingdom*).

2. General Procedures (GPs) for Solid-Phase Peptide Synthesis

Standard 2-CTC Resin Loading (GP1): Loading of the 2-chlorotritylchloride (2-CTC) resin with an amino acid (AA) was carried out by stirring a solution of the 2-CTC-resin (1.60 mmol/g) and the AA (1.5 eq.) in DMF with DIPEA (3.0 eq.) at room temperature for 2 h. Remaining unreacted 2-CTC groups were capped by the addition of methanol (2 mL/g resin) for 15 min. Subsequently the resin was filtered and washed with DMF (8 × 5 mL/g resin) and DCM (3 × 5 mL/g resin) and dried *in vacuo*. Final loading L of the AA was determined by **Equation 2**:

$$L = \frac{(m_2 - m_1) \times 1000}{(MW - M_{HCl}) \times m_2} \quad (2)$$

L = loading [mmol/g]; m_2 = mass of loaded resin [g]; m_1 = mass of unloaded resin [g]; MW = molecular weight of AA [g/mol]; M_{HCl} = molecular weight of HCl [g/mol].

Amide Bond Formation by Coupling to a Resin-Bound Amine (GP2a): For conjugation of a building block to a resin-bound peptide with an unprotected amine, a mixture of TBTU (1.5 eq.) with HOAt (1.5 eq.) was used for pre-activation of the carboxylic acid (1.5 eq.) with DIPEA (4.5 eq.) or, in the case of pre-activating amino acids prone to racemization, like diamino propionic acid and derivatives thereof, 2,4,6-trimethylpyridine (*sym*-collidine, 6.0 eq.) as a base in DMF (10 mL/g resin). After 10 min at rt, the solution was added to the swollen resin. If not otherwise stated in the respective synthesis protocols, the conjugation step was carried out at rt for a period of 2 h. After the reaction, the resin was washed with DMF (6 × 5 mL/g resin).

Amide Bond Formation by Coupling to a Resin-Bound Carboxylic Acid (GP2b): For conjugation of a building block to the resin-bound peptide with an unprotected carboxylic acid, a mixture of TBTU (1.5 eq.) with HOAt (1.5 eq.) and DIPEA (6.0 eq.) dissolved in DMF (10 mL/g resin) was added to the resin for pre-activation. After 20 min at rt, a solution of the amino acid with an unprotected amine (2.0 eq.) in DMF (2 mL/g resin) was added to the resin. If not otherwise stated in the respective synthesis protocols, the conjugation step was carried out at rt for a period of 2 h. After the reaction, the resin was washed with DMF (6 × 5 mL/g resin).

Amide Bond Formation by Coupling Succinic Anhydride to a Resin-Bound Amine (GP2c): For conjugation of succinic anhydride to a resin-bound peptide with an unprotected amine, a mixture of succinic anhydride (7.0 eq.) with DIPEA (7.0 eq.) in DMF (10 mL/g resin) was added to the resin. After 3 h at rt, the resin was washed with DMF (6 × 5 mL/g resin).

On-Resin Acetylation (GP2d): A mixture of NMP/acetic anhydride/DIPEA (*v*/*v*/*v* = 85:10:5) was added to the resin for 15 min. Afterwards, the resin was washed with DMF (6 × 5 mL/g resin).

On-Resin Fmoc-Deprotection (GP3): The resin-bound Fmoc-peptide was treated with 20% piperidine in DMF (*v/v*, 8 mL/g resin) for 5 min and subsequently for 15 min. Afterwards, the resin was washed thoroughly with DMF (8 × 5 mL/g resin).

On-Resin Dde-Deprotection in Absence of Fmoc-Groups (GP4a): The Dde-protected peptide was dissolved in a solution of 2% hydrazine monohydrate in DMF (*v/v*, 5 mL/g resin) and shaken for 20 min. After deprotection the resin was washed with DMF (8 × 5 mL/g resin).

On-Resin Dde-Deprotection in Presence of Fmoc-Groups (GP4b): In the case of present Fmoc-groups, Dde-deprotection of peptides bound to the 2-CTC resin was performed by adding a solution of imidazole (0.92 g/g resin), hydroxylamine hydrochloride (1.26 g/g resin) in NMP (5.0 mL/g resin) and DMF (1.0 mL/g resin) for 3 h at room temperature. After deprotection the resin was washed with DMF (8 × 5 mL/g resin).

Peptide Cleavage off the Resin with Concomitant Cleavage of Acid-Labile Protecting Groups (GP5a): To cleave the peptide from the resin with concomitant cleavage of acid-labile protecting groups, the fully protected resin-bound peptide was dissolved in a mixture of TFA/TIPS/water (*v/v/v*; 95/2.5/2.5) and shaken for 30 min. The solution is filtered off and the resin is treated in the same way for another 30 min. Both filtrates were combined and stirred for additional 1-24 h at rt. Product formation was monitored by HPLC. After removing TFA under a stream of nitrogen, the residue was dissolved in a mixture of *t*BuOH and water and freeze-dried.

Peptide Cleavage off the Resin under Preservation of Acid-Labile Protecting Groups (GP5b): To cleave the peptide from the resin under preservation of acid-labile protecting groups, the fully protected resin-bound peptide was dissolved in a mixture of 1,1,1,3,3,3-hexafluoro-2-propanol/DCM (v/v; 1/4) and shaken for 1 h. The solution was filtered off and the resin was treated in the same way for another 1 h. Both filtrates were combined and concentrated under a stream of nitrogen. The residue was dissolved in a mixture of *t*BuOH and water and freeze-dried.

On-Resin Allyl-/Alloc-Deprotection (GP6): The Allyl-/Alloc-protected, resin-bound peptide was dissolved in a mixture of phenylsilane (24 eq) and $Pd(PPh_3)_4$ (0.1 eq.) in DCM (5 mL/g resin) and kept dark during the reaction for 20 min. The solution was filtered off and the resin was treated in the same way for another 20 min. To remove residual black palladium, the resin was washed alternately with sodium diethyldithiocarbamate in DMF (0.5 wt%, 5 mL/g resin) and 0.5% DIPEA in DMF (5 mL/g resin), each solution 3 × 5min. Afterwards the resin was further washed with DMF (8 × 5 mL/g resin).

On-Resin Urea Bond Formation (GP7): For binding motifs deviant from Glu-urea-Glu (EuE) compounds, the synthesis of X-urea-Glu compounds, e.g. Lys-urea-Glu (KuE), was carried out in a similar way as an on-resin approach. A solution of (*S*)-di-*tert*-butyl-2-(1*H*-imidazole-1-carboxamido)pentanedioate (**chapter II.3.1**, 2.0 eq.) in 1,2-dichloroethane (DCE, 5 mL/g resin) was added to the resin-bound peptide. The suspension was cooled on ice for 30 min and TEA (3.0 eq.) was added. The suspension was heated to 40 °C and stirred gently overnight. After reaction, the resin was washed with DMF (6 × 5 mL/g resin).

3. Synthesis of Building Blocks

3.1. PSMA Binding Motifs and Functionalized Amino Acids

(*S*)-5-(*tert*-Butoxy)-4-(3-((*S*)-1,5-di-*tert*-butoxy-1,5-dioxopentan-2-yl)ureido)-5-oxopentanoic acid ((*t*BuO)EuE(O*t*Bu)$_2$) (prepared according to Wurzer et al.(*126*))

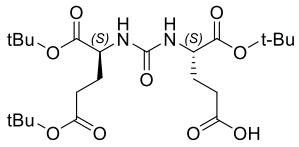

Chemical Formula: $C_{23}H_{40}N_2O_9$
Molecular Weight: 488,58

Di-*tert*-butyl (1*H*-imidazole-1-carbonyl)-L-glutamate (i): A solution of 20 mL DCM containing 2.0 g (7.71 mmol, 1.0 eq.) di-*tert*-butyl-L-glutamate·HCl was cooled on ice for 30 min and afterwards treated with 2.69 mL TEA (19.28 mmol, 2.5 eq.) and 3.3 mg (0.3 mmol, 0.04 eq.) DMAP. After additional stirring for 5 min, 1.38 g (8.84 mmol, 1.1 eq.) of 1,1'-carbonyldiimidazole (CDI) dissolved in DCM were slowly added over a period of 30 min. The reaction mixture was further stirred overnight and enabled to warm to rt. The reaction was stopped using 8 mL saturated $NaHCO_3$ with concomitant washing steps of water (2 × 30 mL) and brine (2 × 30 mL) and dried over Na_2SO_4. The remaining solvent was removed *in vacuo* and the crude product (*S*)-di-*tert*-butyl 2-(1*H*-imidazole-1-carboxamido) pentanedioate (**i**) was used without further purification.

5-Benzyl 1-(*tert*-butyl) (((*S*)-1,5-di-*tert*-butoxy-1,5-dioxopentan-2-yl)carbamoyl)-L-glutamate (ii): In 20 mL 1,2-dichloroethane (DCE) 2.72 g (7.71 mmol, 1.0 eq.) of the crude product (*S*)-di-*tert*-butyl-2-(1*H*-imidazole-1-carboxamido)pentanedioate (**i**) were dissolved and cooled on ice for 30 min. To this solution were added 2.15 mL (15.42 mmol, 2.0 eq.) TEA and 2.54 g (7.71 mmol, 1.0 eq.) H-L-Glu(OBzl)-O*t*Bu·HCl and the solution was stirred overnight at 40 °C. The remaining solvent was evaporated and the crude product purified using silica gel flash-chromatography with an eluent mixture containing EtOAc/hexane/TEA (*v/v/v* = 500:500:0.8). After removal of the solvent, 5-benzyl-1-(*tert*-butyl)-(((*S*)-1,5-di-*tert*-butoxy-1,5-dioxopentan-2-yl)carbamoyl)-L-glutamate (**ii**) was obtained as a colorless oil.

(tBuO)EuE(OtBu)$_2$ (iii): To synthesize (*t*BuO)EuE(O*t*Bu)$_2$**,** 3.17 g (5.47 mmol, 1.0 eq.) of 5-benzyl-1-(*tert*-butyl)-(((S)-1,5-di-*tert*-butoxy-1,5-dioxopentan-2-yl)carbamoyl)-*L*-glutamate (**ii**) were dissolved in 75 mL EtOH and 0.34 g (0.57 mmol, 0.1 eq.) palladium on activated charcoal (10%) were given to this solution. The flask containing the reaction mixture was initially purged with H_2 and the solution was stirred over night at rt under light H_2-pressure (balloon). The crude product was filtered through celite and the solvent evaporated *in vacuo*. The product (**iii**) was obtained as a hygroscopic solid (84%). RP-HPLC (10 to 90% B in 15 min): t_R = 11.3 min. K' = 5.3.

ESI-MS (positive): calculated monoisotopic mass ($C_{23}H_{40}N_2O_9$): 488.3; found: m/z = 489.4 $[M+H]^+$, 516.4 $[M+Na]^+$.

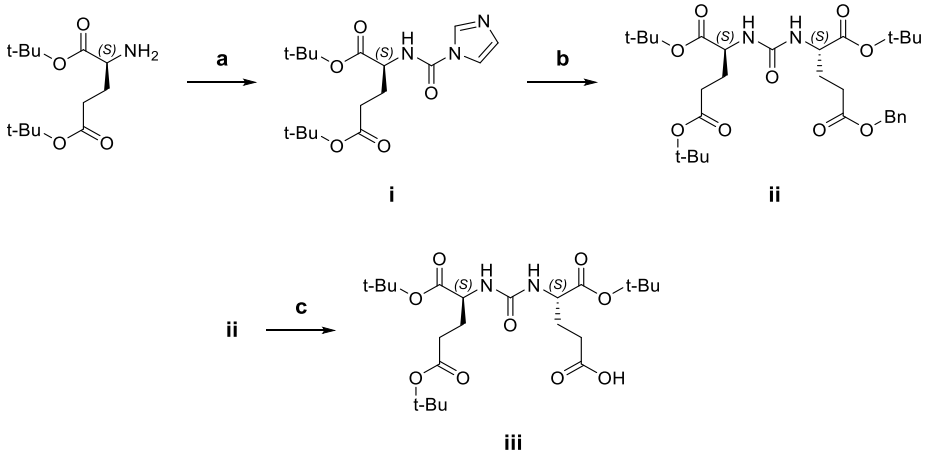

Scheme 1: Synthesis of (*t*BuO)EuE(O*t*Bu)$_2$: a) DCI, TEA, DMAP, 0 °C to rt, overnight (DCM); b) H-L-Glu(OBzl)-O*t*Bu·HCl, TEA, 0 to 40 °C, overnight (DCE); c) Pd/C (10%), H_2, rt, overnight (EtOH).

(tBuO)KuE(OtBu)$_2$ (prepared according to *Weineisen et al.* (*151*))

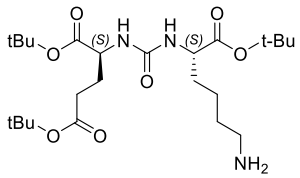

Chemical Formula: $C_{24}H_{45}N_3O_7$
Molecular Weight: 487,64

6-(Benzyloxy)carbonyl-1-(*tert*-butyl) (((*S*)-1,5-di-*tert*-butoxy-1,5-dioxopentan-2-yl)carbamoyl)-L-lysinate (i): In 20 mL 1,2-dichloroethane (DCE) 2.72 g (7.71 mmol, 1.0 eq.) of the crude product (*S*)-di-*tert*-butyl-2-(1*H*-imidazole-1-carboxamido)pentanedioate (see synthesis of (*t*BuO)EuE(O*t*Bu)$_2$) were dissolved and cooled on ice for 30 min. To this solution were added 2.15 mL (15.42 mmol, 2.0 eq.) TEA and 2.87 g (7.71 mmol, 1.0 eq.) H-L-Lys(Z)-O*t*Bu·HCl and the solution was stirred overnight at 40 °C. The remaining solvent was evaporated and the crude product purified using silica gel flash-chromatography with an eluent mixture containing EtOAc/hexane/TEA (*v*/*v*/*v* = 500:500:0.8). After removal of the solvent, (**i**) was obtained as a colorless oil.

(tBuO)KuE(OtBu)$_2$ (ii): To synthesize (*t*BuO)KuE(O*t*Bu)$_2$, 3.40 g (5.47 mmol, 1.0 eq.) of (**i**) were dissolved in 75 mL EtOH and 0.34 g (0.57 mmol, 0.1 eq.) palladium on activated charcoal (10%) were given to the solution. The flask containing the reaction mixture was initially purged with H_2 and the solution was stirred over night at rt under light H_2-pressure (balloon). The crude product was filtered through celite and the solvent evaporated *in vacuo*. The product (**ii**) was obtained as

a hygroscopic solid (92%). RP-HPLC (10 to 90% B in 15 min): t_R = 12.6 min. K' = 6.4. ESI-MS (positive): calculated monoisotopic mass ($C_{24}H_{45}N_3O_7$): 487.6; found: m/z = 488.3 $[M+H]^+$, 510.3 $[M+Na]^+$.

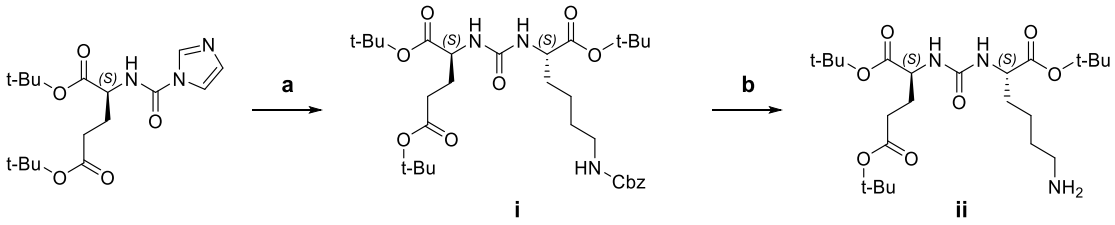

Scheme 2: Synthesis of (*t*BuO)KuE(O*t*Bu)$_2$: a) H-L-Lys(Z)-O*t*Bu·HCl, TEA, 0 to 40 °C, overnight (DCE); b) Pd/C (10%), H_2, rt, overnight (EtOH).

Sn(*n*-Bu)$_3$-BA-(*t*BuO)KuE(O*t*Bu)$_2$

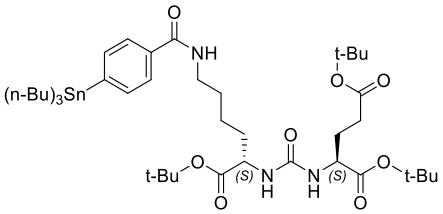

Chemical Formula: $C_{43}H_{75}N_3O_8Sn$
Molecular Weight: 880,80

The stannylated precursor for the radiosynthesis of [^{125}I]I-BA-KuE was kindly provided within our group. As described previously (*151,152*) 86.4 mg (tBuO)KuE(OtBu)$_2$ (0,18 mmol, 1.2 eq.) and 75.0 mg *N*-succinimidyl 4-(tri-*n*-butylstannyl)benzoate were dissolved in 1.5 mL DCM and 92.6 µL TEA (0.66 mmol, 4.5 eq.) were added. After stirring for 12 h at rt, the reaction was stopped by addition of 50 mL H_2O. The organic phase was separated and all volatiles were removed under reduced pressure to obtain the crude product as pale-yellow oil (91%). The obtained precursor was used without further purification. RP-HPLC (20 to 40% B in 20 min): t_R = 12.5 min. K' = 4.7. ESI-MS (positive): calculated monoisotopic mass ($C_{43}H_{75}N_3O_8Sn$): 881.5; found: m/z = 882.7 $[M+H]^+$, 1764.5 $[2M+H]^+$.

Fmoc-(L-Pro)$_3$-OH

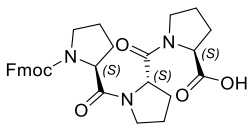

Chemical Formula: $C_{30}H_{33}N_3O_6$
Molecular Weight: 531,61

2-CTC resin was loaded with Fmoc-L-Pro-OH (GP1). The obtained loading of <0.8 mmol/g was sufficient to avoid undesired Fmoc-deprotection during the following coupling steps endangered

by the secondary amine of the resin-bound proline. After alternating Fmoc-deprotection (GP3) and coupling with Fmoc-L-Pro-OH for 3 h at rt (modified GP2a), the Fmoc-protected tripeptide was cleaved off the resin (GP5a). The solvent was removed under nitrogen stream and the crude product was purified by RP-HPFC. The lyophilized product was obtained as colorless solid (35%). RP-HPLC (10 to 90% B in 15 min): t_R = 10.0 min. K' = 4.6. ESI-MS (positive): calculated monoisotopic mass ($C_{30}H_{33}N_3O_6$): 531.2; found: m/z = 532.3 $[M+H]^+$.

H-D-Lys(Dde)-OAll

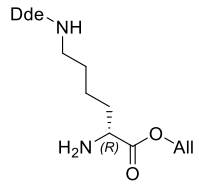

Chemical Formula: $C_{19}H_{30}N_2O_4$
Molecular Weight: 350,46

The not commercially available amino acid was synthesized by allylation of Fmoc-D-Lys(Dde)-OH based on a published procedure used for the conversion of Fmoc-L-Lys(Boc)-OH to H-L-Lys(Boc)-OAll (*153*). Briefly, allylation of Fmoc-D-Lys(Dde)-OH (266.3 mg, 0.5 mmol, 1.0 eq.) was achieved by use of excess Allyl bromide (1.2 mL, 14 mmol, 28 eq.) and DIPEA (170 µL, 1 mmol, 2.0 eq.) in 1 mL MeCN for 4 h at 40 °C. The solvent was removed under reduced pressure and the crude product was dissolved in 5 mL EtOAc, followed by washing with 3 × 3 mL HCl (1 M in H_2O), 2 × 2 mL $NaHCO_3$ (saturated in H_2O) and 1 × 2 mL brine solution. The organic phase was dried over MgSO4, filtered and concentrated under reduced pressure.

The residue was dissolved in 5 ml piperidine/DCM (*v*/*v* = 1:4) and stirred for 30 min for Fmoc-deprotection. The volatiles were removed under reduced pressure The residue was purified by RP-HPFC and the lyophilized product was obtained as colorless solid (73%). RP-HPLC (10 to 90% B in 15 min): t_R = 6.7 min. K' = 2.8. ESI-MS (positive): calculated monoisotopic mass ($C_{19}H_{30}N_2O_4$): 350.2; found: m/z = 351.5 $[M+H]^+$.

Fmoc-[L-Ser(O*t*Bu)]$_3$-OH

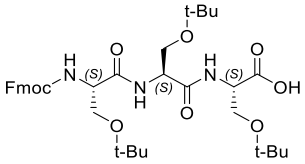

Chemical Formula: $C_{36}H_{51}N_3O_9$
Molecular Weight: 669,82

2-CTC resin was loaded with Fmoc-L-Ser(OtBu)-OH (GP1). After alternating Fmoc-deprotection (GP3) and coupling with Fmoc-L-Ser(OtBu)-OH for 3 h (modified GP2a), the Fmoc-protected tripeptide was cleaved off the resin (GP5b). The solvent was removed under reduced pressure

and the crude product was purified by RP-HPFC. The lyophilized product was obtained as colorless solid (23%). RP-HPLC (10 to 90% B in 15 min): t_R = 15.5 min. K' = 7.7. ESI-MS (positive): calculated monoisotopic mass ($C_{36}H_{51}N_3O_9$): 669.4; found: m/z = 699.7 $[M+H]^+$.

Fmoc-L-Ser(O*t*Bu)-Gly-Gly-OH

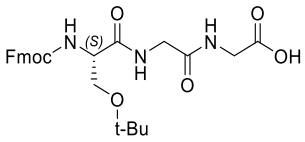

Chemical Formula: $C_{26}H_{31}N_3O_7$
Molecular Weight: 497,55

2-CTC resin was loaded with Fmoc-Gly-OH (GP1). After Fmoc-deprotection (GP3), Fmoc-Gly-OH (GP2a). Fmoc was cleaved (GP3) and the resin-bound peptide was left to react with Fmoc-L-Ser(O*t*Bu)-OH (GP2a). The tripeptide was cleaved off the resin under preservation of acid-labile protecting groups (GP5b). The solvent was removed under reduced pressure and the crude product was purified by RP-HPFC. The lyophilized product was obtained as colorless solid (28%). RP-HPLC (10 to 90% B in 15 min): t_R = 10.9 min. K' = 5.1. ESI-MS (positive): calculated monoisotopic mass ($C_{26}H_{31}N_3O_7$): 497.2; found: m/z = 498.1 $[M+H]^+$.

3.2. Silicon-Based Fluoride Acceptor (SiFA) Building Blocks

All moisture- and oxygen-sensitive reaction steps of SiFA building blocks described in this chapter and indicated by the use of dry, anhydrous solvents were performed in dried reaction vessels under positive argon pressure using standard *Schlenk* techniques.

4-(Di-*tert*-butylfluorosilyl)benzoic acid ((4-SiFA)Bz-OH)
(prepared according to *Wurzer et al*. and *Iovkova et al.* with minor modifications (*152,154*))

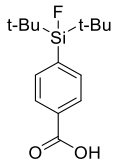

Chemical Formula: $C_{15}H_{23}FO_2Si$
Molecular Weight: 282,43

((4-Bromobenzyl)oxy)(*tert*-butyl)dimethylsilane (i): To a stirred solution of 4-bromobenzylalcohol (4.68 g, 25.0 mmol, 1.0 eq.) in anhydrous DMF (70 mL) imidazole (2.04 g, 30.0 mmol, 1.2 eq.) and TBDMSCl (4.52 g, 30.0 mmol, 1.2 eq.) were added and the resulting mixture was stirred at room temperature (rt) for 16 h. The mixture was then poured into ice-cold H_2O (250 mL) and extracted with Et_2O (5 × 50 mL). The combined organic fractions were washed with sat. aq. $NaHCO_3$ (2 ×100 mL) and brine (100 mL), dried, filtered and concentrated *in vacuo* to

give the crude product which was purified by flash column chromatography (silica, 5% EtOAc/petrol) to give **i** as a colorless oil (7.18 g, 95%). RP-HPLC (50 to 100% B in 15 min): t_R = 15 min. K' = 7.4.

Di-*tert*-butyl[4-((*tert*-butyldimethylsilyloxy)methyl)phenyl]fluorosilane (ii): At –78 °C under magnetic stirring, a solution of *t*BuLi in pentane (7.29 mL, 1.7 mol/L, 12.4 mmol 2.4 eq.) was added to a solution of ((4-bromobenzyl)oxy)(tert-butyl)dimethylsilane (**i**) (1.56 g, 5.18 mmol, 1.0 eq.) in dry THF (15 mL). After the reaction mixture had been stirred for 30 min at –78 °C, the suspension obtained was added dropwise over a period of 30 min to a cooled (–78 °C) solution of di-*tert*-butyldifluorosilane (1.12 g, 6.23 mmol, 1.2 eq.) in dry THF (10 mL). The reaction mixture was allowed to warm to room temperature over a period of 12 h and then hydrolyzed with saturated aqueous NaCl solution (100 mL). The organic layer was separated and the aqueous layer was extracted with diethyl ether (3 × 50 mL). The combined organic layers were dried over magnesium sulfate and filtered. The filtrate was concentrated *in vacuo* to afford **ii** as a yellowish oil (1.88 g, 95%). It was used for subsequent reactions without further purification. RP-HPLC (50 to 100% B in 20 min): t_R = 19.0 min. K' = 9.7.

4-(Di-*tert*-butylfluorosilanyl)benzyl alcohol (iii): A catalytic amount of concentrated aqueous HCl (0.5 mL) was added to a suspension of **ii** (1.88 g, 4.92 mmol, 1.0 eq.) in methanol (50 mL). The reaction mixture was stirred for 18 h at room temperature and then the solvent and the volatiles were removed under reduced pressure. The residue was redissolved in diethyl ether (40 mL) and the solution was washed with saturated aqueous $NaHCO_3$ solution. The aqueous layer was extracted with diethyl ether (3 × 50 mL). The combined organic layers were dried over magnesium sulfate and filtered. The filtrate was concentrated *in vacuo* to afford **iii** as a yellowish oil (1.29 g, 98%) that solidified. The product was used without further purification. RP-HPLC (50 to 100% B in 15 min): t_R = 8.2 min. K' = 3.6.

4-(Di-*tert*-butylfluorosilyl)benzoic acid ((4-SiFA)Bz-OH, iv): At rt, 5.8 g $KmnO_4$ (36.7 mmol, 1.5 eq.) were dissolved in H_2O and added to a solution of of **iii** (6.61 g, 24.6 mmol, 1.0 eq.), *t*BuOH (65 mL), dichloromethane (9 mL), and 1.25 M $NaH_2PO_4 \cdot H_2O$ buffer (36 mL) at pH 4.0–4.5. After the mixture had been stirred for 25 min, it was cooled on ice for 10 min, whereupon excess $KMnO_4$ (7.8 g, 49.2 mmol, 2.0 eq.) was added. The reaction mixture was stirred for 2 h on ice and subsequently allowed to warm to rt for 30 min. The reaction was then quenched by the addition of saturated aqueous Na_2SO_3 solution (50 mL). Upon addition of 2 M aqueous HCl, all of the MnO_2 dissolved. The resulting solution was extracted with diethyl ether (3 × 100 mL). The combined organic layers were washed with saturated aqueous $NaHCO_3$ solution, dried over $MgSO_4$, filtered, and concentrated under reduced pressure to provide a white solid, which was purified by recrystallization from Et_2O/*n*-hexane (1:3, for 12 h) to give **iv** (2.57 g, 37%). ^{1}H NMR (300 MHz,

$CDCl_3$): δ [ppm] = 8.10 (d, 2H $^3J(^1H,^1H)$ = 8.1 Hz; H_m), 7.74 (d, 2H, $^3J(^1H,^1H)$ = 8.1 Hz; H_o), 1.07 (s, 18H; CCH_3); $^{13}C\{^1H\}$ NMR (101 MHz, DMSO-D_6): δ [ppm] = 167.2 (s; COOH), 138.3 (d, $^2J(^{13}C,^{19}F)$ = 14 Hz; C_p), 133.8 (d, $^3J(^{13}C,^{19}F)$ = 4 Hz; C_m), 132.1 (s; C_i), 128.3 (s; C_o), 26.9 (s; CCH_3), 19.7 (d, $^2J(^{13}C,^{19}F)$ = 12 Hz; CCH_3); $^{19}F\{^{29}Si\}$ NMR (376 MHz, DMSO-D_6): δ [ppm] = –187.2; $^{29}Si\{^1H\}$INEPT NMR (79 MHz, DMSO-D_6): δ [ppm] = 14.1 (d, $^1J(^{19}F,^{29}Si)$ = 299 Hz). RP-HPLC (50 to 100% B in 15 min): t_R = 8.5 min. K' = 3.8. ESI-MS (positive): calculated monoisotopic mass ($C_{15}H_{23}FO_2Si$): 282.15; found: m/z = 283.2 $[M+H]^+$, 265.2 $[M–H_2O+H]^+$.

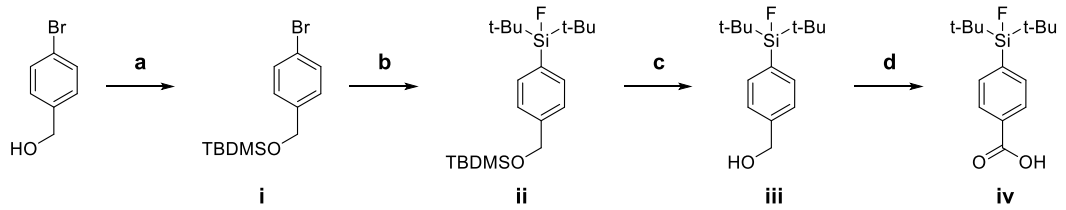

Scheme 3: Synthesis of (4-SiFA)Bz-OH (**iv**): a) TBDMSCl, imidazole, rt, 16 h (DMF); b) *t*BuLi, tBu_2SiF_2, –78 °C to rt, overnight (THF); c) HCl, rt, 18 h (MeOH); d) $KMnO_4$, 0 °C to rt, 2.5 h (DCM/*t*BuOH/ $NaH_2PO_4{\cdot}H_2O$ buffer).

3-(Di-*tert*-butylfluorosilyl)benzoic acid ((3-SiFA)Bz-OH)

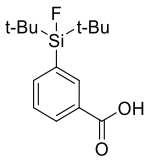

Chemical Formula: $C_{15}H_{23}FO_2Si$
Molecular Weight: 282,43

Di-*tert*-butylfluoro(3-tolyl)silane (i): A solution of 342 mg 3-bromo-toluene (2.0 mmol, 1.0 eq.) in 6 mL dry THF was cooled to –78 °C and 2.59 mL of *t*BuLi (4.40 mmol, 1.6 M in pentane, 2.2 eq.) were added dropwise and stirred for 30 min at –78 °C. The reaction mixture was then added to a solution of 397 mg of di-*tert*-butyldifluorosilane (2.20 mmol, 1.1 eq.) in 4.0 mL THF at –78 °C and stirred overnight allowing to warm to rt under pressure control. The reaction was stopped by addition of 40 mL brine. The aqueous layer was extracted with Et_2O (3 × 20 mL), combined organic phases were dried over $MgSO_4$ and the solvent was removed under reduced pressure to obtain the crude product as yellow oil. The mixture was used in the next step without further purification.

3-(Di-*tert*-butylfluorosilyl)benzoic acid ((3-SiFA)Bz-OH, ii): To a solution of the complete crude product (**i**) (assumption: 2.0 mmol, 1.0 eq.) in 6.4 mL *t*BuOH/DCM (v/v= 7/1) were added 8.1 mL of a $NaH_2PO_4{\cdot}H_2O$ solution (20.0 mmol, 1.25 M in H_2O, 10.0 eq.). To the solution 1.89 g $KMnO_4$ (12.0 mmol, 6.0 eq.) were added at rt, the reaction mixture was carefully heated stepwise to 75 °C and stirred for 24 h. The reaction was quenched by the addition of a saturated aqueous $NaSO_3$ solution (15 mL). Concentrated aqueous HCl (5 mL) was added to completely dissolve MnO_2. The

solution was extracted with Et_2O (3 × 40 mL), the combined organic phases were dried over $MgSO_4$ and the solvent removed under reduced pressure. The crude product was purified by HPFC and lyophilized to obtain **ii** (140 mg, 0.5 mmol, 25% over 2 steps) as colorless solid. ^{1}H NMR (400 MHz, $CDCl_3$): δ [ppm] = 8.36 (s, 1H; H_{Ar-2}), 8.16 (dt, 1H, $^3J(^1H,^1H)$ = 7.8 Hz, $^4J(^1H,^1H)$ = 1.6 Hz; H_{Ar-6}), 7.86 (dt, 1H, $^3J(^1H,^1H)$ = 7.4 Hz, $^4J(^1H,^1H)$ = 1.3 Hz; H_{Ar-4}), 7.51 (t, 1H, $^3J(^1H,^1H)$ = 7.6 Hz; H_{Ar-5}), 1.08 (s, 18H; CCH_3); $^{13}C\{^1H\}$ NMR (101 MHz, DMSO-D_6): δ [ppm] = 167.3 (s; COOH), 137.8 (d, $^3J(^{13}C,^{19}F)$ = 4 Hz; C_{Ar-4}), 134.1 (d, $^3J(^{13}C,^{19}F)$ = 4 Hz; C_{Ar-2}), 133.1 (d, $^2J(^{13}C,^{19}F)$ = 14 Hz; C_{Ar-3}), 130.7 (s; C_{Ar-6}), 130.1 (s; C_{Ar-5}), 128.2 (s; C_{Ar-1}),26.9 (s; CCH_3), 19.7 (d, $^2J(^{13}C,^{19}F)$ = 12 Hz; CCH_3); $^{19}F\{^{29}Si\}$ NMR (376 MHz, DMSO-D_6): δ [ppm] = –187.3; $^{29}Si\{^1H\}$INEPT NMR (79 MHz, DMSO-D_6): δ [ppm] = 13.8 (d, $^1J(^{19}F,^{29}Si)$ = 298 Hz). RP-HPLC (50 to 100% B in 15 min): t_R = 9.2 min. K' = 4.2. ESI-MS (positive): calculated monoisotopic mass ($C_{15}H_{23}FO_2Si$): 282.15; found: m/z = 283.3 $[M+H]^+$, 266.3 $[M–H_2O+H]^+$.

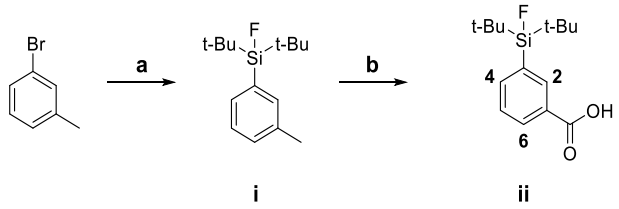

Scheme 4: Synthesis of (3-SiFA)Bz-OH (ii): a) *t*BuLi, tBu_2SiF_2, –78 °C to rt, overnight (THF) b) $KMnO_4$, 75 °C, 24 h (DCM/*t*BuOH/$NaH_2PO_4 \cdot H_2O$ buffer).

3-(Di-*tert*-butylfluorosilyl)-5-((allyloxy)carbonyl)benzoic acid (AllO-(5-SiFA)Ip-OH)

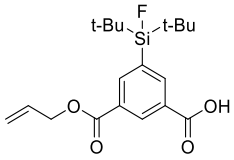

Chemical Formula: $C_{19}H_{27}FO_4Si$
Molecular Weight: 366,50

Di-*tert*-butyl(3,5-dimethylphenyl)fluorosilane (i): A solution of 4.54 g 1-bromo-3,5-dimethylbenzene (25.1 mmol, 1.0 eq.) in 73.1 mL dry THF was cooled to –78 °C and 34.7 mL of *t*BuLi (55.5 mmol, 1.6 M in pentane, 2.2 eq.) were added dropwise and stirred for 30 min at –78 °C. The reaction mixture was then added to a solution of 5.0 g of di-*tert*-butyldifluorosilane (27.7 mmol, 1.1 eq.) in 49.1 mL THF at -78 °C and stirred overnight while allowing to warm to rt under pressure control. The reaction was stopped by addition of 100 mL brine. The aqueous layer was extracted with Et_2O (3 × 100 mL), combined organic phases were dried over $MgSO_4$ and the solvent was removed under reduced pressure to obtain **i** (6.6 g, 24.8 mmol, 99 %) as a colorless solid. ^{1}H NMR (500 MHz, $CDCl_3$): d [ppm] = 7.19 (s, 2H; H_o), 7.04 (s, 1H; H_p), 2.33 (s, 6 H; CH_3), 1.06 (s, 18 H; CCH_3). RP-HPLC (50 to 100% B in 15 min, 100% B for 10 min): t_R = 16.4 min. K' = 8.2.

5-(Di-*tert*-butylfluorosilyl)isophthalic acid ((5-SiFA)Ip-OH, ii): To a solution of 1.1 g di-tert-butyl(3,5-dimethylphenyl)fluorosilane (**i**) (4.0 mmol, 1.0 eq.) in 16.8 mL *t*BuOH/DCM (v/v= 3.5/1) were added 16.0 mL of a $NaH_2PO_4 \cdot H_2O$ solution (40.0 mmol, 2.5 M in H_2O, 10.0 eq.). To the solution 7.6 g $KMnO_4$ (48.0 mmol, 12.0 eq.) were added at rt, the reaction mixture was carefully heated stepwise to 75 °C and stirred for 24 h. The reaction was quenched by the addition of a saturated aqueous $NaSO_3$ solution (50 mL). Concentrated aqueous HCl (10 mL) was added to completely dissolve MnO_2. The solution was extracted with Et_2O (3 × 100 mL), the combined organic phases were dried over $MgSO_4$ and the solvent removed under reduced pressure to obtain **ii** (1.3 g, 4.0 mmol, 100%) as a colorless solid. ^{1}H NMR (400 MHz, DMSO-D_6): δ ppm = 8.53 (t, 1 H, $^4J(^1H,^1H)$ = 1.7 Hz; $H_{Ar\text{-}2}$), 8.32 (d, 2 H, $^4J(^1H,^1H)$ = 1.6 Hz; $H_{Ar\text{-}4,\text{-}6}$), 1.03 (s, 18 H; CH_3); $^{13}C\{^1H\}$ NMR (101 MHz, DMSO-D_6): δ [ppm] = 166.5 (s; COOH), 137.9 (d, $^3J(^{13}C,^{19}F)$ = 4 Hz; $C_{Ar\text{-}4,\text{-}6}$), 134.0 (d, $^2J(^{13}C,^{19}F)$ = 14 Hz; $C_{Ar\text{-}5}$), 131.4 (s; $C_{Ar\text{-}2}$), 130.8 (s; $C_{Ar\text{-}1,\text{-}3}$), 26.8 (s; C*C*$H_3$), 19.7 (d, $^2J(^{13}C,^{19}F)$ = 12 Hz; *C*CH_3); $^{19}F\{^{29}Si\}$ NMR (376 MHz, DMSO-D_6): δ [ppm] = –187.1; $^{29}Si\{^1H\}$INEPT NMR (79 MHz, DMSO-D_6): δ [ppm] = 13.8 (d, $^1J(^{19}F,^{29}Si)$ = 299 Hz). RP-HPLC (50 to 100% B in 15 min): t_R = 5.7 min. K' = 2.20. ESI-MS (positive): calculated monoisotopic mass ($C_{16}H_{23}FO_4Si$): 326.13; found: m/z = 327.2 $[M+H]^+$, 309.2 $[M–H_2O+H]^+$.

3-((Allyloxy)carbonyl)-5-(di-*tert*-butylfluorosilyl)benzoic acid (AllO-(5-SiFA)Ip-OH, iii): A suspension of 1.0 g 5-(di-*tert*-butylfluorosilyl)isophthalic acid (**ii**) (3.1 mmol, 1.0 eq.) and 1.3 g K_2CO_3 (9.2 mmol, 3.0 eq.) in 300 mL DMF was cooled to 0 °C and a solution of 185.0 mg Allyl bromide (132.0 µL, 1.5 mmol, 0.5 eq.) in 10.0 mL DMF was slowly added over 20 min. The mixture was stirred overnight at rt. Subsequently, the mixture was filtered and all volatiles of the filtrate were removed under reduced pressure. The residue was dissolved in 100 mL HCl (1 M) and the aqueous layer was extracted with Et_2O (3 × 200 mL). The combined organic phases were dried over $MgSO_4$ and the solvent was removed under reduced pressure. The crude product was purified by HPFC and lyophilized to yield **iii** as colorless solid (250.9 mg, 684.6 mmol, 19 %). ^{1}H NMR (400 MHz, DMSO-D_6): δ [ppm] = 8.57 (t, 1H, $^4J(^1H,^1H)$ = 1.5 Hz; $H_{Ar\text{-}6}$), 8.36 (t, 1H, $^4J(^1H,^1H)$ = 1.5 Hz; $H_{Ar\text{-}2}$), 8.34 (t, 1H, $^4J(^1H,^1H)$ = 1.5 Hz; $H_{Ar\text{-}4}$), 6.07 (ddt, 1H, $^3J(^1H,^1H)$ = 17.3, 10.7, 5.5 Hz; CH_2–C*H*=CH_2), 5.41 (dd, 1H, $^3J(^1H,^1H)$ = 17.2 Hz, $^2J(^1H,^1H)$ = 1.7 Hz; CH_2–CH=CH_2 (*E*)), 5.30 (dd, 1H, $^3J(^1H,^1H)$ = 10.3 Hz, $^2J(^1H,^1H)$ = 1.6 Hz; CH_2–CH=CH_2 (*Z*)), 4.85 (d, 2H, $^3J(^1H,^1H)$ = 5.6 Hz; CH_2–CH=CH_2), 1.03 (s, 18H; C*C*H_3); $^{13}C\{^1H\}$ NMR (101 MHz, DMSO-D_6): δ [ppm] = 166.3 (COOH), 164.6 (*C*O-OAll), 138.3 (d, $^3J(^{13}C,^{19}F)$ = 4 Hz; $C_{Ar\text{-}4}$), 137.6 (d, $^3J(^{13}C,^{19}F)$ = 4 Hz; $C_{Ar\text{-}6}$), 134.3 (d, $^2J(^{13}C,^{19}F)$ = 14 Hz; $C_{Ar\text{-}5}$), 132.4 (CH_2–*C*H=CH_2), 131.2 ($C_{Ar\text{-}2}$), 131.0 ($C_{Ar\text{-}1}$), 129.7 ($C_{Ar\text{-}3}$), 118.2 (CH_2–CH=*C*H_2), 65.6 (*C*H_2–CH=CH_2), 26.8 (s; C*C*H_3), 19.7 (d, $^2J(^{13}C,^{19}F)$ = 12 Hz; *C*CH_3); $^{19}F\{^{29}Si\}$ NMR (376 MHz, DMSO-D_6): δ [ppm] = –187.0; $^{29}Si\{^1H\}$INEPT NMR (79 MHz, DMSO-D_6): δ [ppm] = 13.8 (d, $^1J(^{19}F,^{29}Si)$ = 299 Hz). RP-HPLC (50 to 100% B in 15 min): t_R = 10.4 min. K' = 4.8.

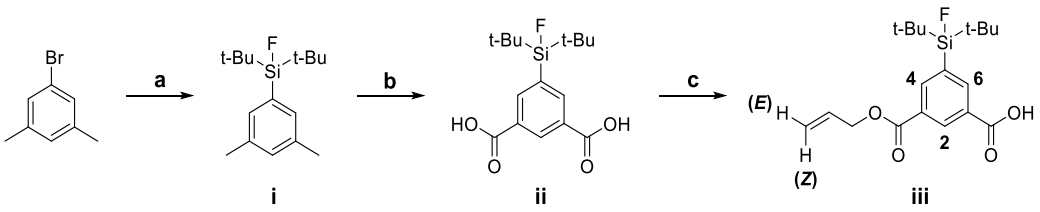

Scheme 5: Synthesis of AllO-(5-SiFA)Ip-OH (iii): a) *t*BuLi, tBu$_2$SiF$_2$, –78 °C to rt, overnight (THF) b) KMnO$_4$, 75 °C, 24 h (DCM/*t*BuOH/NaH$_2$PO$_4$·H$_2$O buffer), c) Allyl-Br, K$_2$CO$_3$, 0 °C to rt, overnight (DMF).

4. Synthesis of PSMA Ligands

4.1. Synthesis of Reference Ligands

DCIBzL (I-BA-KuE) (*70*)

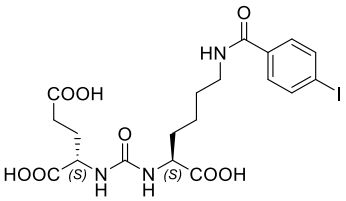

Chemical Formula: $C_{19}H_{24}IN_3O_8$
Molecular Weight: 549,32

2-CTC resin was loaded with Fmoc-L-Lys(Dde)-OH (GP1). After Fmoc-deprotection (GP3), on-resin urea bond formation was conducted using di-*tert*-butyl (1*H*-imidazole-1-carbonyl)-L-glutamate (GP7). The Lys-sidechain was Dde-deprotected (GP4a) and 4-iodobenzoic acid was coupled (GP2a). The peptide was cleaved from the resin (GP5a) and the dried crude product was purified by RP-HPLC. RP-HPLC (20 to 40% B in 15 min): t_R = 14.5 min. K' = 7.1. ESI-MS (positive): calculated monoisotopic mass ($C_{19}H_{24}IN_3O_8$): 549.1; found: m/z = 549.4 $[M+H]^+$.

PSMA-617 (Benešová et al. (*98*); purchased from *MedChemExpress (Monmouth Junction, USA)*)

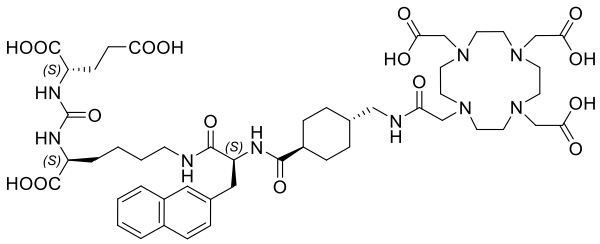

Chemical Formula: $C_{49}H_{71}N_9O_{16}$
Molecular Weight: 1042,15

PSMA I&T (prepared according to *Weineisen et al.* (*99*) and kindly provided within our group)

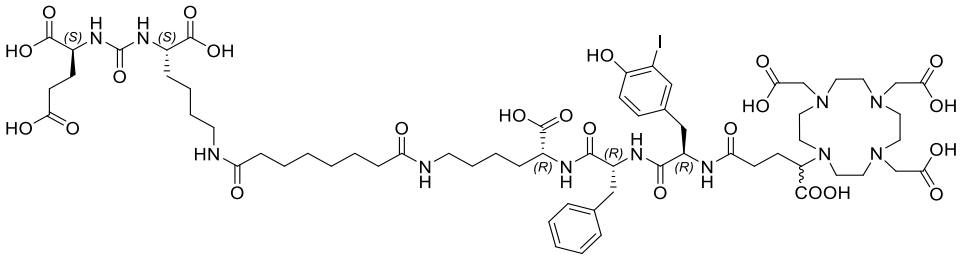

Chemical Formula: $C_{63}H_{92}IN_{11}O_{23}$
Molecular Weight: 1498,39

rhPSMA-7.3

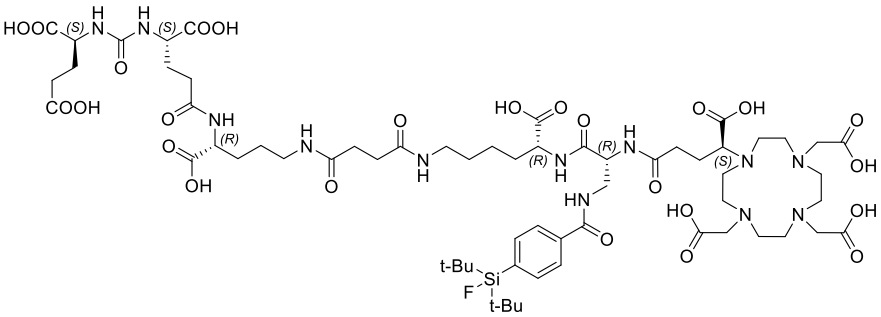

Chemical Formula: $C_{63}H_{99}FN_{12}O_{25}Si$
Molecular Weight: 1471,63

The reference ligand rhPSMA-7.3 was prepared according to the published protocol (*126*). RP-HPLC (10 to 70% B in 15 min): t_R = 10.0 min. K' = 4.7. ESI-MS (positive): calculated monoisotopic mass ($C_{63}H_{99}FN_{12}O_{25}Si$): 1470.7; found: m/z = 1471.4 $[M+H]^+$, 736.7 $[M+2H]^{2+}$.

rhPSMA10.1

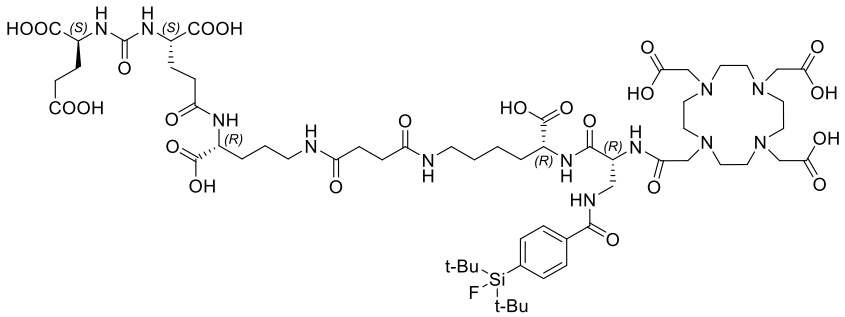

Chemical Formula: $C_{60}H_{95}FN_{12}O_{23}Si$
Molecular Weight: 1399,56

The reference ligand rhPSMA-10.1 was prepared according to the published protocol (*125*). RP-HPLC (10 to 70% B in 15 min): t_R = 9.9 min. K' = 4.0. ESI-MS (positive): calculated monoisotopic mass ($C_{60}H_{95}FN_{12}O_{23}Si$): 1398.6; found: m/z = 1399.6 $[M+H]^+$, 700.6 $[M+2H]^{2+}$.

4.2. Synthesis of Ligands Aiming for Metabolic Instability (MI)

MI-1

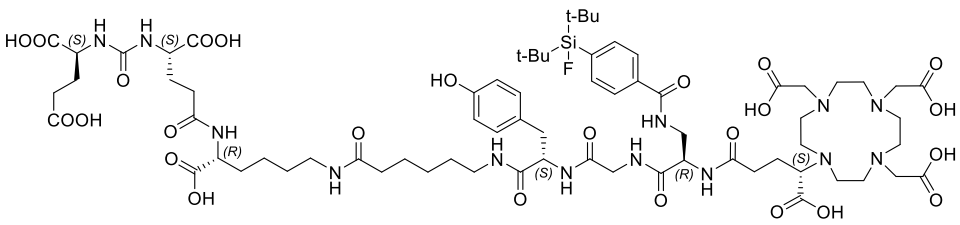

Chemical Formula: $C_{71}H_{108}FN_{13}O_{25}Si$
Molecular Weight: 1590,79

2-CTC resin was loaded with Fmoc-D-Lys(Dde)-OH (GP1). After Fmoc-deprotection (GP3), (*t*BuO)EuE(O*t*Bu)$_2$ (2.0 eq.) was coupled to the amine using HOAt (2.0 eq.), TBTU (2.0 eq.) and DIPEA (6.0 eq.) in DMF at rt for 3 h (modified GP2a). The Lys-sidechain was Dde-deprotected (GP4a) and subsequently, the amino acids Fmoc-Ahx-OH, Fmoc-L-Tyr(O*t*Bu)-OH and Fmoc-Gly-OH were alternately coupled (GP2a) and Fmoc-deprotected (GP3). Next, Fmoc-D-Dap(Dde)-OH was conjugated using *sym*-collidine (GP2a). The Dde-group was removed in the presence of Fmoc (GP4b) and (4-SiFA)Bz-OH was coupled to the sidechain (GP2a). Subsequently, the Fmoc-group was removed (GP3), (*S*)-DOTAGA(*t*Bu)$_4$ was coupled to the resin-bound peptide for 3 h at rt (modified GP2a) and the peptide was cleaved off the resin under concomitant deprotection of acid-labile groups (GP5a). The cleaved, dried crude product was purified by RP-HPLC. After lyophilization, the product was obtained as colorless solid (22%). RP-HPLC (10 to 90% B in 15 min): t_R = 8.7 min. K' = 3.9. ESI-MS (positive): calculated monoisotopic mass ($C_{71}H_{108}FN_{13}O_{25}Si$): 1589.7; found: m/z = 1589.4 $[M+H]^+$, 795.2 $[M+2H]^{2+}$.

MI-2

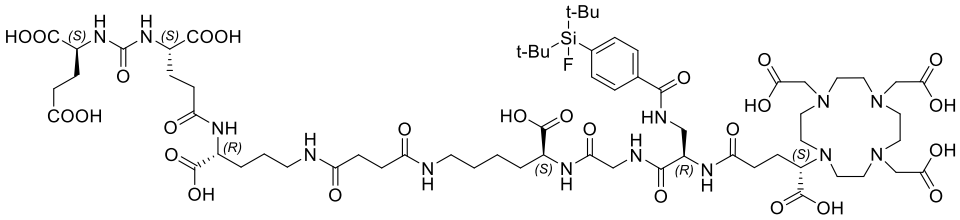

Chemical Formula: $C_{65}H_{102}FN_{13}O_{26}Si$
Molecular Weight: 1528,68

2-CTC resin was loaded with Fmoc-D-Orn(Dde)-OH (GP1). After Fmoc-deprotection (GP3), (*t*BuO)EuE(O*t*Bu)$_2$ (2.0 eq.) was coupled to the amine using HOAt (2.0 eq.), TBTU (2.0 eq.) and DIPEA (6.0 eq.) in DMF at rt for 3 h (modified GP2a). The Orn-sidechain was Dde-deprotected (GP4a) and conjugated to succinic anhydride (GP2c). To the carboxylic acid, Fmoc-L-Lys-O*t*Bu·HCl was coupled (GP2b) followed by Fmoc-deprotection (GP3). Fmoc-Gly-OH was coupled following GP2a and the peptide was Fmoc-deprotected (GP3). Next, Fmoc-D-Dap(Dde)-OH was conjugated using *sym*-collidine (GP2a). The Dde-group was removed in the presence of Fmoc (GP4b) and (4-SiFA)Bz-OH was coupled to the sidechain (GP2a). Subsequently, the Fmoc-group was removed (GP3), (*S*)-DOTAGA(*t*Bu)$_4$ was coupled to the resin-bound peptide for 3 h at rt (modified GP2a) and the peptide was cleaved off the resin under concomitant deprotection of acid-labile groups (GP5a). The cleaved, dried crude product was purified by RP-HPLC. After lyophilization, the product was obtained as colorless solid (31%). RP-HPLC (10 to 90% B in 15 min): t_R = 8.3 min. K' = 3.7. ESI-MS (positive): calculated monoisotopic mass ($C_{65}H_{102}FN_{13}O_{26}Si$): 1527.7; found: m/z = 1529.4 $[M+H]^+$, 765.5 $[M+2H]^{2+}$.

MI-3

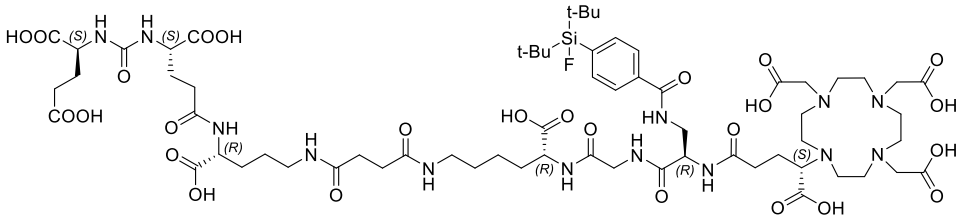

Chemical Formula: $C_{65}H_{102}FN_{13}O_{26}Si$
Molecular Weight: 1528,68

The Synthesis was carried out using the same procedure as described for MI-2 (see above) except for the coupling of Fmoc-L-Lys(O*t*Bu)·HCl. For the synthesis of MI-3, the corresponding D-amino acid was coupled instead. After lyophilization, the product was obtained as colorless solid (28%). RP-HPLC (10 to 90% B in 15 min): t_R = 8.3 min. K' = 3.7. ESI-MS (positive): calculated monoisotopic mass ($C_{65}H_{102}FN_{13}O_{26}Si$): 1527.7; found: m/z = 1527.3 $[M+H]^+$, 764.2 $[M+2H]^{2+}$.

MI-4

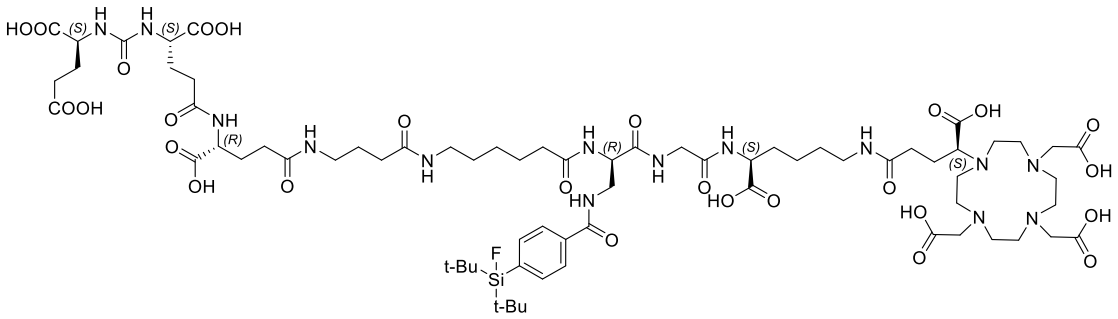

Chemical Formula: $C_{71}H_{113}FN_{14}O_{27}Si$
Molecular Weight: 1641,84

2-CTC resin was loaded with Fmoc-L-Lys(Dde)-OH (GP1). The Dde-group was cleaved (GP4b) and (*S*)-DOTAGA(*t*Bu)$_4$ was conjugated to the resin for 3 h (modified GP2a). After Fmoc-deprotection (GP3), attachment of Fmoc-Gly-OH was realized by a prolonged coupling reaction (GP2a) for 3 h. Fmoc-D-Dap(Dde)-OH (2.0 eq.) was coupled using *sym*-collidine (GP2a). The following orthogonal Dde-deprotection was done using GP4b. (4-SiFA)Bz-OH was reacted with the free amine of the sidechain (GP2a). After Fmoc-deprotection with piperidine (GP3), Fmoc-Ahx-OH was coupled to the resin-bound peptide (GP2a). After another Fmoc-deprotection (GP3), Fmoc-GABA-OH (2.0 eq.) was coupled to the resin for 2 h after pre-activation with HOAt (2.0 eq.), TBTU (2.0 eq.) and DIPEA (6.0 eq.) in DMF for 10 min (modified GP2a). The peptide was Fmoc-deprotected (GP3) and Fmoc-D-Glu-O*t*Bu was conjugated (GP2a). After a final Fmoc-deprotection (GP3), (*t*BuO)EuE(O*t*Bu)$_2$ (2.0 eq.) was coupled with HOAt (2.0 eq.), TBTU (2.0 eq.) and DIPEA (6.0 eq.) in DMF for 3 h (modified GP2a). The peptide was cleaved off the resin (GP5a) and purified by RP-HPLC. After lyophilization, the product was obtained as colorless solid (13%).

RP-HPLC (10 to 90% B in 15 min): t_R = 8.5 min. K' = 3.8. ESI-MS (positive): calculated monoisotopic mass ($C_{71}H_{113}FN_{14}O_{27}Si$): 1640.8; found: m/z = 1642.2 $[M+H]^+$, 821.7 $[M+2H]^{2+}$.

MI-5

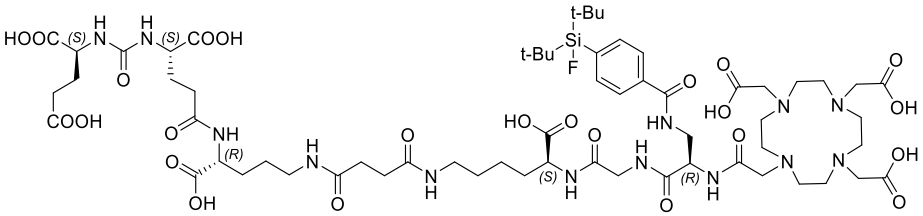

Chemical Formula: $C_{62}H_{98}FN_{13}O_{24}Si$
Molecular Weight: 1456,62

The synthesis was conducted with the same procedure as described for MI-2 with the only difference in using DOTA(tBu)$_4$ instead of DOTAGA(tBu)$_4$ for the last coupling step. The peptide was cleaved off the resin (GP5a) and purified by RP-HPLC. After lyophilization, the product was obtained as colorless solid (17%). RP-HPLC (10 to 90% B in 15 min): t_R = 8.4 min. K' = 3.7. ESI-MS (positive): calculated monoisotopic mass ($C_{62}H_{98}FN_{13}O_{24}Si$): 1455.7; found: m/z = 1457.3 $[M+H]^+$, 729.3 $[M+2H]^{2+}$.

4.3. Synthesis of Branched Linker Constructs (BLC) for HSA Binding Modulation

BLC-1

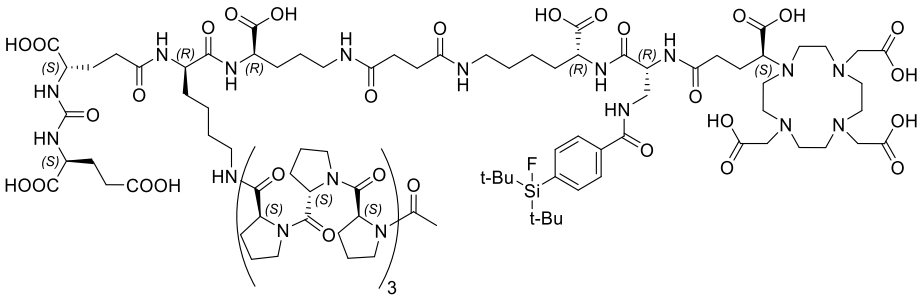

Chemical Formula: $C_{116}H_{176}FN_{23}O_{36}Si$
Molecular Weight: 2515.85

2-CTC resin was loaded with Fmoc-D-Orn(Dde)-OH according to GP1. The Dde-group was cleaved (GP4b) off the sidechain and the deprotected amine was left to react with a solution of succinic anhydride (GP2c). The coupled succinic acid was Allyl-protected using Allyl bromide (30 eq.) in DMF (10 mL/g resin) for 16 h. Fmoc-deprotection was conducted (GP3). In the next step, Fmoc-D-Lys(Dde)-OH was coupled (GP2a). After subsequent Fmoc-deprotection (GP3), (tBuO)EuE(OtBu)$_2$ (2.0 eq.) was conjugated with HOAt (2.0 eq.), TBTU (2.0 eq.) and DIPEA (6.0 eq.) in DMF for 3 h (modified GP2a). After the following Dde-deprotection at the Lys-sidechain (GP4b),

alternating tripeptide-coupling (modified GP2a) with Fmoc-(L-Pro)$_3$-OH (2.0 eq.), HOAt (2.0 eq.), TBTU (2.0 eq.) and DIPEA (6.0 eq.) in DMF for 3 h and Fmoc-deprotection (GP3) was performed to install the nonapeptidyl-linker. The terminal proline was acetylated (GP2d) and the Allyl-group of the succinic acid was cleaved (GP6). Fmoc-D-Lys(O*t*Bu)·HCl was attached to the peptide-bound succinic acid (GP2b). Next, Fmoc-D-Dap(Dde)-OH was conjugated using *sym*-collidine (GP2a). The Dde-group was removed in the presence of Fmoc (GP4b) and (4-SiFA)Bz-OH was coupled to the sidechain (GP2a). Subsequently, the Fmoc-group was removed (GP3), (*S*)-DOTAGA(*t*Bu)$_4$ was coupled to the resin-bound peptide for 3 h at rt (modified GP2a) and the peptide was cleaved off the resin under concomitant deprotection of acid-labile groups (GP5a). The cleaved, dried crude product was purified by RP-HPLC. After lyophilization, the product was obtained as colorless solid (1.3%). RP-HPLC (10 to 90% B in 15 min): t_R = 8.1 min. K' = 3.6. ESI-MS (positive): calculated monoisotopic mass ($C_{116}H_{176}FN_{23}O_{36}Si$): 2514.2; found: m/z = 1256.9 $[M+2H]^{2+}$.

BLC-2

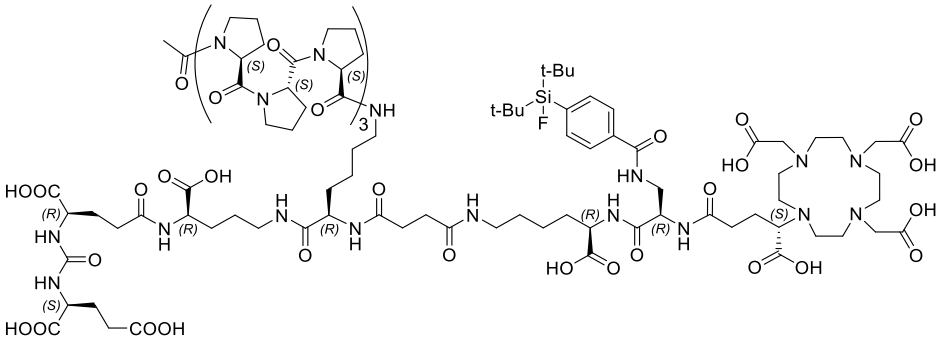

Chemical Formula: $C_{116}H_{176}FN_{23}O_{36}Si$
Molecular Weight: 2515.85

2-CTC resin was loaded with Fmoc-D-Orn(Dde)-OH (GP1). After Fmoc-deprotection (GP3), (*t*BuO)EuE(O*t*Bu)$_2$ (2.0 eq.) was coupled to the amine using HOAt (2.0 eq.), TBTU (2.0 eq.) and DIPEA (6.0 eq.) in DMF at rt for 3 h (modified GP2a). The Orn-sidechain was Dde-deprotected (GP4a) and conjugated to Fmoc-D-Lys(Dde)-OH (GP2a). The Fmoc-group was cleaved (GP3) and the deprotected amine was left to react with succinic anhydride (GP2c). The coupled succinic acid was Allyl-protected using Allyl bromide (30 eq.) in DMF for 16 h. After the following Dde-deprotection at the Lys-sidechain (GP4b), coupling of the tripeptide Fmoc-(L-Pro)$_3$-OH (2.0 eq.) with HOAt (2.0 eq.), TBTU (2.0 eq.) and DIPEA (6.0 eq.) in DMF for 3 h (modified GP2a) and Fmoc-deprotection (GP3) was performed alternately to install the nonapeptidyl-linker. The terminal proline was acetylated (GP2d) and the Allyl-group of the succinic acid was cleaved (GP6). Fmoc-D-Lys(O*t*Bu)·HCl was attached to the peptide-bound succinic acid (GP2b). Next, Fmoc-D-Dap(Dde)-OH was conjugated using *sym*-collidine (GP2a). The Dde-group was removed in the presence of Fmoc (GP4b) and (4-SiFA)Bz-OH was coupled to the sidechain (GP2a). Subsequently,

the Fmoc-group was removed (GP3), (*S*)-DOTAGA(*t*Bu)$_4$ was coupled to the resin-bound peptide for 3 h at rt (modified GP2a) and the peptide was cleaved off the resin under concomitant deprotection of acid-labile groups (GP5a). The cleaved, dried crude product was purified by RP-HPLC. After lyophilization, the product was obtained as colorless solid (1.5%). RP-HPLC (10 to 90% B in 15 min): t_R = 7.7 min. K' = 3.3. ESI-MS (positive): calculated monoisotopic mass ($C_{116}H_{176}FN_{23}O_{36}Si$): 2514.2; found: m/z = 1256.6 $[M+2H]^{2+}$.

BLC-3

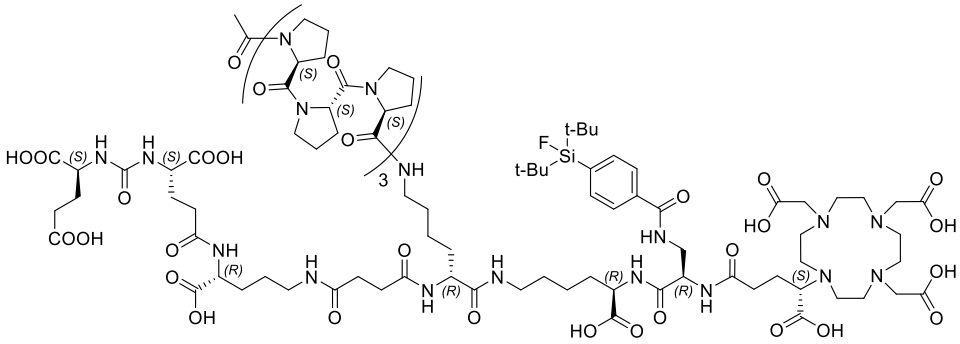

Chemical Formula: $C_{116}H_{176}FN_{23}O_{36}Si$
Molecular Weight: 2515.85

2-CTC resin was loaded with Fmoc-D-Orn(Dde)-OH (GP1). After Fmoc-deprotection (GP3), (*t*BuO)EuE(O*t*Bu)$_2$ (2.0 eq.) was coupled to the amine using HOAt (2.0 eq.), TBTU (2.0 eq.) and DIPEA (6.0 eq.) in DMF at rt for 3 h (modified GP2a). The Orn-sidechain was Dde-deprotected (GP4a) and conjugated to succinic anhydride (GP2c). To the carboxylic acid, H-D-Lys(Dde)-OAll was coupled (GP2b) followed by a modified Dde-deprotection with an addition of Allyl alcohol (100 eq.) to the deprotection solution (GP4a). The installation of the nonapeptidyl-linker was performed by alternately coupling the tripeptide Fmoc-(L-Pro)$_3$-OH (2.0 eq.) with HOAt (2.0 eq.), TBTU (2.0 eq.) and DIPEA (6.0 eq.) in DMF for 3 h (modified GP2a) and Fmoc-deprotection (GP3). The terminal proline was acetylated (GP2d) and the Lys-carboxylate was deprotected (GP6). Fmoc-D-Lys(O*t*Bu)·HCl was attached to the peptide (GP2b). Next, Fmoc-D-Dap(Dde)-OH was conjugated using *sym*-collidine (GP2a). The Dde-group was removed in the presence of Fmoc (GP4b) and (4-SiFA)Bz-OH was coupled to the sidechain (GP2a). Subsequently, the Fmoc-group was removed (GP3), (*S*)-DOTAGA(*t*Bu)$_4$ was coupled to the resin-bound peptide for 3 h at rt (modified GP2a) and the peptide was cleaved off the resin under concomitant deprotection of acid-labile groups (GP5a). The cleaved, dried crude product was purified by RP-HPLC. After lyophilization, the product was obtained as colorless solid (2.6%). RP-HPLC (10 to 90% B in 15 min): t_R = 8.4 min. K' = 3.7. ESI-MS (positive): calculated monoisotopic mass ($C_{116}H_{176}FN_{23}O_{36}Si$): 2514.2; found: m/z = 1257.0 $[M+2H]^{2+}$.

BLC-4

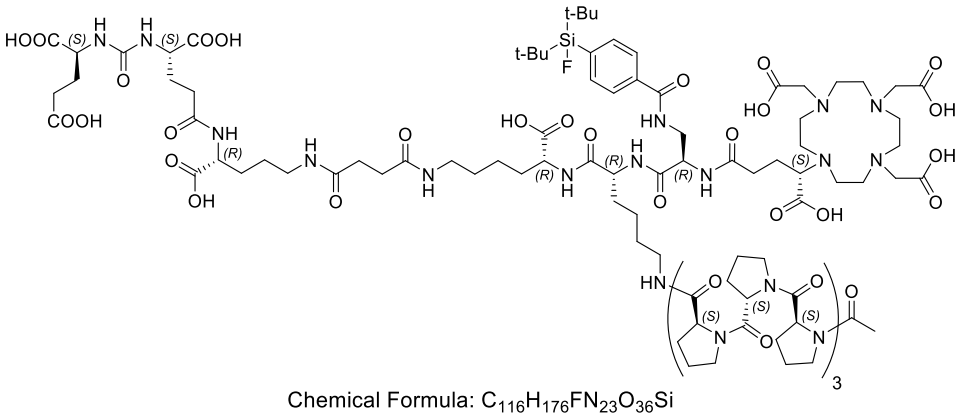

Chemical Formula: $C_{116}H_{176}FN_{23}O_{36}Si$
Molecular Weight: 2515.85

2-CTC resin was loaded with Fmoc-D-Orn(Dde)-OH (GP1). After Fmoc-deprotection (GP3), (*t*BuO)EuE(O*t*Bu)$_2$ (2.0 eq.) was coupled to the amine using HOAt (2.0 eq.), TBTU (2.0 eq.) and DIPEA (6.0 eq.) in DMF at rt for 3 h (modified GP2a). The Orn-sidechain was Dde-deprotected (GP4a) and conjugated to succinic anhydride (GP2c). To the carboxylic acid, Fmoc-L-Lys-O*t*Bu·HCl was coupled (GP2b) followed by Fmoc-deprotection (GP3). Fmoc-D-Dap(Alloc)-OH was conjugated to the resin-bound peptide (GP2a). Next, Fmoc-D-Dap(Dde)-OH was conjugated using *sym*-collidine (GP2a). The Dde-group was removed in the presence of Fmoc (GP4b) and (4-SiFA)Bz-OH was coupled to the sidechain (GP2a). Subsequently, the Fmoc-group was removed (GP3), (*S*)-DOTAGA(*t*Bu)$_4$ was coupled to the resin-bound peptide for 3 h at rt (modified GP2a). The Lys-sidechain was Alloc-deprotected (GP6) and the installation of the nonapeptidyl-linker was performed by alternately coupling the tripeptide Fmoc-(L-Pro)$_3$-OH (2.0 eq.) with HOAt (2.0 eq.), TBTU (2.0 eq.) and DIPEA (6.0 eq.) in DMF for 3 h (modified GP2a) and Fmoc-deprotection (GP3). The terminal proline was acetylated (GP2d) and the peptide was cleaved off the resin under concomitant deprotection of acid-labile groups (GP5a). The cleaved, dried crude product was purified by RP-HPLC. After lyophilization, the product was obtained as colorless solid (1.2%). RP-HPLC (10 to 90% B in 15 min): t_R = 8.3 min. K' = 3.7. ESI-MS (positive): calculated monoisotopic mass ($C_{116}H_{176}FN_{23}O_{36}Si$): 2514.2; found: m/z = 1256.9 $[M+2H]^{2+}$.

BLC-5

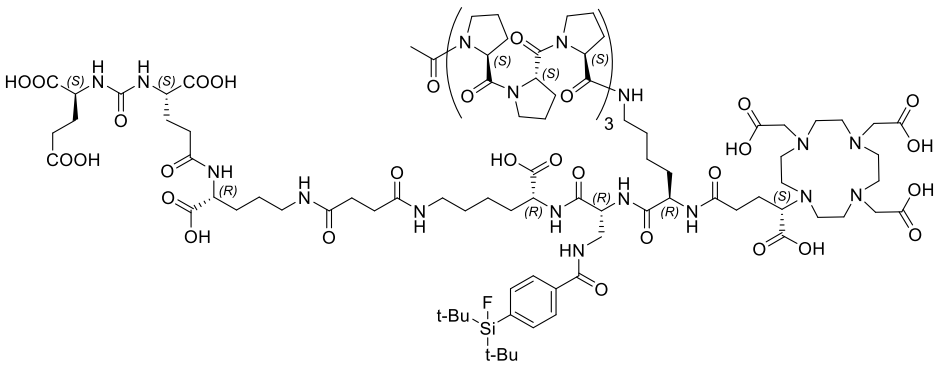

Chemical Formula: $C_{116}H_{176}FN_{23}O_{36}Si$
Molecular Weight: 2515.85

2-CTC resin was loaded with Fmoc-D-Orn(Dde)-OH (GP1). After Fmoc-deprotection (GP3), (*t*BuO)EuE(O*t*Bu)$_2$ (2.0 eq.) was coupled to the amine using HOAt (2.0 eq.), TBTU (2.0 eq.) and DIPEA (6.0 eq.) in DMF at rt for 3 h (modified GP2a). The Orn-sidechain was Dde-deprotected (GP4a) and conjugated to succinic anhydride (GP2c). To the carboxylic acid, Fmoc-L-Lys-O*t*Bu·HCl was coupled (GP2b) followed by Fmoc-deprotection (GP3). Next, Fmoc-D-Dap(Dde)-OH was conjugated using *sym*-collidine (GP2a). The Dde-group was removed in the presence of Fmoc (GP4b) and (4-SiFA)Bz-OH was coupled to the sidechain (GP2a). Subsequently, the Fmoc-group was removed (GP3), and Fmoc-D-Lys(Dde)-OH was conjugated (GP2a). The Fmoc-group was cleaved (GP3) and (*S*)-DOTAGA(*t*Bu)$_4$ was coupled to the resin-bound peptide for 3 h at rt (modified GP2a). After the following Dde-deprotection at the Lys-sidechain (GP4a), coupling of the tripeptide Fmoc-(L-Pro)$_3$-OH (2.0 eq.) with HOAt (2.0 eq.), TBTU (2.0 eq.) and DIPEA (6.0 eq.) in DMF for 3 h (modified GP2a) and Fmoc-deprotection (GP3) was performed alternately to install the nonapeptidyl-linker. The terminal proline was acetylated (GP2d) and the peptide was cleaved off the resin under concomitant deprotection of acid-labile groups (GP5a). The cleaved, dried crude product was purified by RP-HPLC. After lyophilization, the product was obtained as colorless solid (5.4%). RP-HPLC (10 to 90% B in 15 min): t_R = 7.4 min. K' = 3.2. ESI-MS (positive): calculated monoisotopic mass ($C_{116}H_{176}FN_{23}O_{36}Si$): 2514.2; found: m/z = 1256.9 $[M+2H]^{2+}$.

BLC-6

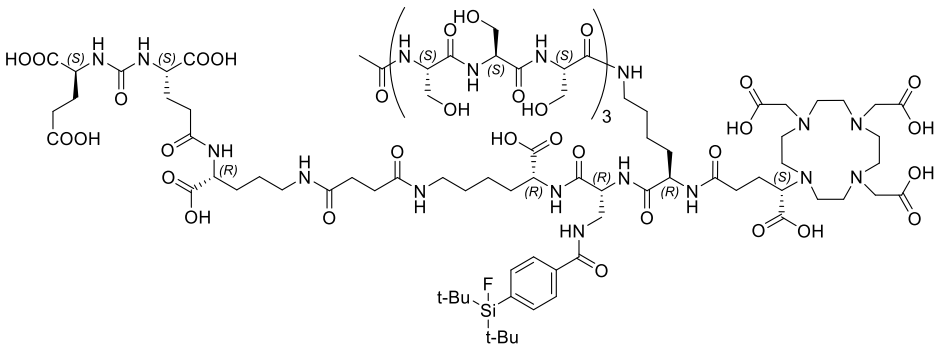

Chemical Formula: $C_{98}H_{158}FN_{23}O_{45}Si$
Molecular Weight: 2425.51

The synthesis was conducted analog to BCL-5, as described above. Instead of the nonaprolyl linker, a nonaseryl linker was conjugated to the Dde-deprotected Lys-sidechain by alternately coupling of the tripeptide Fmoc-[L-Ser(O*t*Bu)]$_3$-OH (2.0 eq.), HOAt (2.0 eq.), TBTU (2.0 eq.) and DIPEA (6.0 eq.) in DMF for 3 h (modified GP2a) and Fmoc-deprotection (GP3). Although different amounts of tripeptide and prolonged reaction time were investigated, the tripeptide-couplings with Fmoc-[L-Ser(O*t*Bu)$_3$]-OH did not show complete conversion. The terminal serine was acetylated (GP2d) and the peptide was cleaved off the resin under concomitant deprotection of acid-labile groups (GP5a). The cleaved, dried crude product was purified by RP-HPLC. After lyophilization, the product was obtained as colorless solid (2.9%). RP-HPLC (10 to 90% B in 15 min): t_R = 7.5 min. K' = 3.2. ESI-MS (positive): calculated monoisotopic mass ($C_{98}H_{158}FN_{23}O_{45}Si$): 2424.1; found: m/z = 1213.7 $[M+2H]^{2+}$.

BLC-7

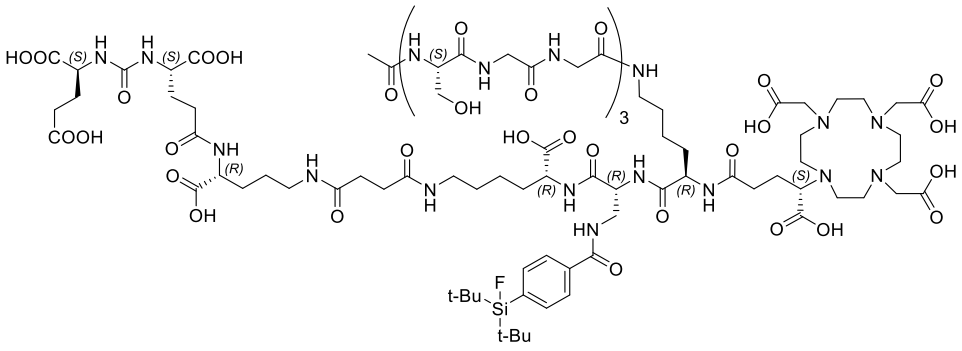

Chemical Formula: $C_{92}H_{146}FN_{23}O_{39}Si$
Molecular Weight: 2245.35

The synthesis was conducted analog to BCL-5, as described above. Instead of the nonaprolyl linker, a (L-Ser-Gly-Gly)$_3$-linker was conjugated to the Dde-deprotected Lys-sidechain by alternately coupling of the tripeptide Fmoc-L-Ser(O*t*Bu)-Gly-Gly-OH (2.0 eq.), HOAt (2.0 eq.), TBTU (2.0 eq.) and DIPEA (6.0 eq.) in DMF for 3 h (modified GP2a) and Fmoc-deprotection (GP3 The terminal serine was acetylated (GP2d) and the peptide was cleaved off the resin under

concomitant deprotection of acid-labile groups (GP5a). The cleaved, dried crude product was purified by RP-HPLC. After lyophilization, the product was obtained as colorless solid (3.6%). RP-HPLC (10 to 90% B in 15 min): t_R = 7.6 min. K' = 3.3. ESI-MS (positive): calculated monoisotopic mass ($C_{92}H_{146}FN_{23}O_{39}Si$): 2244.0; found: m/z = 1123.3 $[M+2H]^{2+}$.

BLC-8

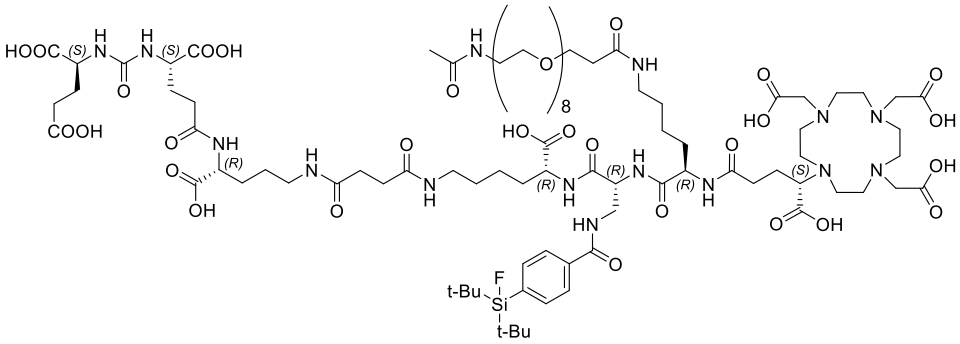

Chemical Formula: $C_{90}H_{150}FN_{15}O_{36}Si$
Molecular Weight: 2065.31

The synthesis was conducted analog to BLC-5, as described above. Instead of the nonaprolyl linker, a PEG_8-linker was conjugated to the Dde-deprotected Lys-sidechain (modified GP2a) using Fmoc-NH-PEG_8-propionic acid (2.0 eq.), HOAt (2.0 eq.), TBTU (2.0 eq.) and DIPEA (6.0 eq.) in DMF for 3 h. The Fmoc-group was cleaved (GP3) and the terminal amine was acetylated (GP2d). The peptide was cleaved off the resin under concomitant deprotection of acid-labile groups (GP5a). The cleaved, dried crude product was purified by RP-HPLC. After lyophilization, the product was obtained as colorless solid (8.9%). RP-HPLC (10 to 90% B in 15 min): t_R = 8.2 min. K' = 3.6. ESI-MS (positive): calculated monoisotopic mass ($C_{90}H_{150}FN_{15}O_{36}Si$): 2064.0; found: m/z = 1034.1 $[M+2H]^{2+}$.

BLC-9

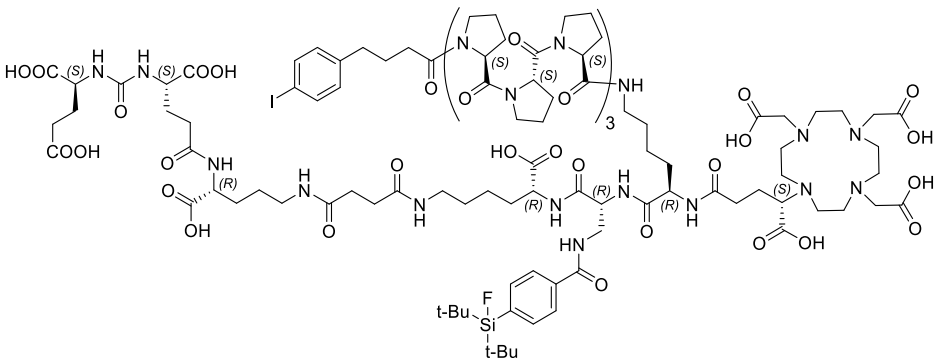

Chemical Formula: $C_{124}H_{183}FIN_{23}O_{36}Si$
Molecular Weight: 2745.89

The synthesis was conducted analog to BLC-5, as described above. Instead of the acetylation step, coupling of 4-(*p*-iodophenyl)butyric acid (2.0 eq.) with HOAt (2.0 eq.), TBTU (2.0 eq.) and

DIPEA (6.0 eq.) in DMF for 3 h (modified GP2a) was performed. The peptide was cleaved off the resin under concomitant deprotection of acid-labile groups (GP5a). The cleaved, dried crude product was purified by RP-HPLC. After lyophilization, the product was obtained as colorless solid (7.9%). RP-HPLC (10 to 90% B in 15 min): t_R = 11.8 min. K' = 5.6. ESI-MS (positive): calculated monoisotopic mass ($C_{124}H_{183}FIN_{23}O_{36}Si$): 2744.2; found: m/z = 1371.8 $[M+2H]^{2+}$.

BLC-10

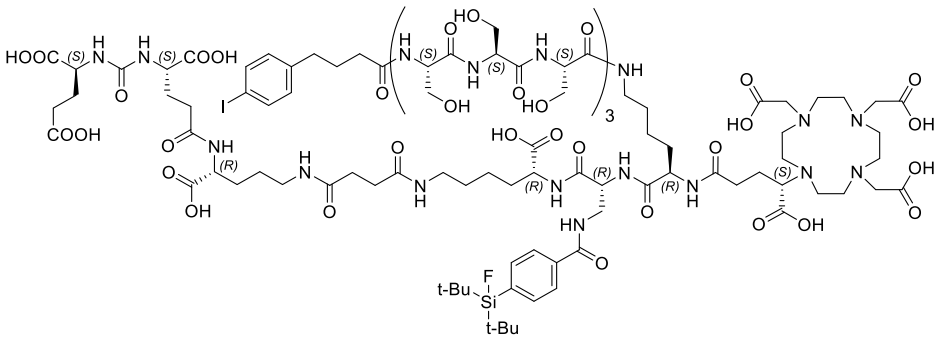

Chemical Formula: $C_{106}H_{165}FIN_{23}O_{45}Si$
Molecular Weight: 2655,59

The synthesis, described as follows, resulted in a mixture of which the shown product could not be isolated. The synthesis was conducted analog to BLC-6, as described above. Instead of the acetylation step, coupling of 4-(*p*-iodophenyl)butyric acid (2.0 eq.) with HOAt (2.0 eq.), TBTU (2.0 eq.) and DIPEA (6.0 eq.) in DMF for 3 h (modified GP2a) was performed. The peptide was cleaved off the resin and dried under nitrogen stream (GP5a). The attempt to purify the dried crude product by RP-HPLC was insufficient. The product could not be separated from deletion peptides formed due to incomplete couplings with Fmoc-[L-Ser(O*t*Bu)]$_3$-OH.

BLC-11

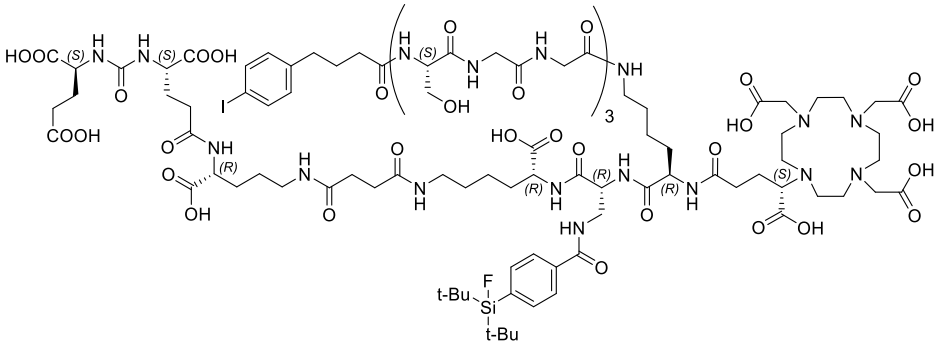

Chemical Formula: $C_{100}H_{153}FIN_{23}O_{39}Si$
Molecular Weight: 2475.40

The synthesis was conducted analog to BLC-7, as described above. Instead of the acetylation step, coupling of 4-(*p*-iodophenyl)butyric acid (2.0 eq.) with HOAt (2.0 eq.), TBTU (2.0 eq.) and DIPEA (6.0 eq.) in DMF for 3 h (modified GP2a) was performed. The peptide was cleaved off the

resin under concomitant deprotection of acid-labile groups (GP5a). The cleaved, dried crude product was purified by RP-HPLC. After lyophilization, the product was obtained as colorless solid (3.0%). RP-HPLC (10 to 90% B in 15 min): t_R = 8.9 min. K' = 4.0. ESI-MS (positive): calculated monoisotopic mass ($C_{100}H_{153}FIN_{23}O_{39}Si$): 2473.9; found: m/z = 1236.5$[M+2H]^{2+}$.

BLC-12

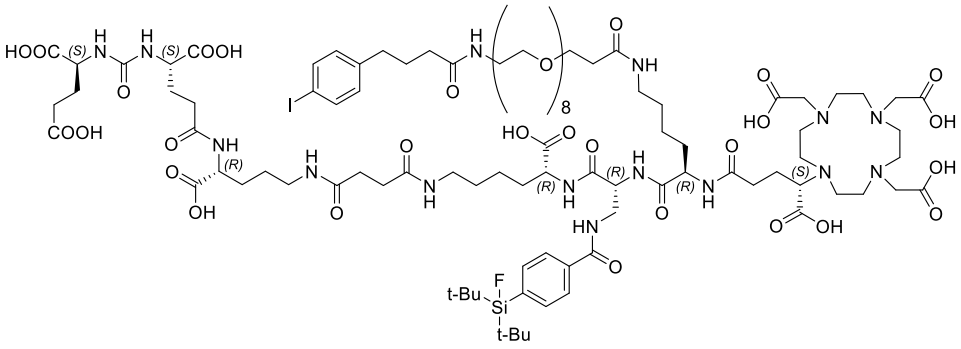

Chemical Formula: $C_{98}H_{157}FIN_{15}O_{36}Si$
Molecular Weight: 2295.36

The synthesis was conducted analog to BLC-8, as described above. Instead of the acetylation step, coupling of 4-(*p*-iodophenyl)butyric acid (2.0 eq.) with HOAt (2.0 eq.), TBTU (2.0 eq.) and DIPEA (6.0 eq.) in DMF for 3 h (GP2) was performed. The peptide was cleaved off the resin under concomitant deprotection of acid-labile groups (GP5a). The cleaved, dried crude product was purified by RP-HPLC. After lyophilization, the product was obtained as colorless solid (11%). RP-HPLC (10 to 90% B in 15 min): t_R = 10.3 min. K' = 4.8. ESI-MS (positive): calculated monoisotopic mass ($C_{98}H_{157}FIN_{15}O_{36}Si$): 2294.0; found: m/z = 1147.1 $[M+2H]^{2+}$.

4.4. Synthesis of Ligands with Reduced Net Charge (RNC)

RNC-1

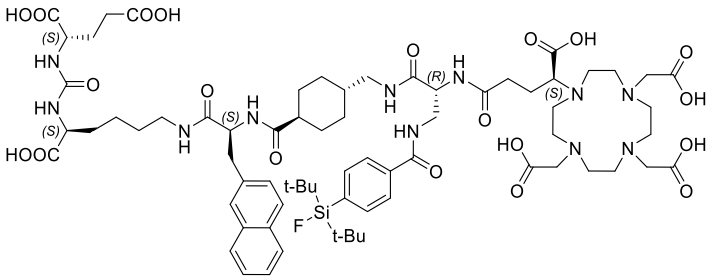

Chemical Formula: $C_{70}H_{102}FN_{11}O_{20}Si$
Molecular Weight: 1464,73

2-CTC resin was loaded with Fmoc-L-Lys(Dde)-OH according to GP1. The Fmoc-group was cleaved (GP3) and a urea bond was formed with di-*tert*-butyl (1*H*-imidazole-1-carbonyl)-*L*-glutamate (2.0 eq.) and TEA (3.0 eq.) in DCE at 40 °C overnight (GP7). Dde-deprotection was

conducted (GP4a) and subsequently, Fmoc-L-2-Nal-OH and Fmoc-tranexamic acid were attached to the resin-bound peptide by alternately coupling (GP2a) and Fmoc-deprotection (GP3). Next, Fmoc-D-Dap(Dde)-OH was conjugated using *sym*-collidine (GP2a). The Dde-group was removed in the presence of Fmoc (GP4b) and (4-SiFA)Bz-OH was coupled to the sidechain (GP2a). Subsequently, the Fmoc-group was removed (GP3), (*S*)-DOTAGA(*t*Bu)$_4$ was coupled to the resin-bound peptide for 3 h at rt (modified GP2a) and the peptide was cleaved off the resin under concomitant deprotection of acid-labile groups (GP5a). The cleaved, dried crude product was purified by RP-HPLC. After lyophilization, the product was obtained as colorless solid (23%). RP-HPLC (10 to 90% B in 15 min): t_R = 10.1 min. K' = 4.7. ESI-MS (positive): calculated monoisotopic mass ($C_{70}H_{102}FN_{11}O_{20}Si$): 1463.7; found: m/z = 1463.4 $[M+H]^+$, 732.3 $[M+2H]^{2+}$.

RNC-2

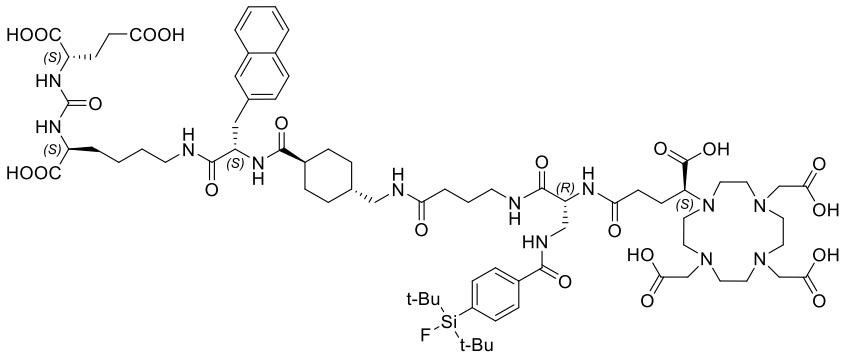

Chemical Formula: $C_{74}H_{109}FN_{12}O_{21}Si$
Molecular Weight: 1549,83

2-CTC resin was loaded with Fmoc-L-Lys(Dde)-OH according to GP1. The Fmoc-group was cleaved (GP3) and a urea bond was formed with di-*tert*-butyl (1*H*-imidazole-1-carbonyl)-*L*-glutamate (2.0 eq.) and TEA (3.0 eq.) in DCE at 40 °C overnight (GP7). Dde-deprotection was conducted (GP4a) and subsequently, Fmoc-L-2-Nal-OH, Fmoc-tranexamic acid and Fmoc-GABA-OH were attached to the resin-bound peptide by alternately coupling (GP2a) and Fmoc-deprotection (GP3). Next, Fmoc-D-Dap(Dde)-OH was conjugated using *sym*-collidine (GP2a). The Dde-group was removed in the presence of Fmoc (GP4b) and (4-SiFA)Bz-OH was coupled to the sidechain (GP2a). Subsequently, the Fmoc-group was removed (GP3), (*S*)-DOTAGA(*t*Bu)$_4$ was coupled to the resin-bound peptide for 3 h at rt (modified GP2a) and the peptide was cleaved off the resin under concomitant deprotection of acid-labile groups (GP5a). The cleaved, dried crude product was purified by RP-HPLC. After lyophilization, the product was obtained as colorless solid (28%). RP-HPLC (10 to 90% B in 15 min): t_R = 10.0 min. K' = 4.6. ESI-MS (positive): calculated monoisotopic mass ($C_{74}H_{109}FN_{12}O_{21}Si$): 1548.8; found: m/z = 1548.4 $[M+H]^+$, 774.8 $[M+2H]^{2+}$.

RNC-3

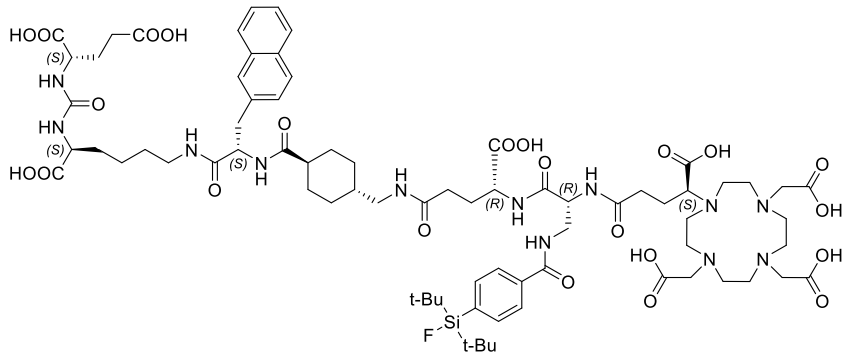

Chemical Formula: $C_{75}H_{109}FN_{12}O_{23}Si$
Molecular Weight: 1593,84

The synthesis was conducted analog to the synthesis of RNC-2 (see above) with the only difference in coupling Fmoc-D-Glu-O*t*Bu (GP2a) instead of Fmoc-GABA-OH. After completion of the resin-bound peptide sequence, the peptide was cleaved off the resin under concomitant deprotection of acid-labile groups (GP5a). The cleaved, dried crude product was purified by RP-HPLC. After lyophilization, the product was obtained as colorless solid (35%). RP-HPLC (10 to 90% B in 15 min): t_R = 9.8 min. K' = 4.5. ESI-MS (positive): calculated monoisotopic mass ($C_{75}H_{109}FN_{12}O_{23}Si$): 1592.8; found: m/z = 1592.9 $[M+H]^+$, 797.1 $[M+2H]^{2+}$.

RNC-4

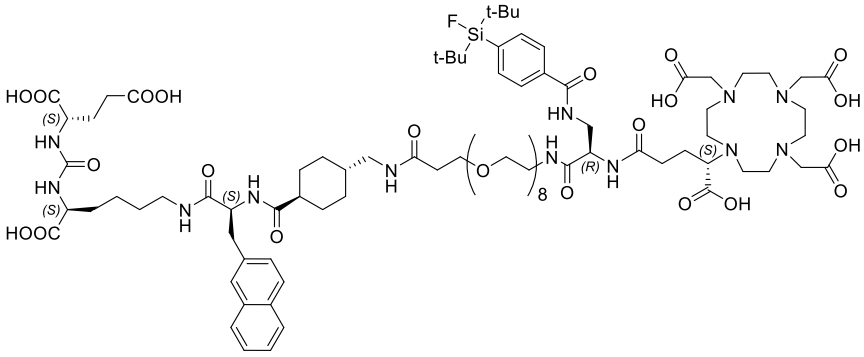

Chemical Formula: $C_{89}H_{139}FN_{12}O_{29}Si$
Molecular Weight: 1888.20

The synthesis was conducted analog to the synthesis of RNC-2 (see above) with the only difference in coupling Fmoc-NH-PEG_8-propionic acid instead of Fmoc-GABA-OH. After completion of the resin-bound peptide sequence, the peptide was cleaved off the resin under concomitant deprotection of acid-labile groups (GP5a). The cleaved, dried crude product was purified by RP-HPLC. After lyophilization, the product was obtained as colorless solid (21%). RP-HPLC (10 to 90% B in 15 min): t_R = 9.8 min. K' = 4.5. ESI-MS (positive): calculated monoisotopic mass ($C_{89}H_{139}FN_{12}O_{29}Si$): 1887.0; found: m/z = 1888.6 $[M+H]^+$, 944.7 $[M+2H]^{2+}$.

RNC-5

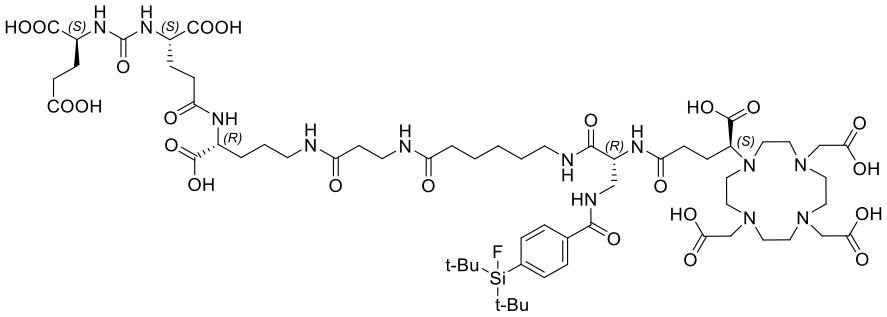

Chemical Formula: $C_{62}H_{99}FN_{12}O_{23}Si$
Molecular Weight: 1427,62

2-CTC resin was loaded with Fmoc-D-Orn(Dde)-OH (GP1). After Fmoc-deprotection (GP3), (*t*BuO)EuE(O*t*Bu)$_2$ (2.0 eq.) was coupled to the amine using HOAt (2.0 eq.), TBTU (2.0 eq.) and DIPEA (6.0 eq.) in DMF at rt for 3 h (modified GP2a). The Orn-sidechain was Dde-deprotected (GP4a) and conjugated to Fmoc-*b*-Ala-OH (GP2a) with a subsequent Fmoc-deprotection (GP3). Fmoc-Ahx-OH was coupled following GP2a and the peptide was Fmoc-deprotected (GP3). Next, Fmoc-D-Dap(Dde)-OH was conjugated using *sym*-collidine (GP2a). The Dde-group was removed in the presence of Fmoc (GP4b) and (4-SiFA)Bz-OH was coupled to the sidechain (GP2a). Subsequently, the Fmoc-group was removed (GP3), (*S*)-DOTAGA(*t*Bu)$_4$ was coupled to the resin-bound peptide for 3 h at rt (modified GP2a) and the peptide was cleaved off the resin under concomitant deprotection of acid-labile groups (GP5a). The cleaved, dried crude product was purified by RP-HPLC. After lyophilization, the product was obtained as colorless solid (18%). RP-HPLC (10 to 90% B in 15 min): t_R = 8.5 min. K' = 3.8. ESI-MS (positive): calculated monoisotopic mass ($C_{62}H_{99}FN_{12}O_{23}Si$):1426.7; found: m/z = 1427.9 $[M+H]^+$, 714.1 $[M+2H]^{2+}$.

RNC-6

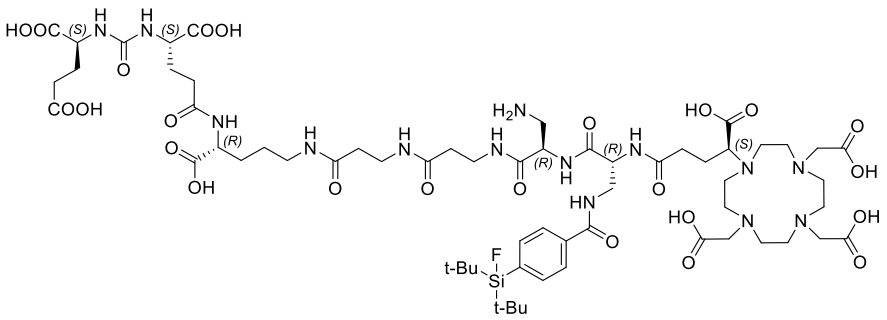

Chemical Formula: $C_{62}H_{99}FN_{14}O_{24}Si$
Molecular Weight: 1471,63

2-CTC resin was loaded with Fmoc-D-Orn(Dde)-OH (GP1). After Fmoc-deprotection (GP3), (*t*BuO)EuE(O*t*Bu)$_2$ (2.0 eq.) was coupled to the amine using HOAt (2.0 eq.), TBTU (2.0 eq.) and DIPEA (6.0 eq.) in DMF at rt for 3 h (modified GP2a). The Orn-sidechain was Dde-deprotected (GP4a) followed twice by the conjugation of Fmoc-*b*-Ala-OH (GP2a) by alternate coupling steps

(GP2a) and Fmoc-deprotection (GP3). Fmoc-D-Dap(Boc)-OH was coupled according to GP2a using *sym*-collidine as base and the peptide was Fmoc-deprotected (GP3). Next, Fmoc-D-Dap(Dde)-OH was conjugated, again using *sym*-collidine (GP2a). The Dde-group was removed in the presence of Fmoc (GP4b) and (4-SiFA)Bz-OH was coupled to the sidechain (GP2a). Subsequently, the Fmoc-group was removed (GP3), (*S*)-DOTAGA(*t*Bu)$_4$ was coupled to the resin-bound peptide for 3 h at rt (modified GP2a) and the peptide was cleaved off the resin under concomitant deprotection of acid-labile groups (GP5a). The cleaved, dried crude product was purified by RP-HPLC. After lyophilization, the product was obtained as colorless solid (21%). RP-HPLC (10 to 90% B in 15 min): t_R = 8.0 min. K' = 3.5. ESI-MS (positive): calculated monoisotopic mass ($C_{62}H_{99}FN_{14}O_{24}Si$): 1470.7; found: m/z = 1471.9 $[M+H]^+$, 736.3 $[M+2H]^{2+}$.

RNC-7

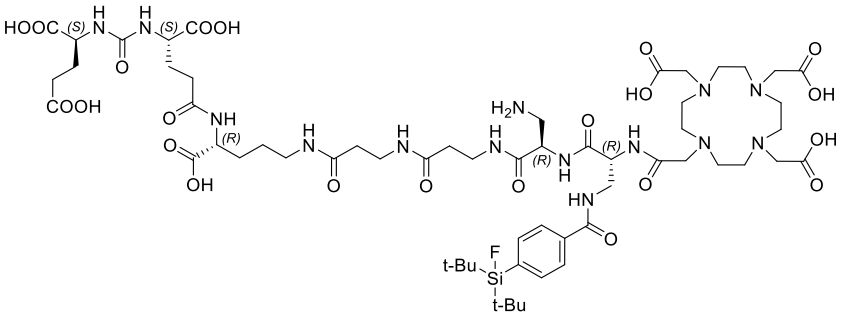

Chemical Formula: $C_{59}H_{95}FN_{14}O_{22}Si$
Molecular Weight: 1399,57

The synthesis was conducted analog to the synthesis of RNC-6 (see above) with the only difference in coupling DOTA(*t*Bu)$_4$ instead of DOTAGA(*t*Bu)$_4$. After completion of the resin-bound peptide sequence, the peptide was cleaved off the resin under concomitant deprotection of acid-labile groups (GP5a). The cleaved, dried crude product was purified by RP-HPLC. After lyophilization, the product was obtained as colorless solid (15%). RP-HPLC (10 to 70% B in 15 min): t_R = 9.8 min. K' = 4.5. ESI-MS (positive): calculated monoisotopic mass ($C_{59}H_{95}FN_{14}O_{22}Si$): 1398.7; found: m/z = 1399.8 $[M+H]^+$, 700.3 $[M+2H]^{2+}$, 467.3 $[M+H]^{3+}$.

4.5. Synthesis of Ligands with Modified SiFA Moieties (MSM)

MSM-1

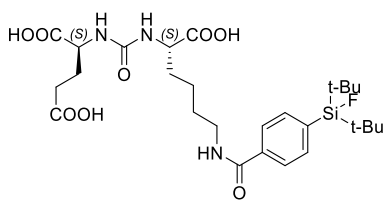

Chemical Formula: $C_{27}H_{42}FN_3O_8Si$
Molecular Weight: 583,73

A similar synthesis of this compound was published previously.(*115*) (4-SiFA)Bz-OH (4.2 mg, 14.9 µmol, 1.0 eq.) was pre-activated with HOAt (2.0 mg, 14.9 µmol, 1.0 eq.), TBTU (4.8 mg, 14.9 µmol, 1.0 eq.) and DIPEA (4.5 eq.) in 1 mL DMF for 15 min at rt. For coupling, 500 µL of a solution of (*t*BuO)KuE(O*t*Bu)$_2$ (1.0 eq.) in DMF were added to the pre-activated SiFA building block and stirred for 2 h at rt. Next, the solvent was evaporated under reduced pressure at 60 °C. The residue was dissolved in 1 mL of TFA/TIPS/DCM (*v/v/v* = 95:2.5:2.5) and left to react for 1 h at rt. Subsequently, the volatiles were removed under a stream of nitrogen, the dried crude product was purified by RP-HPLC and lyophilized to obtain a colorless solid (3.24 mg, 5.55 mmol, 37%). RP-HPLC (10 to 70% B in 15 min): t_R = 11.7 min. K' = 5.6. ESI-MS (positive): calculated monoisotopic mass ($C_{27}H_{42}FN_3O_8Si$): 583.3; found: m/z = 583.8 $[M+H]^+$.

MSM-2

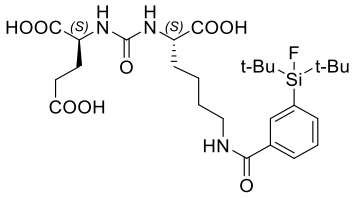

Chemical Formula: $C_{27}H_{42}FN_3O_8Si$
Molecular Weight: 583,73

(3-SiFA)Bz-OH (4.2 mg, 14.9 µmol, 1.0 eq.) was pre-activated with HOAt (2.0 mg, 14.9 µmol, 1.0 eq.), TBTU (4.8 mg, 14.9 µmol, 1.0 eq.) and DIPEA (4.5 eq.) in 1 mL DMF for 15 min at rt. For coupling, 500 µL of a solution of (*t*BuO)KuE(O*t*Bu)$_2$ (1.0 eq.) in DMF were added to the pre-activated SiFA building block and stirred for 2 h at rt. Next, the solvent was evaporated under reduced pressure at 60 °C. The residue was dissolved in 1 mL of TFA/TIPS/DCM (*v/v/v* = 95:2.5:2.5) and left to react for 1 h at rt. Subsequently, the volatiles were removed under a stream of nitrogen, the dried crude product was purified by RP-HPLC and lyophilized to obtain a colorless solid (7.92 mg, 13.57 µmol, 91%). RP-HPLC (10 to 70% B in 15 min): t_R = 11.5 min. K' = 5.5. ESI-MS (positive): calculated monoisotopic mass ($C_{27}H_{42}FN_3O_8Si$): 583.3; found: m/z = 584.4 $[M+H]^+$.

MSM-3

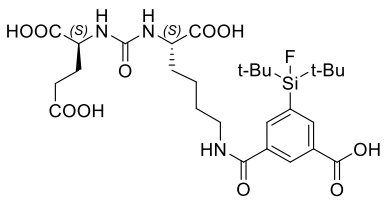

Chemical Formula: $C_{28}H_{42}FN_3O_{10}Si$
Molecular Weight: 627,74

2-CTC resin was loaded with Fmoc-L-Lys(Dde)-OH (GP1). The resin-bound amino acid was Fmoc-deprotected (GP3). On-resin urea-bond formation was conducted with (*S*)-di-*tert*-butyl-2-(1*H*-imidazole-1-carboxamido)pentanedioate according to GP7. The Lys-sidechain was Dde-deprotected (GP4a) and AllO-(5-SiFA)Ip-OH was coupled (GP2a). The peptide was Allyl-deprotected (GP6) followed by cleaving off the resin with concomitant deprotection of acid-labile protecting groups (GP5a). The cleaved, dried crude product was purified by RP-HPLC and lyophilized to obtain a colorless solid (41%). RP-HPLC (10 to 70% B in 15 min): t_R = 10.0 min. K' = 4.6. ESI-MS (positive): calculated monoisotopic mass ($C_{28}H_{42}FN_3O_{10}Si$): 627.3; found: m/z = 627.8 $[M+H]^+$.

MSM-4

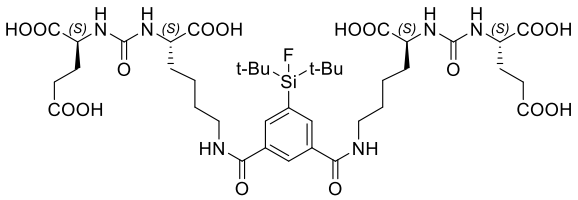

Chemical Formula: $C_{40}H_{61}FN_6O_{16}Si$
Molecular Weight: 929,04

(5-SiFA)Ip-OH (7.15 mg, 14.9 µmol, 1.0 eq.) was pre-activated with HOAt (4.1 mg, 29.8 µmol, 2.0 eq.), TBTU (9:6 mg, 29.8 µmol, 2.0 eq.) and DIPEA (9.0 eq.) in 1 mL DMF for 15 min at rt. For coupling, 500 µL of a solution of (*t*BuO)KuE(O*t*Bu)$_2$ (14.5 mg, 29.8 µmol, 2.0 eq.) in DMF were added to the pre-activated SiFA building block and stirred for 2 h at rt. Next, the solvent was evaporated under reduced pressure at 60 °C. The residue was dissolved in 1 mL of TFA/TIPS/DCM (*v*/*v*/*v* = 95:2.5:2.5) and left to react for 1 h at rt. Subsequently, the volatiles were removed under a stream of nitrogen, the dried crude product was purified by RP-HPLC and lyophilized to obtain a colorless solid (1.43 mg, 1.54 µmol, 10%). RP-HPLC (10 to 70% B in 15 min): t_R = 8.8 min. K' = 3.9. ESI-MS (positive): calculated monoisotopic mass ($C_{40}H_{61}FN_6O_{16}Si$): 928.4; found: m/z = 928.6 $[M+H]^+$.

MSM-5

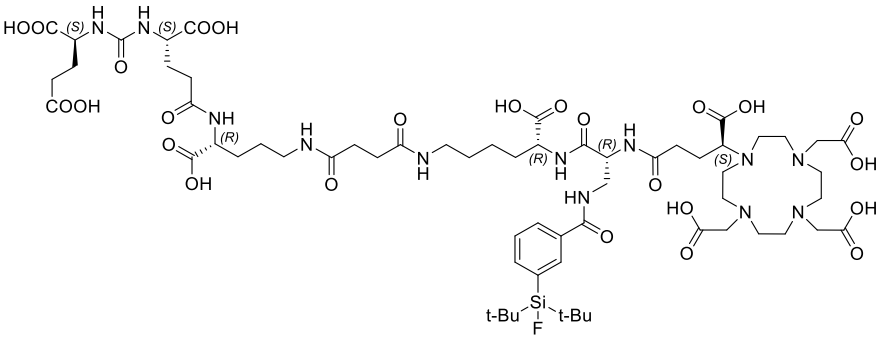

Chemical Formula: $C_{63}H_{99}FN_{12}O_{25}Si$
Molecular Weight: 1471,63

2-CTC resin was loaded with Fmoc-D-Orn(Dde)-OH (GP1). After Fmoc-deprotection (GP3), (*t*BuO)EuE(O*t*Bu)$_2$ (2.0 eq.) was coupled to the amine using HOAt (2.0 eq.), TBTU (2.0 eq.) and DIPEA (6.0 eq.) in DMF at rt for 3 h (modified GP2a). The Orn-sidechain was Dde-deprotected (GP4a) and conjugated to succinic anhydride (GP2c). To the carboxylic acid, Fmoc-D-Lys-O*t*Bu·HCl was coupled (GP2b) followed by Fmoc-deprotection. Next, Fmoc-D-Dap(Dde)-OH was conjugated using *sym*-collidine (GP2a). The Dde-group was removed in the presence of Fmoc (GP4b) and (3-SiFA)Bz-OH was coupled to the sidechain (GP2a). Subsequently, the Fmoc-group was removed (GP3), (*S*)-DOTAGA(*t*Bu)$_4$ was coupled to the resin-bound peptide for 3 h at rt (modified GP2a) and the peptide was cleaved off the resin under concomitant deprotection of acid-labile groups (GP5a). The cleaved, dried crude product was purified by RP-HPLC. After lyophilization, the product was obtained as colorless solid (33%). RP-HPLC (10 to 70% B in 15 min): t_R = 9.9 min. K' = 4.6. ESI-MS (positive): calculated monoisotopic mass ($C_{63}H_{99}FN_{12}O_{25}Si$): 1470.7; found: m/z = 1471.9 $[M+H]^+$, 736.7 $[M+2H]^{2+}$.

MSM-6

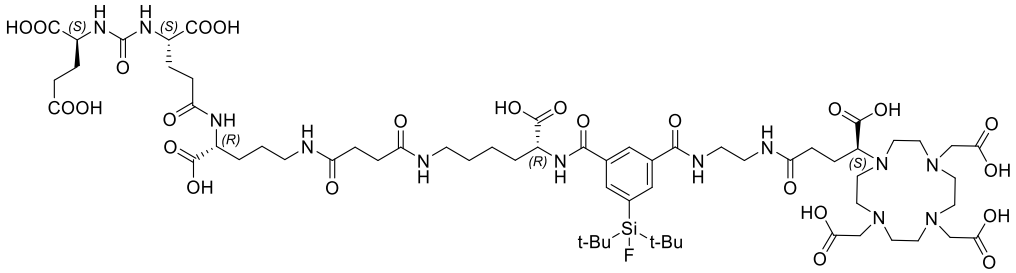

Chemical Formula: $C_{63}H_{99}FN_{12}O_{25}Si$
Molecular Weight: 1471,63

2-CTC resin was loaded with Fmoc-D-Orn(Dde)-OH (GP1). After Fmoc-deprotection (GP3), (*t*BuO)EuE(O*t*Bu)$_2$ (2.0 eq.) was coupled to the amine using HOAt (2.0 eq.), TBTU (2.0 eq.) and DIPEA (6.0 eq.) in DMF at rt for 3 h (modified GP2a). The Orn-sidechain was Dde-deprotected (GP4a) and conjugated to succinic anhydride (GP2c). To the carboxylic acid, Fmoc-D-Lys-

O*t*Bu·HCl was coupled (GP2b) followed by Fmoc-deprotection. Next, AllO-(5-SiFA)Ip-OH was conjugated (GP2a) and Allyl-deprotected (GP6). Fmoc-EDA·HCl was coupled to the unprotected carboxylic acid (GP2b). Subsequently, the Fmoc-group was removed (GP3), (*S*)-DOTAGA(*t*Bu)$_4$ was coupled to the resin-bound peptide for 3 h at rt (modified GP2a) and the peptide was cleaved off the resin under concomitant deprotection of acid-labile groups (GP5a). The cleaved, dried crude product was purified by RP-HPLC. After lyophilization, the product was obtained as colorless solid (20%). RP-HPLC (10 to 70% B in 15 min): t_R = 8.9 min. K' = 4.0. ESI-MS (positive): calculated monoisotopic mass ($C_{63}H_{99}FN_{12}O_{25}Si$): 1470.7; found: m/z = 1471.4 $[M+H]^+$, 736.2 $[M+2H]^{2+}$.

5. Synthesis of ^{nat}Lu-DOTAGA and ^{nat}Lu-DOTA Complexes

The corresponding ^{nat}Lu-complexes were prepared from a 2 mM solution of the PSMA inhibitor (1.0 eq.) in DMSO with a 20 mM aqueous solution of $LuCl_3$ (2.5 eq.), heated to 95 °C for 30 min. After cooling, the ^{nat}Lu-chelate formation was confirmed using RP-HPLC and ESI-MS.

^{nat}Lu-Complexes of Reference Ligands (*125*)

^{nat}Lu-PSMA-I&T: RP-HPLC (10 to 70% B in 15 min): t_R = 7.2 min, K' = 3.3. ESI-MS (positive): calculated monoisotopic mass ($C_{63}H_{89}ILuN_{11}O_{23}$): 1669.5; found: m/z = 1670.5 $[M+H]^+$, 1113.8 $[2M+3H]^{3+}$.

^{nat}Lu-PSMA-617: RP-HPLC (10 to 70% B in 15 min): t_R = 6.5 min, K' = 2.8. ESI-MS (positive): calculated monoisotopic mass ($C_{49}H_{68}LuN_9O_{16}$): 1213.4; found: m/z = 1213.6 $[M+H]^+$, 607.5 $[M+2H]^{2+}$.

^{nat}Lu-rhPSMA-7.3: RP-HPLC (10 to 70% B in 15 min)*:* t_R = 9.6 min*,* K' = 3.8*.* ESI-MS (positive): calculated monoisotopic mass ($C_{63}H_{96}FLuN_{12}O_{25}Si$): 1642.6; found: m/z = 1643.4 $[M+H]^+$, 822.3 $[M+2H]^{2+}$.

^{nat}Lu-rhPSMA-10.1: RP-HPLC (10 to 70% B in 15 min): t_R = 9.9 min, K' = 4.0*.* ESI-MS (positive): calculated monoisotopic mass ($C_{60}H_{92}FLuN_{12}O_{23}Si$): 1570.6; found: m/z = 1571.8 $[M+H]^+$, 786.2 $[M+2H]^{2+}$.

^{nat}Lu-Complexes of Ligands Aiming for Metabolic Instability (MI)

^{nat}Lu-MI-1: RP-HPLC (10 to 90% B in 15 min): t_R = 8.4 min. K' = 3.7. ESI-MS (positive): calculated monoisotopic mass ($C_{71}H_{105}FLuN_{13}O_{25}Si$): 1761.7; found: m/z = 1762.7 $[M+H]^+$, 881.7 $[M+2H]^{2+}$.

^{nat}Lu-MI-2: RP-HPLC (10 to 90% B in 15 min): t_R = 8.1 min. K' = 3.6. ESI-MS (positive): calculated monoisotopic mass ($C_{65}H_{99}FLuN_{13}O_{26}Si$): 1699.6; found: m/z = 1702.2 $[M+H]^+$, 851.2 $[M+2H]^{2+}$.

^{nat}Lu-MI-3: RP-HPLC (10 to 90% B in 15 min): t_R = 8.0 min. K' = 3.5. ESI-MS (positive): calculated monoisotopic mass ($C_{65}H_{99}FLuN_{13}O_{26}Si$): 1699.6; found: m/z =1700.6 $[M+H]^+$, 850.7 $[M+2H]^{2+}$.

^{nat}Lu-MI-4: RP-HPLC (10 to 90% B in 15 min): t_R = 8.5 min. K' = 3.8. ESI-MS (positive): calculated monoisotopic mass ($C_{71}H_{110}FLuN_{14}O_{27}Si$): 1812.7; found: m/z =1816.1 $[M+H]^+$, 908.2 $[M+2H]^{2+}$.

^{nat}Lu-MI-5: RP-HPLC (10 to 90% B in 15 min): t_R = 8.7 min. K' = 3.9. ESI-MS (positive): calculated monoisotopic mass ($C_{62}H_{95}FLuN_{13}O_{24}Si$): 1627.6; found: m/z =1629.9 $[M+H]^+$, 815.1 $[M+2H]^{2+}$.

^{nat}Lu-Complexes of Branched Linker-Constructs (BLC) for Albumin Binding Modulation

^{nat}Lu-BLC-1: HPLC (10 to 90% B in 15 min): t_R = 8.0 min. K' = 3.6. ESI-MS (positive): calculated monoisotopic mass ($C_{116}H_{173}FLuN_{23}O_{36}Si$): 2686.2; found: m/z = 1344.8 $[M+2H]^{2+}$.

^{nat}Lu-BLC-2: HPLC (10 to 90% B in 15 min): t_R = 7.5 min. K' = 3.2. ESI-MS (positive): calculated monoisotopic mass ($C_{116}H_{173}FLuN_{23}O_{36}Si$): 2686.2; found: m/z = 1344.9 $[M+2H]^{2+}$.

^{nat}Lu-BLC-3: HPLC (10 to 90% B in 15 min): t_R = 8.1 min. K' = 3.6. ESI-MS (positive): calculated monoisotopic mass ($C_{116}H_{173}FLuN_{23}O_{36}Si$): 2686.2; found: m/z = 1344.8 $[M+2H]^{2+}$.

^{nat}Lu-BLC-4: HPLC (10 to 90% B in 15 min): t_R = 8.0 min. K' = 3.5. ESI-MS (positive): calculated monoisotopic mass ($C_{116}H_{173}FLuN_{23}O_{36}Si$): 2686.2; found: m/z = 1345.4 $[M+2H]^{2+}$.

^{nat}Lu-BLC-5: HPLC (10 to 90% B in 15 min): t_R = 7.3 min. K' = 3.1. ESI-MS (positive): calculated monoisotopic mass ($C_{116}H_{173}FLuN_{23}O_{36}Si$): 2686.2; found: m/z = 1344.6 $[M+2H]^{2+}$.

^{nat}Lu-BLC-6: HPLC (10 to 90% B in 15 min): t_R = 7.1 min. K' = 3.0. ESI-MS (positive): calculated monoisotopic mass ($C_{98}H_{155}FLuN_{23}O_{45}Si$): 2596.0; found: m/z = 1299.9 $[M+2H]^{2+}$.

^{nat}Lu-BLC-7: HPLC (10 to 90% B in 15 min): t_R = 7.2 min. K' = 3.0. ESI-MS (positive): calculated monoisotopic mass ($C_{92}H_{143}FLuN_{23}O_{39}Si$): 2415.9; found: m/z = 1209.8 $[M+2H]^{2+}$.

^{nat}Lu-BLC-8: HPLC (10 to 90% B in 15 min): t_R = 8.0 min. K' = 3.5. ESI-MS (positive): calculated monoisotopic mass ($C_{90}H_{147}FLuN_{15}O_{36}Si$): 2235.9; found: m/z = 1119.8 $[M+2H]^{2+}$.

^{nat}Lu-BLC-9: HPLC (10 to 90% B in 15 min): t_R = 9.4 min. K' = 4.3. ESI-MS (positive): calculated monoisotopic mass ($C_{124}H_{180}FILuN_{23}O_{36}Si$): 2916.1; found: m/z = 1458.3 $[M+2H]^{2+}$.

^{nat}Lu-BLC-11: HPLC (10 to 90% B in 15 min): t_R = 8.7 min. K' = 3.9. ESI-MS (positive): calculated monoisotopic mass ($C_{100}H_{150}FILuN_{23}O_{39}Si$): 2645.9; found: m/z = 1323,9 $[M+2H]^{2+}$.

^{nat}Lu-BLC-12: HPLC (10 to 90% B in 15 min): t_R = 9.8 min. K' = 4.5. ESI-MS (positive): calculated monoisotopic mass ($C_{98}H_{154}FILuN_{15}O_{36}Si$): 2465.9; found: m/z = 1235.3 $[M+2H]^{2+}$.

^{nat}Lu-Complexes of Ligands with Reduced Net Charge (RNC)

^{nat}Lu-RNC-1: RP-HPLC (10 to 90% B in 15 min): t_R = 9.7 min. K' = 4.4. ESI-MS (positive): calculated monoisotopic mass ($C_{74}H_{106}FLuN_{12}O_{21}Si$): 1720.7; found: m/z = 1722.1 $[M+H]^{+}$, 861.5 $[M+2H]^{2+}$.

^{nat}Lu-RNC-2: RP-HPLC (10 to 90% B in 15 min): t_R = 9.5 min. K' = 4.3. ESI-MS (positive): calculated monoisotopic mass ($C_{75}H_{106}FLuN_{12}O_{23}Si$): 1764.7; found: m/z = 1765.5 $[M+H]^{+}$, 883.3 $[M+2H]^{2+}$.

^{nat}Lu-RNC-3: RP-HPLC (10 to 90% B in 15 min): t_R = 9.9 min. K' = 4.6. ESI-MS (positive): calculated monoisotopic mass ($C_{70}H_{99}FLuN_{11}O_{20}Si$): 1635.6; found: m/z = 1636.9 $[M+H]^+$, 818.8 $[M+2H]^{2+}$.

^{nat}Lu-RNC-4: RP-HPLC (10 to 90% B in 15 min): t_R = 9.6 min. K' = 4.4. ESI-MS (positive): calculated monoisotopic mass ($C_{89}H_{136}FLuN_{12}O_{29}Si$): 2058.9; found: m/z = 1031.3 $[M+2H]^{2+}$.

^{nat}Lu-RNC-5: RP-HPLC (10 to 90% B in 15 min): t_R = 8.5 min. K' = 3.8. ESI-MS (positive): calculated monoisotopic mass ($C_{62}H_{96}FLuN_{12}O_{23}Si$): 1598.6; found: m/z = 1599.8 $[M+H]^+$, 799.9 $[M+2H]^{2+}$.

^{nat}Lu-RNC-6: RP-HPLC (10 to 90% B in 15 min): t_R = 8.5 min. K' = 3.8. ESI-MS (positive): calculated monoisotopic mass ($C_{62}H_{96}FLuN_{14}O_{24}Si$): 1642.6; found: m/z = 1644.1 $[M+H]^+$, 821.9 $[M+2H]^{2+}$.

^{nat}Lu-RNC-7: RP-HPLC (10 to 70% B in 15 min): t_R = 10.0 min. K' = 4.6. ESI-MS (positive): calculated monoisotopic mass ($C_{59}H_{92}FLuN_{14}O_{22}Si$): 1570.6; found: m/z = 1572.3 $[M+H]^+$, 786.5 $[M+2H]^{2+}$.

^{nat}Lu-Complexes of Ligands with Modified SiFA Moieties (MSM)

^{nat}Lu-MSM-5: RP-HPLC (10 to 70% B in 15 min): t_R = 9.9 min. K' = 4.6. ESI-MS (positive): calculated monoisotopic mass ($C_{63}H_{96}FLuN_{12}O_{25}Si$): 1642.6; found: m/z = 1644.6 $[M+H]^+$, 822.7 $[M+2H]^{2+}$.

^{nat}Lu-MSM-6: RP-HPLC (10 to 70% B in 15 min): t_R = 8.9 min. K' = 4.0. ESI-MS (positive): calculated monoisotopic mass ($C_{63}H_{96}FLuN_{12}O_{25}Si$): 1642.6; found: m/z = 1644.9 $[M+H]^+$, 822.4 $[M+2H]^{2+}$.

6. Synthesis of SiFA Model Peptides (MPs)

(4-SiFA)Bz-Gly-L-Lys-OH (MP-1GK)

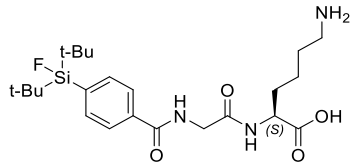

Chemical Formula: $C_{23}H_{38}FN_3O_4Si$
Molecular Weight: 467,66

2-CTC-resin was loaded with Fmoc-L-Lys(Boc)-OH (GP1). After Fmoc-deprotection (GP3), Fmoc-Gly-OH was coupled to the resin-bound amino acid (GP2a). After another Fmoc-deprotection (GP3), (4-SiFA)Bz-OH was conjugated to the free amine (GP2a). The peptide was cleaved from the resin under concomitant deprotection (GP5a) and isolated after lyophilization as colorless solid (77%). $^{19}F\{^{29}Si\}$ NMR (376 MHz, DMSO-D_6): δ [ppm] = –187.17; $^{29}Si\{^{1}H\}$INEPT NMR (79 MHz, DMSO-D_6): δ [ppm] = 14.08 (d, $^{1}J(^{19}F,^{29}Si)$ = 299 Hz). RP-HPLC (30 to 90% B in 15 min): t_R = 7.4 min. K' = 3.2. ESI-MS (positive): calculated monoisotopic mass ($C_{23}H_{38}FN_3O_4Si$): 467.26; found: m/z = 468.4 $[M+H]^+$.

(4-SiFA)Bz-Gly-L-Asp-OH (MP-1GD)

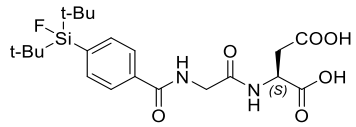

Chemical Formula: $C_{21}H_{31}FN_2O_6Si$
Molecular Weight: 454,57

2-CTC-resin was loaded with Fmoc-L-Asp(*t*Bu)-OH (GP1). After Fmoc-deprotection (GP3), Fmoc-Gly-OH was coupled to the resin-bound amino acid (GP2a). After another Fmoc-deprotection (GP3), (4-SiFA)Bz-OH was conjugated to the free amine (GP2a). The peptide was cleaved from the resin under concomitant deprotection (GP5a) and isolated after lyophilization as colorless solid (86%). $^{19}F\{^{29}Si\}$ NMR (376 MHz, DMSO-D_6): δ [ppm] = –187.17; $^{29}Si\{^{1}H\}$INEPT NMR (79 MHz, DMSO-D_6): δ [ppm] = 14.08 (d, $^{1}J(^{19}F,^{29}Si)$ = 298 Hz). RP-HPLC (30 to 90% B in 15 min): t_R = 9.1 min. K' = 4.1. ESI-MS (positive): calculated monoisotopic mass ($C_{21}H_{31}FN_2O_6Si$): 454.19; found: m/z = 455.3 $[M+H]^+$.

(4-SiFA)Bz-Gly-L-Tyr-OH (MP-1GY)

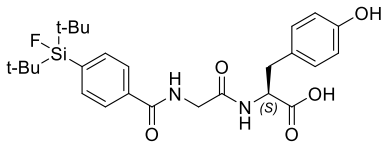

Chemical Formula: $C_{26}H_{35}FN_2O_5Si$
Molecular Weight: 502,66

2-CTC-resin was loaded with Fmoc-L-Tyr(O*t*Bu)-OH (GP1). After Fmoc-deprotection (GP3), Fmoc-Gly-OH was coupled to the resin-bound amino acid (GP2a). After another Fmoc-deprotection (GP3), (4-SiFA)Bz-OH was conjugated to the free amine (GP2a). The peptide was cleaved from the resin under concomitant deprotection (GP5a) and isolated after lyophilization as colorless solid (90%). $^{19}F\{^{29}Si\}$ NMR (376 MHz, DMSO-D_6): δ [ppm] = –187.12; $^{29}Si\{^{1}H\}$INEPT NMR (79 MHz, DMSO-D_6): δ [ppm] = 14.09 (d, $^{1}J(^{19}F,^{29}Si)$ = 298 Hz). RP-HPLC (30 to 90% B in 15 min): t_R = 10.2 min. K' = 4.7. ESI-MS (positive): calculated monoisotopic mass ($C_{26}H_{35}FN_2O_5Si$): 502.23; found: m/z = 503.3 $[M+H]^+$.

(3-SiFA)Bz-Gly-L-Lys-OH (MP-2GK)

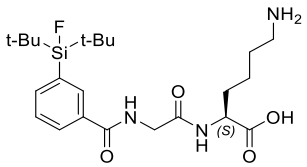

Chemical Formula: $C_{23}H_{38}FN_3O_4Si$
Molecular Weight: 467,66

2-CTC-resin was loaded with Fmoc-L-Lys(Boc)-OH (GP1). After Fmoc-deprotection (GP3), Fmoc-Gly-OH was coupled to the resin-bound amino acid (GP2a). After another Fmoc-deprotection (GP3), (3-SiFA)Bz-OH was conjugated to the free amine (GP2a). The peptide was cleaved from the resin under concomitant deprotection (GP5a) and isolated after lyophilization as colorless solid (95%). $^{19}F\{^{29}Si\}$ NMR (376 MHz, DMSO-D_6): δ [ppm] = –186.90; $^{29}Si\{^{1}H\}$INEPT NMR (79 MHz, DMSO-D_6): δ [ppm] = 13.98 (d, $^{1}J(^{19}F,^{29}Si)$ = 298 Hz). RP-HPLC (20 to 90% B in 15 min): t_R = 11.3 min. K' = 5.4. ESI-MS (positive): calculated monoisotopic mass ($C_{23}H_{38}FN_3O_4Si$): 467.26; found: m/z = 468.5 $[M+H]^+$.

(3-SiFA)Bz-Gly-L-Asp-OH (MP-2GD)

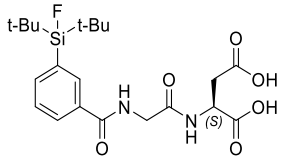

Chemical Formula: $C_{21}H_{31}FN_2O_6Si$
Molecular Weight: 454,57

2-CTC-resin was loaded with Fmoc-L-Asp(O*t*Bu)-OH (GP1). After Fmoc-deprotection (GP3), Fmoc-Gly-OH was coupled to the resin-bound amino acid (GP2a). After another Fmoc-deprotection (GP3), (3-SiFA)Bz-OH was conjugated to the free amine (GP2a). The peptide was cleaved from the resin under concomitant deprotection (GP5a) and isolated after lyophilization as colorless solid (79%). $^{19}F\{^{29}Si\}$ NMR (376 MHz, DMSO-D_6): δ [ppm] = –186.90; $^{29}Si\{^{1}H\}$INEPT NMR (79 MHz, DMSO-D_6): δ [ppm] = 13.98 (d, $^{1}J(^{19}F,^{29}Si)$ = 298 Hz). RP-HPLC (20 to 90% B in 15 min): t_R = 10.3 min. K' = 4.8. ESI-MS (positive): calculated monoisotopic mass ($C_{21}H_{31}FN_2O_6Si$): 454.19; found: m/z = 455.4 $[M+H]^+$.

(3-SiFA)Bz-Gly-L-Tyr-OH (MP-2GY)

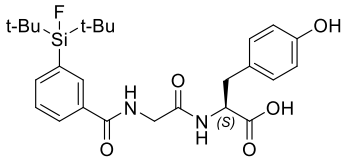

Chemical Formula: $C_{26}H_{35}FN_2O_5Si$
Molecular Weight: 502,66

2-CTC-resin was loaded with Fmoc-L-Tyr(O*t*Bu)-OH (GP1). After Fmoc-deprotection (GP3), Fmoc-Gly-OH was coupled to the resin-bound amino acid (GP2a). After another Fmoc-deprotection (GP3), (3-SiFA)Bz-OH was conjugated to the free amine (GP2a). The peptide was cleaved from the resin under concomitant deprotection (GP5a) and isolated after lyophilization as colorless solid (77%). $^{19}F\{^{29}Si\}$ NMR (376 MHz, DMSO-D_6): δ [ppm] = –186.86; $^{29}Si\{^{1}H\}$INEPT NMR (79 MHz, DMSO-D_6): δ [ppm] = 13.99 (d, $^{1}J(^{19}F,^{29}Si)$ = 298 Hz). RP-HPLC (20 to 90% B in 15 min): t_R = 8.8 min. K' = 3.9. ESI-MS (positive): calculated monoisotopic mass ($C_{26}H_{35}FN_2O_5Si$): 502.23; found: m/z = 503.8 $[M+H]^+$.

(5-SiFA)Ip-Gly-L-Lys-OH (MP-3GK)

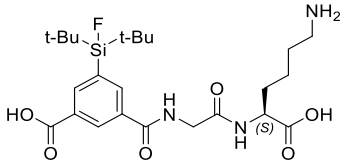

Chemical Formula: $C_{24}H_{38}FN_3O_6Si$
Molecular Weight: 511,67

2-CTC-resin was loaded with Fmoc-L-Lys(Boc)-OH (GP1). After Fmoc-deprotection (GP3), Fmoc-Gly-OH was coupled to the resin-bound amino acid (GP2a). After another Fmoc-deprotection (GP3), AllO-(5-SiFA)Ip-OH was conjugated to the free amine (GP2a). Allyl-deprotection was conducted (GP6), the peptide was cleaved from the resin under concomitant deprotection (GP5a) and isolated after HPFC-based purification and lyophilization as colorless solid (25%).

$^{19}F\{^{29}Si\}$ NMR (376 MHz, DMSO-D_6): δ [ppm] = –186.66; $^{29}Si\{^{1}H\}$INEPT NMR (79 MHz, DMSO-D_6): δ [ppm] = 13.96 (d, $^{1}J(^{19}F,^{29}Si)$ = 299 Hz). RP-HPLC (20 to 90% B in 15 min): t_R = 9.6 min. K' = 4.4. ESI-MS (positive): calculated monoisotopic mass ($C_{24}H_{38}FN_3O_6Si$): 511.25; found: m/z = 512.1 $[M+H]^+$.

(5-SiFA)Ip-L-Lys-Gly-OH (MP-3KG)

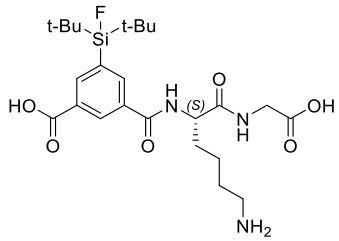

Chemical Formula: $C_{24}H_{38}FN_3O_6Si$
Molecular Weight: 511,67

2-CTC-resin was loaded with Fmoc-Gly-OH (GP1). After Fmoc-deprotection (GP3), Fmoc-L-Lys(Boc)-OH was coupled to the resin-bound amino acid (GP2a). After another Fmoc-deprotection (GP3), AllO-(5-SiFA)Ip-OH was conjugated to the free amine (GP2a). Allyl-deprotection was conducted (GP6), the peptide was cleaved from the resin under concomitant deprotection (GP5a) and isolated after RP-HPLC-based purification and lyophilization as colorless solid (26%). RP-HPLC (20 to 90% B in 15 min): t_R = 7.6 min. K' = 3.3. ESI-MS (positive): calculated monoisotopic mass ($C_{24}H_{38}FN_3O_6Si$): 511.25; found: m/z = 511.6 $[M+H]^+$.

(5-SiFA)Ip-Gly-L-Asp-OH (MP-3GD)

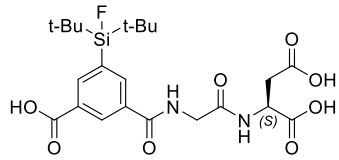

Chemical Formula: $C_{22}H_{31}FN_2O_8Si$
Molecular Weight: 498,58

2-CTC-resin was loaded with Fmoc-L-Asp(O*t*Bu)-OH (GP1). After Fmoc-deprotection (GP3), Fmoc-Gly-OH was coupled to the resin-bound amino acid (GP2a). After another Fmoc-deprotection (GP3), AllO-(5-SiFA)Ip-OH was conjugated to the free amine (GP2a). Allyl-deprotection was conducted (GP6), the peptide was cleaved from the resin under concomitant deprotection (GP5a) and isolated after HPFC-based purification and lyophilization as colorless solid (38%). $^{19}F\{^{29}Si\}$ NMR (376 MHz, DMSO-D_6): δ [ppm] = –186.65; $^{29}Si\{^{1}H\}$INEPT NMR (79 MHz, DMSO-D_6): δ [ppm] = 13.94 (d, $^{1}J(^{19}F,^{29}Si)$ = 299 Hz). RP-HPLC (20 to 90% B in 15 min): t_R = 8.6 min. K' = 3.8. ESI-MS (positive): calculated monoisotopic mass ($C_{22}H_{31}FN_2O_8Si$): 498.18; found: m/z = 499.1 $[M+H]^+$.

(5-SiFA)Ip-Gly-L-Tyr-OH (MP-3GY)

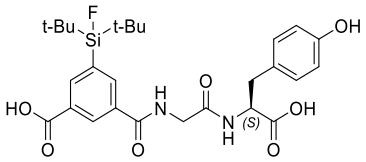

Chemical Formula: $C_{27}H_{35}FN_2O_7Si$
Molecular Weight: 546,67

2-CTC-resin was loaded with Fmoc-L-Tyr(O*t*Bu)-OH (GP1). After Fmoc-deprotection (GP3), Fmoc-Gly-OH was coupled to the resin-bound amino acid (GP2a). After another Fmoc-deprotection (GP3), AllO-(5-SiFA)Ip-OH was conjugated to the free amine (GP2a). Allyl-deprotection was conducted (GP6), the peptide was cleaved from the resin under concomitant deprotection (GP5a) and isolated after HPFC-based purification and lyophilization as colorless solid (18%). $^{19}F\{^{29}Si\}$ NMR (376 MHz, DMSO-D_6): δ [ppm] = –186.62; $^{29}Si\{^1H\}$INEPT NMR (79 MHz, DMSO-D_6): δ [ppm] = 13.96 (d, $^1J(^{19}F,^{29}Si)$ = 299 Hz). RP-HPLC (20 to 90% B in 15 min): t_R = 9.6 min. K' = 4.4. ESI-MS (positive): calculated monoisotopic mass ($C_{27}H_{35}FN_2O_7Si$): 546.22; found: m/z = 547.0 $[M+H]^+$.

HO-L-Lys-(5-SiFA)Ip-Gly-L-Lys-OH (MP-K4GK)

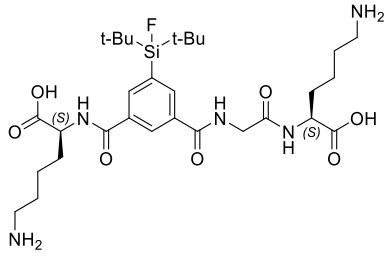

Chemical Formula: $C_{30}H_{50}FN_5O_7Si$
Molecular Weight: 639,84

2-CTC-resin was loaded with Fmoc-L-Lys(Boc)-OH (GP1). After Fmoc-deprotection (GP3), Fmoc-Gly-OH was coupled to the resin-bound amino acid (GP2a). After another Fmoc-deprotection (GP3), AllO-(5-SiFA)Ip-OH was conjugated to the free amine (GP2a). Allyl-deprotection was conducted (GP6) and H-L-Lys(Boc)-O*t*Bu·HCl was coupled to the deprotected carboxylic acid (GP2b). The peptide was cleaved from the resin under concomitant deprotection (GP5a) and isolated after HPFC-based purification and lyophilization as colorless solid (16%). $^{19}F\{^{29}Si\}$ NMR (376 MHz, DMSO-D_6): δ [ppm] = –186.19; $^{29}Si\{^1H\}$INEPT NMR (79 MHz, DMSO-D_6): δ [ppm] = 14.09 (d, $^1J(^{19}F,^{29}Si)$ = 299 Hz). RP-HPLC (20 to 90% B in 15 min): t_R = 5.7 min. K' = 2.2. ESI-MS (positive): calculated monoisotopic mass ($C_{30}H_{50}FN_5O_7Si$): 639.35; found: m/z = 640.6 $[M+H]^+$.

HO-L-Lys-(5-SiFA)Ip-Gly-L-Asp-OH (MP-K4GD)

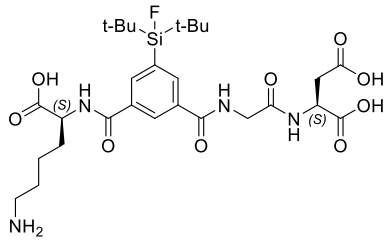

Chemical Formula: $C_{28}H_{43}FN_4O_9Si$
Molecular Weight: 626,75

2-CTC-resin was loaded with Fmoc-L-Asp(O*t*Bu)-OH (GP1). After Fmoc-deprotection (GP3), Fmoc-Gly-OH was coupled to the resin-bound amino acid (GP2a). After another Fmoc-deprotection (GP3), AllO-(5-SiFA)Ip-OH was conjugated to the free amine (GP2a). Allyl-deprotection was conducted (GP6) and H-L-Lys(Boc)-O*t*Bu·HCl was coupled the deprotected carboxylic acid (GP2b). The peptide was cleaved from the resin under concomitant deprotection (GP5a) and isolated after HPFC-based purification and lyophilization as colorless solid (21%). $^{19}F\{^{29}Si\}$ NMR (376 MHz, DMSO-D_6): δ [ppm] = –186.22; $^{29}Si\{^1H\}$INEPT NMR (79 MHz, DMSO-D_6): δ [ppm] = 14.09 (d, $^1J(^{19}F,^{29}Si)$ = 299 Hz). RP-HPLC (20 to 90% B in 15 min): t_R = 6.6 min. K' = 2.7. ESI-MS (positive): calculated monoisotopic mass ($C_{28}H_{43}FN_4O_9Si$): 626.28; found: m/z = 627.5 $[M+H]^+$.

HO-L-Lys-(5-SiFA)Ip-Gly-L-Tyr-OH (MP-K4GY)

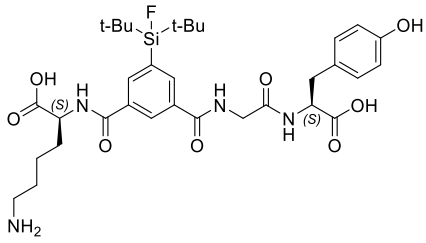

Chemical Formula: $C_{33}H_{47}FN_4O_8Si$
Molecular Weight: 674,84

2-CTC-resin was loaded with Fmoc-L-Tyr(O*t*Bu)-OH (GP1). After Fmoc-deprotection (GP3), Fmoc-Gly-OH was coupled to the resin-bound amino acid (GP2a). After another Fmoc-deprotection (GP3), AllO-(5-SiFA)Ip-OH was conjugated to the free amine (GP2a). Allyl-deprotection was conducted (GP6) and H-L-Lys(Boc)-O*t*Bu·HCl was coupled to the deprotected carboxylic acid (GP2b). The peptide was cleaved from the resin under concomitant deprotection (GP5a) and isolated after HPFC-based purification and lyophilization as colorless solid (9%). $^{19}F\{^{29}Si\}$ NMR (376 MHz, DMSO-D_6): δ [ppm] = –186.28; $^{29}Si\{^1H\}$INEPT NMR (79 MHz, DMSO-D_6): δ [ppm] = 14.06 (d, $^1J(^{19}F,^{29}Si)$ = 299 Hz). RP-HPLC (20 to 90% B in 15 min): t_R = 7.3 min. K' = 3.1. ESI-MS (positive): calculated monoisotopic mass ($C_{33}H_{47}FN_4O_8Si$): 674.31; found: m/z = 675.5 $[M+H]^+$.

HO-L-Glu-(5-SiFA)Ip-Gly-L-Lys-OH (MP-E4GK)

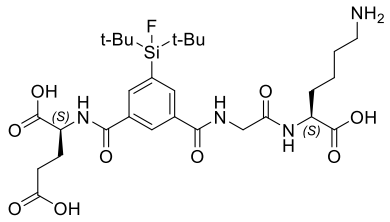

Chemical Formula: $C_{29}H_{45}FN_4O_9Si$
Molecular Weight: 640,78

2-CTC-resin was loaded with Fmoc-L-Lys(Boc)-OH (GP1). After Fmoc-deprotection (GP3), Fmoc-Gly-OH was coupled to the resin-bound amino acid (GP2a). After another Fmoc-deprotection (GP3), AllO-(5-SiFA)Ip-OH was conjugated to the free amine (GP2a). Allyl-deprotection was conducted (GP6) and H-L-Glu(O*t*Bu)-O*t*Bu·HCl was coupled to the deprotected carboxylic acid (GP2b). The peptide was cleaved from the resin under concomitant deprotection (GP5a) and isolated after HPFC-based purification and lyophilization as colorless solid (12%). RP-HPLC (20 to 90% B in 15 min): t_R = 6.7 min. K' = 2.8. ESI-MS (positive): calculated monoisotopic mass ($C_{29}H_{45}FN_4O_9Si$): 640.29; found: m/z = 640.7 $[M+H]^+$.

HO-L-Glu-(5-SiFA)Ip-Gly-L-Asp-OH (MP-E4GD)

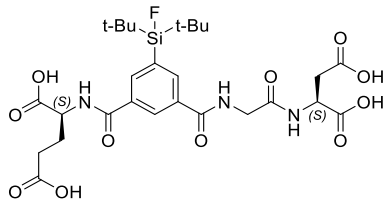

Chemical Formula: $C_{27}H_{38}FN_3O_{11}Si$
Molecular Weight: 627,69

2-CTC-resin was loaded with Fmoc-L-Asp(O*t*Bu)-OH (GP1). After Fmoc-deprotection (GP3), Fmoc-Gly-OH was coupled to the resin-bound amino acid (GP2a). After another Fmoc-deprotection (GP3), AllO-(5-SiFA)Ip-OH was conjugated to the free amine (GP2a). Allyl-deprotection was conducted (GP6) and H-L-Glu(O*t*Bu)-O*t*Bu·HCl was coupled to the deprotected carboxylic acid (GP2b). The peptide was cleaved from the resin under concomitant deprotection (GP5a) and isolated after HPFC-based purification and lyophilization as colorless solid (23%). RP-HPLC (20 to 90% B in 15 min): t_R = 7.5 min. K' = 3.2. ESI-MS (positive): calculated monoisotopic mass ($C_{27}H_{38}FN_3O_{11}Si$): 627.23; found: m/z = 627.7 $[M+H]^+$.

HO-L-Glu-(5-SiFA)Ip-Gly-L-Tyr-OH (MP-E4GY)

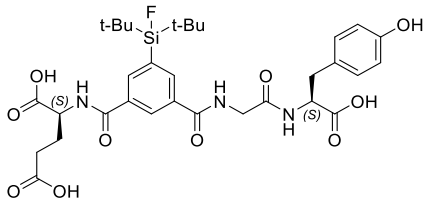

Chemical Formula: $C_{32}H_{42}FN_3O_{10}Si$
Molecular Weight: 675,78

2-CTC-resin was loaded with Fmoc-L-Tyr(O*t*Bu)-OH (GP1). After Fmoc-deprotection (GP3), Fmoc-Gly-OH was coupled to the resin-bound amino acid (GP2a). After another Fmoc-deprotection (GP3), AllO-(5-SiFA)Ip-OH was conjugated to the free amine (GP2a). Allyl-deprotection was conducted (GP6) and H-L-Glu(O*t*Bu)-O*t*Bu·HCl was coupled to the deprotected carboxylic acid (GP2b). The peptide was cleaved from the resin under concomitant deprotection (GP5a) and isolated after HPFC-based purification and lyophilization as colorless solid (15%). RP-HPLC (20 to 90% B in 15 min): t_R = 8.3 min. K' = 3.7. ESI-MS (positive): calculated monoisotopic mass ($C_{32}H_{42}FN_3O_{10}Si$): 675.26; found: m/z = 675.7 $[M+H]^+$.

HOOC-PEG$_8$-(5-SiFA)Ip-Gly-L-Lys-OH (MP-PEG$_8$4GK)

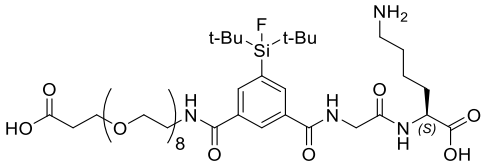

Chemical Formula: $C_{43}H_{75}FN_4O_{15}Si$
Molecular Weight: 935,17

For the preparation of the MP-PEG$_8$4GK, a combined solution phase and solid phase peptide synthesis strategy was used. At first, the dipeptide H-Gly-L-Lys(Boc)-O*t*Bu·TFA was synthesized by pre-activation of 178 mg Fmoc-Gly-OH (0.6 mmol, 1.2 eq.) with 82 mg HOAt (0.6 mmol, 1.2 eq.), 228 mg HATU (0.6 mmol, 1.2 eq.) in 5 mL DMF and addition of 510 µL DIPEA (3.0 mmol, 5.0 eq.). After 15 min at rt, 1 mL of a solution of 169 mg H-L-Lys(Boc)-O*t*Bu (0.5 mmol, 1.0 eq.) in DMF was added and stirred for 4 h at rt. For subsequent Fmoc-deprotection with 30 vol.-% piperidine in DMF, 2.5 mL piperidine were added to the solution. After 30 min, the solvents were removed under reduced pressure at 60 °C. HPFC-purification and subsequent lyophilization of the dipeptide yielded 184 mg of a colorless solid (78%). RP-HPLC (10 to 90% B in 15 min): t_R = 8.9 min. K' = 4.0. ESI-MS (positive): calculated monoisotopic mass ($C_{17}H_{33}N_3O_5$): 359.24; found: m/z = 359.8 $[M+H]^+$.

2-CTC-resin was loaded with Fmoc-NH-PEG$_8$-CH_2-CH_2-COOH (GP1). After Fmoc-deprotection (GP3), AllO-(5-SiFA)Ip-OH was conjugated to the free amine (GP2a). Allyl-deprotection was conducted (GP6) and H-Gly-L-Lys(Boc)-O*t*Bu·TFA was coupled to the deprotected carboxylic acid

(GP2b). The peptide was cleaved from the resin under concomitant deprotection (GP5a) and isolated after RP-HPLC-based purification and lyophilization as colorless solid (25%). RP-HPLC (20 to 90% B in 15 min): t_R = 7.5 min. K' = 3.2. ESI-MS (positive): calculated monoisotopic mass ($C_{43}H_{75}FN_4O_{15}Si$): 934.50; found: m/z = 934.4 $[M+H]^+$.

Gal6N-(5-SiFA)Ip-Gly-L-Lys-OH (MP-Gal6N4GK)

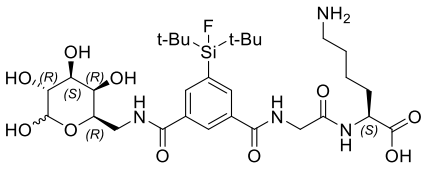

Chemical Formula: $C_{30}H_{49}FN_4O_{10}Si$
Molecular Weight: 672,82

2-CTC-resin was loaded with Fmoc-L-Lys(Boc)-OH (GP1a). After Fmoc-deprotection (GP3), Fmoc-Gly-OH was coupled to the resin-bound amino acid (GP2a). After another Fmoc-deprotection (GP3), AllO-(5-SiFA)Ip-OH was conjugated to the free amine (GP2a). Allyl-deprotection was conducted (GP6) and 6-amino-6-deoxy-1,2;3,4-di-*O*-isopropylidene-D-galactopyranoside was coupled to the deprotected carboxylic acid (GP2b). The peptide was cleaved from the resin under concomitant deprotection (GP5a) and isolated after RP-HPLC-based purification and lyophilization as colorless solid (17%). RP-HPLC (20 to 90% B in 15 min): t_R = 5.8 min. K' = 2.3. ESI-MS (positive): calculated monoisotopic mass ($C_{30}H_{49}FN_4O_{10}Si$): 672.32; found: m/z = 672.8 $[M+H]^+$.

7. Radiolabeling

7.1. ^{18}F-Labeling

The described two-step procedure for ^{18}F-labeling was previously optimized in our group by *Daniel Di Carlo* (unpublished data).

Drying of Aqueous [^{18}F]Fluoride Solution: An aqueous [^{18}F]fluoride solution (*in vitro*-studies*:* 100–300 MBq, biodistribution study: up to 1.7 GBq; approximately 0.6–2.0 GBq/mL by the time of use; obtained from the *Klinikum rechts der Isar, Munich, Germany*), was passed through an SAX cartridge (*Sep-Pak Accell Plus QMA Carbonate Plus Light, 46 mg, 40 µm, Waters*), which was preconditioned with 10 mL of ultrapure water. The [^{18}F]fluoride-loaded cartridge was dried by rinsing with 8 mL anhydrous DMSO followed by 10 mL air. For elution with an extraction efficiency of 78 ± 9%, a solution of 40 mg of ammonium formate in 500 µL anhydrous DMSO was slowly passed through the cartridge followed by 5 mL air.

Labeling of SiFA Modified Peptides with the Dried [^{18}F]Fluoride Solution: For labeling, 125–500 µL of the eluted [^{18}F]fluoride solution were added to a proportional amount of precursor solution (7.5–30 nmol, 1 mM in anhydrous DMSO). After 5 min at rt, a sample was taken to determine the radiochemical conversion (RCC) by thin-layer chromatography (TLC). The labeling mixture was diluted with 10 mL PBS* (pH 3, adjusted with 1 M aq. HCl) and passed through an Oasis HLB Plus Light cartridge (30 mg, 30 µm, freshly preconditioned with 10 mL EtOH and 10 mL ultrapure H_2O, *Waters*) followed by 10 mL PBS* and 10 mL air. The mixture of ^{18}F-labeled peptide and its chemically identical, cold precursor was eluted with 300 µL EtOH/PBS* (*v*/*v* = 7:3). The radiochemical purity of the ^{18}F-labeled compound was determined by radio-RP-HPLC and radio-TLC (silica gel 60 F_{254}, mobile phase: MeCN/PBS (*v*/*v* = 3:2), +10% of NaOAc solution (2 M in H_2O), +1% TFA). The radiochemical yield (RCY) was determined using a dose calibrator and calculated considering decay-correction.

**NOTE*: In cases of subsequent stability studies, the PBS used for purification was substituted by ultrapure H_2O. Only the PBS used for TLC was not substituted as the TLC analysis after the cartridge-based purification displayed a proportion of less than 1% free [^{18}F]fluoride for all labeled compounds.

7.2. ^{125}I-Labeling

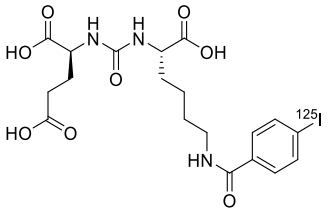

([^{125}I]I-BA)KuE
Chemical Formula: $C_{19}H_{24}{}^{125}IN_3O_8$
Molecular Weight: 547,32

The reference ligand ([^{125}I]I-BA)KuE for *in vitro* studies was prepared according to a previously published procedure (*151,155*). For the iodination, the peracetic acid solution was freshly prepared by the incubation of 50 µL acetic acid in 130 µL of 30 vol.-% H_2O_2 in H_2O for 2 h at rt. Approximately 0.1 mg of the stannylated precursor (*n*-Bu)$_3$Sn-BA-(*t*BuO)KuE(O*t*Bu)$_2$ was dissolved in a mixture of 20 µL peracetic acid, 5.0 µL [^{125}I]NaI (20 ± 5 MBq, 74 TBq/mmol, 40 mM in NaOH, *Hartmann Analytic, Braunschweig, Germany*), 20 µL MeCN and 10 µL acetic acid. The reaction solution was incubated for 15 min at rt, diluted in 10 mL H_2O and loaded on a Sep-Pak C18-Plus Short cartridge (360 mg, 55-105 µm, *Waters*, preconditioned with 10 mL MeOH followed by 10 mL H_2O). After purging the cartridge with 10 mL H_2O followed by 10 mL air, the peptide was eluted with 1.5 mL EtOH/MeCN (*v*/*v* = 1:1). The eluate was evaporated to dryness under a gentle nitrogen stream at 70°C and treated with 500 µL TFA for 45 min. After removing TFA in a stream of nitrogen, the crude product was purified by radio-RP-HPLC, yielding ([^{125}I]I-BA)KuE (10 ± 2 MBq). HPLC (20 to 40% B in 20 min): t_R = 13.0 min.

7.3. ^{177}Lu-Labeling

For ^{177}Lu-labeling, a previously published procedure was applied with minor modifications (*156*). The labeling precursor (1.0 nmol, 5 µL, 0.2 mM in DMSO) was added to 10 µL of AcOH/NaOAc buffer (1.0 M in H_2O, pH 5.5, 1.0 M). Subsequently, 10 to 70 MBq [^{177}Lu]$LuCl_3$ (Specific Activity >3000 GBq/mg, 740 MBq/mL, 0.04 M HCl, *ITM, Garching, Germany*) were added and the mixture was filled up to 100 µL with 0.04 M aq. HCl. The reaction mixture was heated for 20 min at 90 °C and after addition of sodium ascorbate (0.1 M in PBS) the radiochemical purity was determined using radio-HPLC and radio-TLC (0.1 M sodium citrate buffer and 1.0 M NH_4OAc/DMF buffer (*v*/*v* = 1:1)).

8. *In Vitro* Experiments

8.1. Cell Culture

PSMA$^+$ LNCaP cells (*ACC 256; DSMZ-German Collection of Microorganisms and Cell Cultures GmbH, Braunschweig, Germany*) were cultivated in Dulbecco modified Eagle medium/Nutrition Mixture F-12 with Glutamax (1:1) (DMEM-F12*, Biochrom GmbH, Berlin, Germany*) supplemented with fetal bovine serum (10%, FBS Superior*, Biochrom GmbH, Berlin, Germany*) and kept at 37°C in a humidified CO_2-atmosphere (5%). A mixture of trypsin and EDTA (0.05%, 0.02%) in PBS (*Biochrom GmbH, Berlin, Germany*) was used to harvest cells. Cells were counted with a Neubauer hemocytometer (*Paul Marienfeld, Lauda-Königshofen, Germany*).

8.2. Determination of PSMA Affinity (IC_{50})

For PSMA affinity (IC_{50}) determinations, the respective ligand was diluted (serial dilution 10^{-4} to 10^{-10} M) in Hank's balanced salt solution (HBSS, *Biochrom GmbH, Berlin, Germany*), supplemented with 1% bovine serum albumin (BSA, *Biowest, Nuaillé, France*). In the case of metal-complexed ligands, the crude reaction mixture was diluted analogously, without further purification. Cells were harvested 24 ± 2 hours prior to the experiment and seeded in 24-well plates (1.5×10^5 cells in 1 mL/well). After removal of the culture medium, the cells were carefully washed with 500 µL of HBSS (1% BSA) and left 15 min on ice for equilibration in 200 µL HBSS (1% BSA). Next, 25 µL per well of solutions, containing either HBSS (1% BSA, control) or the respective test ligand in increasing concentration (10^{-10}–10^{-4} M in HBSS) were added with subsequent addition of 25 µL of [^{125}I]I-BA-KuE (2.0 nM) as radio-labeled competitor in HBSS (1% BSA). For each concentration, the experiment was performed in triplicate. After incubation on ice for 60 min, the experiment was terminated by removal of the medium and consecutive rinsing with 200 µL of HBSS (1% BSA). The media of both steps were combined in one fraction and represent the amount of free radioligand. Afterwards, the cells were lysed with 250 µL of NaOH (1 M in H_2O) for at least 15 min. After a washing step with NaOH (250 µL, 1 M in H_2O), both fractions, representing the amount of bound ligand, were united. Quantification of all collected fractions was accomplished in a γ-counter. IC_{50} values were calculated using GraphPad PRISM software (*GraphPad Software Inc.*, La Jolla, United States). The whole PSMA-affinity determination was repeated (n ≥ 3).

8.3. Determination of PSMA-mediated Internalization

For internalization studies, LNCaP cells were harvested 24 ± 2 hours before the experiment and seeded in poly-L-lysine coated 24-well plates (1.25×10^5 cells in 1 mL/well, *Greiner Bio-One, Kremsmünster, Austria*). After removal of the culture medium, the cells were washed once with

500 µL DMEM-F12 (5% BSA) and left to equilibrate for at least 15 min at 37 °C in humidified CO_2-atmosphere (5%) in 200 µL DMEM-F12 (5% BSA). Each well was treated with either 25 µL of either DMEM-F12 (5% BSA, control) or 25 µL of a 100 µM 2-PMPA (2-(Phosphonomethyl)-pentanedioic acid, *Tocris Bioscience, Bristol, UK*) solution in PBS, for blockade. Next, 25 µL of the radioactive-labeled PSMA inhibitor (10.0 nM in DMEM-F12 (5% BSA)) were added and the cells were incubated at 37 °C for 60 min. The experiment was terminated by placing the 24-well plate on ice for 3 min and consecutive removal of the medium. Each well was carefully washed with 250 µL of ice-cold HBSS. Both fractions from the first steps, representing the amount of free radioligand, were combined. Removal of surface bound activity was accomplished by incubation of the cells with 250 µL of ice-cold 2-PMPA solution (10 µM in PBS) for 5 min and rinsed again with another 250 µL of ice-cold PBS. The internalized activity was determined by incubation of the cells in 250 µL NaOH (1 M in H_2O) for at least 15 min. The obtained fractions were combined with those of the subsequent washing step with 250 µL NaOH (1 M in H_2O). Each experiment (control and blockade) was performed in triplicate. Free, surface-bound and internalized activity was quantified in a γ-counter. All internalization studies were accompanied by external reference studies, using ([^{125}I]I-BA)KuE (c = 0.2 nM), which were performed analogously. Data were corrected for non-specific binding, determined by the blockade fractions, and normalized to the specific internalization observed for the radio-iodinated reference compound.

8.4. Determination of *n*-Octanol/PBS Partition Coefficient ($logD_{pH\ 7.4}$)

Approximately 1 MBq of the ^{177}Lu-labeled tracer or 0.5 MBq of the ^{18}F-labeled tracer was dissolved in 1 mL of *n*-octanol/PBS (*v/v* = 1:1) in a reaction vial (1.5 mL). After vigorous mixing of the suspension for 3 min at rt, the vial was centrifuged at 15000 g for 5 min (*Biofuge 15, Heraeus Sepatech, Osterode, Germany*) and 100 µL aliquots of both layers were measured in a γ-counter. The experiment was repeated (n ≥ 6).

8.5. Determination of Human Serum Albumin (HSA) Binding

8.5.1. High-Performance Affinity Chromatography (HPAC)

HSA binding of compounds by HPAC was determined according to a previously published procedure via HPLC (*157*). A Chiralpak HSA column (50 x 3 mm, 5 µm, H13H-2433, Daicel, Tokyo, Japan) was used at a constant flow rate of 0.5 mL/min at rt. Mobile phase A was a freshly prepared 50 mM aqueous solution of NH_4OAc (pH 6.9) and mobile phase B was isopropanol (HPLC grade, VWR). The applied gradient for all experiments was 100% A (0 to 3 min), followed by 80% A (3 to 40 min). Prior to the experiment, the column was calibrated using nine reference substances with a HSA binding, known from literature, in the range of 13 to 99% (*157,158*). All reference- and test-substances were dissolved in a 1:1 mixture (*v/v*) of isopropanol and a 50 mM aqueous solution of

NH_4OAc (pH 6.9) with a final concentration of approximately 0.5 mg/mL. Non-linear regression (**Figure 12**) was established with the OriginPro 2016G software (Northampton, United States).

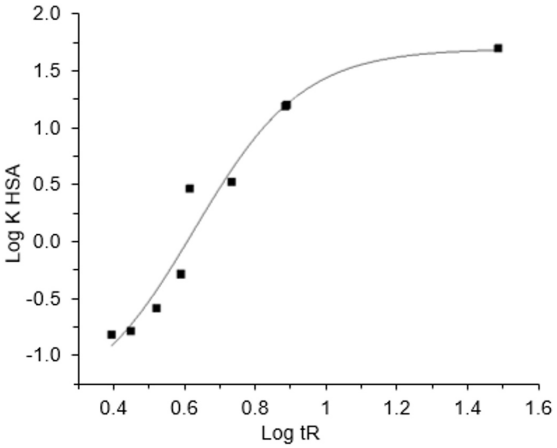

Reference	t_R [min]	Log t_R	lit. HSA [%]	Log K HSA
p-Benzyl Alcohol	2.50	0.40	13.15	–0.82
Aniline	2.83	0.45	14.06	–0.79
Phenol	3.35	0.52	20.69	–0.59
Benzoic Acid	3.92	0.59	34.27	–0.29
Carabamazepine	4.15	0.62	75.00	0.46
p-Nitrophenol	5.45	0.74	77.65	0.52
Estradiol	7.71	0.89	94.81	1.19
Probenecid	7.78	0.89	95.00	1.20
Glibenclamide	30.76	1.49	99.00	1.69

Figure 12: Exemplary sigmoidal plot, showing the correlation between human serum albumin (HSA) binding of selected reference substances and retention time (t_R). The values of HSA binding were obtained from literature (lit. HSA [%]) (*157,158*). Log t_R: logarithmic value of experimentally determined retention time. Log K HSA: logarithmic value of HSA binding values.

8.5.2. Albumin-Mediated Size Exclusion Chromatography (AMSEC)

The AMSEC approach is a novel size exclusion chromatography-based method recently established in our group by *Kunert et al.* (*159*). A gel filtration column Superdex 75 Increase 10/300 GL (GE Healthcare, Uppsala, Sweden) was beforehand calibrated at constant flow rate of 0.8 mL/min at rt with PBS as mobile phase following the producer's recommendations with a commercially available gel filtration calibration kit (GE Healthcare, Buckinghamshire, UK) comprising conalbumin (MW: 75 kDa), ovalbumin (44 kDa), carbonic anhydrase (29 kDa), ribonuclease A (13.7 kDa) and aprotinin (6.5 kDa) as reference proteins of known molecular weight (**Figure 13**).

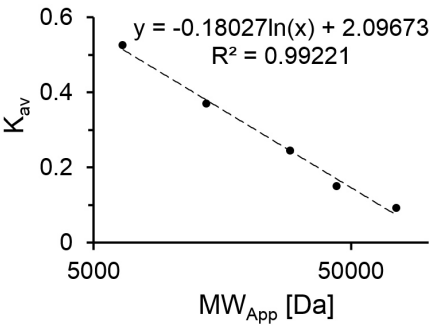

Reference	MW_{App} [Da]	t_R [min]	V_e [mL]	K_{av}
Blue Dextran 2000		10.034	8.0272	
Conalbumin	75000	11.859	9.4872	0.091405
Ovalbumin	44000	13.034	10.4272	0.150255
Carbonic Anhydrase	29000	14.912	11.9296	0.244315
Ribonuclease A	13700	17.398	13.9184	0.368827
Aprotinin	6500	20.531	16.4248	0.525743

Figure 13: Calibration plot of a Superdex 75 Increase gel filtration column using a low molecular weight gel filtration calibration kit. MW: molecular weight. t_R: experimentally determined retention time. V_e: elution volume. K_{av}: partition coefficient.

Investigations of test substances/ligands were conducted with ^{177}Lu-labeled compounds at molar activities of 10–20 GBq/µmol (**chapter II.7.3**). Probes of 1.0 MBq of the radioligand were injected directly from the labeling solution. All AMSEC experiments were conducted using a constant flow

rate of 0.8 mL/min at rt with a solution of HSA in PBS (700 µM) or solely PBS as mobile phase as indicated below. To calculate the ligand's apparent molecular weight (MW_{App}) as an indicator of HSA binding strength four different retention times had to be measured (**Table 2**).

Table 2: Experimental retention times and corresponding conditions required for the calculation of a ligand's apparent molecular weight (MW_{App}) corrected for ligand-specific interactions with the column matrix. All retention times were corrected for the delay between the UV- and radio-detector.

Retention Time	Signal	Probe	Mobile Phase
t_{AMSEC}	Radio	1.0 MBq of ^{177}Lu-ligand (labeling solution)	PBS + HSA (700 µM)
t_{HSA}	UV	10 mg/mL HSA in PBS, 100 µL	PBS
t_{Ligand}	Radio	1.0 MBq of ^{177}Lu-ligand (labeling solution)	PBS
$t_{Acetone}$	UV	2% acetone in PBS, 100 µL	PBS

It was assumed that during the measurement of the ligand's retention time in the presence of HSA (t_{AMSEC}) only two states are available for the tested ligand – 1) HSA-bound or 2) freely dissolved – in the mobile phase (PBS + HSA). Therefore, it was approximated for the respective state that the ligand exhibits either a retention behavior equal to HSA or shows a retention time in the column's cut-off region according to its low molecular weight. However, in these experiments only one peak was observed indicating a dynamic equilibrium between those two states. The corresponding retention time t_{AMSEC} of this peak is interpreted as the result of a temporal average of the two states.

It was concluded, that t_{AMSEC} can be described as a linear combination of the respective retention times of the HSA-bound state and the freely dissolved ligand (measured as t_{HSA} and t_{Ligand}, respectively; see **Table 2**). **Equation 3** describes the relation of the three measurables with the proportion factor x ($x \in [0;1]$) representing the temporal proportion of the HSA-bound state and the freely dissolved state during the measurement of t_{AMSEC}:

$$t_{AMSEC} = x \cdot t_{HSA} + (1 - x) \cdot t_{Ligand} \quad (3)$$

According to **Equation 3** the proportion factor x can be defined as:

$$x = \frac{|t_{AMSEC} - t_{Ligand}|}{|t_{HSA} - t_{Ligand}|} \quad (3')$$

It turned out that although all tested ligands possessed low molecular weights in the column's cut-off region, retention times t_{Ligand} clearly varied. Consequently, t_{Ligand} and also t_{AMSEC} had to be influenced by ligand-specific interactions with the column matrix and thus, are lacking comparability between different test ligands. To ensure comparability $t_{Acetone}$ was determined as a universal reference value for the retention time of a compound exhibiting neither HSA binding nor unspecific interactions with the column matrix. Consequently, t_{AMSEC} can be referenced ($t_{AMSEC,ref}$) to the retention time $t_{Acetone}$ transforming **Equation 3** to **4**:

$$t_{AMSEC,ref} = x \cdot t_{HSA} + (1 - x) \cdot t_{Acetone} \quad (4)$$

Furthermore, $t_{AMSEC,ref}$ was calculated by the insertion of the ligand-specific proportion factor x (**Equation 3'**) into **Equation 4** resulting in **Equation 5**:

$$t_{AMSEC,ref} = \frac{|t_{AMSEC} - t_{Ligand}|}{|t_{HSA} - t_{Ligand}|} \cdot t_{HSA} + \left(1 - \frac{|t_{AMSEC} - t_{Ligand}|}{|t_{HSA} - t_{Ligand}|}\right) \cdot t_{Acetone} \quad (5)$$

Finally, the referenced, apparent molecular weight (MW_{App}) was calculated from the retention time $t_{AMSEC,ref}$ using the determined calibration curve and should constitute a helpful parameter with comparable values reflecting HSA-binding strength of compounds. Higher values in MW_{App} are associated with increased HSA binding strength as they are interpreted to be linked with a higher temporal proportion of the ligand in an HSA-bound state.

8.6. Determination of Relative Radiochemical Conversion (rRCC)

In a first step, the aqueous [^{18}F]fluoride solution provided by the *Klinikum Rechts der Isar* was dried according to the aforementioned procedure (**chapter II.7.1**). For a competitive labeling reaction, 167 µL of the dried [^{18}F]fluoride solution (30–50 MBq) in DMSO were added to 10 µL of an equimolar mixture of the test compound and the corresponding (4-SiFA)Bz-reference compound (5 nmol each in DMSO). After 5 min at rt, a sample was taken and instantly analyzed *via* radio-RP-HPLC. If necessary, the standard solvent gradient (10 to 90% B in 15 min) was modified to achieve baseline-separation ((3-SiFA)Bz-Gly-L-X vs. (4-SiFA)Bz-Gly-L-X with X = Tyr: 45 to 65% B in 15 min; X = Asp: 40 to 60% B in 15 min; X = Lys: 35 to 55% B in 15 min). In these cases, a mixture of the cold precursors with an approximate 3-fold excess of the (3-SiFA)Bz- compared to the (4-SiFA)Bz-compound was analyzed with the corresponding gradients for unambiguous peak assignment. The relative radiochemical conversion (rRCC) was calculated by peak integration and is expressed as the ratio of test-to-reference-compound [%]. The experiment was repeated (n = 3).

8.7. ^{18}F-Defluorination Experiments

^{18}F-Defluorination under Chemically Simulated *In Vivo*-Conditions of Blood (pH 7.4, 37 °C): The test compound was labeled according to the aforementioned procedure (**chapter II.7.1**) starting with 200–300 MBq of aqueous [^{18}F]fluoride solution. The ^{18}F-labeled compound (10 µL per vial, approximately 0.8–1.0 nmol, 2.5–5.0 MBq) was added to 90 µL K_2CO_3 solution (3 mM in ultrapure H_2O, pH 7.4 adjusted with formic acid) per vial. The pH-value of the incubation solution was controlled by a test strip (resolution: 0.5). After incubation for 0, 30, 60, 90 and 120 min at 37 °C in separate reaction vials, samples were analyzed *via* radio-TLC (silica gel 60 F_{254}, mobile phase: MeCN/PBS (*v/v* = 3:2), +10% of NaOAc solution (2 M in H_2O), +1% TFA) differentiating between released [^{18}F]fluoride, immobilized at the baseline, and labeled test-compound. The experiment was repeated (n = 3). The proportions of intact ^{18}F-labeled peptide at the different time

points were used to calculate the half-life of the ^{18}F-defluorination. For the calculation of exponential regression, GraphPad PRISM software (*GraphPad Software Inc*., La Jolla, United States) was used.

^{18}F-Defluorination under ^{177}Lu-Labeling Conditions for Radiohybrids (pH 5.5, 90 °C): The test compound was labeled according to the aforementioned procedure (**chapter II.7.1**) starting with 200–300 MBq of aqueous [^{18}F]fluoride solution. The ^{18}F-labeled compound (10 µL per vial, approximately 0.8–1.0 nmol, 2.5–5.0 MBq) was added to a solution of 80 µL aqueous HCl (40 mM) and 10 µL AcOH/NaOAc buffer (1.0 M in H_2O, pH 5.5, 1.0 M) per vial. The pH-value of the incubation solution was controlled by a test strip (resolution: 0.5). After incubation for 0, 30, 60, 90 and 120 min at 37 °C in separate reaction vials, samples were analyzed *via* radio-TLC (silica gel 60 F_{254}, mobile phase: MeCN/PBS (*v/v* = 3:2), +10% of NaOAc solution (2 M in H_2O), +1% TFA) differentiating between released [^{18}F]fluoride, immobilized at the baseline, and labeled test-compound. The experiment was repeated (n = 3). The proportions of intact ^{18}F-labeled peptide at the different time points were used to calculate the half-life of the ^{18}F-defluorination. For the evaluation, the GraphPad PRISM software (*GraphPad Software Inc*., La Jolla, United States) was used.

^{18}F- to ^{nat}F-Isotopic Exchange in Aqueous Solution (1 mM NaF, pH 6.5, rt): The test compound was labeled according to the aforementioned procedure (**chapter II.7.1**) starting with 200–300 MBq of aqueous [^{18}F]fluoride solution. The ^{18}F-labeled compound (10 µL per vial, approximately 0.8–1.0 nmol, 2.5–5.0 MBq) was added to a solution of 80 µL ultrapure H_2O and 10 µL NaF solution (10 mM in H_2O) per vial. The pH-value of the incubation solution was controlled by a test strip (resolution: 0.5). After incubation for 0, 30, 60, 90 and 120 min at 37 °C in separate reaction vials, samples were analyzed *via* radio-TLC (silica gel 60 F_{254}, mobile phase: MeCN/PBS (*v/v* = 3:2), +10% of NaOAc solution (2 M in H_2O), +1% TFA) differentiating between released [^{18}F]fluoride, immobilized at the baseline, and labeled test-compound. The experiment was repeated (n = 3). The proportions of intact ^{18}F-labeled peptide at the different time points were used to calculate the half-life of the ^{18}F-defluorination. For the evaluation, the GraphPad PRISM software (*GraphPad Software Inc*., La Jolla, United States) was used.

9. *In Vivo* Experiments

All animal experiments were conducted in accordance with general animal welfare regulations in Germany (German animal protection act, in the edition of the announcement, dated May 18th, 2006, as amended by article 280 of June 19th 2020, approval no. ROB-55.2-1-2532.Vet_02-18-109 by the General Administration of Upper Bavaria) and the institutional guidelines for the care and use of animals. To establish tumor xenografts, LNCaP cells (approximately 1.5×10^7 cells) were suspended in 200 µL of a 1:1 mixture (*v/v*) of DMEM F-12 and Matrigel (BD Biosciences, Germany), and inoculated subcutaneously onto the right shoulder of 6–8 weeks old CB-17 SCID mice (*Charles River, Sulzfeld, Germany*). Mice were used for experiments when tumors had grown to a diameter of 2–6 mm (4–20 weeks after inoculation).

NOTE: Due to a limited availability of the LNCaP passage initially used for *in vivo* experiments two further passages were used, consequently resulting in datasets with deviating tumor uptakes and referred to as LNCaP I, LNCaP II and LNCaP III in the text. For better comparability experiments of reference compounds were partially repeated and depicted in the figures as available, respectively. Data within set LNCaP I were previously published by our group (*125,160*).

9.1. Biodistribution Experiment

Approximately 2–5 MBq (50–120 pmol) of the ^{177}Lu-labeled PSMA inhibitors or approximately 1–2 MBq (50–120 pmol) of the ^{18}F-labeled ligand were administered by injection into the tail vein of LNCaP tumor-bearing male CB-17 SCID mice and sacrificed after 1 h or 24 h post injection (p.i.). Selected organs were removed, weighted and measured in a γ-counter. Results were all decay-corrected and given in % injected dose per gram of tissue (%ID/g). Tumor-to-organ ratios were calculated from animals' individual ratios and are given as mean ± standard deviation.

9.2. µSPECT/CT Imaging

Static images were recorded of sacrificed mice, 1 h or 24 h p.i. directly after blood collection by cardiac puncture and prior to the subsequent biodistribution experiment. The acquisition time was 45 min. The HE-GP-RM collimator and a stepwise multi-planar bed movement were used. For imaging studies, an MILabs VECTor4 small-animal SPECT/PET/OI/CT from MILabs (Utrecht, Netherlands) was applied. Furthermore, data were reconstructed using the MILabs-Rec software (version 10.02) and a pixel-based Similarity-Regulated Ordered Subsets Expectation Maximization (SROSEM) algorithm with a window-based scatter correction (20% below and 20% above the photopeak, respectively). Moreover, further data analysis was accomplished using the PMOD4.0 software acquired from PMOD TECHNOLOGIES LLC (Zurich, Switzerland) at defined settings (voxel size CT: 80 µm, voxel size SPECT: 0.8 mm, 1.6 mm (FWHM) Gaussian blurring post

processing filter, with calibration factor in kBq/mL and decay correction and no attenuation correction).

9.3. Metabolite Analysis

For determinations of metabolic stability, 4–6 MBq or 10–12 MBq of the radioactive-labeled PSMA inhibitors were injected into the tail vein of LNCaP tumor-bearing male CB-17 SCID mice and sacrificed after 4 h or 24 h p.i., respectively. The corresponding work-up for each sample is listed below. Each sample was analyzed *via* radio-RP-HPLC with the same gradient used for quality control (QC) of the respective ^{177}Lu-labeled compound prior to injection into mice (gradient and extraction efficiency given in **chapter III.1.4**).

Urine: Urine samples of the sacrificed mice were pooled, centrifuged at 16000 × g for 5 min and directly analyzed *via* radio-RP-HPLC.

Blood: Blood was collected by cardiac puncture and diluted with 1 mL H_2O. The sample was centrifuged at 16000 × g for 5 min. The supernatant was collected, the residue was diluted with 1 mL H_2O and centrifuged once more. Both supernatants were combined and loaded on a Strata X cartridge (33 µm Polymeric Reversed-Phase 500 mg, pre-conditioned with 5 mL MeOH, followed by 5 mL H_2O). After washing with 5 mL H_2O, the adsorbed activity was eluted with MeCN/H_2O (*v/v* = 6:4, supplemented with 1% TFA). All eluates (one per mouse) were pooled and diluted with H_2O to the respective MeCN proportion of the start value of the gradient used for radio-RP-HPLC.

Kidney: Each kidney (two per mouse) was cut into 3–5 pieces and placed in a micro reaction tube equipped with steel and ceramic beads (*Lysis Tubes W, analytikjena, Jena, Germany*). To the sample, 1050 µL of an extraction buffer were added (850 µL HEPES, 1 M, pH 7.4; 100 µL 2-PMPA solution in H_2O, 20 mM; 100 µL NaCl solution in H_2O, 1 M) prior to homogenization in a MM-400 ball mill (*Retsch GmbH, Haan, Germany*) at 30 Hz for 15 min. The homogenate was transferred into an empty micro reaction tube and centrifuged (25830 × g, 10 min). The supernatant was collected, and the residue was suspended in 1050 µL extraction buffer for an additional washing step and transferred to the tube with steel and ceramic beads for another round of homogenization at 30 Hz for 15 min. Afterwards, this second fraction of homogenate was transferred into a new, empty micro reaction tube and centrifuged (25830 × g, 10 min). The supernatant of the second fraction was combined with the first fraction and loaded on a Strata X cartridge (33 µm Polymeric Reversed-Phase 500 mg, pre-conditioned with 5 mL MeOH, followed by 5 mL H_2O). After washing with 5 mL H_2O, the adsorbed activity was eluted with MeCN/H_2O (*v/v* = 6:4, supplemented with 1% TFA). All eluates (two per mouse) were pooled and diluted with H_2O to the respective MeCN proportion of the start value of the gradient used for radio-RP-HPLC.

III. RESULTS AND DISCUSSION

A tabular overview of all determined *in vitro* and *in vivo* data of this work is provided in the supplemental information (**chapters V.1 and V.2**).

1. Evaluation of Ligands Aiming for Metabolic Instability (MI)

1.1. Background and Design of MI Ligands

In PSMA-targeted radioligand therapy (PRLT), the kidneys are estimated to be an organ at risk and thus, could potentially pose a dose-limiting-factor (*161-163*). To achieve an overall low dose of non-target tissue in PRLT, usually a fast clearance kinetic realized by a predominant renal excretion route is favored. Following the renal excretion path, a certain proportion of kidney retention is related to the physiological PSMA expression localized in healthy tissue of the proximal tubules (*44*).

To reduce vector-mediated activity accumulation and accelerate renal clearance, the installation of a cleavable linker connecting the targeting vector and the radionuclide-bearing moiety could serve as a useful approach (**Figure 14**). To ensure an unrestricted tumor accumulation, an unaltered stability in blood as well as in tumor tissue should be maintained, while a selective cleavage in kidney tissue would release a radiometabolite with lost target affinity. In the case of such a PSMA-targeting radioligand, the resulting radiometabolite would exhibit no more PSMA-mediated tubular reabsorption and the renal activity accumulation would probably be decreased. In literature, several approaches are described exploiting enzymatically cleavable linkers recognized by renal brush border enzymes (BBE).

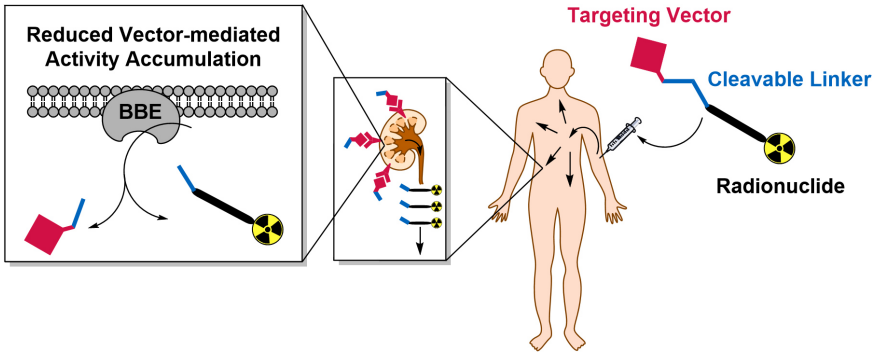

Figure 14: Illustration of a ligand comprised of a targeting vector attached to a radionuclide-bearing moiety *via* a cleavable linker. In this example, the linker should be enzymatically cleaved by a renal brush border enzyme (BBE) to reduce vector-mediated activity accumulation in the kidney.

Various cleavable linkers for the labeling of antibody fragments were investigated by *Arano et al.* with the Met-Val-Lys sequence being one of them (*164-167*). This sequence was reported to be cleaved by the neutral endopeptidase (NEP), an enzyme highly expressed on the renal brush border membrane (BBM), hydrolyzing the Met–Val bond while the recognition should be facilitated

in the presence of the free Lys-carboxylate (*167-170*). The study of *Arano et al.* revealed a 7-fold improvement of the tumor-to-kidney ratio 3 h p.i. with similar tumor uptakes for an Ga-NOTA-Met-Val-Lys-Fab fragment opposed to the corresponding Ga-NOTA-Fab fragment (*166*). This strategy was also successfully applied to an exendin 4 ligand with a 3-fold increase of the tumor-to-kidney ratio 3 h p.i. while a high tumor uptake was preserved (*171*).

Furthermore, an attempt to translate this approach to a PSMA ligand based on HTK01166 as a lead structure was conducted. To allow for a theranostic use, the terminal sequence was altered into a DOTA-AmBz-Met-Val-Lys construct. Preliminary experiments conducted with a model peptide – not yet attached to the PSMA targeting lead structure – exhibited an efficient cleavage *in vitro*, a fast renal clearance *in vivo* and the hypothesized DOTA-AmBz-Met fragment was verified as the main metabolite observed in urine (>90%) but to a low proportion (<5%) in blood, as expected. In a next step, the cleavable DOTA-AmBz-Met-Val-Lys sequence was implemented into the HTK01166 lead structure. Unfortunately, a high instability of the modified PSMA ligand (9% intact) was observed in blood 5 min p.i. with the main metabolite unidentified. As a result, 1 h p.i. only an insignificant (p = 0.055), moderate reduction of kidney uptake to 70% of the reference compound was achieved (*172*).

As mentioned above, the group of *Arano* also investigated additional linker sequences like the Gly-Lys and the Gly-Tyr sequence (*164,167*). *C*-terminal Gly-Lys containing peptides and Fab fragments, were determined to be recognized as substrates of the carboxypeptidase M (CPM), highly expressed in human kidneys (*164,173,174*). The Gly-Tyr sequence seems to be converted by more than one BBE and displayed a higher conversion *in vitro* compared to the Gly-Lys sequence (*167*). In a work published by *Vaidyanathan et al.*, the Gly-Tyr fragment was implemented into the structure of the well-known PSMA ligand DCIBzL, also named I-BA-KuE (*175*). At first, the novel ligand was directly compared to DCIBzL by co-injection in BALB/c normal mice using deviating radioisotopes of iodine ([^{131}I]I-BA-Gly-Tyr-KuE vs. [^{125}I]I-BA-KuE). The kidney-uptake at 21 h p.i. was remarkably lower for the Gly-Tyr derivative by a factor of 161. The experiment was repeated with SCID mice bearing PC3-PIP (PSMA^{+}) tumor xenografts. Interestingly, the choice of mouse strains seems to heavily influence the metabolization as described similarly in previous work (*176*). Therefore, it seems comprehensible that the difference in kidney uptake was less drastic in SCID mice with only a 6- to 7-fold decrease 21 h p.i. for the Gly-Tyr derivative. At the same time, a concomitant reduction of tumor uptake was observed by a factor of 3, still resulting in an approximately 2-fold improved tumor-to-kidney ratio (*175*).

In our group, previous investigations focused on the implementation of the Gly-Lys sequence into the PSMA I&T structure (*115*). The modification of the linker was well tolerated regarding *in vitro* parameters but resulted in high instability observed in a murine blood sample 30 min p.i. which was generally associated with poor tumor targeting potential. Despite the encouraging results for the described cleavable Fab fragments as well as the cleavable exendin 4-based polypeptide, so far BBE-cleavable linkers could be introduced to small molecule PSMA inhibitors with only limited

success. In this work, results are presented investigating the use of BBE-cleavable Gly-Tyr and Gly-Lys linkers by insertion into the radiohybrid lead structure rhPSMA-7.3. Structures corresponding to the subsequent development steps are depicted in **Figure 15**.

In a first generation, both latter fragments were inserted at a position distant to the Glu-urea-Glu (EuE) binding motif with minimal modifications of the lead structure. For the Gly-Lys fragment, the geometry of the lead structure was only slightly changed by the inversion of the stereocenter of the already present D-Lys in the linker region and the addition of Gly resulting in ligand MI-2. The Gly-Tyr derivative MI-1 contains the cleavable fragment in a similar position, hypothetically leading to the same metabolite Lu-DOTAGA-D-Dap[(4-SiFA)Bz]-Gly-OH. As a presumably non-cleavable D-Lys counterpart (*164*), MI-3 was synthesized for direct comparison with MI-2 and for the validation of a possibly superior *in vivo* performance of a cleavable derivative.

In a second generation, the postulated cleaving site was shifted into the radiohybrid unit consisting of the SiFA moiety and a chelator. In this case, the Gly-Lys cleavage would result in a pseudo-radiohybrid compound as chemically different radiometabolites would occur depending on which prosthetic group was labeled. Nevertheless, as this project is focused on therapeutic use, the hypothesized, obviously more hydrophilic Lys-(Lu-DOTAGA) metabolite was believed to potentially possess a faster clearance kinetic opposed to the metabolite of the first generation.

In a third generation, a combinatorial approach was used. As it was determined in our group, the choice of the chelator clearly influences the pharmacokinetics and thus, tumor-to-organ ratios (*125*). Therefore, MI-2 was modified by the attachment of DOTA instead of DOTAGA resulting in ligand MI-5. This compound is structurally also closely related to the DOTA-conjugate rhPSMA-10.1 (DOTA-derivative of rhPSMA-7.3).

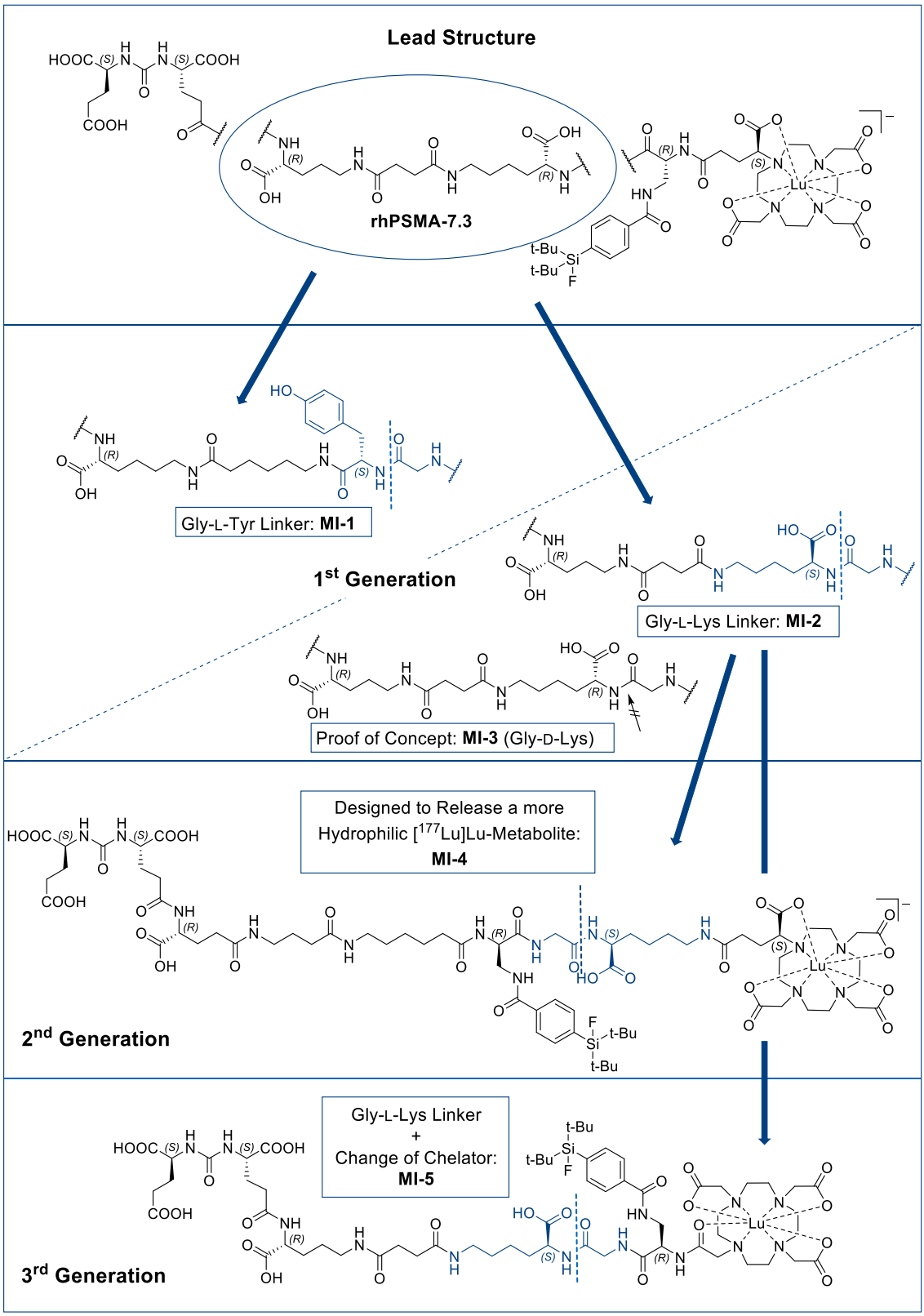

Figure 15: Structures and development steps of the MI ligands derived from the lead structure rhPSMA-7.3; desired cleaving sites are indicated with dashed lines while the D-Lys derivative MI-3 is supposed to be stable.

1.2. *In Vitro* Evaluation of MI Ligands

In vitro data of the depicted MI ligands as well as previously published data of the reference ligands rhPSMA-7.3, -10.1, PSMA-617 and PSMA I&T (*125*) are shown in **Figure 16**.

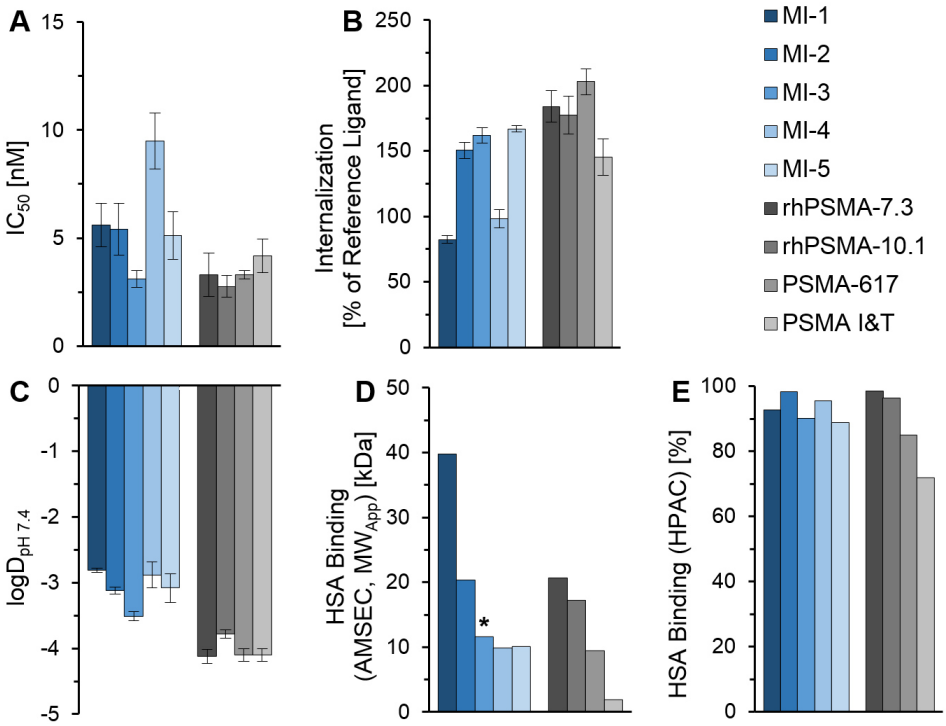

Figure 16: *In vitro* data of PSMA ligands aiming for metabolic instability (MI, blue) and reference ligands (grey), all evaluated as [$^{177/nat}$Lu]Lu-compounds; **A)** affinities (IC_{50} [nM]) determined in a binding assay of ^{nat}Lu-compounds (10^{-10}–10^{-5} M) with [^{125}I]I-BA-KuE (0.2 nM) as competitor on PSMA$^+$ LNCaP cells (1 h, on ice, n = 3); **B)** PSMA-mediated internalization of [^{177}Lu]Lu-compounds in PSMA$^+$ LNCaP cells (1 h, 37 °C) as percentage of the reference ligand [^{125}I]I-BA-KuE (n = 3); **C)** lipophilicity of [^{177}Lu]Lu-compounds expressed as *n*-octanol/PBS partition coefficient ($logD_{pH\ 7.4}$, n ≥ 6); **D)** apparent molecular weight (MW_{App}) of [^{177}Lu]Lu-compounds determined by human serum albumin-mediated size exclusion chromatography (AMSEC); **E)** human serum albumin binding of ^{nat}Lu-compounds determined on a Chiralpak HSA column. Data depicted for reference compounds in A–D) were previously published by our group (*125*); only AMSEC data were modified by a correction factor explained in **chapter II.8.5.2**. *The MW_{App} of MI-3 was determined with a different batch of HSA which might contribute to limited comparability.

All ligands exhibited a high PSMA affinity in the low nanomolar range of 3–6 nM, as expected for the minor structural modifications in MI-2, -3 and -5. The Tyr-residue in MI-1 was placed in a structural distance to the EuE binding motif, where numerous aromatic modifications were reported with predominantly little influence on the affinity (*115,177*). Only for ligand MI-4 a 3-fold decline in affinity compared to rhPSMA-7.3 was determined. This finding is in well accordance with previous data describing superior affinity for structurally related derivatives by a decrease of linker length between the chelator and the SiFA moiety (rhPSMA 101 and rhPSMA 201) (*152*).

Internalization rates of MI-2, -3 and -5 were measured between 150% and 170% of the assay-internal reference [^{125}I]I-BA-KuE being slightly lower than the rhPSMA references. MI-1 displayed about a 2-fold drop in internalization possibly correlating with the drastically increased apparent molecular weight (MW_{App}) which was associated with a strong HSA binding. Seemingly, the observed internalization into LNCaP cells of ligands was limited by their binding strength to

bovine serum albumin (BSA) contained in the supernatant. Previous work in our group indicated a strong influence by the absence or presence of BSA in the assay medium on the observed internalization behavior of ligands with strong HSA binding (*177*). On the other hand, the use of BSA in the assay medium was initially established to avoid non-specific ligand association with plates and vials (*115*). To keep data as consistent as possible, no assay parameters were changed in this project. Regarding MI-4, the inferior internalization kinetic was likely a product of its decreased affinity.

As expected, all MI ligands demonstrated a loss in hydrophilicity compared to the lead structure rhPSMA-7.3 by either the substitution of a carboxylic acid by a more lipophilic aromatic residue (MI-1), an increase of the distance between the lipophilic SiFA moiety and carboxylic acid/DOTAGA (MI-2 to -4) or the use of DOTA with one carboxylic acid less (MI-5). However, the structural alterations resulted in $logD_{pH\ 7.4}$ values still in a reasonable range (–2.8 to –3.5).

The two methods for characterization of HSA binding delivered partially diverging results. Because of certain structural similarities with ibuprofen, it is assumed that the SiFA moiety predominantly interacts with the HSA binding site II (Sudlow II, see also **chapter III.3.4**). This binding site is known for binding ibuprofen, an *para*-isopropyl substituted aromatic compound (*178*). In general, HSA binding is predominantly observed for fatty acids and aromatic entities (*178,179*). Therefore, it is comprehensible that an additional aromatic moiety in MI-1 increased the MW_{App} opposed to rhPSMA-7.3 (39.9 kDa vs. 21.6 kDa). Contradictorily, the high-performance affinity chromatography (HPAC) indicated a decrease in HSA binding (92.7% vs. 98.6%). MI-2 exhibited quite similar values compared to rhPSMA-7.3 in both methods representing the high structural similarity. The inversion of the Lys-stereocenter in MI-3, the increased distance to the carboxylic acid group of DOTAGA in MI-4 and the removal of one carboxylic acid using DOTA instead of DOTAGA in MI-5 was accompanied by a decrease of MW_{App} (11.6 kDa, 9.9 kDa and 10.2 kDa, respectively) even below the value of rhPSMA-10.1 (17.2 kDa).

These data are well in line with literature indicating a strong influence of charged groups in proximity to lipophilic *para*-substituted aromatic moieties on their HSA binding. *Deberle et al*. demonstrated a pivotal role of positively, neutral, or negatively charged groups in proximity to an ibuprofen entity on HSA binding (*146*). *Kelly et al.* revealed a drastic influence on HSA binding by variation of linker lengths between a carboxylic acid and a *p*-iodophenyl moiety (*180*). Furthermore, our group could already present an influence by stereoinformation in the rhPSMA-7 diastereomers as well as by a change of the chelator (rhPSMA-7 isomers opposed to rhPSMA-10 isomers) on HSA binding (*125*). On the other hand, this expected trend was not as consistent for HPAC-derived data with the HSA binding of MI-4 exceeding the value of MI-3 (95.6% vs. 90.2%).

1.3. Biodistribution of MI Ligands

In the following, *ex vivo* biodistribution data of the MI ligands are compared to the lead compound rhPSMA-7.3 (**Figure 17**). MI-1 was investigated in only one mouse as it clearly revealed an inferior biodistribution compared to rhPSMA-7.3 with a drastically prolonged blood retention and a tumor-to-blood ratio about 26-fold lower. Reasons might be the elevated HSA binding as well as metabolic degradation in blood (see next chapter) – in contrast to the desired cleavage in the kidneys immediately followed by urinary excretion. Moreover, the increased lipophilicity of MI-1 (as well as potential metabolites) probably raised the proportion of a hepatobiliary excretion (T/Liver: 23.0 vs. 53.7 ± 1.7 for MI-1 and rhPSMA-7.3, respectively). As a result, the kidney accumulation could be more than halved but at the cost of a tumor uptake decreased to one-third. The lowered tumor-targeting potential was in well accordance with the found instability in blood (see next chapter).

MI-2 and MI-3 were originally designed to investigate a structurally closely related pair of a cleavable (L-Lys) and a non-cleavable (D-Lys) ligand, respectively. *Ex vivo* biodistribution data revealed an unexpected negligible difference in their performance showing no advantage of the hypothesized cleavability on kidney retention. Both ligands exhibited about the half of the tumor uptake as well as the kidney uptake concerning the lead compound rhPSMA-7.3. Interestingly, an extraordinarily high standard deviation was observed for kidney uptakes of MI-2 and -3 across respective mouse cohorts with no obvious single outlier. Calculating the tumor-to-organ ratios for each mouse individually, the comparison of the subsequently derived mean values revealed a slight but negligible improvement of tumor-to-kidney ratios (2.4 ± 1.5, 1.9 ± 1.0 and 1.2 ± 0.3 for MI-2, MI-3 and rhPSMA-7.3, respectively). Tumor-to-liver ratios of MI-2 and MI-3 were also increased by a factor of 2.4 and 3.7 whereas tumor-to-blood ratios declined to a respective ratio of 40% and 47% compared to rhPSMA-7.3.

While kidney and liver uptakes of MI-4 were found to be similar to rhPSMA-7.3, tumor uptake was reduced to about one-half of the lead compound with concomitant decreased tumor-to-kidney and -liver ratios. This might be associated with the lower target affinity and PSMA-mediated internalization as determined *in vitro*. The tumor-to-blood ratio was doubled but the increase appeared irrelevant due to the high standard deviation.

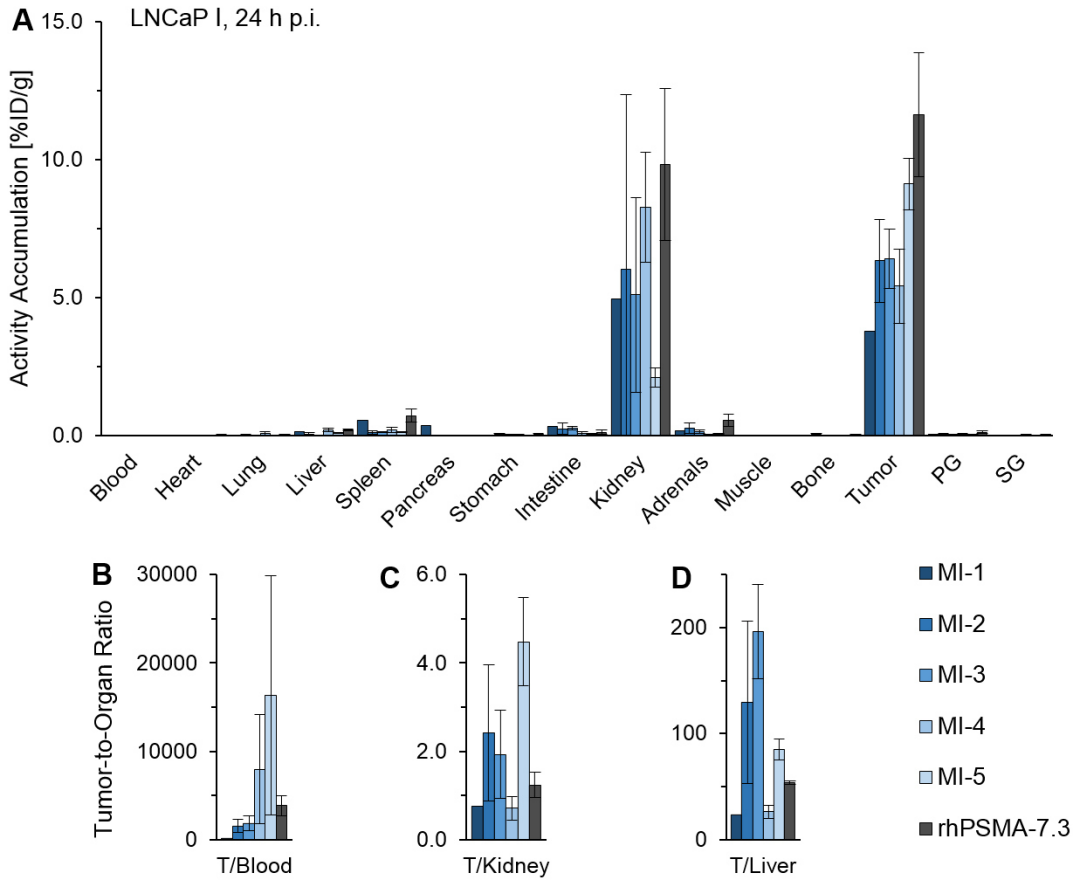

Figure 17: A) *Ex vivo* biodistribution of MI-1 (n = 1), MI-2 (n = 5), MI-3 (n = 3), MI-4 (n = 4), MI-5 (n = 4) and rhPSMA-7.3 (n = 4) as [^{177}Lu]Lu-compounds at 24 h p.i. in male LNCaP I tumor-bearing CB-17SCID mice; PG = parotid glands, SG = submandibular glands; data expressed as percentage of the injected dose per gram (%ID/g) and mean ± standard deviation; **B–D)** tumor-to-organ ratios (tumor-to-blood/-kidney/-liver) calculated individually for each mouse and expressed as mean ± standard deviation. Data of rhPSMA-7.3 were previously published by our group (*125*).

Within the MI-series, MI-5 clearly possessed the most favorable biodistribution pattern with the lowest kidney uptake (2.1 ± 0.3 %ID/g) and only a minor decrease in tumor uptake compared to rhPSMA-7.3 (9.1 ± 0.9 %ID/g vs. 11.6 ± 2.2 %ID/g, respectively). All depicted tumor-to-organ ratios could be improved opposed to the DOTAGA-bearing ligand rhPSMA-7.3.

Especially the decreased kidney uptake was clearly visualized in µSPECT/CT images. However, MI-5 showed a quite equal biodistribution pattern as determined for rhPSMA-10.1, also reflected by µSPECT/CT images (**Figure 18**).

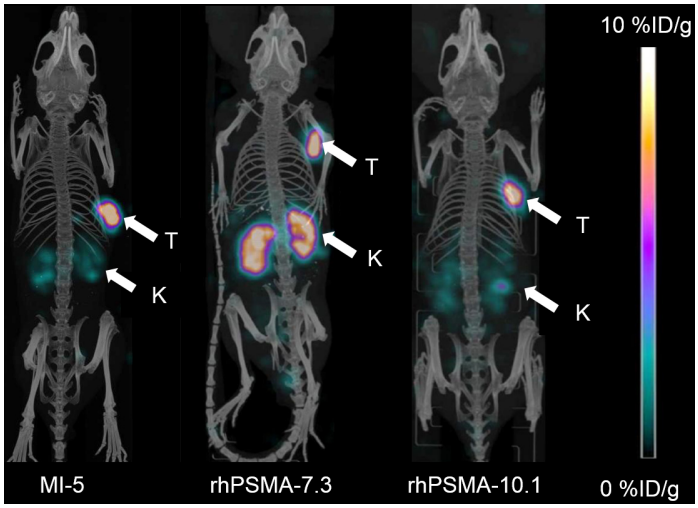

Figure 18: Static µSPECT/CT images (maximum intensity projections) of MI-5, rhPSMA7.3 and rhPSMA-10.1 as ^{177}Lu-labeled compounds in LNCaP I tumor-bearing CB-17 SCID mice. Tumors (T) and kidneys (K) are indicated by white arrows. Mice were sacrificed 24 h p.i. and imaged directly after blood collection by cardiac puncture. Images of rhPSMA-7.3 and -10.1 depicted as reference were previously published by our group (*125*).

Nevertheless, the comparison with the remaining reference compounds, especially with the DOTA-conjugate rhPSMA-10.1, which is the structurally more closely related compound to MI-5, revealed no advantage (**Figure 19**).

This leads to the conclusion that, if MI-5 was recognized as BBE substrate, its cleavability constituted no beneficial effect over the choice of DOTA as chelator alone. Furthermore, all investigated implementations of cleavable linkers in the MI-series were followed by a minor decrease in kidney uptake opposed to the effect by the choice of a different chelator. Therefore, the focus of further investigations was shifted to modifications varying HSA binding and net charge. These parameters were estimated as key parameters responsible for the high tumor-to-organ ratios found for rhPMSA-10.1 and PSMA-617.

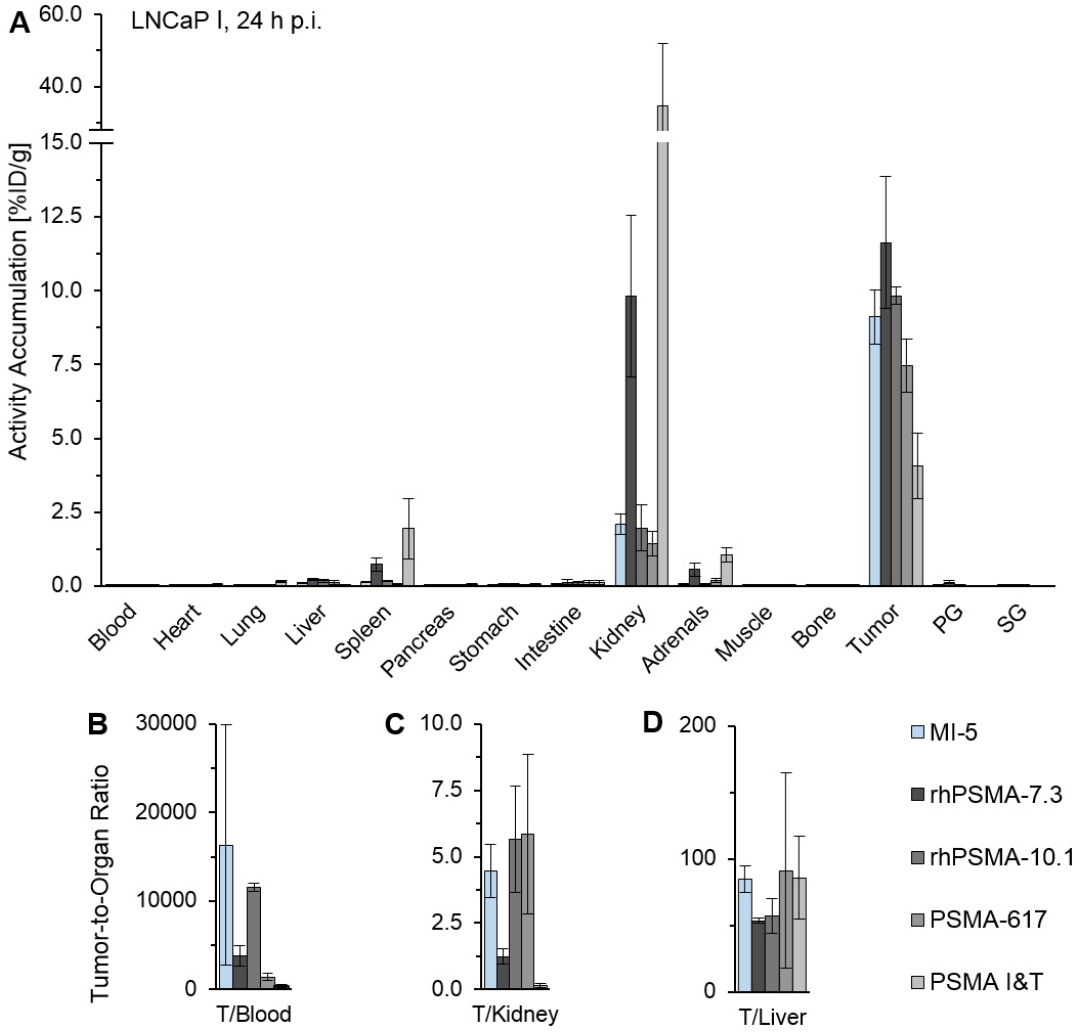

Figure 19: A) *Ex vivo* biodistribution of MI-5 (n = 4) and the reference ligands rhPSMA-7.3 (n = 4), rhPSMA-10.1 (n = 5), PSMA-617 (n = 4) and PSMA I&T (n = 4) as [^{177}Lu]Lu-compounds at 24 h p.i. in male LNCaP I tumor-bearing CB17-SCID mice; PG = parotid glands, SG = submandibular glands; data expressed as percentage of the injected dose per gram (%ID/g) and mean ± standard deviation; **B–D)** tumor-to-organ ratios (tumor-to-blood/-kidney/-liver) calculated individually for each mouse and expressed as mean ± standard deviation. Data of reference ligands were previously published by our group (*125,160*).

1.4. Metabolization of MI Ligands

In a first attempt within the MI-series, the Gly-L-Tyr sequence was introduced as BBE cleavable sequence in the ligand MI-1. Opposed to the reported 2-fold improvement of the tumor-to-kidney ratio for a PSMA ligand by *Vaidyanathan et al.* (*175*), the drastically lowered tumor uptake of MI-1 to one-third compared to rhPSMA-7.3 had a decreased tumor-to-kidney ratio as a consequence. This decreased tumor targeting potential seemed to be reflected by the high metabolic instability found in blood (**Figure 20**).

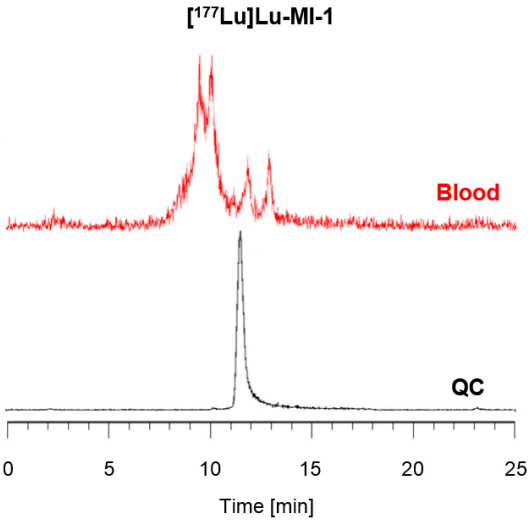

Figure 20: Chromatograms obtained by radio-RP-HPLC using the same gradient (10 to 70% B in 15 min, 95% B for 5 min, 10% B for min); **top chromatogram:** analysis of a blood sample obtained by cardiac puncture of one CB-17 SCID mouse 24 h p.i. of [^{177}Lu]Lu-MI-1 (11.6 MBq, 170 pmol) and subsequent purification via cartridge (**chapter II.9.3**); **bottom chromatogram:** quality control (QC) of [^{177}Lu]Lu-MI-1 by RP-HPLC after [^{177}Lu]Lu-labeling (**chapter II.7.3**).

The blood sample was obtained of one CB-17 SCID mouse 24 h p.i. by cardiac puncture. After a cartridge-based purification for the removal of solid particles and biomolecules insoluble in acetonitrile (MeCN, used solvent in subsequent HPLC analysis), the analyzed sample was yielded in an overall extraction efficiency of 88.4%. The comparison of the corresponding chromatogram with the quality control (QC) displayed only 12% intact tracer at 24 h post injection. This drastic instability paired with the concomitant poor biodistribution pattern promoted the shift towards the implementation of a different cleavable sequence.

Results on metabolic stability of the alternatively used Gly-L-Lys sequence of the first ligand in this subgroup, MI-2, and the ligand with the most favorable pharmacokinetics, MI-5, are depicted in **Figure 21**. As the initially chosen timepoint of 24 h p.i. of MI-1 resulted in a low remaining activity in the kidneys and consequently with an unsatisfying signal intensity in the chromatogram (data not shown), MI-2 and MI-5 were investigated 4 h post injection. Additionally, groups of two and three mice, respectively, were injected to pool samples for a mean metabolic observation and to ensure the collection of a sufficient amount of urine.

The DOTAGA-conjugate MI-2 was yielded in an overall extraction efficiency of 72% from blood and 40% from kidney homogenate. The DOTA-conjugate MI-5 revealed extraction efficiencies of 59% from blood and 56% from kidney homogenate.

As expected, no metabolites were observed in the blood for MI-2. In the kidney and urine 84% and 64% intact tracer were found, respectively. Surprisingly, the two compounds only differing in the choice of DOTAGA or DOTA as chelator revealed a quite different metabolization pattern. Only 26% of MI-5 were found to be intact in blood which was contrary to the highest determined tumor uptake within the MI-series. Urine and kidney samples of MI-5 exhibited higher proportions of intact tracer of 62% and 88%, respectively.

Moreover, the main metabolite of MI-5 in blood and urine possessed an extremely short retention time associated with high hydrophilicity. In contrast, the expected DOTA-/DOTAGA-D-dap[(4-SiFA)Bz]-Gly-OH metabolites were estimated to exhibit a tendential loss in hydrophilicity compared to the intact tracers bearing several additional carboxylic acids.

For MI-2, the expected trend was observed for the main metabolite in urine. Obviously, MI-5 was degraded in a different way which might include the cleavage of the SiFA moiety off the chelator explaining the short retention time.

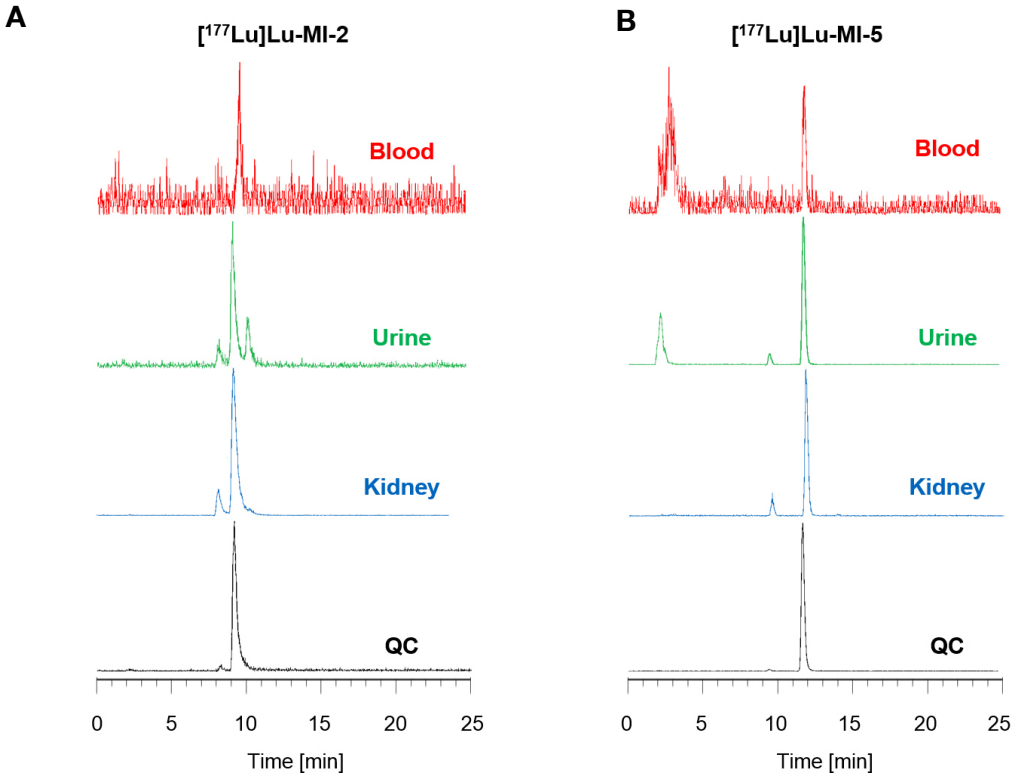

Figure 21: Chromatograms obtained by radio-RP-HPLC comparing samples of blood, urine and kidney of CB-17 SCID mice 4 h p.i. prepared according to **chapter II.9.3** with the corresponding quality control (QC) of the compounds after [^{177}Lu]Lu-labeling (**chapter II.7.3**); **A:** Analysis of [^{177}Lu]Lu-MI-2 (pooled from mice after injection of 5.6 ± 0.4 MBq, 93.6 ± 6.1 pmol; n = 2; gradient: 10 to 90% B in 15 min, 95% B for 5 min, 10% B for 5 min); **B:**[^{177}Lu]Lu-MI-5 (pooled from mice after injection of 4.9 ± 0.4 MBq, 79.0 ± 6.5 pmol; n = 3; gradient: 20 to 60% B in 15 min, 95% B for 5 min, 20% B for 5 min).

Additionally, a second peak in urine and kidney samples was observed with an only slightly decreased retention time regarding the peak corresponding to intact tracer. These peaks could also be recognized in trace amounts within the quality control and are most probably side products emerging from the instable F–Si bond within the SiFA moiety as organofluorosilanes are known to be prone to hydrolysis (*140*).

The formation of such trace impurities during [^{177}Lu]Lu-labeling was typically observed for SiFA-bearing compounds within this work. While a former protocol for [^{177}Lu]Lu-labeling (*156*) with NH_4OAc/AcOH (pH 5.9) at 95 °C for 30 min revealed 8.3% side product in the labeling of rhPSMA-7.3, the formation of side product could be minimized to 1.0% by the choice of a slightly more acidic buffer (NaOAc/AcOH: pH 5.5) at 90 °C. To proof the side product as a result of

hydrolysis of the F-Si bond, the former protocol was also conducted in the presence of 1000-fold excess of NaF. The use of additional fluoride competing with the hypothesized hydroxide as reactant of the side reaction clearly suppressed the formation of side product assumed as HO-Si(*t*Bu)$_2$–R species (8.3% vs. 2.7%) (unpublished data determined by *Kunert* in our group).

In conclusion, some metabolites could be indeed observed for a choice of ligands designed to be cleavable. In contrast to expectations, the detection of metabolites was not restricted to kidney and urine samples but did also partially occur in blood samples – which commonly is associated with reduced tumor-targeting potential. The ligand MI-5 revealed the most favorable biodistribution pattern within the MI-series despite a remarkable instability in blood and the virtual formation of an unexpectedly hydrophilic metabolite. This pointed to a metabolization deviant from the initial aim of this project. Surprisingly, the comparison of the biodistribution of MI-5 with the structural parent ligand rhPSMA-10.1 revealed a negligible difference, though. Assuming that rhPSMA-10.1 was metabolically stable according to results for the related rhPSMA-7 isomers (*77*), present findings suggest that an insertion of such metabolically instable linkers holds no benefit for pharmacokinetics in the context of this ligand scaffold.
While some questions were not fully answered in this project with regard to the exact metabolization pattern, it is unambigious that none of the investigated modifications resulted in a compound with clearly improved properties opposed to the reference ligands. The comparison with literature discussed above rather drives the impression that a clear benefit using the strategy of cleavable linkers might be restricted to larger scaffolds with significantly slower clearance kinetics of the intact tracer opposed to the respective released metabolite.

2. Evaluation of Branched Linker Constructs (BLC) for HSA Binding Modulation

2.1. Background and Design of BLC Ligands

One key parameter to influence pharmacokinetics of a compound, particularly blood and kidney clearance, is the binding property towards plasma proteins. In this context, human serum albumin (HSA) plays a pivotal role as the most abundant protein in human blood (*123*). Regarding PSMA ligands several approaches have been investigated to increase HSA binding aiming for a prolonged blood circulation and enhanced bioavailability for a superior tumor accumulation. The following examples should display the state of the art and some possibilities of fine-tuned HSA binding modulation. Nevertheless, these derivatives mostly suffer from heavily decreased tumor-to-blood ratios. Thus, ligands within this work were aiming for a more balanced HSA binding.

In 2008, *Dumelin et al.* published D-Lys(IPB)-OH (IPB = 4-(*p*-iodophenyl)butyric acid) as a strong binding motif towards human as well as murine serum albumin (*123*). Later on, *Kelly et al.* investigated small molecule PSMA ligands derived from MIP-1095 bearing similar *p*-iodophenyl entities for a modified HSA binding (*180*). The series clearly revealed the highest HSA binding for Lys(IPB)-OH compounds whereas small changes in the number of bonds between the *p*-iodophenyl moiety and the free Lys-carboxylate drastically decreased HSA affinity.

From there on, several groups included the IPB moiety in their design of PSMA ligands with increased HSA binding (*121,122,144,145,147,181*). *Schibli's* group explored the applicability of the IPB moiety on the PSMA-617 scaffold with altered structural modifications in vicinity to the HSA binder. In a first series, IPB alone (PSMA-ALB-02), IPB-Asp_2 (PSMA-ALB-05) and IPB-Asp_3 (PSMA-ALB-07) were conjugated to the Lys-$N\alpha$ of the Lys(DOTA)-Txa-Nal-KuE platform. While the addition of carboxylic acids in proximity to the HSA binder produced a beneficial compensation of lipophilicity (logD: –2.8 vs. –3.5 vs. –3.9, respectively, opposed to [^{177}Lu]Lu-PSMA-617: –4.4), within the ALB-series PSMA-ALB-02 revealed the fastest blood clearance and lowest kidney retention (area under the curve (AUC) opposed to PSMA-617: 2.8- and 11.4-fold raised, respectively) whereas tumor uptakes were similar among the ALB-derivatives (AUC ~2-fold of PSMA-617). Noteworthy, comparing PSMA-ALB-05 and -07 the additional Asp led to a ~2-fold tumor-to-blood ratio but an almost halved tumor-to-kidney ratio. This is an important hint for the development of hydrophilic linkers as the introduction of charges might be disadvantageous for kidney retention (*145*).

In a next PSMA-ALB-generation, the positions of DOTA and IPB were interchanged to receive PSMA-ALB-53 with a DOTA-Lys(IPB)-motif instead of the IPB-Lys(DOTA)-entity within the parent compound PSMA-ALB-02. Obviously, the novel constitutional isomer possessed the same HSA binder but with a more pronounced exposure. This led to a 10.7-fold increased AUC in blood but an only 1.2-fold raised AUC in the tumor. Moreover, the analog PSMA-ALB-56 was investigated and received by a replacement of the iodo- by a methyl-substituent to yield a weaker HSA binder.

The determined AUC in blood was still double the value of PSMA-ALB-02, but the AUCs for tumor and kidney were improved (+27% and –28%, respectively) (*147*).

Kuo et al. proceeded the modulation of HSA binding on a structural basis very similar to PSMA-ALB-02 by investigation of further *para*-substituents on the 4-phenylbutyric acyl entity. The observed trend for an enhanced blood retention assumed as a consequence of serum albumin binding was well correlated with the trend of increasing lipophilicity of the HSA binder (%ID/g in blood at 3 h p.i. with the altered substituents; I: ~24, Br: ~21, Cl: ~17, CH_3: ~13, OCH_3: ~6.6, NO_2: ~2.5, F: ~2.1, NH_2: ~0.5). These data appear to illustrate a quite helpful strategy in fine-tuning HSA binding for optimal tumor-to-organ ratios. Indeed, the optimized, Cl-substituted derivative [^{177}Lu]Lu-HTK03121 of *Kuo et al.* revealed a remarkable uptake in the LNCaP tumor model of 104 %ID/g at 24 h p.i. and according to dosimetry calculations even a 2.9-fold improvement of the tumor-to-kidney absorbed dose ratio opposed to [^{177}Lu]Lu-PSMA-617. Nevertheless, the drastically prolonged blood retention (4.3 %ID/g at 24 h p.i.) would obviously result in a dose-limiting factor (*181*).

After determination of a suitable anchoring position for the attachment of an HSA binding entity in their lead structure under preservation of low nanomolar PSMA affinity (*182*), a set of four 'RPS'-derivatives was investigated by *Kelly et al.* (*144*). Two structural parameters and respective alterations were tested. The first parameter was the use of either Lys(IPB)-OH or the truncated Lys(IPA)-OH (IPA: 4-(*p*-iodophenyl)acetic acid) as HSA binder. As mentioned above, the distance between the carboxylic acid and the *p*-iodophenyl moiety in the Lys(IPB)-OH fragment was found to exhibit the highest HSA affinity while several alterations of linker lengths in between led to a reduction, inclusively for the Lys(IPA)-OH fragment (*180*).

The second parameter was the insertion or omission of a polyethylene glycol 8 (PEG_8) linker connecting the HSA binder with the optimized anchoring position in the lead structure. Independently of the used HSA binder, the insertion of the PEG_8-linker was accompanied by a reduction of affinity towards PSMA as well as HSA. As expected, the use of the weaker HSA binder as well as the PEG_8-linker led to a faster blood clearance with the strongest effect for a combination thereof. Interestingly, the PEG_8-Lys(IPB)-OH ligand exhibited a significantly lower kidney retention while possessing a slower blood clearance opposed to the Lys(IPA)-OH ligand without a PEG-linker (AUC in kidney: 585 vs. 4676; AUC in blood: 420 vs. 22) leading to the highest tumor-to-kidney AUC ratio of 4.7 for the PEG_8-Lys(IPB)-OH ligand among the four ligands in LNCaP-tumor-bearing mice. The authors concluded that the lowered kidney value by their use of a PEG-linker was a synergistic result of two factors. On the one hand, a reduced HSA binding promotes a faster whole-body clearance. On the other hand, it was speculated that the increased linker size by the use of the PEG-linker reduced kidney retention by an 'accelerated clearance before tubular reabsorption' (*144*). Inspired by the finding of *Kelly et al.*, the concept of a branched linker construct with a terminally attached HSA binder should be investigated in this work. This modular scaffold seems to possess several advantages. First, after the determination of a suitable

branching position (optimization of number of bonds m and n in **Figure 22**) the target affinity of the whole construct is likely to be maintained independently of further modifications at the distant HSA binder. This should facilitate the modulation of HSA binding aiming for a blood half-life resulting in optimal tumor-to-background ratios. As indicated by the above-discussed literature, structural parameters for the modulation might be the variation of substituents at the HSA binding entity (*181*), the exposure or steric shielding of the HSA binder (*145,147*) or the variation of the linker by positioning or absence of functional groups like carboxylic acids in proximity to the HSA binder (*144,145,180*). Furthermore, *Kelly's* assumption of reducing tubular reabsorption and thus, kidney retention, by the use of larger linker constructs might be confirmed (*144*). Therefore, the linker moiety itself might be exploited to reduce the kidney dose not only as a function of blood clearance. Lastly, we hypothesize that a suitable linker length with an appropriate structural distance of the targeting vector and the HSA binder might allow for target binding of the ligand in an HSA-bound state possibly providing an enhanced tumor accumulation opposed to a comparable smaller ligand.

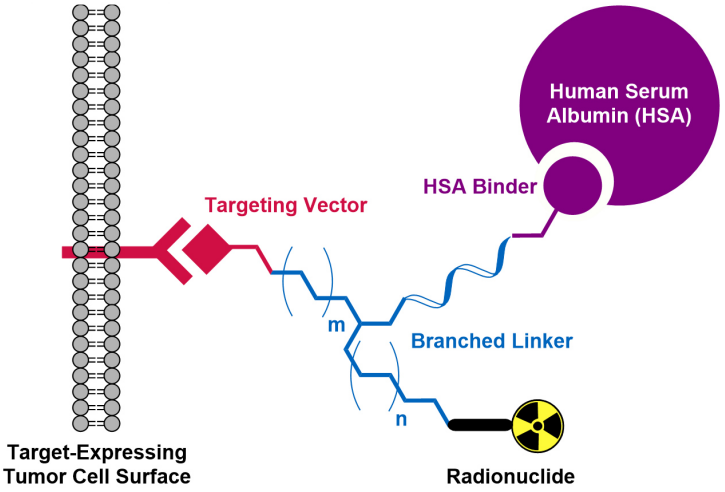

Figure 22: Illustration of a ligand comprised of a branched linker construct (BLC) connecting a targeting vector, a radionuclide-bearing moiety and an HSA binder with all functional moieties in a distance allowing for simultaneous binding to HSA and to the target expressed on tumor tissue. This structural basis should allow for a facilitated fine-tuning of pharmacokinetics and tumor accumulation independent of a residence time in an HSA-bound state.

Development steps and structures of respective investigated [$^{177/nat}$Lu]Lu-compounds in this project are depicted in **Figure 23**. To investigate our hypothesis, a sufficient spatial distance between the PSMA-targeting vector EuE and the HSA binder was indispensable. Thus, a rigid poly-L-proline spacer was initially chosen for investigations as it was previously shown by fluorescence energy transfer (FRET) studies that spatial distance could be efficiently retained (*183*). The poly-L-proline type II helix was described with a length of 3.1 Å per amino acid summing up to a total length of almost 28 Å for a Pro_9-linker (*184*). The entrance funnel of PSMA was reported to be approximately 20 Å deep (*71*). Therefore, the linker was estimated to keep a sufficient space between the PSMA targeting vector and HSA binding motif.

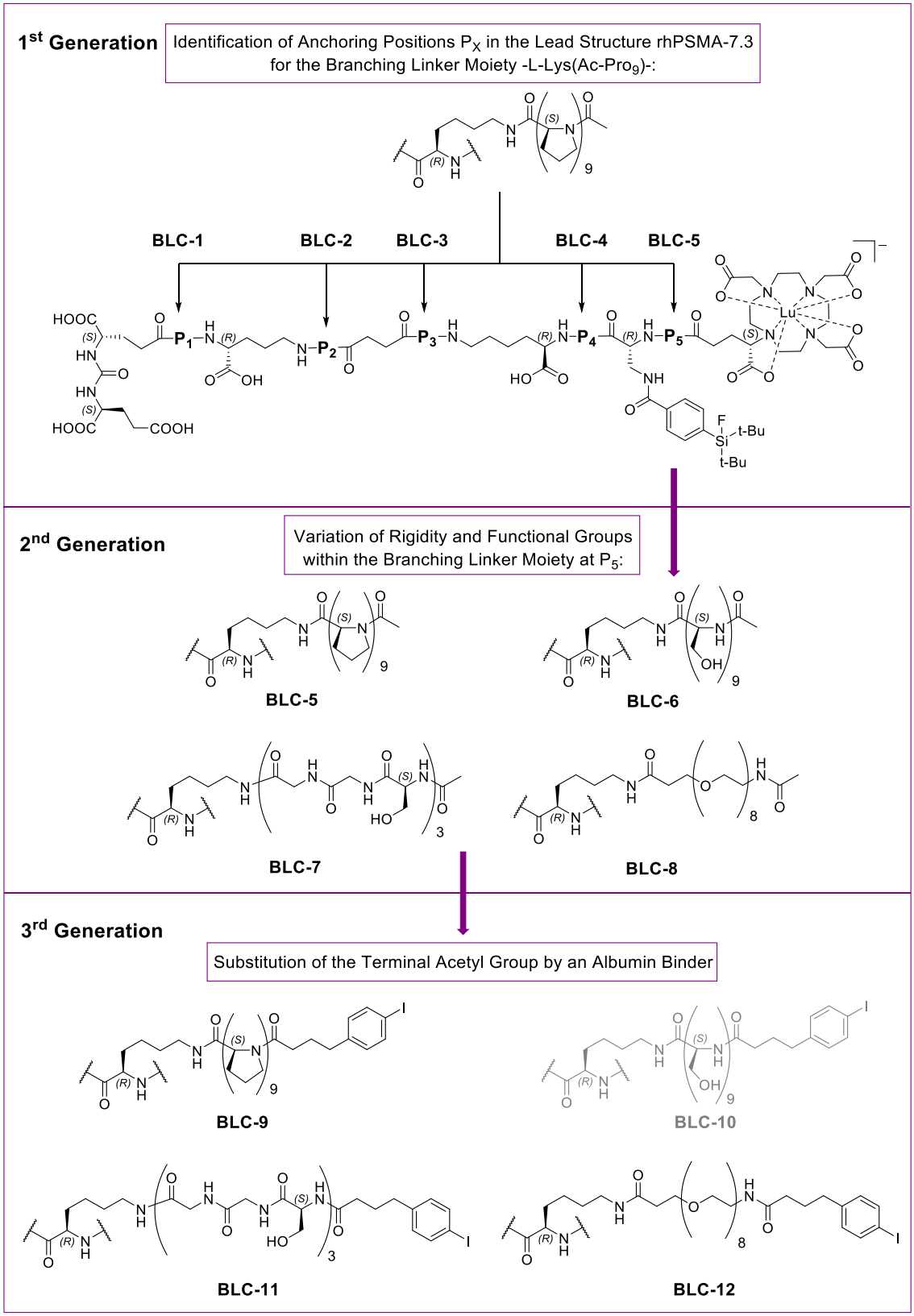

Figure 23: Structures and development steps of the BLC ligands derived from the lead structure rhPSMA-7.3. The nonaseryl-derivative BLC-10 could not be isolated due to low coupling yields within the linker moiety and no separation from respective deletion peptides.

In a first step, the optimal branching position by the insertion of a -Lys(Ac-Pro_9)-moiety (Ac =acetyl) into the lead-structure rhPSMA-7.3 among the positions P1 to P5 was determined resulting in the ligands BLC-1 to -5 (1st Generation).

In the second generation, the Pro_9-spacer was substituted by a Ser_9-, $(Ser\text{-}Gly\text{-}Gly)_3$- or PEG_8-spacer (BLC-6 to -8) possessing the same spacer lengths according to the number of bonds but different numbers of hydrophilic groups and grades of flexibility to examine influences on PSMA affinity as well as hydrophilicity.

In a third generation, the terminal acetyl group in the model compounds BLC-5 to -8 was replaced by the reported albumin binding moiety IPB (BLC-9 to -12). However, BLC-10 could not be isolated because of incomplete coupling reactions during the installation of the Ser_9-spacer resulting in deletion peptides which could not be separated from the product.

2.2. *In Vitro* Evaluation of BLC Ligands

The insertion of the Lys(Ac-Pro_9) spacer at branching positions P1–3 resulted in a significant loss of target affinity whereas positions P4 and P5 were moderately tolerated with IC_{50} values in a low nanomolar range and a loss of affinity within a factor of 2.3–2.8 compared to rhPSMA-7.3 (3.3 ± 1.0 nM) (**Figure 24**).

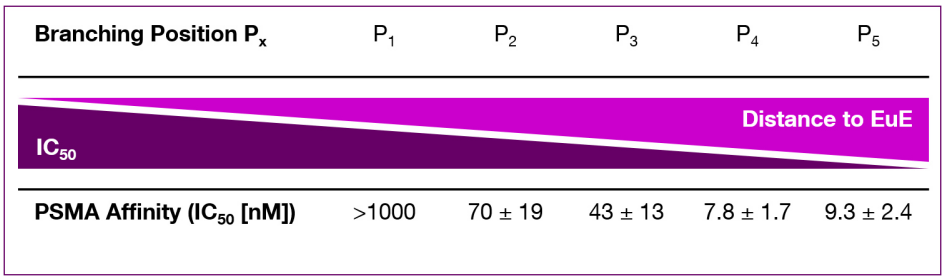

Figure 24: PSMA affinities (IC_{50} [nM]) of of BLC-1 to BLC-5 correlated to their branching position P_x and determined in a binding assay based on respective ^{nat}Lu-compounds (10^{-10}–10^{-5} M) with [^{125}I]I-BA-KuE (0.2 nM) as competitor on $PSMA^+$ LNCaP cells (1 h, on ice, n = 3).

The two respective derivatives BLC-4 and -5 were further evaluated as potential scaffolds for continuing optimizations (**Figure 25**).

The insertion of the rigid spacer in proximity to the SiFA moiety was followed by a remarkable decrease in HSA binding according to both methods (HPAC: 76.7% and 87.9%; AMSEC: 3.6 kDa and 4.4 kDa, respectively). Two factors were considered to be responsible. As described within the MI-series, altered distances between carboxylic acids/DOTAGA and the SiFA moiety influence HSA binding. On the other hand, the decrease in HSA binding observed for the two BLC ligands was more drastic compared to differences within the MI-series. Thus, it was concluded that the SiFA moiety could be sterically shielded by the used spacer and therefore, the affinity towards HSA was lowered. This finding seemed useful to minimize the influence of the SiFA moiety on the

overall HSA binding. Thus, this construct should allow for a more flexible modification of the HSA binding simply by the attachment of different HSA binding moieties at the terminus of the spacer. Not surprisingly, the insertion of the moderately polar Pro_9-spacer increased the lipophilicity as it can be seen from the $logD_{7.4}$ values (BLC-4: -3.0 and BLC-5: -2.8 vs. rhPSMA-7.3: –4.1).

The internalization values differed for the two positions. BLC-4 showed an increase of internalization by a factor of 1.2 while BLC-5 revealed a decrease of 14%, comparing both directly to rhPSMA-7.3.

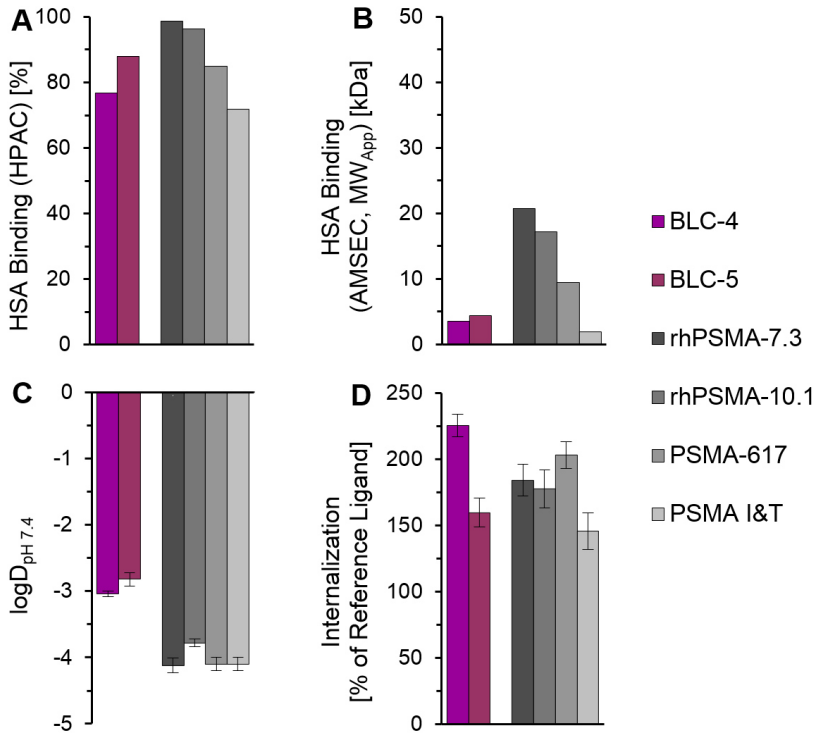

Figure 25: *In vitro* data of BLC-4, -5 (violet) and reference ligands (grey), all evaluated as [$^{177/nat}$Lu]Lu-compounds; **A)** human serum albumin binding of ^{nat}Lu-compounds determined on a Chiralpak HSA column; **B)** apparent molecular weight (MW_{App}) of [^{177}Lu]Lu-compounds determined by human serum albumin-mediated size exclusion chromatography (AMSEC); **C)** lipophilicity of [^{177}Lu]Lu-compounds expressed as *n*-octanol/PBS partition coefficient ($logD_{pH\ 7.4}$, n ≥ 6);**D)** PSMA-mediated internalization of [^{177}Lu]Lu-compounds in PSMA$^+$ LNCaP cells (1 h, 37 °C) as percentage of the reference ligand [^{125}I]I-BA-KuE (n = 3). Data depicted for reference compounds in B-D) were previously published by our group (*125*); only AMSEC data were modified by a correction factor explained in **chapter II.8.5.2**.

Although BLC-4 demonstrated slightly better *in vitro* characteristics, further investigations were conducted based on BLC-5. The synthetic route of BLC-5 proofed to be more robust delivering higher conversions during the realization of the spacer moiety and less impurities for final purification resulting in a higher yield (1.2% vs. 5.4%).

On the basis of BLC-5 (Ac-Pro_9), three further spacer moieties with equal chain lengths in respect to the number of atom bonds but with different grades of rigidity (*183,185,186*) and hydrophilicity were tested (BCL-6: Ac-Ser_9; BLC-7: Ac-$(Ser\text{-}Gly\text{-}Gly)_3$; BCL-8: Ac-NH-$PEG_8$-propionyl). Results regarding hydrophilicity and affinity are depicted in **Figure 26**.

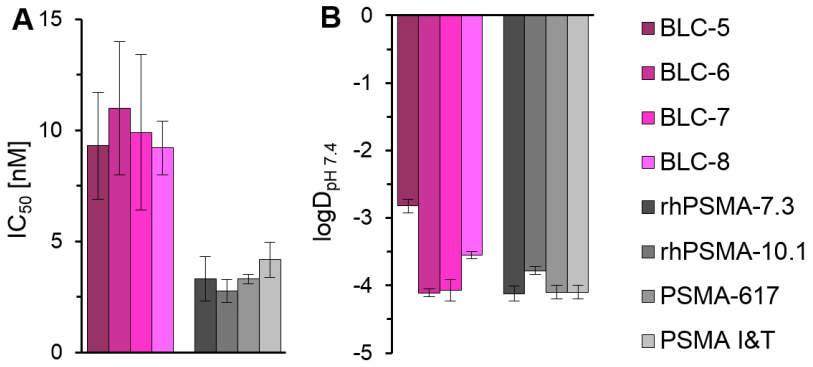

Figure 26: *In vitro* data of branched linker constructs (BLC, pink) and reference ligands (grey), all evaluated as [$^{177/nat}$Lu]Lu-compounds; **A)** affinities (IC_{50} [nM]) determined in a binding assay of ^{nat}Lu-compounds (10^{-10}–10^{-5} M) with [^{125}I]I-BA-KuE (0.2 nM) as competitor on PSMA$^+$ LNCaP cells (1 h, on ice, n = 3); **B)** PSMA-mediated internalization of [^{177}Lu]Lu-compounds in PSMA$^+$ LNCaP cells (1 h, 37 °C) as percentage of the reference ligand [^{125}I]I-BA-KuE (n = 3). Data depicted for reference compounds were previously published by our group (*125*); only AMSEC data were modified by a correction factor explained in **chapter II.8.5.2**.

The determined PSMA affinity for these derivatives was moderate and not significantly influenced by the type of spacer suggesting that the PSMA binding pocket tolerated these modifications at this position in the ligand structure regardless of the linker rigidity or inherent functional groups. Noteworthy, couplings of Fmoc-[L-Ser(OtBu)]$_3$-OH in the synthesis of BLC-6 were incomplete leading to a low overall yield.

As expected, the addition of hydroxyl groups by the installation of the Ser_9- and (Ser-Gly-Gly)$_3$-spacer realized in compounds BLC-6 and -7 led to a remarkable increase of hydrophilicity compared to BLC-5 ($logD_{7.4}$: –4.1 each vs. –2.8). Opposingly, the PEG_8-spacer in compound BLC-8 caused a minor improvement of hydrophilicity (–3.6).

Based on results determined for BLC-1 to -8, branched linker constructs bearing an IPB moiety as an HSA binder (*123*), were investigated. *In vitro* data of the corresponding ligands BLC-9 to -12 are depicted in **Figure 27**.

The substitution of the acetyl group by the IPB moiety showed no significant effect on the affinity. Still, about a 3- to 4-fold increase of the IC_{50} values compared to rhPSMA-7.3 was observed.

The internalization was dramatically affected by the introduction of the IPB moiety with a 3.0-, 4.6- and 10.1-fold lower value opposed to rhPSMA-7.3 for the compounds BLC-9, -11 and -12, respectively. As mentioned above, a strong HSA or BSA binding seemed to drastically decrease the observed internalization value determined in the applied assay with BSA in incubation media (*177*).

Due to the heavily exposed lipophilic IPB moiety, all HSA binder constructs showed a severe decrease in hydrophilicity compared to their acetylated parent compounds as well as opposed to the lead compound rhPSMA-7.3. Although $logD_{7.4}$ values of the acetylated BLC-compounds BLC-5 to -8 were strongly influenced by the functional groups within the spacer, a terminal lipophilic HSA binder seemed to dominate the lipophilicity with only minor effects of the spacer.

As expected, the apparent molecular weight MW_{App}, as a parameter for HSA binding, was clearly increased by the IPB moiety for the derivatives BLC-11 and -12 by a factor of 1.4 and 1.5,

respectively, in comparison to the lead compound. Interestingly, BLC-9 showed a quite similar HSA binding compared with rhPSMA-7.3 in both methods but a 5-fold increased MW_{App} compared to the acetylated analog BLC-5. The HPAC method revealed a comparingly low value for BLC-12 (92.9%). But still, all IPB-derivatives clearly exhibited HSA bindings of >90%.

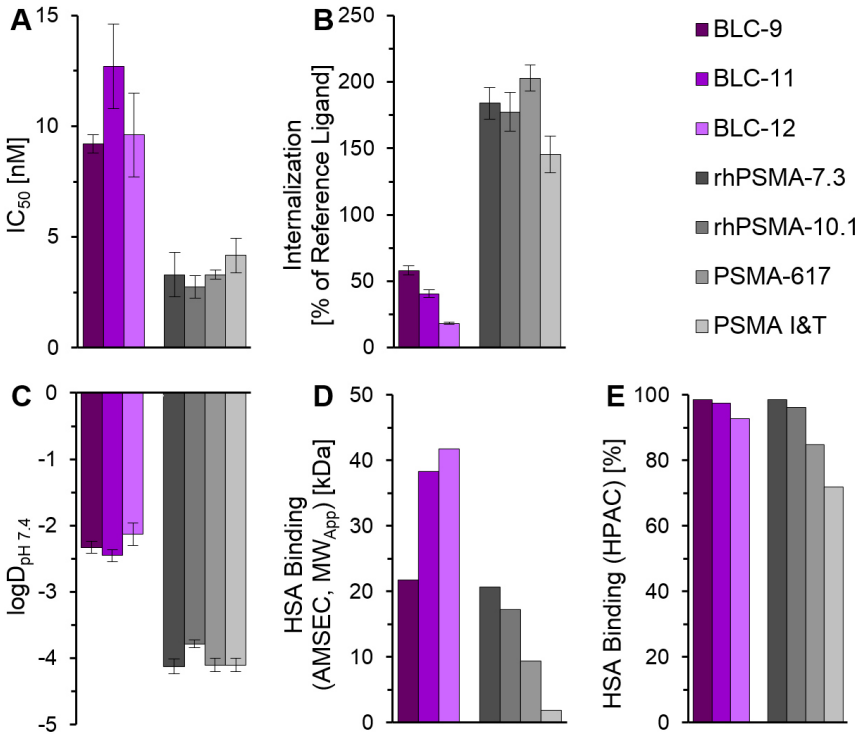

Figure 27: *In vitro* data of BLC-9 to -12 (violet) and reference ligands (grey), all evaluated as [$^{177/nat}$Lu]Lu-compounds; **A)** affinities (IC_{50} [nM]) determined in a binding assay of ^{nat}Lu-compounds (10^{-10}–10^{-5} M) with [^{125}I]I-BA-KuE (0.2 nM) as competitor on PSMA$^+$ LNCaP cells (1 h, on ice, n = 3); **B)** PSMA-mediated internalization of [^{177}Lu]Lu-compounds in PSMA$^+$ LNCaP cells (1 h, 37 °C) as percentage of the reference ligand [^{125}I]I-BA-KuE (n = 3); **C)** lipophilicity of [^{177}Lu]Lu-compounds expressed as *n*-octanol/PBS partition coefficient ($logD_{pH\ 7.4}$, n ≥ 6); **D)** apparent molecular weight (MW_{App}) of [^{177}Lu]Lu-compounds determined by human serum albumin-mediated size exclusion chromatography (AMSEC); **E)** human serum albumin binding of ^{nat}Lu-compounds determined on a Chiralpak HSA column. Data depicted for reference compounds in A–D) were previously published by our group (*125*); only AMSEC data were modified by a correction factor explained in **chapter II.8.5.2**.

In conclusion, high HSA binding was observed for compounds with flexible spacers while the rigid proline-based linker significantly decreased HSA binding and could serve in principle as a structural platform for ligands with fine-tuned HSA binding from this perspective. However, general problems of these branched linker constructs were an overelaborated synthesis with difficulties corresponding to incomplete coupling steps, moderate affinity and a high lipophilicity due to the strongly exposed HSA binder. A replacement of the IPB moiety by a different, more hydrophilic HSA binder to reduce the $logD_{7.4}$ values seemed difficult as HSA is known to bind predominantly lipophilic aromatic entities (*178,179*).

Throughout the investigations regarding HSA binding modulation within this work and critical literature analysis it became evident that a heavily prolonged blood retention by increasing HSA binding mostly resulted in inferior tumor-to-background ratios (*121,122,144-147,181*). Importantly, blood retention of radioactive compounds can be a dose-limiting factor considering

hematotoxic effects (*187*). Moreover, eventual long-term effects by radiation exposure of the kidneys as main excretion organ have to be taken into account (*161,162*). These findings level out an optional increased absolute tumor uptake. In parallel to this project, our group investigated the [^{177}Lu]Lu-rhPSMA-7 and -10 isomers which already revealed significant differences in HSA binding just by alterations of the structural vicinity surrounding the SiFA moiety. Moreover, these data suggested that even rhPSMA-7.3 possessed suboptimal slow pharmacokinetics and tumor-to-organ ratios could be improved by a reduction of HSA binding *(125)*.

Thus, the aim of the following work was shifted to a reduction of HSA binding. Noticing, that the SiFA moiety itself already represented an HSA binder with an HSA affinity in a useful range, additional attachments of HSA binding moieties were avoided as far as possible, and the concept of branched linker constructs was discarded.

3. Evaluation of Ligands with Reduced Net Charge (RNC)

3.1. Background and Design of RNC Ligands (1st Generation)

Accumulation and retention of PSMA ligands in the kidneys are a product of several parameters. High hydrophilicity is commonly accepted as a discriminator for a mainly renal excretion route. Consequently, most PSMA ligands are predominantly excreted by the kidney. Moreover, the respective area under the curve is dependent on blood clearance and thus, HSA binding as partly described in **chapter III.2**.

Another parameter linked to kidney retention is tubular reabsorption. For a variety of peptides reabsorption mechanisms related to molecular charge seem to play a role. It could be shown in animals and patients that an application of basic, positively charged amino acid solutions containing either lysine or arginine contribute to a significantly lower kidney retention of antibody fragments (*188-190*). This concept could be transferred successfully on the application of positively charged somatostatin receptor ligands [^{90}Y]Y-DOTATOC and [^{111}In][In-DTPA^{0}]octreotide and is also recommended for the application of the FDA-approved [^{177}Lu]Lu-DOTA-TATE (*191-193*). For the negatively charged, Glu-rich peptide [^{111}In]In-DTPA-D-Glu^{1}-minigastrin a similar approach was investigated in mice. After pre-injection of polyglutamic acid a reduction of up to >80% of the accumulated activity in the kidneys 4 h p.i. was observed (*194*).

One well-known candidate responsible for tubular reabsorption of many ligands is the scavenger receptor megalin (*195,196*). *Vegt* and *Melis et al*. could demonstrate for their choice of peptide-based ligands comprising of [^{111}In]In-octreotide, -octreotate, -exendin, -minigastrin and -neurotensin a megalin-mediated kidney uptake. In comparison with wild-type mice, a reduction of renal activity accumulation in megalin-deficient mice to a proportion between 22% and 65% was found in well accordance with previous results of *de Jong et al*. (*148,149*). In the case of PSMA ligands, a significant proportion of the reabsorption is target-mediated as PSMA is found to be expressed in healthy proximal tubules (*44*). Therefore, activity accumulation can be blocked by co-injection of cold PSMA ligands or even monosodium glutamate at the cost of a decreased tumor uptake (*197,198*).

To modify a ligand's inherent reabsorption behavior another approach seems promising. As implied above, several examples indicate molecular charge as a key parameter for tubular reabsorption of a compound albeit it is important to have in mind that repositioning or omission of charged groups is also likely to affect further parameters such as hydrophilicity or HSA binding. Thus, not surprisingly diverging results are found in literature. On the one hand, for instance, a series of modified [^{99m}Tc]Tc-chelators attached to the same affibody or the comparison of various analogs of the α-melanocyte-stimulating hormone (α-MSH) supported the impression of reduced kidney uptake as a result of a reduced net charge (*199,200*). On the other hand, a pharmacokinetic improvement of [^{68}Ga]Ga-PSMA-11 by the insertion of zwitterionic spacers was reported (*201*).

Findings of *Pomper et al.* promoted the hypothesis of decreased tubular reabsorption by a reduced net charge. They investigated the DOTA-bearing PSMA ligand [^{125}I]VK-02-90 once with the free chelator and once more as the respective ^{nat}Lu-chelate. While the blood clearance turned out to be similar, the kidney clearance of the ^{nat}Lu-chelate was significantly improved with a more than 9-fold lower activity accumulation at 24 h post injection. A similar, even though less accentuated pattern was observed for the respective pair of [^{125}I]VK-03-03 and its ^{nat}Lu-chelate within the same publication (*150*). Another example is presented by the aforementioned comparison of PSMA-ALB-05 and -07 distinguished by an Asp_2- or Asp_3-linker (AUC_{kidney}: 1837 vs. 3395) (*145*).

Based on the literature-driven hypothesis that reduced net charge (NC) could be related with a ligand's decreased tubular reabsorption, the omission and alteration of non-required carboxylic acids within the rhPSMA-7.3 scaffold were investigated and results are herein described. The scaffold obtains nine carboxylic acids of which three positions were assumed to be non-essential for neither nanomolar target affinity nor (radio)metal chelation as indicated by the supposed positioning within the binding cavity of PSMA (**Figure 28**).

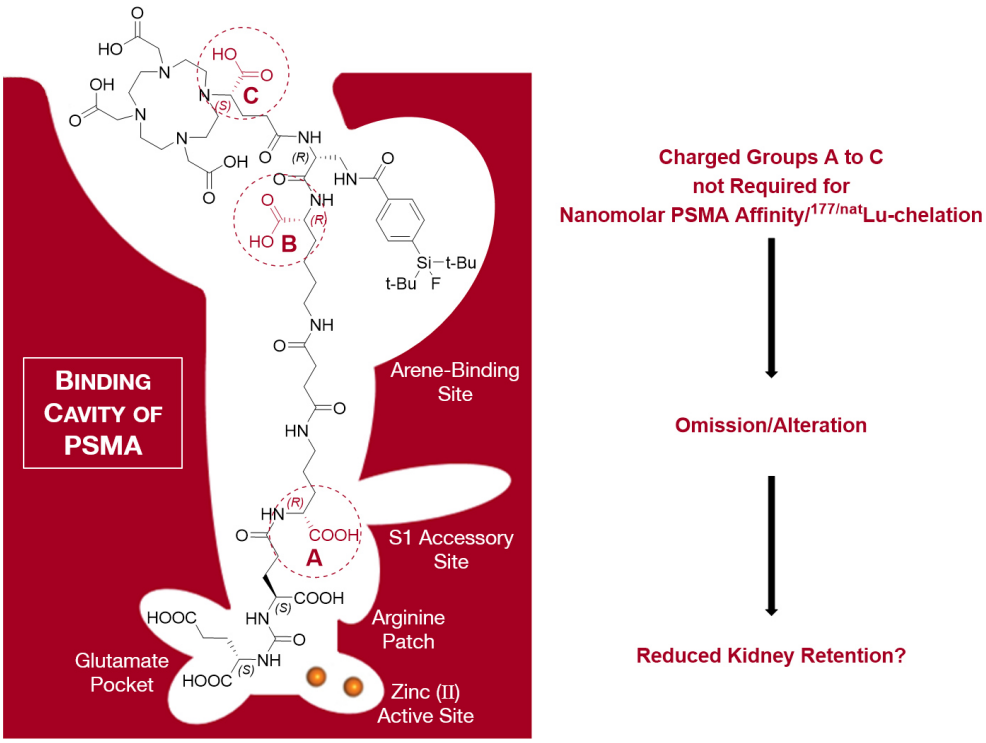

Figure 28: Illustration of the supposed positioning of rhPSMA-7.3 in the schematic binding cavity of PSMA comprising of the glutamate pocket, zinc (II) active site (zinc ions in orange), arginine patch, S1 accessory site and arene-binding site adapted from *Kopka et al.* (*71*). PSMA ligands with reduced net charge (RNC) within this chapter are modified by omission or alteration of the carboxylic acids A to C aiming for reduced kidney retention.

As depicted, the carboxylic acids of the EuE binding motif are required for the attractive interactions with the glutamate pocket and the arginine patch (*36,65*). Charge reduction might be accomplished in position A by implementing a KuE binding motif similar to established therapeutic agents as PSMA-617 and PSMA-I&T (*98,99*). The latter comprises a suberic acid linker attached

to KuE. However, this linker structure was also implemented by *Wurzer et al.* in Ga-rhPSMA-6. For this radiohybrid compound a decrease to a minor extent for PSMA affinity but in particular for internalization was determined compared to Ga-rhPSMA-7 (*126*). These results as well as affinity values observed for a series of [^{99m}Tc]Tc-PSMA ligands published by *Hillier et al.* indicated that carboxylic acid A might also contribute to an attractive interaction with the arginine patch (*202*).

To maintain a high PSMA affinity and favorable internalization behavior while omitting the charge in position A, the use of the Txa-L-2-Nal-KuE sequence, already optimized for the PSMA-617 scaffold (*203*), was investigated in combination with the radiohybrid unit comprised of the (4-SiFA)Bz- and a chelating moiety. This attempt aimed for a radiohybrid tracer possessing the beneficial pharmacokinetic properties of [^{177}Lu]Lu-PSMA-617 showing a fast whole-body clearance and especially renal clearance in mice with a high and well-retained tumor accumulation (*98*). Furthermore, comparing clinical results with [^{177}Lu]Lu-PSMA I&T, the lower net charge-bearing [^{177}Lu]Lu-PSMA-617 also displayed a lower kidney retention although a slower blood clearance was observed (*204*).

But this approach not only promises to decrease the net charge and thus possibly improve renal retention. The combinatorial use of an L-2-Nal-based linker and the SiFA moiety in a suitable distancing might enable the targeting of both prominent hydrophobic pockets within the PSMA binding cavity, namely the S1 accessory site and the remote arene-binding site (*47,69,71*). This could result in an improved PSMA affinity with concomitant superior tumor uptake.

Figure 29 depicts the first generation of rhPSMA ligands RNC-1 to -4 comprised of the PSMA-617's expanded binding motif and the radiohybrid unit of rhPSMA-7.3 directly attached or *via* different spacers X to optimize for target affinity (spacer length) as well as hydrophilicity (carboxylic acid/polyether). Furthermore, the PEG-spacer was inserted to investigate the assumption of a reduced tubular reabsorption of 'larger linkers' by *Kelly et al* (*144*).

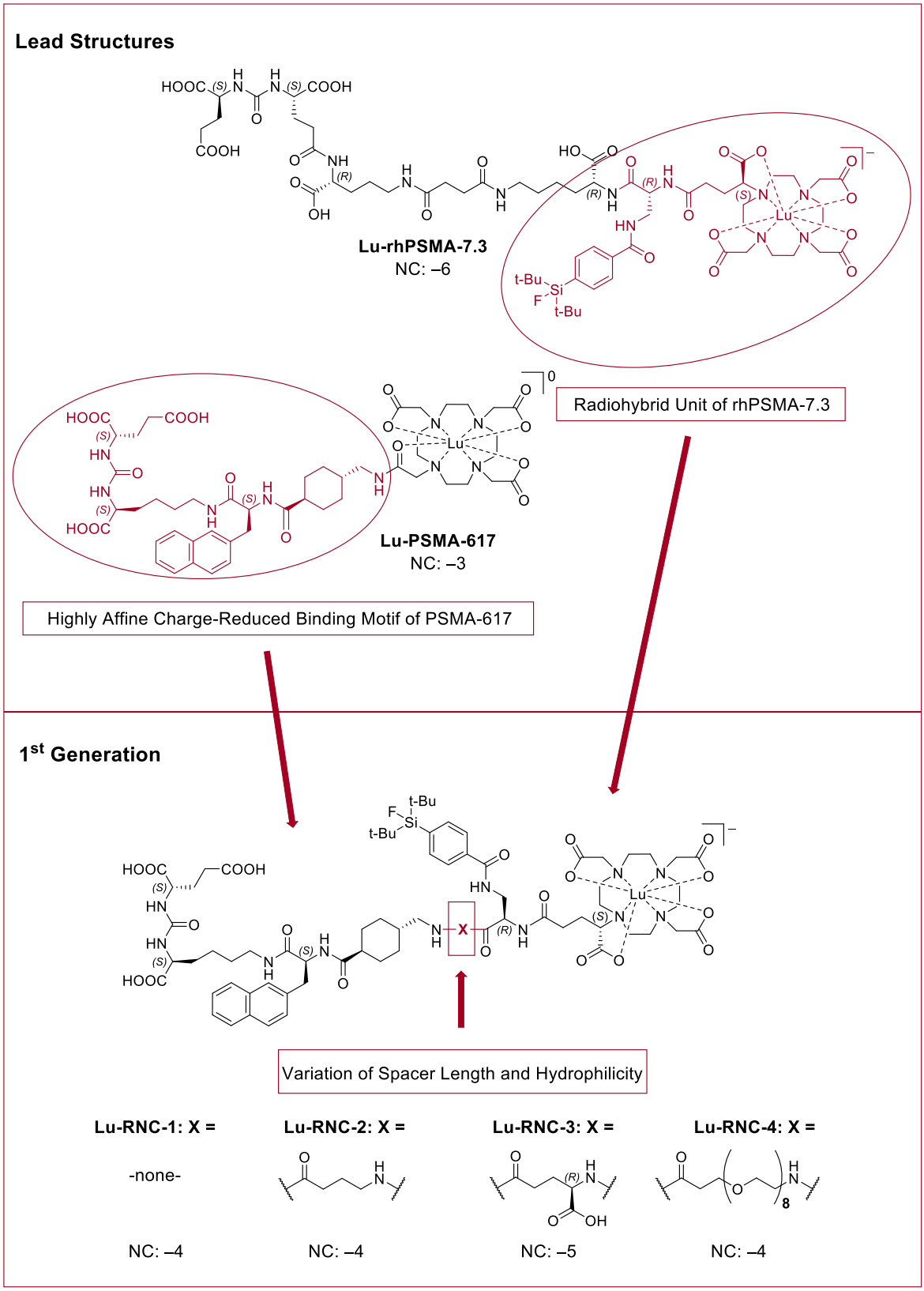

Figure 29: Structures of the first generation of ligands with reduced net charge (RNC) derived from the reference structures rhPSMA-7.3 and PSMA-617 depicted with the net charge (NC) under physiological pH conditions.

3.2. *In Vitro* Evaluation of RNC Ligands (1st Generation)

In vitro data of the compounds RNC-1 to -4 are shown in **Figure 30**. Despite expectations of increased affinity, derivative RNC-1 and to a lower extend derivatives RNC-2 and RNC-3 exhibited a loss of affinity with IC_{50}-values of 62 ± 8.3, 30 ± 12 and 17 ± 2.7 nM, respectively. Driven by the hypothesis that the sterically demanding L-2-Nal forces the spacer to sidestep and thus, resulting in steric repulsion of the SiFA moiety in the entrance funnel instead of attractive interactions with the arene-binding site, a longer PEG-spacer was used in derivative RNC-4. Indeed, compared to the shorter analogs RNC-1 to -3 the affinity of RNC-4 was increased to a value of 8.1 ± 0.9 nM. Unfortunately, in respect to the reference compounds no gain in affinity could be achieved. Additionally, internalization was drastically decreased for derivatives RNC-2 to -4 with values ranging from ~10 to 22% relative to PSMA-617. Again, these data might be obscured by the compounds' serum albumin binding (*177*).

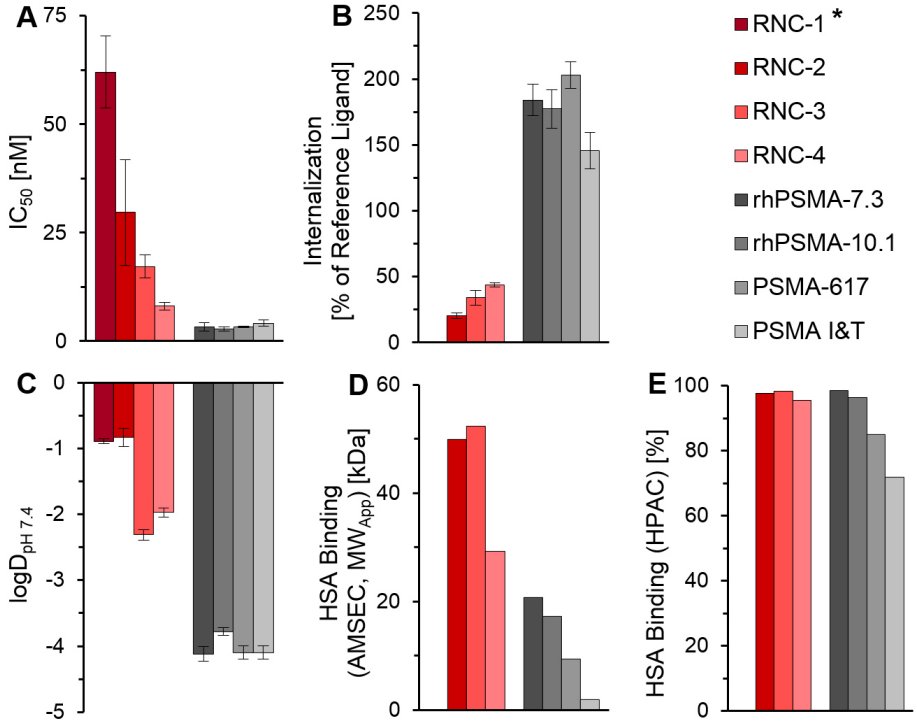

Figure 30: *In vitro* data of RNC-1 to -4 (red) and reference ligands (grey), all evaluated as [$^{177/nat}$Lu]Lu-compounds; **A)** affinities (IC_{50} [nM]) determined in a binding assay of ^{nat}Lu-compounds (10^{-10}–10^{-5} M) with [^{125}I]I-BA-KuE (0.2 nM) as competitor on PSMA$^+$ LNCaP cells (1 h, on ice, n = 3); **B)** PSMA-mediated internalization of [^{177}Lu]Lu-compounds in PSMA$^+$ LNCaP cells (1 h, 37 °C) as percentage of the reference ligand [^{125}I]I-BA-KuE (n = 3); **C)** lipophilicity of [^{177}Lu]Lu-compounds expressed as *n*-octanol/PBS partition coefficient ($logD_{pH\ 7.4}$, n ≥ 6); **D)** apparent molecular weight (MW_{App}) of [^{177}Lu]Lu-compounds determined by human serum albumin-mediated size exclusion chromatography (AMSEC); **E)** human serum albumin binding of ^{nat}Lu-compounds determined on a Chiralpak HSA column. *Internalization and HSA binding were not determined for RNC-1. Data depicted for reference compounds in A–D) were previously published by our group (*125*); only AMSEC data were modified by a correction factor explained in **chapter II.8.5.2**.

Obviously, the use of the two bulky, lipophilic building blocks L-2-Nal and (4-SiFA)Bz in one ligand had a great impact on the hydrophilicity. Determined $logD_{7.4}$ values were about three logarithmic units more lipophilic for RNC-1 and -2 in respect to the references. The attempt of compensation

by one more carboxylic acid (RNC-3) or a PEG-spacer (RNC-4) led only to a partial recovery of hydrophilicity with still about two logarithmic units mor lipophilic than the references.

The MW_{App} was heavily increased for RNC-2 in respect to PSMA-617 and also rhPSMA-7.3 demonstrating that both aromatic systems, *L*-2-Nal and (4-SiFA)Bz, were bearing a certain affinity to HSA and the binding coud be even strengthened combining both moieties within one molecule. Noteworthy, the MW_{App} was even slightly more increased for RNC-3 by placing a carboxylic acid in between these two moieties. This finding was in accordance with the reported structure of the suspected, addressed HSA binding site II (Sudlow II) with two inherent positively charged amino acids, namely R410 and K414 (*178*). Avoiding this additional carboxylic acid and placing the two aromatic moieties further apart by a moderately hydrophilic PEG-spacer in derivative RNC-4 ended up with a MW_{App} significantly closer to the reference value of rhPSMA-7.3 (29.9 kDa vs. 21.6 kDa) and even lower comparing these both compounds by values determined with HPAC.

3.3. Biodistribution of an RNC Ligand (1st Generation)

Despite the lower PSMA affinity, the effect of a reduced net charge as well as a potentially positive effect of the PEG-spacer on renal clearance were investigated *in vivo* by a biodistri-bution study at 24 h p.i. with compound RNC-4. An inferior tumor uptake compared to rhPSMA-7.3 and -10.1 is visualized in respective µSPECT/CT images shown in **Figure 31**. The moderate kidney uptake of RNC-4 was ranked between the two radiohybrid references.

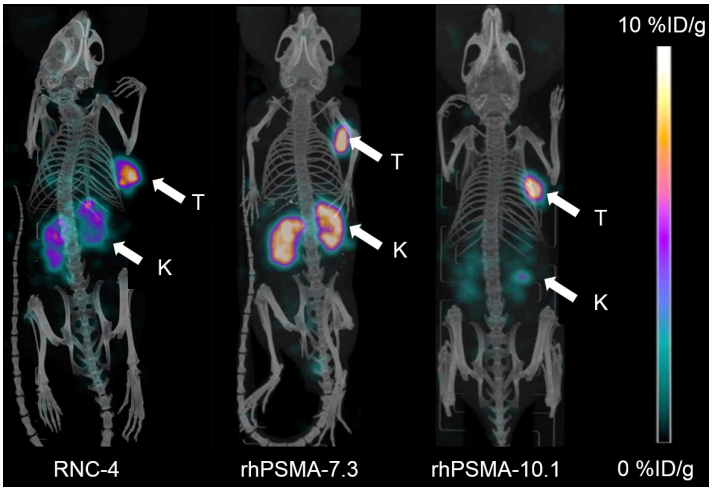

Figure 31: Static µSPECT/CT images (maximum intensity projections) of RNC-4, rhPSMA7.3 and rhPSMA-10.1 as ^{177}Lu-labeled compounds in LNCaP I tumor-bearing CB-17 SCID mice. Tumors (T) and kidneys (K) are indicated by white arrows. Mice were sacrificed 24 h p.i. and imaged directly after blood collection by cardiac puncture. Images of rhPSMA-7.3 and -10.1 depicted as reference were previously published by our group (*125*).

Biodistribution data in comparison with the reference compounds are shown in **Figure 32**. As expected, compared to rhPSMA-7.3 the kidney uptake was ~1.5-fold reduced, albeit the difference seemed irrelevant due to standard deviation. Unfortunately, the tumor uptake was also decreased by a factor of ~1.7 resulting in a nearly identical tumor-to-kidney ratio (1.27 vs 1.24).

Apparently, the tumor-targeting potential was diminished by the worse affinity and internalization behavior limiting tumor accumulation despite the drastically enhanced input function.

Obviously, as a consequence of the increased HSA binding the whole-body clearance was markedly decelerated ending up with a tumor-to-blood ratio of 13.8 ± 2.3 for RNC-4 vs. 3843 ± 1145 for rhPSMA-7.3 and 1423 ± 455 for PSMA-617.

Furthermore, the high lipophilicity was accompanied by a raised proportion of hepatobiliary excretion compared to rhPSMA-7.3 manifested in increased uptakes in liver (0.74 ± 0.12 %ID/g vs. 0.22 ± 0.04 %ID/g) and intestines (0.41 ± 0.27 %ID/g vs. 0.13 ± 0.08 %ID/g). Consequently, RNC-4 also exhibited the lowest tumor-to-liver ratio of 9.3 ± 1.3.

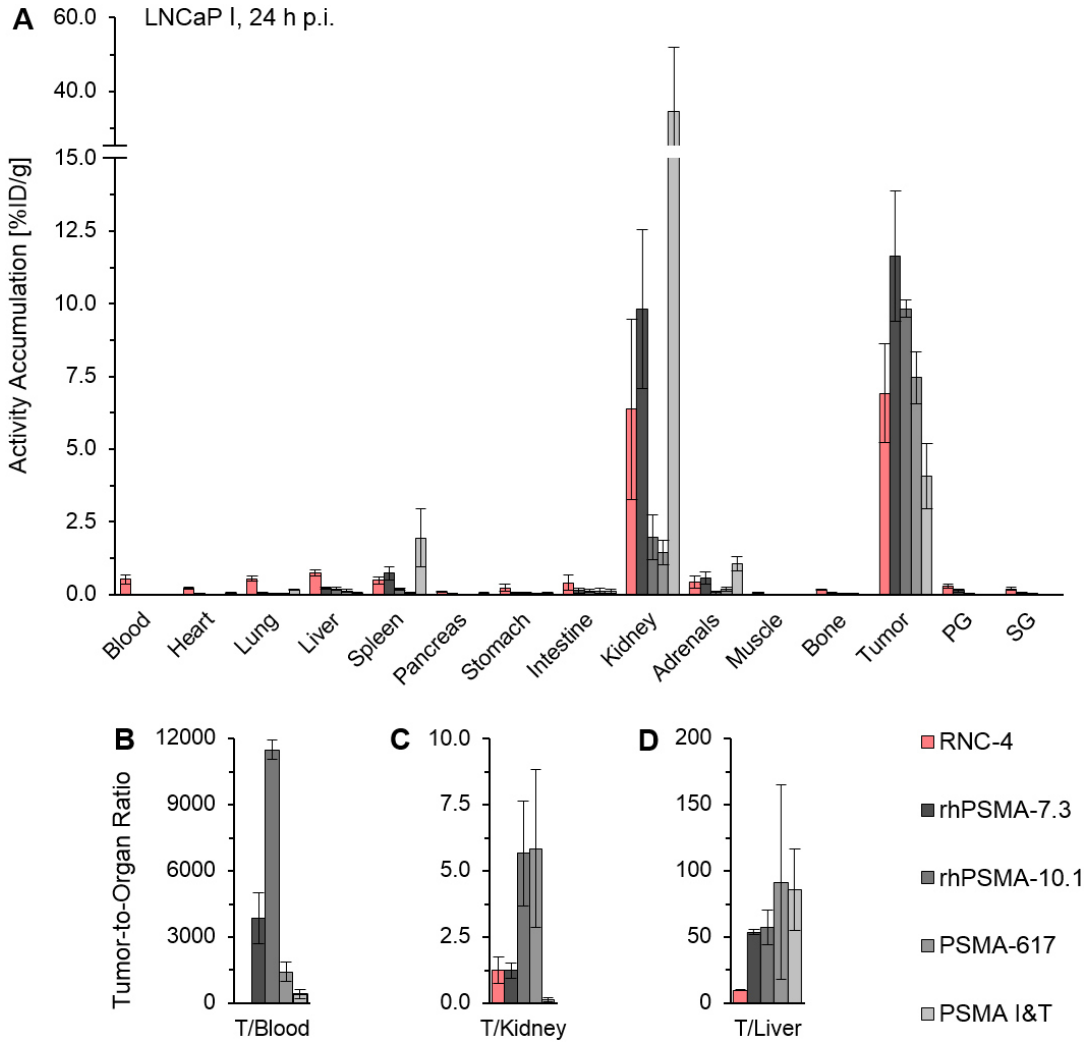

Figure 32: A) *Ex vivo* biodistribution of RNC-4 (n = 5) and the reference ligands rhPSMA-7.3 (n = 4), rhPSMA-10.1 (n = 5), PSMA-617 (n = 4) and PSMA I&T (n = 4) as [^{177}Lu]Lu-compounds at 24 h p.i. in male LNCaP I tumor-bearing CB17-SCID mice; PG = parotid glands, SG = submandibular glands; data expressed as percentage of the injected dose per gram (%ID/g) and mean ± standard deviation; **B–D)** tumor-to-organ ratios (tumor-to-blood/-kidney/-liver) calculated individually for each mouse and expressed as mean ± standard deviation. Data of reference ligands were previously published by our group (*125,160*).

In conclusion, the idea of charge reduction in position A in combination with addressing the S1 accessory site by a lipophilic aromatic moiety like a naphthyl residue was refused. *In vivo* data

demonstrated a clear disadvantage of such a loss in hydrophilicity as well as in the raise of HSA binding.

3.4. Extended Concept and Design of RNC Ligands (2nd Generation)

As radiohybrid ligands RNC-1 to -4 drastically suffered from lipophilicity and strong HSA binding induced by the L-2-Nal-modification in position A, a series of RNC ligands with a modified approach was investigated. The hydrophilic D-Orn-EuE binding motif was conserved, and the focus was shifted to modifications in position B and C. These positions were located in structural vicinity to the HSA binding SiFA moiety and their modification regarding reduced net charge was also aiming for fine-tuned HSA binding.

For a better understanding how affinity towards HSA can be modulated, the main binding sites are briefly described in the following. Drug binding sites I and II, also known as Sudlow's site I and II, are characterized for the binding of aromatic moieties. While both binding sites appear to form mainly hydrophobic pockets with polar patches containing positively charged amino acids or proton donors, they are distinguishable by size (site I > site II) and number of polar patches (site I: 2; site II: 1). Thus, structurally bulkier drugs like warfarin with more than one aromatic entity and/or two or more electron-donating groups in a defined distance preferably bind to site I. On the other hand, drugs like ibuprofen with only one aromatic entity and one electron-donating group tend to bind more efficiently to site II (*178*).

These facts are well reflected by the publication of *Deberle et al.* introducing ibuprofen as HSA binding moiety to the PSMA-617 scaffold. At the attachment point of ibuprofen three different amino acids of same size were inserted in between to investigate the pharmacokinetic influence of a negatively (L^-), neutrally (L^0) or positively (L^+) charged amino acid in proximity to the ibuprofen entity. *In vitro* results displayed the expected trend for plasma protein binding in human as well as murine plasma ($L^- > L^0 > L^+$). Surprisingly, whereas the AUC (0–192 h) values in blood differed only slightly (144 ± 10 vs. 143 ± 15 vs. 129 ± 8 for L^-, L^0 and L^+, respectively), differences in the kidneys were more pronounced (1211 ± 61 vs. 868 ± 91 vs. 652 ± 29 for L^-, L^0 and L^+, respectively) underlining the hypothesis of reduced tubular reabsorption by a reduced net charge (*146*).

Assuming a similar binding mode for the SiFA moiety as for the ibuprofen entity, this concept was applied on the rhPSMA-7.3 scaffold resulting in the second generation of RNC ligands (**Figure 33**). While carboxylic acid B of the lead compound was omitted in RNC-5, it was substituted by an aminomethyl group to yield RNC-6. Lastly, for derivative RNC-7 the carboxylic acid in position C was omitted using DOTA instead of DOTAGA in addition of the aminomethyl substituent in position B.

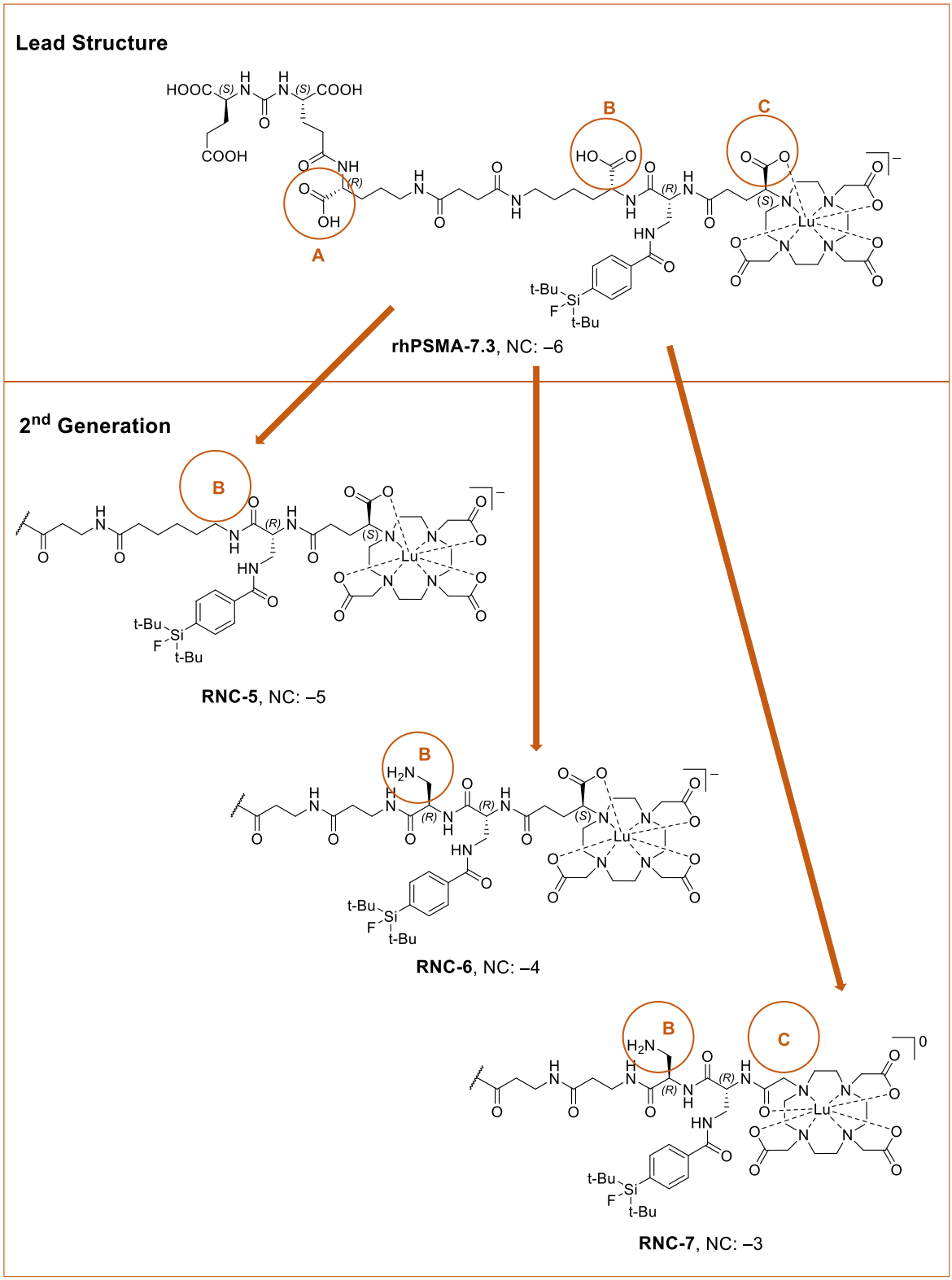

Figure 33: Structures of the second generation of ligands with reduced net charge (RNC) derived from the reference compound rhPSMA-7.3 depicted with the net charge (NC) under physiological pH conditions.

3.5. *In Vitro* Evaluation of RNC Ligands (2nd Generation)

In **Figure 34**, *in vitro* data of derivatives RNC-5 to -7 and data of the reference compounds are depicted. IC_{50} values revealed a trend of a slight decreased affinity with a less negative net charge but still in a nanomolar range (4.9–7.5 nM). This finding most probably correlates with the composition of the remote arene-binding site comprised of the positively charged amino acids R463, R511 and W541 (*69*). Therefore, the absence of carboxylic acid B or the substitution with an even positively charged aminomethyl group and the further optional omission of carboxylic acid C was likely to weaken the attractive interaction of the SiFA moiety with the arene-binding site.

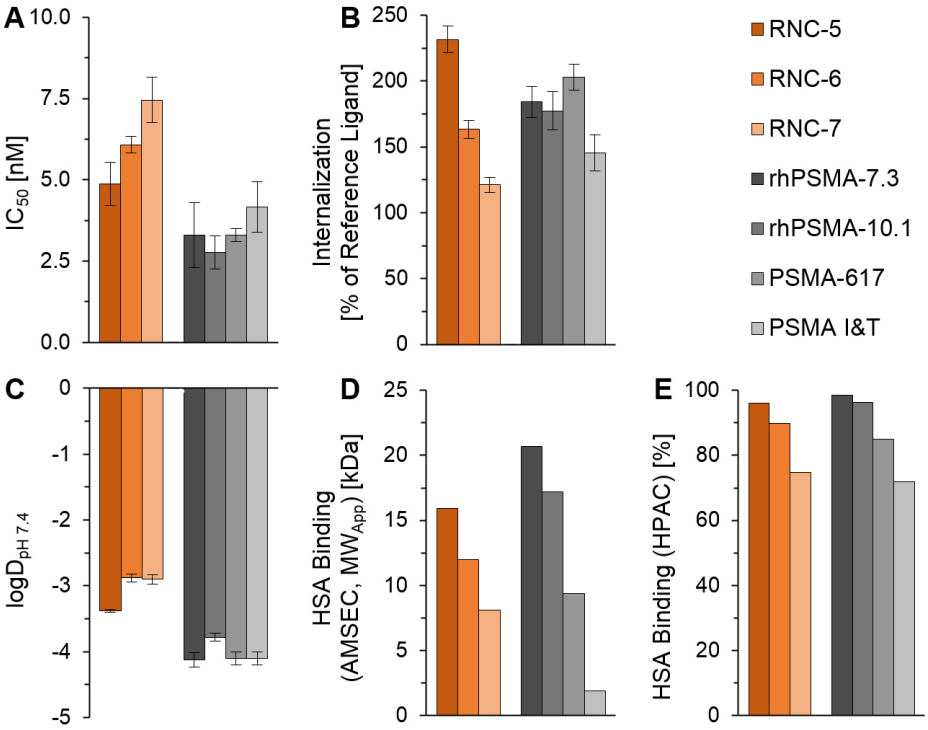

Figure 34: *In vitro* data of RNC-5 to -7 (orange) and reference ligands (grey), all evaluated as [$^{177/nat}$Lu]Lu-compounds; **A)** affinities (IC_{50} [nM]) determined in a binding assay of ^{nat}Lu-compounds (10^{-10}–10^{-5} M) with [^{125}I]I-BA-KuE (0.2 nM) as competitor on PSMA$^+$ LNCaP cells (1 h, on ice, n = 3); **B)** PSMA-mediated internalization of [^{177}Lu]Lu-compounds in PSMA$^+$ LNCaP cells (1 h, 37 °C) as percentage of the reference ligand [^{125}I]I-BA-KuE (n = 3); **C)** lipophilicity of [^{177}Lu]Lu-compounds expressed as *n*-octanol/PBS partition coefficient ($logD_{pH\ 7.4}$, n ≥ 6); **D)** apparent molecular weight (MW_{App}) of [^{177}Lu]Lu-compounds determined by human serum albumin-mediated size exclusion chromatography (AMSEC); **E)** human serum albumin binding of ^{nat}Lu-compounds determined on a Chiralpak HSA column. Data depicted for reference compounds in A–D) were previously published by our group (*125*); only AMSEC data were modified by a correction factor explained in **chapter II.8.5.2**.

Surprisingly, the internalization into LNCaP cells of RNC-5 exceeded the values of the reference compounds (232 ± 10% of I-BA-KuE vs. 145 ± 14% of I-BA-KuE for PSMA I&T to 203 ± 10% of I-BA-KuE for PSMA-617) while the trend within the RNC-series followed the decreased affinity (163 ± 6.9 and 121 ± 6.0% of I-BA-KuE for RNC-6 and -7, respectively).

Regarding carboxylic acids B and C, RNC-5 and rhPSMA-10.1 built a pair of ligands with the same number of charged groups and the same net charge but with an altered placement of carboxylic acids. However, the placement of the lipophilic SiFA moiety surrounded by acid B and DOTA

(rhPSMA-10.1: $logD_{pH7.4}$ = –3.78 ± 0.06) proofed to be more efficient in retaining hydrophilicity than shifting the charged group from position B into the chelator in form of DOTAGA (RNC-5: $logD_{pH7.4}$ = –3.38 ± 0.02). The reduction of net charge by the alteration of acid B to an aminomethyl group was accompanied by a further loss in hydrophilicity (RNC-6: $logD_{pH7.4}$ = –2.88 ± 0.06) and remained equal by an additional substitution of the chelator (RNC-7: $logD_{pH7.4}$ = –2.90 ± 0.07). The impression was driven that a balanced placement of hydrophilic groups within one compound could serve for a higher hydrophilicity than the pure number of charged groups.

As predicted, based on the results of *Deberle et al.*, the HSA binding could be clearly lowered in this series of RNC ligands. Each step of omitting an electron-donor (carboxylic acid) or replacing an electron-donor by an electron-acceptor (amine) in proximity to the SiFA moiety was followed by a weakened HSA binding observed in both methods. RNC-7 exhibited an even lower HSA binding in respect to PSMA-617 (8.1 kDa and 74.8% vs. 9.4 kDa and 84.9%).

3.6. Biodistribution of RNC Ligands (2nd Generation)

In the following, three different reference datasets are depicted as it became evident that the three different LNCaP cell passages used for inoculation within *in vivo* experiments during the course of this thesis resulted in clearly deviating tumor uptakes between the respective groups of mice. To allow at least for a limited comparability, for each group one reference compound (rhPSMA-10.1) or more were re-evaluated. Consequently, values within each figure are only depicted for reference compounds determined in mice inoculated with the same LNCaP cell passage as the test substance (indicated as LNCaP I to III, respectively).

In **Figure 35**, biodistribution data of RNC-5 in comparison with rhPSMA-10.1 are depicted, both evaluated in mice inoculated with cell passage LNCaP II.

Both ligands displayed a high tumor uptake of ~16%ID/g. While rhPSMA-10.1 revealed a low kidney accumulation (1.5 ± 0.33%ID/g) in well accordance with the previous dataset (LNCaP I: 2.0 ± 0.78%ID/g), RNC-5 showed an inferior kidney retention (8.4 ± 2.0%ID/g) and a 5.3-fold decreased tumor-to-kidney ratio. This finding is surprising as both ligands share the same net charge only differing in the placement of one carboxylic acid and thus – following the working hypothesis – an equal tubular reabsorption was expected.

One parameter presumably at least partially responsible for the higher kidney value was the prolonged blood retention of RNC-5. Contradictorily to the almost equal HSA binding determined *in vitro* (RNC-5: 15.9 kDa and 96.0% vs. rhPSMA-10.1: 17.2 kDa and 96.3%) a 2.6-fold decreased tumor-to-blood ratio compared with rhPSMA-10.1 was observed. This *in vitro* vs. *in vivo* discrepancy potentially originates from a species-dependent deviating trend of serum albumin binding (human vs. murine). It was previously demonstrated that the determined plasma protein binding can significantly vary depending on the use of human or murine plasma (*145,146*). The

tumor-to-liver ratios appeared to be quite similar indicating a predominantly renal excretion for both ligands.

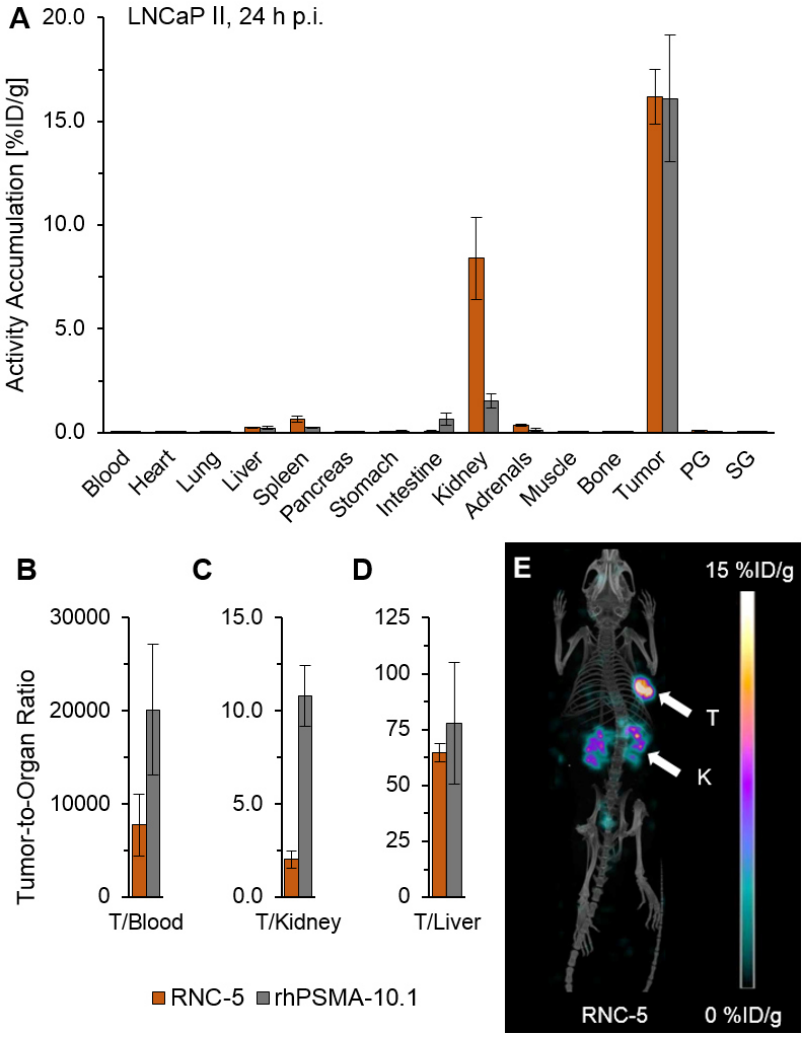

Figure 35: A) *Ex vivo* biodistribution of RNC-5 (n = 4) and the reference ligand rhPSMA-10.1 (n = 4) as [^{177}Lu]Lu-compounds at 24 h p.i. in male LNCaP II tumor-bearing CB17-SCID mice; PG = parotid glands, SG = submandibular glands; data expressed as percentage of the injected dose per gram (%ID/g) and mean ± standard deviation; **B–D)** tumor-to-organ ratios (tumor-to-blood/-kidney/-liver) calculated individually for each mouse and expressed as mean ± standard deviation. **E)** Static µSPECT/CT image (maximum intensity projections) of RNC-5 as ^{177}Lu-labeled compound in a LNCaP II tumor-bearing CB-17 SCID mouse. Tumors (T) and kidneys (K) are indicated by white arrows. The mouse was sacrificed 24 h p.i. and imaged directly after blood collection by cardiac puncture.

Results of the biodistribution of RNC-6 in comparison with the reference compounds are shown in **Figure 36**. In this case, the concept of reduced tubular reabsorption by reduced net charge was applied successfully. A low kidney uptake of only 2.1 ± 0.5%ID/g was observed.

Since the activity accumulation in the tumor stayed unalteredly high (RNC-6: 12 ± 0.75%ID/g vs. rhPSMA-7.3: 12 ± 2.2%ID/g) a superior tumor-to-kidney ratio in respect to rhPSMA-7.3 (5.9 ± 1.3 vs. 1.2 ± 0.3) was achieved. However, this value was comparable to the ratios obtained for rhPSMA-10.1 (5.7 ± 2.0) and PSMA-617 (5.9 ± 3.0).

In relation to the weak HSA binding characterized for RNC-6 the tumor-to-blood ratio was unexpectedly low with a value corresponding to 77% of rhPSMA-7.3 and only 26% of rhPSMA-10.1.

As the uptake values of RNC-6 in liver (1.3- and 5.9-fold) and intestine (1.7- and 1.9-fold) were increased in respect to the references rhPSMA-7.3 and -10.1 and were in well accordance with the reduced hydrophilicity determined *in vitro*, the proportion of hepatobiliary excretion seemed to be slightly raised. This aspect might also contribute to an apparently slower blood clearance because of intestinal reabsorption.

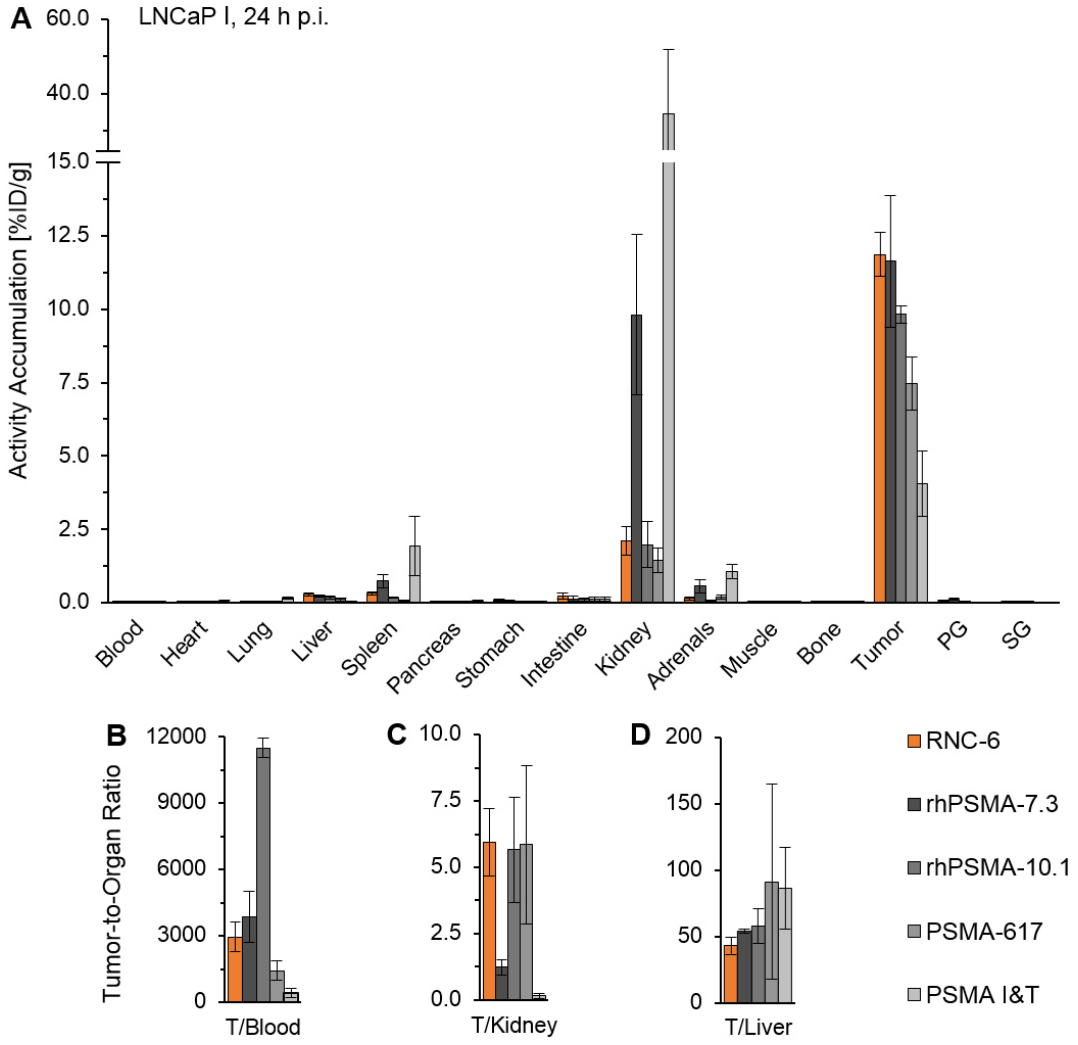

Figure 36: A) *Ex vivo* biodistribution of RNC-6 (n = 4) and the reference ligands rhPSMA-7.3 (n = 4), rhPSMA-10.1 (n = 5), PSMA-617 (n = 4) and PSMA I&T (n = 4) as [^{177}Lu]Lu-compounds at 24 h p.i. in male LNCaP I tumor-bearing CB17-SCID mice; PG = parotid glands, SG = submandibular glands; data expressed as percentage of the injected dose per gram (%ID/g) and mean ± standard deviation; **B–D)** tumor-to-organ ratios (tumor-to-blood/-kidney/-liver) calculated individually for each mouse and expressed as mean ± standard deviation. Data of reference ligands were previously published by our group (*125,160*).

Comparative µSPECT/CT images visualize the significant reduction of kidney retention of RNC-6 opposed to rhPSMA-7.3 to a level similar to rhPSMA-10.1 (**Figure 37**). The equally high tumor uptake compared with rhPSMA-7.3 seemed to be underrated in the image of RNC-6 due to the relatively small tumor size.

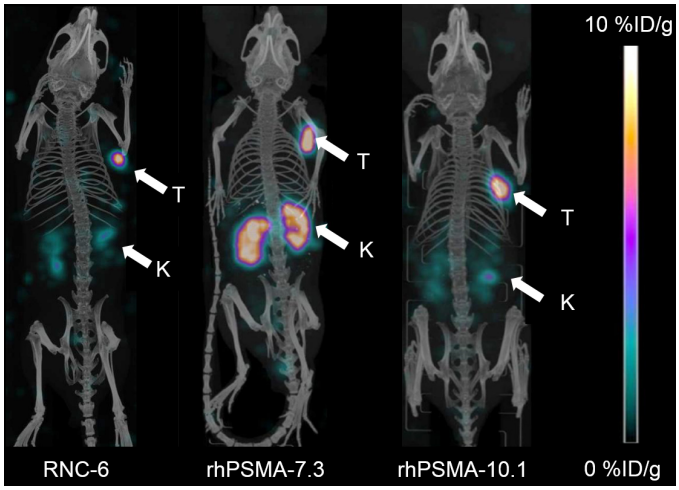

Figure 37: Static µSPECT/CT images (maximum intensity projections) of RNC-6, rhPSMA7.3 and rhPSMA-10.1 as ^{177}Lu-labeled compounds in LNCaP I tumor-bearing CB-17 SCID mice. Tumors (T) and kidneys (K) are indicated by white arrows. Mice were sacrificed 24 h p.i. and imaged directly after blood collection by cardiac puncture. Images of rhPSMA-7.3 and -10.1 depicted as reference were previously published by our group (*125*).

In **Figure 38**, biodistribution data of RNC-7 with the most recent passage of LNCaP cells (LNCaP III) are depicted together with the corresponding re-evaluated references. This new dataset exhibited surprising values, especially for PSMA-617. While the ranking of tumor accumulation between the references stayed unchanged, PSMA-617 revealed a drastically faster whole-body clearance (tumor-to-blood ratios: 16323 ± 3998 in LNCaP III mice vs. 1424 ± 455 in LNCaP I mice vs. 1058 from original publication in LNCaP-bearing BALB/c *nu/nu* mice (*98*)) unexpectedly raising the bar for the remaining candidates.

In comparison with the radiohybrid references, RNC-7 attracted the attention by its fast blood clearance in well accordance with the low *in vitro* HSA binding. This resulted in improved tumor-to-blood ratios (RNC-7: 8430 ± 4118 vs. rhPSMA-7.3: 4256 ± 1030 and rhPSMA-10.1: 6111 ± 1215). Nevertheless, the fast clearance of RNC-7 was accompanied by clearly reduced tumor accumulation (5.2 ± 1.8%ID/g) ending up with a tumor-to-blood ratio surpassed by a factor of 1.9 by the re-determined data of PSMA-617; even though absolute blood values were equal.

Similar as for RNC-6, the positively charged group in the linker of RNC-7 led to a significantly decreased kidney retention (0.89 ± 0.11%ID/g) and a tumor-to-kidney ratio comparable to rhPSMA-10.1 (RCN-7: 6.0 ± 2.3 vs. rhPSMA-10.1: 5.5 ± 1.9). However, within this dataset no compound reached the tumor-to-kidney ratio of PSMA-617 (37 ± 11).

In respect to the reference compounds no increased proportion of hepatobiliary excretion was found as indicated by the uptake values in liver and intestine. The apparently decreased tumor-to-liver ratio rather was a consequence of poor tumor uptake.

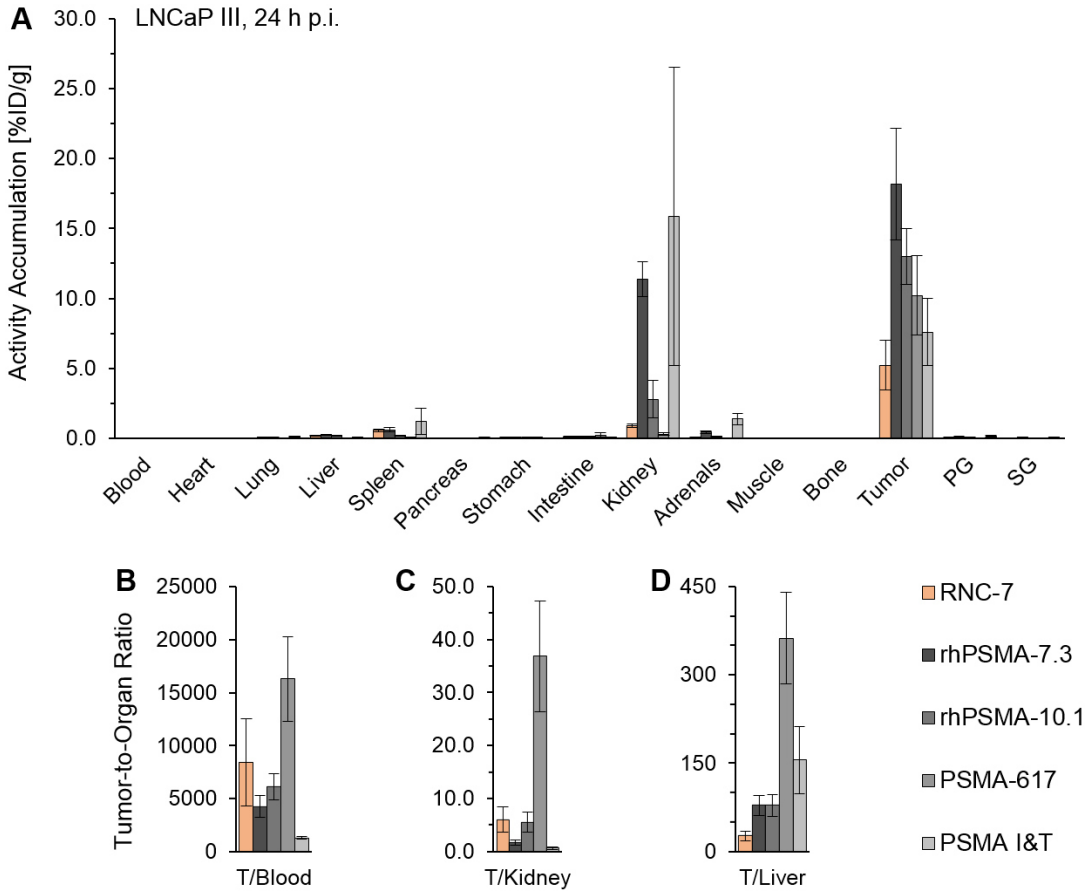

Figure 38: A) *Ex vivo* biodistribution of RNC-7 (n = 5) and the reference ligands rhPSMA-7.3 (n = 5), rhPSMA-10.1 (n = 4), PSMA-617 (n = 5) and PSMA I&T (n = 5) as [^{177}Lu]Lu-compounds at 24 h p.i. in male LNCaP III tumor-bearing CB17-SCID mice; PG = parotid glands, SG = submandibular glands; data expressed as percentage of the injected dose per gram (%ID/g) and mean ± standard deviation; **B–D)** tumor-to-organ ratios (tumor-to-blood/-kidney/-liver) calculated individually for each mouse and expressed as mean ± standard deviation.

In conclusion, the concept of reduced net charge could be translated successfully into decreased kidney retention for ligands bearing a positively charged group in proximity to the SiFA moiety. It was expected to modulate two parameters: 1) reduction of kidney retention by lower net charge and 2) accelerated blood clearance by decreased HSA binding. While the former postulation could be indeed observed *in vivo*, the predicted trend of blood clearance by the *in vitro* values for HSA binding could not be transferred as clearly. Further parameters which might interfere with a precise prediction of blood clearance, were a species-deviant serum albumin binding as well as a concomitant increasing lipophilicity for ligands with a reduced net charge.

Therefore, a novel concept is described in the next chapter investigating a possibility of modifying HSA binding and hydrophilicity of SiFA-bearing ligands with a modular approach.

4. Evaluation of Compounds with Modified SiFA Moieties (MSM)

Passages of this chapter were adopted from a patent application (EP22187845.7; submitted to the European Patent Office; date of receipt: 29.07.2022).

4.1. Motivation and Concept for a Novel SiFA Moiety

In the **chapters III.3.4–III.3.6**, it could be successfully demonstrated that HSA binding can be reduced by the positioning of positive charges in proximity to the SiFA entity. However, the promising trends of *in vitro* data could only partially be translated into beneficial properties in the *in vivo* application. Furthermore, the alteration of charged groups was accompanied by an increase of lipophilicity. Thus, a novel approach to facilitate the modulation of HSA binding as well as hydrophilicity needed to be developed.

As already described in **chapter III.2.1**, *Kuo et al*. could demonstrate a correlation between an increased lipophilicity of the *para*-substituent at 4-phenylbutyric acyl entities used as HSA binder and a prolonged blood retention of the respective PSMA ligands (*181*). Unfortunately, the lipophilic *tert*-butyl groups as well as the phenyl group within the SiFA entity cannot as easily be replaced as their bulkiness is reported to be required for a sufficient steric shielding of the Si–F bond to prevent its hydrolysis (*140*).

Opposingly, the constitutional isomer to the (4-SiFA)Bz entity carrying the silyl group in *meta*- instead of *para*-position revealed a high *in vivo* stability in a protein labeling application (*205*). This finding together with the results of *Dumelin et al.* serve as a valuable hint. Their HSA binder library pointed out that aromatic moieties exhibit strong HSA binding with lipophilic substituents predominantly in *para*-position (*123*). Consequently, an altered substituent pattern at the aromatic moiety within the SiFA entity might decrease HSA binding.

Moreover, a less pronounced exposure or even steric shielding of the SiFA entity might contribute to a modulation of HSA binding. A corresponding is given by a >10-fold increase of the blood AUC value for PSMA-ALB-53 compared with PSMA-ALB-02. The main structural difference between these two derivatives consists in the longer distance between the same HSA binder and the peptide backbone for PSMA-ALB-53 (*145,147*). It is also displayed by the derivatives BLC-9, -11 and -12 within this work that the rigidity of the structural environment of an HSA binding entity within a compound can heavily impact the HSA binding property (**chapter III.2.2**).

Furthermore, the lipophilicity issue of SiFA-bearing compounds should be faced. One successful possibility was published by the synthesis of a positively charged SiFA building block by *Kostikov et al.* and the further implementation in the development of a SiFA*lin*-modified TATE derivative by *Niedermoser et al.* (*141,142*). This approach demonstrated an impressive shift from a (4-SiFA)Bz-modified TATE ligand with long blood retention, poor tumor-to-background ratios and a high proportion of hepatobiliary excretion to a SiFA*lin* derivative with a fast clearance and high contrast on PET/SPECT/CT scans in mice.

Nevertheless, the positively charged SiFA building block leaves some room for further improvements as 1) a reduction of HSA affinity by alteration of the substitution pattern as implied by *Dumelin's* results was not applied yet, 2) the lipophilic silyl substituent in *para*-position is highly exposed whereas HSA binding and hydrophilicity might be modulated by the introduction of further hydrophilic groups in direct vicinity to sterically shield the silyl group, 3) a permanent positive charge within a ligand is not necessarily tolerated by each target regarding structure-activity relationships and might be even counterproductive in terms of hydrophilicity by lowering the net charge (compare **chapter III.3.5**).

To encounter the need of a SiFA entity with improved *in vitro* characteristics, a novel building block was developed by the change of the substitution pattern to provoke steric repulsion with the HSA binding pocket. Additionally, a second carboxylic acid was installed and utilized to efficiently boost the hydrophilicity. Alternatively, this carboxylic acid can act as a conjugation side for further modulators efficiently able to modulate HSA binding and hydrophilicity aided by the structural proximity (**Figure 39**).

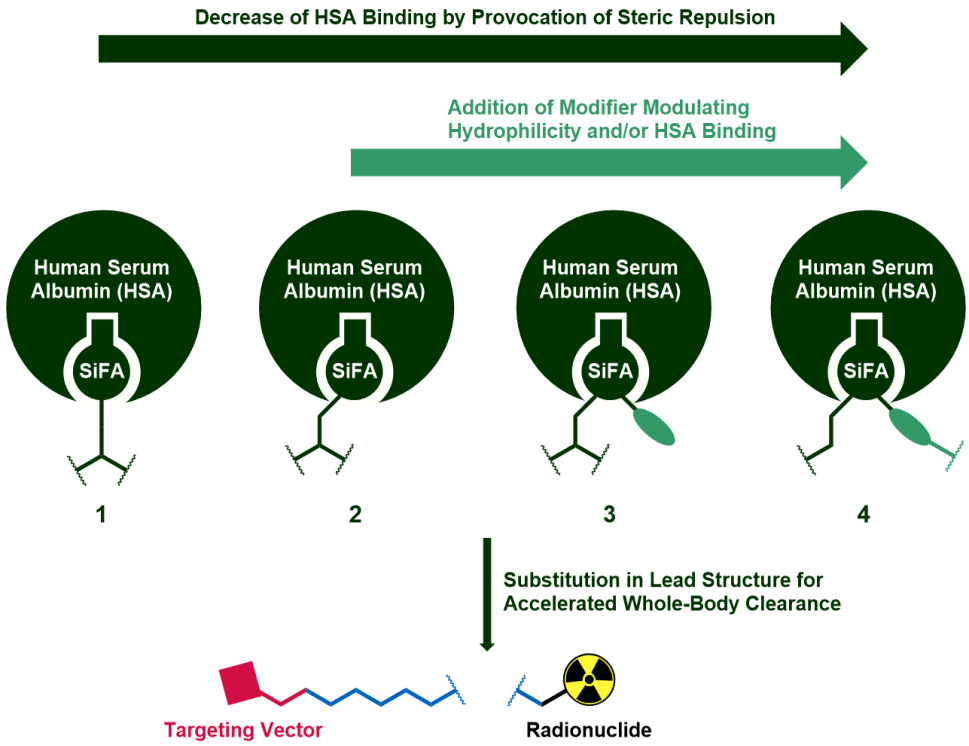

Figure 39: Development steps of a novel SiFA entity as prosthetic group for ^{18}F-labeling with improved readily modulated HSA binding and hydrophilicity characteristics by the change of the substitution pattern (2) and the addition of a hydrophilic group (3) which can be used as a conjugation side for efficient modulators directly attached at the SiFA entity (4).

4.2. Synthesis of SiFA Building Blocks

In **Scheme 6**, three different routes for the synthesis of SiFA benzoic acid derivatives are depicted.

Classical Route A (according to *Wurzer et al.* and *Iovkova et al.* (*126,154*))

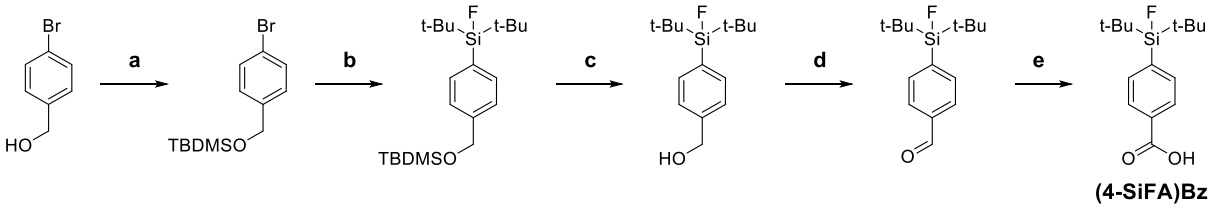

(4-SiFA)Bz

Simplified Classical Route B (this work)

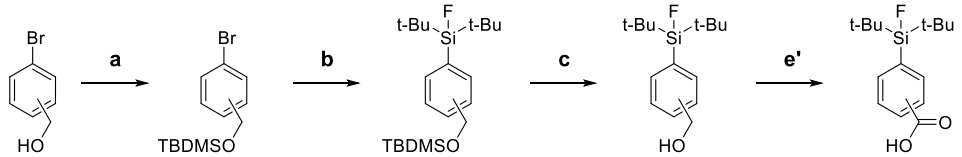

(4-SiFA)Bz/(3-SiFA)Bz

Novel Route C (this work)

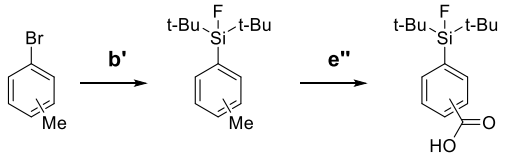

(4-SiFA)Bz/(3-SiFA)Bz

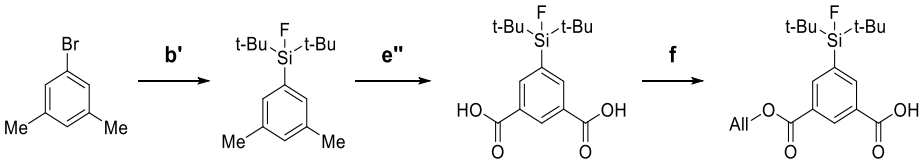

AllO-(5-SiFA)Ip

Scheme 6: Routes for the synthesis of *p*-/*m*-SiFA-benzoic acid [(4-SiFA)Bz/(3-SiFA)Bz] and 3-Allyl-5-SiFA-isophtalic acid [AllO-(5-SiFA)Ip]: a) 1.2 eq. TBDMSCl, 1.2 eq.imidazole, rt, 16 h (DMF); b) 2.4 eq. *t*BuLi, 1.2 eq. tBu$_2$SiF$_2$, –78 °C to rt, overnight (THF); b') 2.2 eq. *t*BuLi, 1.1 eq. tBu$_2$SiF$_2$, –78 °C to rt, overnight (THF);c) HCl, rt, 18 h (MeOH); d) pyridinium chlorochromate, 0 °C to rt, 3 h (DCM); e) 7.0 eq. $KMnO_4$, 0 °C to rt, 2.5 h (DCM/*t*BuOH/NaH_2PO_4·H_2O buffer); e') 3.5 eq. $KMnO_4$, 0 °C to rt, 2.5 h (DCM/*t*BuOH/NaH_2PO_4·H_2O buffer); e'') 6.0 eq./Me group $KMnO_4$, 75 °C reflux, 24 h (DCM/*t*BuOH/NaH_2PO_4·H_2O buffer); f) 0.5 eq. Allyl-Br, 3.0 eq. K_2CO_3, 0 °C to rt, overnight (DMF).

The **Classical Route A** was first published by *Iovkova et al.* and applied later on by *Wurzer et al.* (*126,154*). This route could be simplified by the direct oxidation of *p*-/*m*-SiFA benzyl alcohol **iii** to the corresponding *p*-/*m*-SiFA benzoic acid (**Route B**). The use of toluene or xylene compounds as educts in the **Novel Route C** even allowed for an omission of the protection/deprotection steps required for the respective benzyl alcohols.

Noteworthy, to achieve high conversions for the oxidation of benzylic methyl groups, elevated temperature and a prolonged reaction time were necessary. Overall yields obtained by the various routes are depicted in **Table 3**.

Table 3: Comparison of overall yields obtained for (4-SiFA)Bz, (3-SiFA)Bz and AllO-(5-SiFA)Ip by the use of the classical route (**A**)/simplified classical route (**B**) or the novel route (**C**). *Determined by *Wurzer et al.* (*126*); **determined by *Iovkova et al.* (*154*); n.d. = not determined.

Building Block	(Simplified) Classical Route Overall Yield [%]	Novel Route Overall Yield [%]
(4-SiFA)Bz	51*/80** (**A**), 34 (**B**)	18 (**C**)
(3-SiFA)Bz	27 (**B**)	25 (**C**)
(5-SiFA)Ip/ AllO-(5-SiFA)Ip	n.d.	99/19 (**C**)

Worth mentioning, altered purification steps of the final products yielded *via* **Route C** were required as side products formed which could not be separated by re-crystallization. Thus, RP-HPFC-based purification was applied ending up with comparably low isolated yields probably due to incomplete cartridge elution. Nevertheless, **Route C** offered a convenient strategy with inexpensive starting materials, especially in the case of 5-SiFA isophthalic acid [(5-SiFA)Ip] albeit the purification step is worth to be optimized in interest of higher yields.

4.3. *In Vitro* Evaluation of SiFA MPs

To investigate the structural influence of the novel SiFA building block (5-SiFA)Ip in comparison to the gold-standard (4-SiFA)Bz and the previously published (3-SiFA)Bz entity on labeling properties, stability of the silicone fluoride bond, lipophilicity and HSA binding, each prosthetic group was coupled to three different model peptides (MPs). These three series comprised of the *C*-terminal dipeptides GK, GD and GY to portray determined trends with respect to the presence of a cationic, anionic or aromatic amino acid (**Figure 40**, **1st Generation**).

As mostly similar trends were observed for these three series, the modifiability of *in vitro* properties was then only investigated by an extension of the GK-series offering differences in HSA binding strengths within a region better distinguishable *via* the high-performance affinity chromatography (HPAC) method (**Figure 40**, **2nd Generation**).

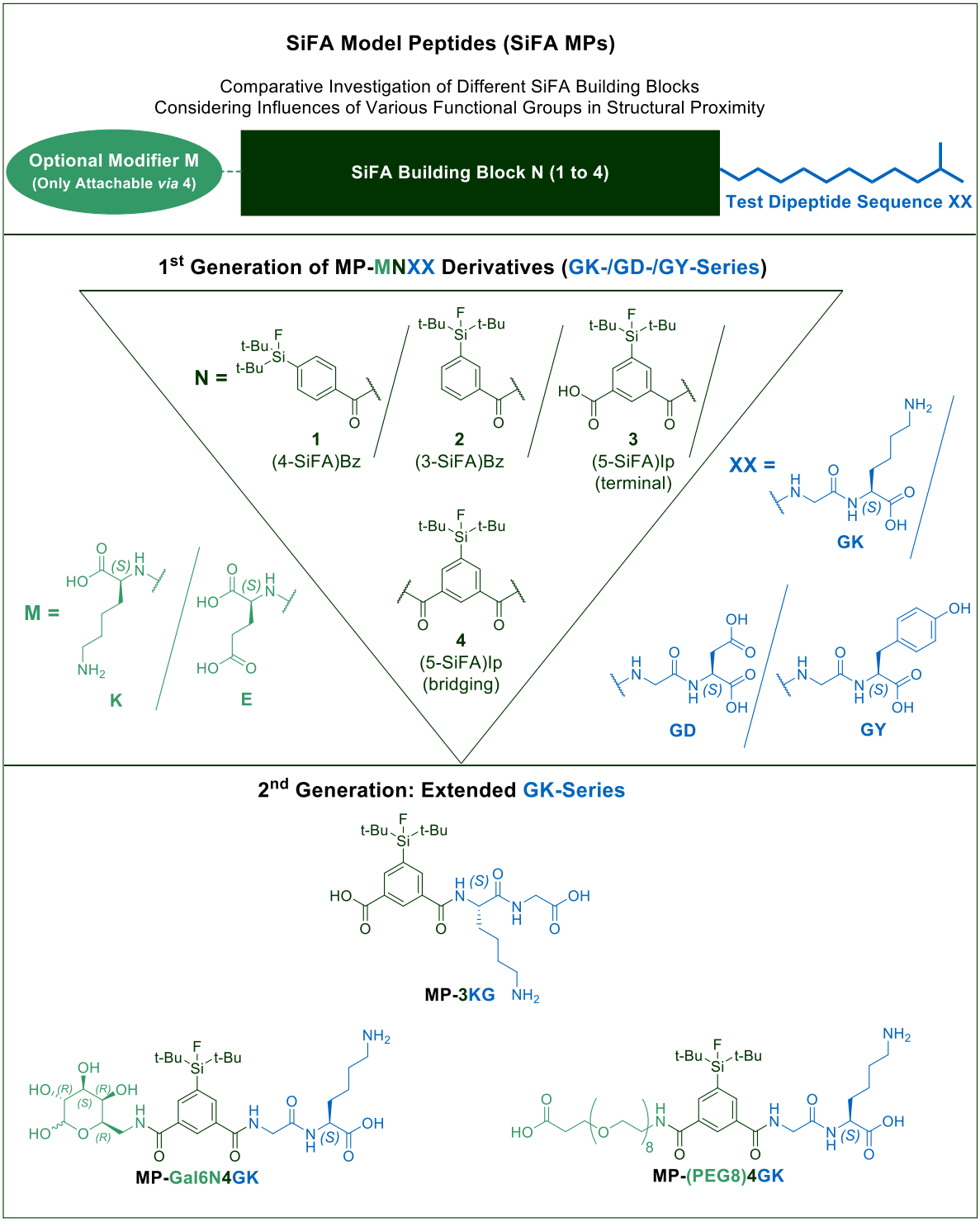

Figure 40: Compounds are entitled as follows: MP-MNXX with MP = model peptide, M = modifier in the one letter code of amino acids/Gal6N = 6-amino-6-deoxy-D-galactopyranose/(PEG8) = amino-(polyethylene glycol 8)-propionic acid, N = number of SiFA building block 1 to 4, XX = test dipeptide sequence in the one letter code of amino acids.

The efficiency of the isotopic exchange for ^{18}F-labeling was evaluated by the determination of the radiochemical conversion (RCC, $n \geq 3$) analyzing a sample of the reaction mixture by thin-layer chromatography (TLC). Besides, the decay-corrected radiochemical yield (RCY, $n \geq 3$) after purification *via* cartridge was determined and referenced to the applied activity of a pre-dried [^{18}F]fluoride solution. All derivatives showed good to high RCCs and RCYs within a range of

approximately 60–80% with molar activities of 3.1 ± 1.8 GBq/µmol. A certain trend was observable with quite similar values for (4-SiFA)Bz and terminal (5-SiFA)Ip derivatives, while both values tended to be slightly decreased for the (3-SiFA)Bz and slightly increased for di-conjugated/bridging (5-SiFA)Ip derivatives (**Figure 41**).

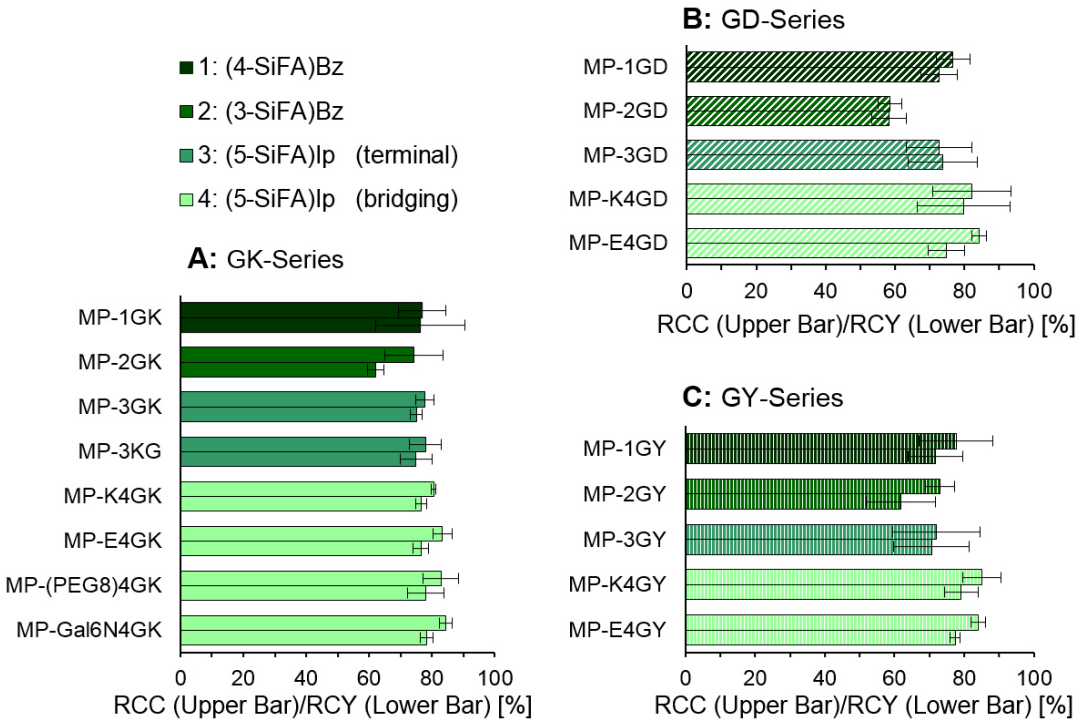

Figure 41: Radiochemical conversion (RCC, n ≥ 3) and radiochemical yield (RCY, n ≥ 3) of ^{18}F-labeling reactions (5 min, rt, molar activity = 3.1 ± 1.8 GBq/µmol; **chapter II.7.1**) of model peptides (MPs) divided into subsets **A:** GK-Series (full), **B:** GD-Series (diagonal stripes) and **C:** GY-Series (vertical stripes). Compounds sharing equal SiFA entities (1 to 4) are depicted in the same color. RCYs are decay-corrected and refer to the applied activity of the pre-dried [^{18}F]fluoride solution in anhydrous DMSO.

However, as the determined differences occurred to be mostly insignificant, a more precise comparison was strived for. Indeed, this could be achieved by the determination of relative radiochemical conversions (rRCC) in competitive isotopic exchange reactions. Herein, each corresponding (4-SiFA)Bz compound was chosen as internal reference. Equal amounts of the test- and reference-compound were added as one solution to an anhydrous [^{18}F]fluoride solution. After 5 min at rt, a sample was analyzed *via* radio-RP-HPLC. The relative radiochemical conversion (rRCC) was calculated by peak integration and expressed as the ratio of test-to-reference compound [%].

As it can be seen in **Figure 42**, differences in rRCC values were more pronounced and allowed for a better comparability with the respective (4-SiFA)Bz compound as an internal reference for each experiment under the very same conditions. The observed trend [(3-SiFA)Bz: ~75% < (4-SiFA)Bz: 100% < terminal (5-SiFA)Ip: ~125% < bridging (5-SiFA)Ip: 150-250%)] clearly demonstrated that derivatives with the novel (5-SiFA)Ip building block in terminal and even more in a bridging position exhibited improved labeling properties, in particular increased reactivities (rRCCs) resulting in higher RCYs.

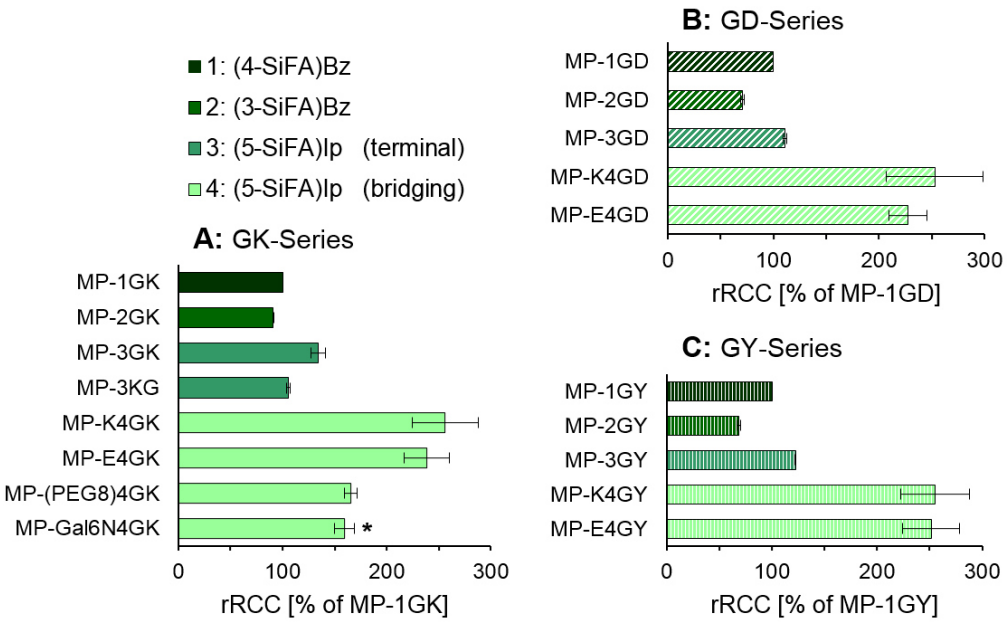

Figure 42: Relative radiochemical conversion (rRCC) of competitive ^{18}F-labeling reactions standardized to the conversion of the corresponding (4-SiFA)Bz compound MP-1XX individually determined (n = 3) by the labeling of an equimolar precursor mixture of the test compound and its MP-1XX counterpart (**chapter II.8.6**). Data are divided into subsets **A:** GK-Series (full), **B:** GD-Series (diagonal stripes) and **C:** GY-Series (vertical stripes). Compounds sharing equal SiFA entities (1 to 4) are depicted in the same color. *Quality controls *via* HPLC show the formation of two unidentified side products (approximately 5–10%) for the Gal6N-derivative which were added to the test compound integral and are estimated to occur by virtue of keto- and enol tautomerism at the sugar moiety.

On the downside, it was expected that a higher reactivity in labeling reactions was accompanied by a decreased stability. Similar to the labeling reaction with [^{18}F]fluoride, an S_N2 mechanism was proposed for the hydrolysis with hydroxide acting as a nucleophile and fluoride as a leaving group (*140*). In general, a cleavage of [^{18}F]fluoride in a diagnostic application is highly undesired as the loss of the radioactive label would not only lead to a limited targeting potential. Additionally, [^{18}F]fluoride is well-known for its bone uptake characteristic which would cause an unwanted off-target activity accumulation (*206*). Thus, a sufficient stability is of major importance.

On the search for a parameter capable of predicting a first estimate for a trend of stability/reactivity, it was assumed that the chemical shift δ within ^{29}Si- and ^{19}F-NMR spectra could be correlated with the bond properties of the Si–F compounds. Chemical shifts of a choice of model peptides representing all SiFA building blocks and test peptide-series are depicted in **Figure 43**.

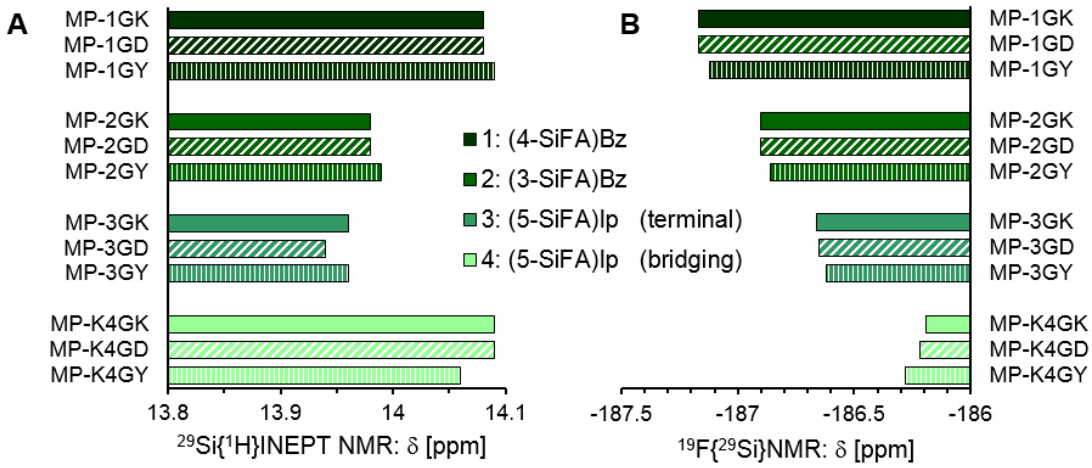

Figure 43: Chemical shifts δ [ppm] of model peptides of the GK-series (full), GD-series (diagonal stripes) and GY-series (vertical stripes) measured by **A:** $^{29}Si\{^{1}H\}$INEPT NMR (79 MHz, DMSO-D_6) and **B:** $^{19}F\{^{29}Si\}$ NMR (376 MHz, DMSO-D_6).

Data of *Höhne et al.* show a certain similarity (albeit no linear correlation) between the trend of partial charges at the Si and F atoms and the trend of determined half-lives during hydrolysis of respective compounds *(140)*. This observation was assumed to be transferable to chemical shifts determined in this work. It was concluded that a higher electron density at the Si atom (lower resonance frequency [ppm]) and a lower electron density at the F atom (higher resonance frequency [ppm]) would be attributes of a more reactive compound with a less stable Si–F bond. While the observed trend of reactivity derived from rRCCs for MPs with the different SiFA building blocks ($2 < 1 < 3 << 4$) did clearly not fit to the trend of Si signals ($1 \sim 4 > 2 > 3$), the trend of F signals ($1 < 2 < 3 < 4$) seemed to correctly predict the higher expected reactivity of the novel SiFA building block opposed to the (4-SiFA)Bz entity. However, it is undeniable that the prediction obviously was quite unprecise and did not accurately reflect proportions of reactivities found in form of rRCC values. Moreover, the electron density at the F atom surely is not the only parameter influencing the reactivity of the model compounds. This fact was clearly reflected by the comparison of rRCCs of different bridging (5-SiFA)Ip derivatives within the GK-series (MP-K4GK and MP-E4GK: ~250% vs. MP-(PEG8)4GK and MP-Gal6N4GK: ~160%). Nevertheless, the chemical shift of the ^{19}F NMR might be useful as a first estimate of stability.

To investigate the *in vitro* stability of the SiFA building blocks more closely, a choice of model peptides was incubated at various conditions to determine half-lives and estimate the potential for *in vivo* applications. Results are depicted in **Figure 44**.

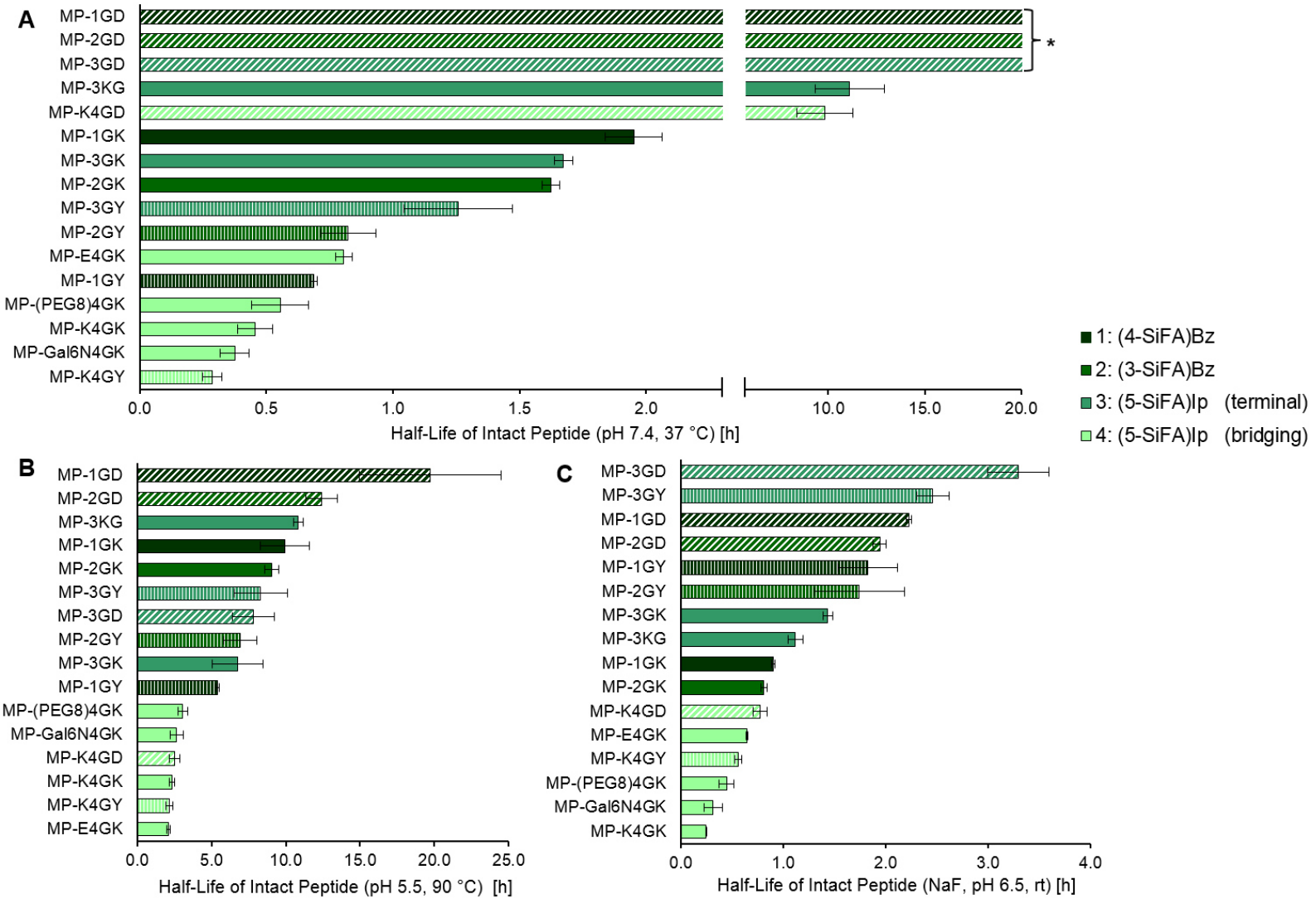

Figure 44: Half-lives (n = 3) of the intact ^{18}F-labeled MPs calculated with values obtained after incubation for 0, 30, 60, 90 and 120 min at conditions: **A:** pH 7.4 at 37 °C simulated blood conditions); **B:** pH 5.5 at 90 °C (^{177}Lu-labeling protocol for SiFA-radiohybrids); **C:** NaF (1 mM in H_2O, pH 6.5 at rt (reversed isotopic exchange in aqueous medium); *Exact half-lives not given because of unprecise regression (R^2 << 90%) with stabilities of >95% intact MP after 2 h.

For quantification of the ^{18}F-defluorination kinetics, samples were taken over a period of 2 h (t = 0, 30, 60, 90 and 120 min) and the proportion of intact, ^{18}F-labeled peptide was monitored by radio-TLC. Three different conditions were chosen to investigate the stability of the Si–F bond within model peptides: 1) Simulation of the *in vivo* stability in blood (pH 7.4, 37 °C); 2) conditions of the ^{177}Lu-labeling protocol for SiFA-radiohybrids used by our group (pH 5.5, 90 °C) to ensure the prerequisite for a theranostic approach; and 3) conditions of a reversed isotopic exchange in aqueous media (1 mM NaF-solution) as *Wurzer et al.* proposed the reversed reaction with cold fluoride in urine of mice as responsible for the formation of free [^{18}F]fluoride detected in a metabolite analysis of rhPSMA-7 isomers (*126*).

It was expected that the trends of an enhanced reactivity determined under ^{18}F-labling conditions (rRCC of MPs with SiFA building blocks 1 to 4: 2 < 1 < 3 << 4) would also be reflected by a concomitant decreased stability in aqueous media. Opposingly, stability investigations only partially verified this assumption. Indeed, under all conditions the bridging (5-SiFA)Ip derivatives mostly revealed unequivocal shorter half-lives compared to the remaining model peptides (blood condition: group 4: ~15 – 50 min vs. group 1 – 3: mostly ~1 – 2 h and up to >>10 h; ^{177}Lu-labeling condition: group 4: ~2 – 3 h vs. group 1 – 3: mostly ~5 – 12 h and up to ~20 h; reversed isotopic exchange: group 4: ~15 – 50 min vs. group 1 – 3: ~1 – 3 h).

The stability comparison of MPs belonging to groups 1 – 3 appears more complex. The stability ranking of the different SiFA groups was inconsistent between the various test peptide series (GK/GD/GY). Data rather suggest that the trend of reactivity of the SiFA groups was perturbed by the influence of functionalities within the individual structural vicinity of an MP. This finding was already indicated for deviating rRCCs in the GK-series (MP-**M**4GK with **M** = K/E/(PEG8)/Gal6N). Moreover, *Höhne et al.* also observed deviating stabilities for quite similar SiFA compounds with the general formula *p*-(*t*Bu$_2$Si)-Ph-CH$_2$-R (R: -CH$_2$OTHP/-(CH$_2$)$_{0\text{-}2}$-OH/-COOH) (*140*). In the comparison of stabilities of MPs with an equal SiFA group, one trend of half-lives was found several times: blood/^{177}Lu-labeling condition GD > GK > GY; reversed isotopic exchange: GD > GY > GK. One reason for superior stabilities of the GD-series might be an electrostatic repulsion between the nucleophiles (OH^-/$^{nat}F^-$) initiating the cleavage of [^{18}F]fluoride and the negatively charged, deprotonated aspartate carboxylates (pK_A ~2 – 4) (*207,208*). The predominantly protonated ammonium group of the Lys sidechains (pK_A ~10.7) (*207,208*) of the GK-series might weaken the nucleophilicity of attacking anions by protonation equilibria [R-NH_3^+ + OH^-/F^- $\rightleftharpoons$ R-NH_2 + H_2O/HF]. On the other hand, an electrostatic attraction might also facilitate the nucleophilic attack by pre-coordination.

In summary, *in vitro* data indicatet a higher reactivity and instability of compounds with a bridging (5-SiFA)Ip entity. However, not only the choice of the prosthetic group but also the functional groups in the structural environment of SiFA entities appeared to play a pivotal role for the stability of Si–F bonds. Noteworthy, previous *in vivo* experiences with [^{68}Ga]Ga-rhPSMA-7.3 vs. ^{18}F-rhPSMA-7.3 validated the stability of this (4-SiFA)Bz-containing derivative as sufficient (*126*).

If this is also true for the novel (5-SiFA)Ip group will be further discussed in the **chapters III.4.5** and **III.4.6**.

However, besides the results above regarding reactivity/stability of the different SiFA entities as a requirement for a potential *in vivo* application, following data of the MPs clearly demonstrated the improvement in hydrophilicity and HSA binding using the novel (5-SiFA)Ip building block. The comparison of $logD_{7.4}$-values (n ≥ 8) as a measurable of hydrophilicity is depicted in **Figure 45**.

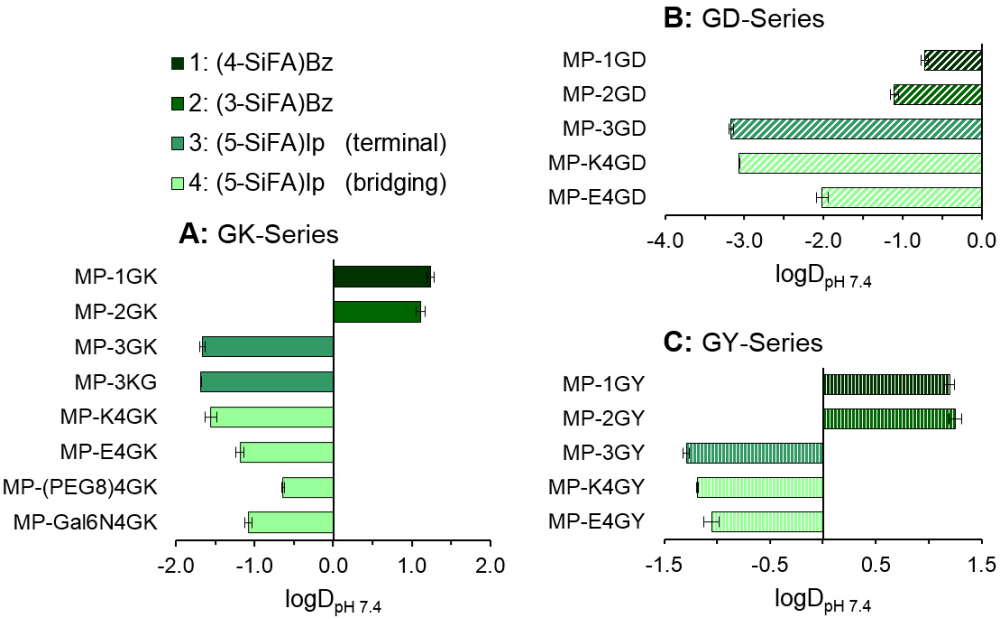

Figure 45: Hydrophilicity determined as *n*-octanol/PBS partition coefficient ($logD_{pH\ 7.4}$; n ≥ 8) of model peptides (MPs) divided into subsets **A:** GK-Series (full), **B:** GD-Series (diagonal stripes) and **C:** GY-Series (vertical stripes). Compounds sharing equal SiFA entities (1 to 4) are depicted in the same color.

As expected for the constitutional isomers, results indicated only minor differences in hydrophilicity between (4-SiFA)Bz and (3-SiFA)Bz derivatives. In contrast, the additional negative charge by the introduction of a further carboxylic acid in the terminal (5-SiFA)Ip derivatives proofed a superior hydrophilicity with a shift of $logD_{pH\ 7.4}$ values by 2–3 logarithmic units. Regarding a gain of hydrophilicity, the terminal use of the novel entity appeared to be most efficient. The conjugation of Lys as a zwitterionic modifier delivered almost equal results whereas the addition of Glu with even one more carboxylic acid led to a loss in hydrophilicity compared to the terminal (5-SiFA)Ip group. This finding demonstrated the superiority of direct proximity of hydrophilic functionalities to the lipophilic SiFA entity over an increased number of more distant hydrophilic modifiers. Furthermore, this clarified that this overall strategy of developing a novel prosthetic group opens a possibility to design compounds with a more efficiently boosted hydrophilicity opposed to ligands with the same persistent prosthetic group and only a fine-tuned hydrophilic linker.

Within the extended GK-series, the (PEG8) modification exhibited a more decent but significant improvement over the (4-SiFA)Bz compound (Δ = ~1.5 logarithmic units). The use of the still quite

hydrophilic sugar-based modifier Gal6N (Δ = ~2 logarithmic units) might serve as a useful alternative if an avoidance of charged groups is required (compare **chapter III.3.1**).

Besides hydrophilicity – as already emphasized – HSA binding constitutes an important parameter in modulating a compound's pharmacokinetics. A strong HSA binding was associated with a comparably slow and unfavored blood clearance *in vivo*. Results of HSA binding determined by HPAC are depicted in **Figure 46**.

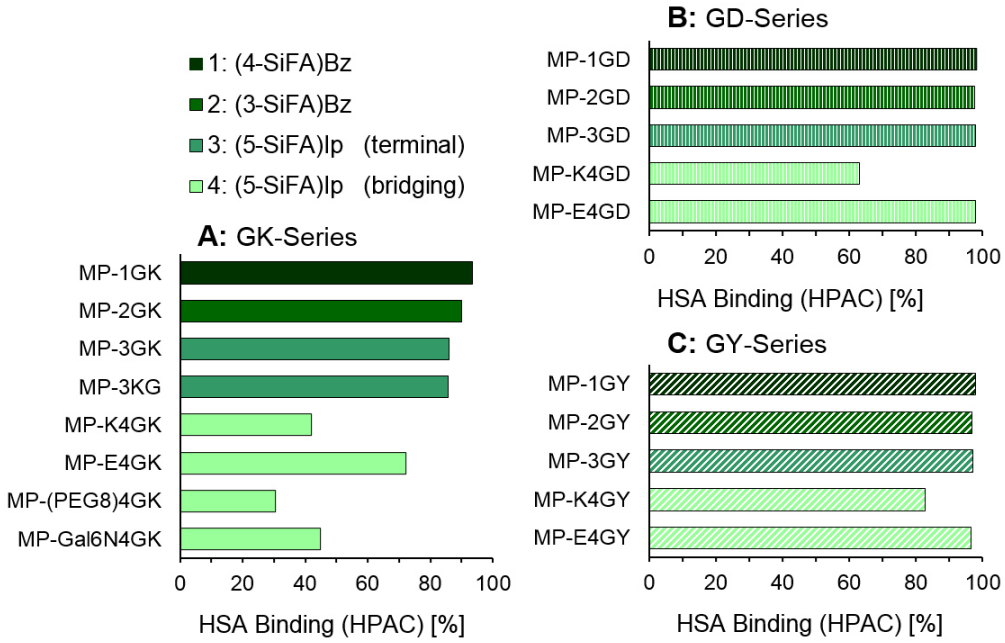

Figure 46: HSA binding determined by HPAC of model peptides (MPs) divided into subsets **A:** GK-Series (full), **B:** GD-Series (diagonal stripes) and **C:** GY-Series (vertical stripes). Compounds sharing equal SiFA entities (1 to 4) are depicted in the same color.

Only minor differences in HSA binding were observed comparing (3-SiFA)Bz and terminal (5-SiFA)Ip with (4-SiFA)Bz derivatives in the GD- and GY-series. Analogously to the PSMA ligands RNC-6 and -7 (**chapter III.3.5**), the introduction of a positively charged group in vicinity to the SiFA entity reduced HSA binding. This could already be recognized by differences between the test peptide series. While MP-1GY, -2GY, -3GY, -1-GD, -2GD and -3GD exhibited values in the upper limit region of the method (>96%) and could not be well distinguished, MP-1GK possessed a comparably lower HSA binding (93%) and small further improvements could be observed by the alteration of the SiFA entity (90% and 86% for MP-2GK and MP-3GK/-3KG, respectively).
Fortunately, the HSA binding could be drastically decreased by conjugation of further modifiers to the (5-SiFA)Ip moiety. The coupling of Lys to the second carboxylic acid of the (5-SiFA)Ip entity was assumed to reduce the HSA binding by two mechanisms: 1) introduction of a (additional) positive charge or proton donor; and 2) provoking steric repulsions with the HSA binding pocket simply by increasing the molecule's size in an unfavored position. Indeed, a substantial reduction

of HSA binding was revealed in all series and the effect was even more pronounced for MP-K4GK, comprising two amino groups.

Compound MP-E4GK underlined the assumption of the two reduction mechanisms as the Glu modification did not contain a positive charge but decreased HSA binding due to a similar steric demand. Thus, it was comprehensible to observe a moderate reduction (MP-3GK > MP-E4GK > MP-K4GK).

Derivative MP-(PEG8)4GK contains the structurally bulkiest modifier and thus, presumably poses the best example within the series for reduced HSA binding by steric shielding of the SiFA group. Herein, the HSA binding was measured to be at impressively low 30%.

Again, the sugar derivative MP-Gal6N4GK might also possess a useful modifier with an HSA binding of just 45% and representing the only SiFA entity with high hydrophilicity, low HSA binding and being free of a charged functional group.

Advantages of the novel (5-SiFA)Ip-based platform are once more visualized by **Figure 47**.

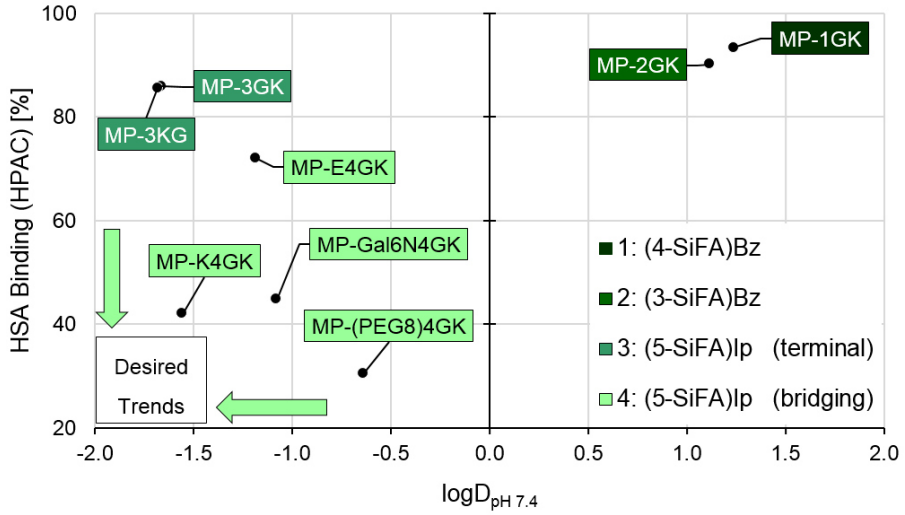

Figure 47: Illustration of the beneficial use of the novel (5-SiFA)Ip entity in modulating hydrophilicity ($logD_{pH\ 7.4}$) and HSA binding exemplified by derivatives of the GK-series.

In conclusion, it can be summarized that the (5-SiFA)Ip moiety could serve as an extremely useful platform for ^{18}F-labeling not only with improved hydrophilicity but also as an HSA binding moiety with an HSA binding easily modulated over a broad range of binding strength. This could be achieved by conjugating suitable modifiers of choice to the additional carboxylic acid of the newly developed (5-SiFA)Ip moiety to adjust pharmacokinetic properties of a ligand exactly to the requirements of an *in vivo* application.

4.4. *In Vitro* Evaluation of MSM Ligands

Further investigations were conducted using ligands addressing the prostate-specific membrane antigen (PSMA). In a first row, simplistic, non-radiohybrid MSM ligands were tested to proof the concept of increased hydrophilicity and explore the effect of alterations on target affinity (**Figure 48**). Data were determined with the kind help of *Jan-Philip Kunert*.

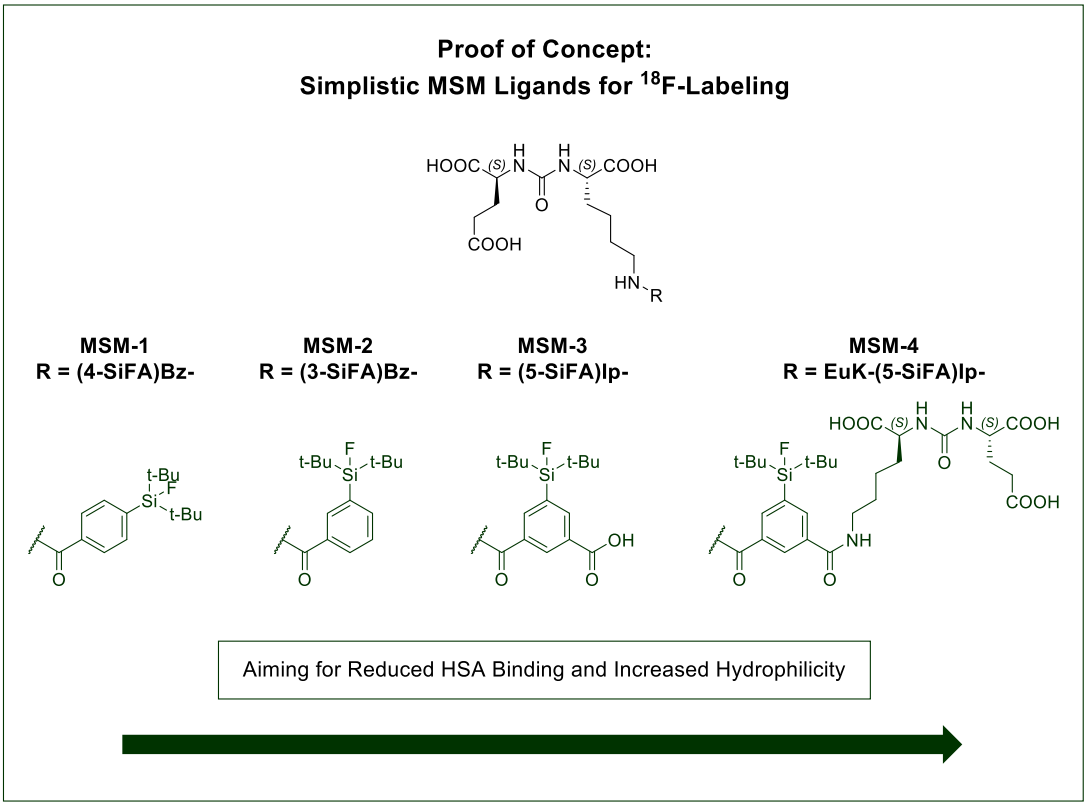

Figure 48: Structures of simplistic PSMA ligands with various modified SiFA moieties (MSM) attached to the PSMA-binding motif EuK aiming for reduced HSA binding and increased hydrophilicity.

The (4-SiFA)Bz-bearing ligand MSM-1 was first synthesized by *Martina Wirtz* in our group, entitled as '(SiFA-BA)KuE', but was independently re-evaluated herein (*115*). The poor PSMA affinity (IC_{50}: 820 ± 246 nM) determined by her was speculated to constitute a good starting point to demonstrate the usefulness of an alternative substitution pattern at the SiFA entity in structure-activity relationships. As alterations MSM-2 to -4 were synthesized as respective (3-SiFA)Bz, terminal (5-SiFA)Ip and even a dimeric bridging EuK-(5-SiFA)Ip derivative.

Indeed, the determined IC_{50}-values represented a positive example for a structural-activity relationship where the shift of the silyl group at the aromatic moiety was clearly beneficial for a superior affinity. The simple shift of the silyl group from *para*- [MSM-1, (4-SiFA)Bz] to *meta*-position [MSM-2, (3-SiFA)Bz] caused a more than 20-fold increase in affinity which could be further improved by a factor of two attaching a carboxylic acid [MSM-3, (5-SiFA)Ip]. Obviously, steric repulsion of the silyl group with the binding pocket could be diminished by the repositioning. The addition of a further carboxylic acid might allow for an extra attractive interaction with the arginine

patch as also assumed for EuE-orn-OH derivatives (*126,202*). Using a dimeric approach by conjugating a second equivalent of the binding motif EuK to the free carboxylic acid at the (5-SiFA)Ip moiety resulted even in a slightly higher affinity of 4.1 ± 1.9 nM. Thus, this example illustrates the use of altered SiFA entities as a simple opportunity to potentially increase target affinity (**Figure 49**).

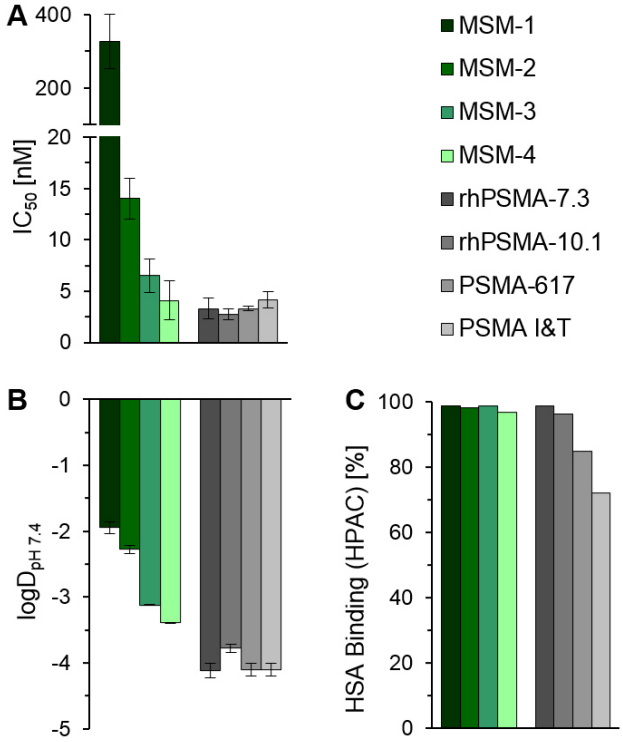

Figure 49: *In vitro* data of MSM-1 to -4 (green) evaluated as [$^{18/nat}$F]F-compounds and reference ligands (grey) evaluated as [$^{177/nat}$Lu]Lu-compounds; **A)** affinities (IC_{50} [nM]) determined in a binding assay of ^{nat}F-MSM ligands and ^{nat}Lu-references (10^{-10}–10^{-5} M) with [^{125}I]I-BA-KuE (0.2 nM) as competitor on PSMA^{+} LNCaP cells (1 h, on ice, n = 3); **B)** lipophilicity of [^{18}F]F-MSM ligands and [^{177}Lu]Lu-references expressed as *n*-octanol/PBS partition coefficient ($logD_{pH\ 7.4}$, n ≥ 6); **D)** human serum albumin binding of ^{nat}F-MSM ligands and ^{nat}Lu-references determined on a Chiralpak HSA column. Data depicted for reference compounds in A) and B) were previously published by our group (*125*).

Once more, this dataset points out that the additional carboxylic acid directly attached to the SiFA moiety drastically boosts the hydrophilicity as a difference of about one logarithmic unit was observed comparing MSM-3 with MSM-1 and -2. Interestingly, the dimeric MSM-4 bearing two additional carboxylic acids opposed to MSM-3, exhibited only a slightly further increase in hydrophilicity (–3.12 ± 0.01 vs. –3.39 ± 0.01). Again, this finding emphasizes the importance of structural proximity of hydrophilic modifiers to the lipophilic SiFA moiety.

The values for HSA binding were nearly equal with only a minor decrease for the dimeric MSM-4 (96.7% vs. >98%). This was in accordance with expectations of a decreased HSA binding caused by the steric shielding of the second binding motif. It was assumed that analogously to results of the GD- and GY-series of MPs, the observation of clear differences in HSA binding is limited by the upper plateau of the HPAC method. A comparison with AMSEC data would be interesting. But the availability of AMSEC was temporally restricted due to technical difficulties.

Another dataset was determined comprised of radiohybrid PSMA ligands with modified SiFA moieties (**Figure 50**).

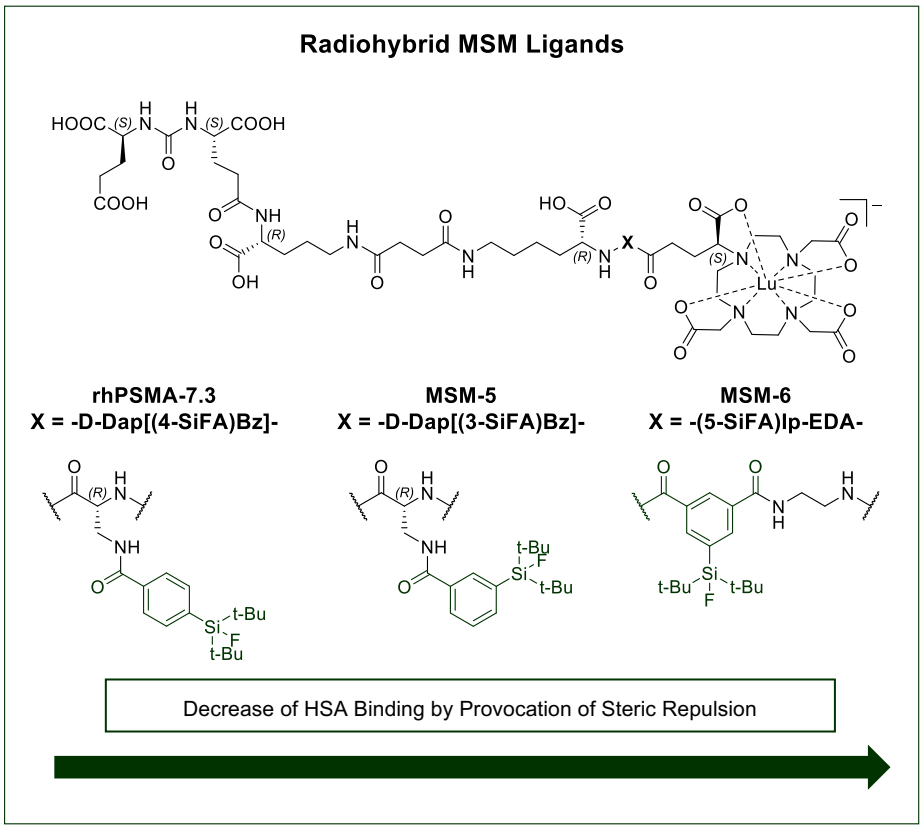

Figure 50: Structures of radiohybrid PSMA ligands with modified SiFA moieties (MSM) derived from the reference compound rhPSMA-7.3 aiming for reduced HSA binding.

The aim of this development step was the design of a ligand with *in vitro* data comparable to those of Lu-rhPSMA-7.3 with the only difference in a reduced HSA binding. This should impact the pharmacokinetics and proof the concept of expected superior tumor-to-organ ratios by an accelerated whole-body clearance. Therefore, the number of carboxylic acids and the net charge was not altered. *In vitro* results are depicted in **Figure 51**.

Fortunately, the modifications had little impact on the target affinity as well as the internalization behavior indicating that this application of the modified SiFA moieties (3-SiFA)Bz and (5-SiFA)Ip in bridging constitution were still tolerated by the remote arene-binding site (*69*).

Also, the differences in hydrophilicity between [^{177}Lu]Lu-rhPSMA-7.3 and [^{177}Lu]Lu-MSM-6 appeared negligible whereas [^{177}Lu]Lu-MSM-5 exhibited a small loss of hydrophilicity. These findings were expected as the net charge was not changed and the ligand geometry was only slightly modified.

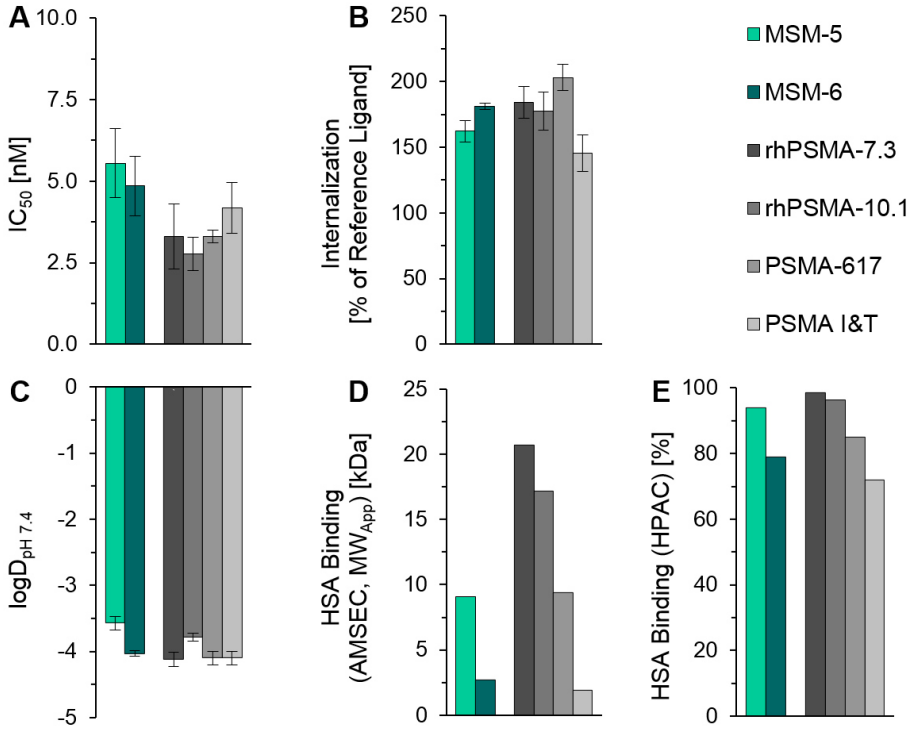

Figure 51: *In vitro* data of MSM-5 and -6 (green) and reference ligands (grey), all evaluated as [$^{177/nat}$Lu]Lu-compounds; **A)** affinities (IC_{50} [nM]) determined in a binding assay of ^{nat}Lu-compounds (10^{-10}–10^{-5} M) with [^{125}I]I-BA-KuE (0.2 nM) as competitor on PSMA$^+$ LNCaP cells (1 h, on ice, n = 3); **B)** PSMA-mediated internalization of [^{177}Lu]Lu-compounds in PSMA$^+$ LNCaP cells (1 h, 37 °C) as percentage of the reference ligand [^{125}I]I-BA-KuE (n = 3); **C)** lipophilicity of [^{177}Lu]Lu-compounds expressed as *n*-octanol/PBS partition coefficient ($logD_{pH\ 7.4}$, n ≥ 6); **D)** apparent molecular weight (MW_{App}) of [^{177}Lu]Lu-compounds determined by human serum albumin-mediated size exclusion chromatography (AMSEC); **E)** human serum albumin binding of ^{nat}Lu-compounds determined on a Chiralpak HSA column. Data depicted for reference compounds in A–D) were previously published by our group (*125*); only AMSEC data were modified by a correction factor explained in **chapter II.8.5.2**.

In this example, the use of the (3-SiFA)Bz instead of the (4-SiFA)Bz group already indicated a decrease in HSA binding by the AMSEC method (rhPSMA-7.3: 21.6 kDa vs. MSM-5: 9.1 kDa) as well as by the HPAC method (rhPSMA-7.3: 98.6% vs. MSM-5: 94.0%). The effect could be drastically enhanced using the (5-SiFA)Ip-building block as a bridging element. This type of structural arrangement seemed to possess limited possibilities of spatial adaptations to the HSA binding site opposed to the attachment of the SiFA entity at a protruding sidechain. Thus, the exposure of the SiFA entity next to the sterically demanding chelator would be reduced. As a result, the HSA binding was decreased to 2.7 kDa and 78.9% even below the level of [^{177}Lu]Lu-PSMA-617 (9.4 kDa; 84.9%).

Following these promising *in vitro* results, biodistribution studies were conducted examining the effect on pharmacokinetics and the *in vivo* stability of the novel SiFA entity.

4.5. Biodistribution of MSM Ligands

The attempt of translating the successfully reduced HSA binding into faster pharmacokinetics *in vivo* delivered diverging results (**Figure 52**).

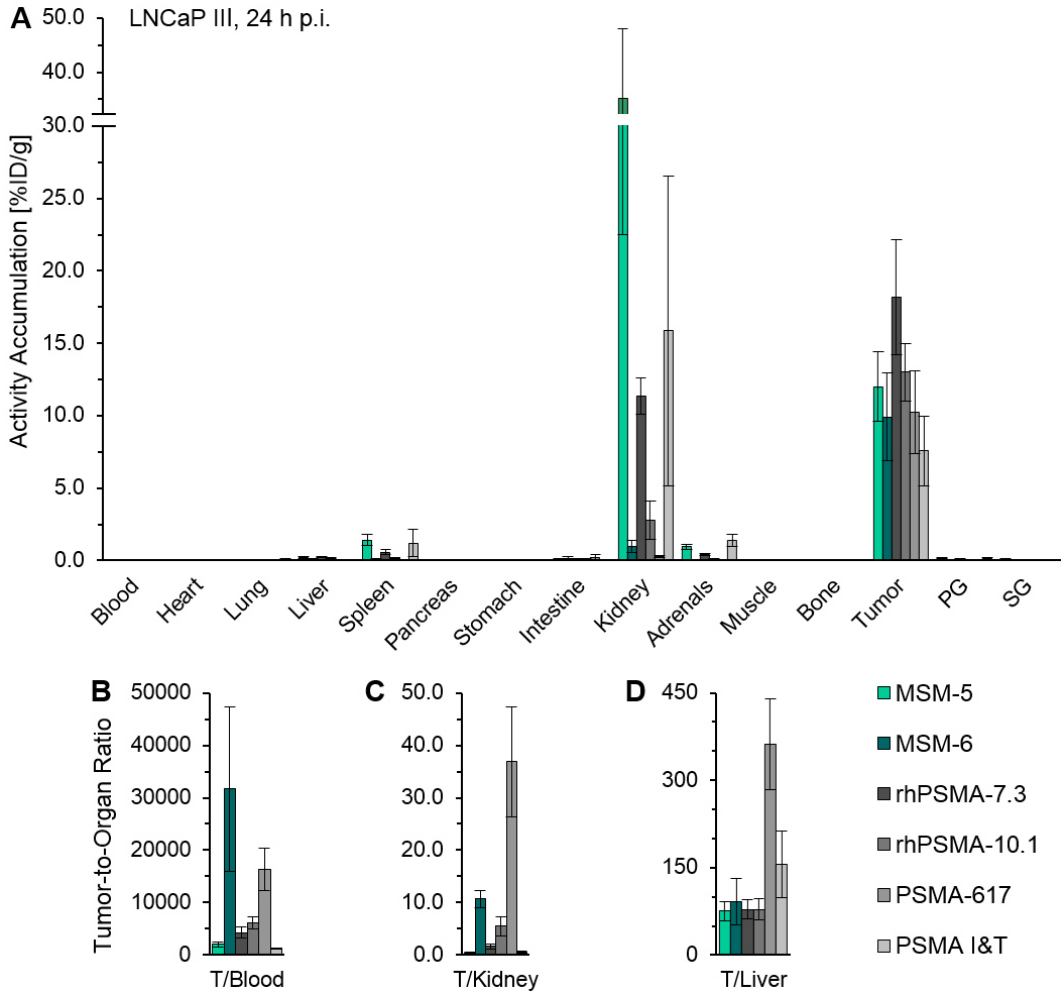

Figure 52: A) *Ex vivo* biodistribution of MSM-5 (n = 5), MSM-6 (n = 5) and the reference ligands rhPSMA-7.3 (n = 5), rhPSMA-10.1 (n = 4), PSMA-617 (n = 5) and PSMA I&T (n = 5) as [^{177}Lu]Lu-compounds at 24 h p.i. in male LNCaP III tumor-bearing CB17-SCID mice; PG = parotid glands, SG = submandibular glands; data expressed as percentage of the injected dose per gram (%ID/g) and mean ± standard deviation; **B–D)** tumor-to-organ ratios (tumor-to-blood/-kidney/-liver) calculated individually for each mouse and expressed as mean ± standard deviation.

Contradictorily to the decreased HSA binding found for MSM-5, obtained blood- and kidney-values were increased (1.3-fold and 3.1-fold, respectively) compared to [^{177}Lu]Lu-rhPSMA-7.3. A possible explanation could be a species-specific deviation in binding strength to human and murine serum albumin for [^{177}Lu]Lu-MSM-5. A substantially stronger interaction with the murine protein compared to the human serum albumin would lead to a misfit between *in vitro* and *in vivo* data. Similar counterintuitive observations were made in mouse experiments comparing [^{177}Lu]Lu-PSMA I&T (0.0061 ± 0.0027%ID/g blood, 15.8 ± 12.0 %ID/g kidney) and [^{177}Lu]Lu-PSMA-617 (0.0007 ± 0.0004 %ID/g blood, 0.29 ± 0.08 %ID/g kidney) although the *in vitro* experiment for HSA binding showed values with a reversed trend (71.9% [^{177}Lu]Lu-PSMA I&T vs. 84.9% for [^{177}Lu]Lu-PSMA-617) (unpublished data of our group). In this case, the *in vitro* data determined *via* HPAC appeared to fit more appropriate translated to clinical data of patients (*204,209*).

Opposingly, the reduced HSA binding and otherwise preserved *in vitro* parameters observed for MSM-6 indeed accelerated its pharmacokinetics compared with [^{177}Lu]Lu-rhPSMA-7.3. As

expected, a faster blood clearance also effected the input-function limiting tumor accumulation (18.2 ± 4.0 %ID/g vs. 9.9 ± 3.1 %ID/g determined for [^{177}Lu]Lu-rhPSMA-7.3 and [^{177}Lu]Lu-MSM-6, respectively). Nevertheless, especially the blood clearance (0.0046 ± 0.0018%ID/g vs. 0.0004 ± 0.0003%ID/g determined for [^{177}Lu]Lu-rhPSMA-7.3 and [^{177}Lu]Lu-MSM-6, respectively) and kidney retention (11.4 ± 1.3 %ID/g vs. 0.97 ± 0.43 %ID/g determined for [^{177}Lu]Lu-PSMA-7.3 and [^{177}Lu]Lu-MSM-6, respectively) could both be drastically decreased by a factor of more than ten resulting in about 5-fold improved tumor-to-blood and -kidney ratios for [^{177}Lu]Lu-MSM-6.

The tumor-to-blood ratio of [^{177}Lu]Lu-MSM-6 even surpassed the one of [^{177}Lu]Lu-PSMA-617 by a factor of two. However, data regarding tumor-to-kidney and tumor-to-liver ratios of [^{177}Lu]Lu-PSMA-617 (3.7-fold and 4.0-fold higher, respectively) determined with cell passage LNCaP III were still undefeated. Noteworthy, the dataset of [^{177}Lu]Lu-PSMA-617 determined with the cell passage LNCaP III exhibited an undeclared surprisingly-fast whole-body clearance in respect to previous data determined with the passage LNCaP I as well as to data of the original publication (tumor-to-blood ratios: 16323 ± 3998 in LNCaP III mice vs. 1424 ± 455 in LNCaP I mice vs. 1058 from original publication in LNCaP-bearing BALB/c *nu/nu* mice (*98*).

The trend in improvement of tumor-to-kidney ratios found in *ex vivo* biodistribution studies is well reflected by corresponding µSPECT/CT images (**Figure 53**).

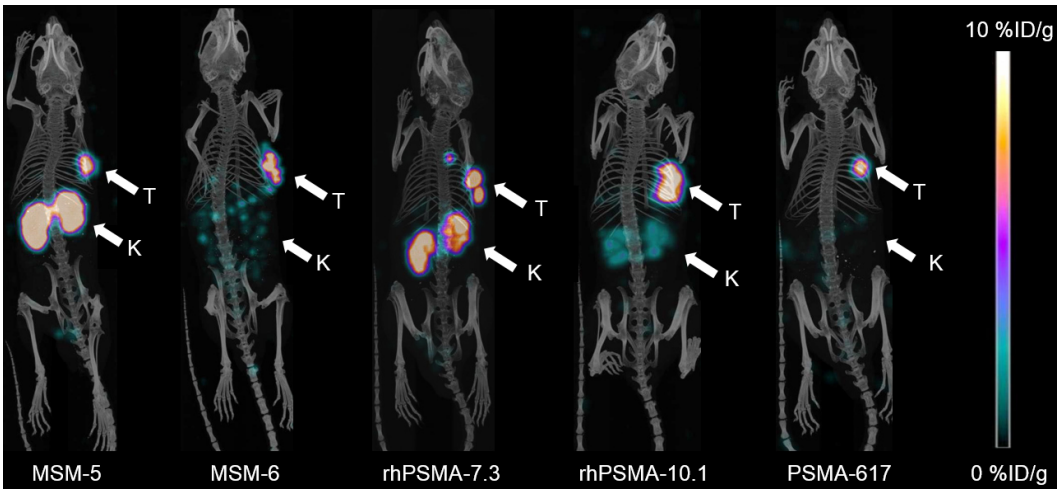

Figure 53: Static µSPECT/CT images (maximum intensity projections) of MSM-5, MSM-6, rhPSMA7.3, rhPSMA-10.1 and PSMA-617 as ^{177}Lu-labeled compounds in LNCaP III tumor-bearing CB-17 SCID mice. Tumors (T) and kidneys (K) are indicated by white arrows. Mice were sacrificed 24 h p.i. and imaged directly after blood collection by cardiac puncture.

Another dataset was analyzed comparing respective ^{18}F-labeled compounds of all herein tested SiFA entities *in vivo* (**Figure 54**), not only validating the effect on pharmacokinetics, but also indicating the stability of the respective [^{18}F]F–Si bond by the trend of bone uptake (*206*).

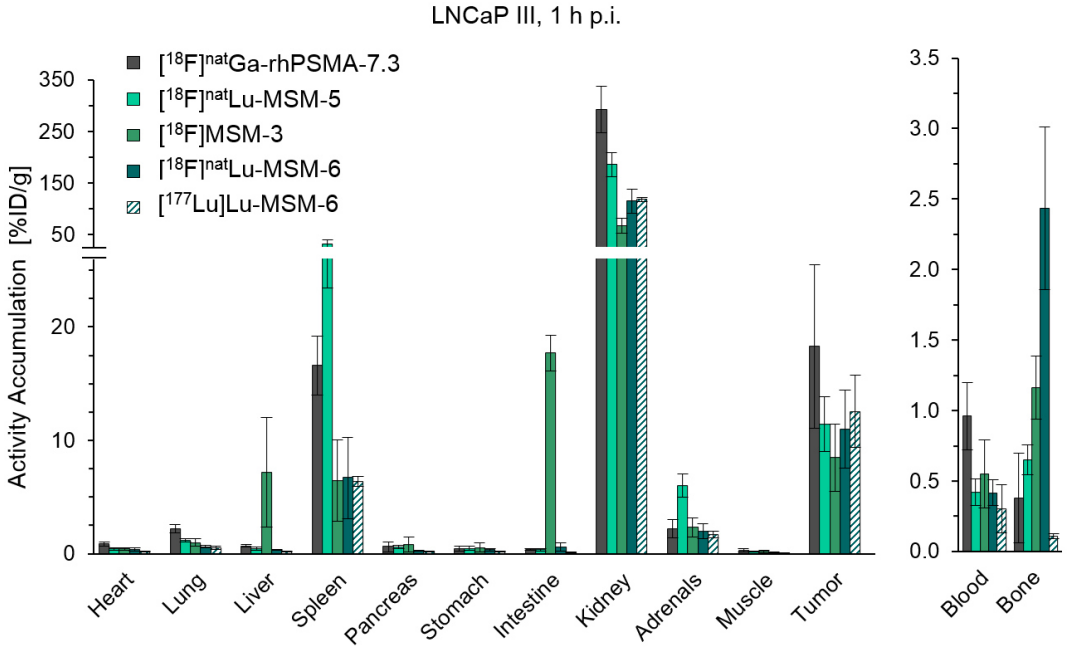

Figure 54: *Ex vivo* biodistribution of the compounds [^{18}F]^{nat}Ga-rhPSMA-7.3 (n = 4), [^{18}F]MSM-3 (n = 5), [^{18}F]^{nat}Lu-MSM-5 (n = 5), [^{18}F]^{nat}Lu-MSM-6 (n = 5) and [^{177}Lu]Lu-MSM-6 (n = 3) at 1 h p.i. in male LNCaP III tumor-bearing CB17-SCID mice; data expressed as percentage of the injected dose per gram (%ID/g) and mean ± standard deviation. *Data of [^{18}F]^{nat}Ga-rhPSMA-7.3 were previously published by our group (*77*).

Already 1 h p.i., all derivatives showed a faster blood clearance with a blood value ranging between 0.3–0.6 %ID/g compared to 0.96 %ID/g for [^{18}F]^{nat}Ga-rhPSMA-7.3.

Moreover, kidney uptakes were drastically lowered by using alternative SiFA moieties deviant from the (4-SiFA)Bz entity in [^{18}F]^{nat}Ga-rhPSMA-7.3 (186 ± 23.4 %ID/g and 114 ± 22.9 %ID/g vs. 292 ± 45.1 %ID/g for [^{18}F]^{nat}Lu-MSM-5 and [^{18}F]^{nat}Lu-MSM-6 vs. [^{18}F]^{nat}Ga-rhPSMA-7.3, respectively). Noteworthy, [^{18}F]^{nat}Ga-rhPSMA-7.3 was the only derivative in this comparison investigated as ^{nat}Ga-complex. This leads to a different polarity opposed to the lutetium complexes in [^{18}F]^{nat}Lu-MSM-5 and [^{18}F]^{nat}Lu-MSM-6 which might also affect the kidney retention known to be influenced by charge (*210,211*). Obviously, the low kidney value (67.1 ± 13.9 %ID/g) of [^{18}F]MSM-3 was not directly comparable as this derivative seemed to suffer from insufficient hydrophilicity resulting in hepatobiliary excretion as indicated by increased accumulation in liver (7.2 ± 4.8 %ID/g) and intestine (17.7 ± 1.6 %ID/g).

Obviously, pharmacokinetics of these derivatives were clearly not identical and resulted in unequal plasma half-lives. Thus, deviating incubation conditions were faced by the [^{18}F]F–Si bond within the derivatives. Nevertheless, the trend of values for bone uptake, mainly caused by cleaved [^{18}F]fluoride (compare [^{18}F]^{nat}Lu-MSM-6: 2.43 ± 0.58 %ID/g vs. [^{177}Lu]Lu-MSM-6: 0.11 ± 0.019 %ID/g), was well reflected by the trend of reactivity found for related model peptides (stability: (4-SiFA)Bz ~ (3-SiFA)Bz > terminal (5-SiFA)Ip > bridging (5-SiFA)Ip). A closer comparison is given in the next chapter.

4.6. *In Vitro* vs. *In Vivo* Stability of SiFA Moieties

Herein, the trend of reactivity for a choice of model peptides determined *in vitro* is correlated with results of bone uptakes observed for various PSMA-targeting MSM ligands as indicator for the *in vivo* stability of the respective type of Si–F bond (**Figure 55**).

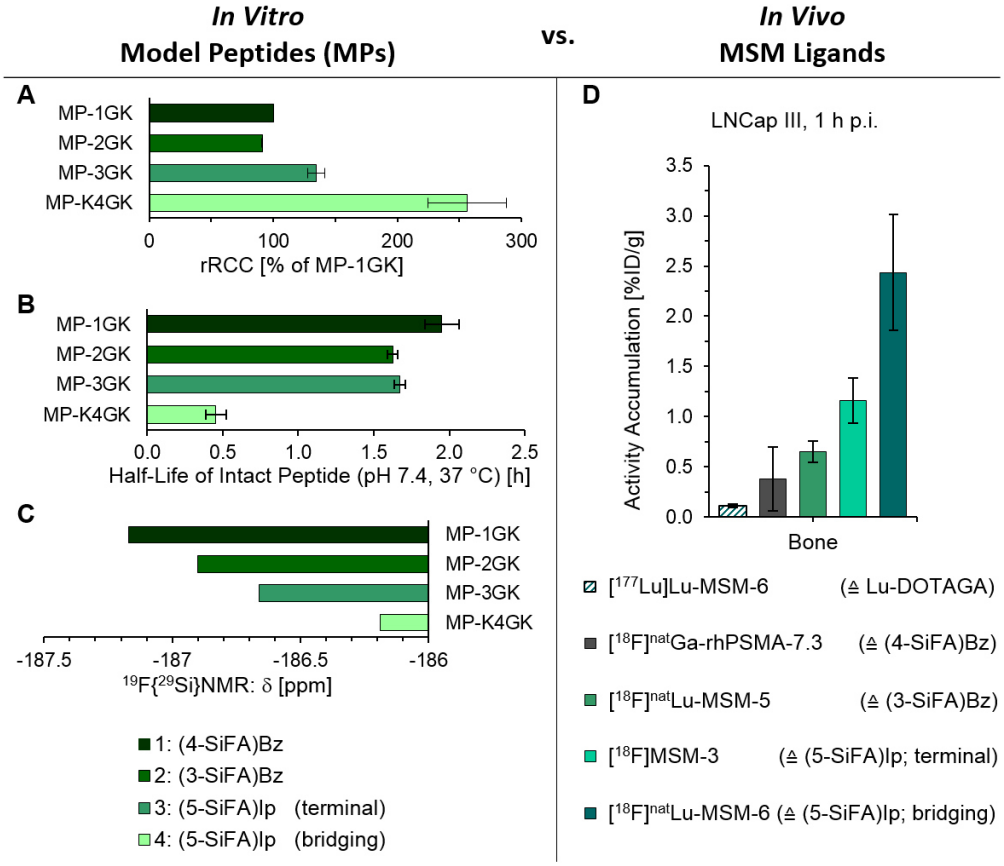

Figure 55: Comparison of *in vitro* vs. *in vivo* data regarding reactivity and stability of the [^{18}F]F–Si bond as part of the different SiFA moieties [(4-SiFA)Bz-, (3-SiFA)Bz-, terminal (5-SiFA)Ip- and bridging -(5-SiFA)Ip-]: **A**: reactivity of model peptides (MPs) from the GK-series under anhydrous ^{18}F-labeling conditions expressed as relative radiochemical conversion (rRCC); **B**: half-lives of intact ^{18}F-labeled MPs from the GK-Series incubated in an aqueous K_2CO_3-solution (pH 7.4, 37 °C; simulated blood conditions); **C:** chemical Shifts δ [ppm] of ^{19}F{^{29}Si}NMR spectra (376 MHz, DMSO-D_6) of the GK-series; **D**: activity accumulation (%ID/g) in CB-17 SCID mice (n ≥ 4) 1 h p.i. of ^{18}F-labeled PSMA ligands and [^{177}Lu]Lu-MSM-6 sharing the same SiFA moieties as depicted for the GK-series and indicated in brackets. Data of [^{18}F]^{nat}Ga-rhPSMA-7.3 were previously published by our group (*77*).

Relative radiochemical conversions (rRCCs) depicted in **Figure 55A** displayed a trend in reactivity with the (3-SiFA)Bz compound similar to the normalized value of the (4-SiFA)Bz derivative, a slightly higher rRCC for the terminal (5-SiFA)Ip entity by a factor of 1.3 and a clearly higher rRCC for the bridging (5-SiFA)Ip moiety by a factor of about 2.6.

The increased reactivity was also found to be accompanied by a lower stability (**Figure 55B**) with a half-life of the [^{18}F]F–Si bond within the MPs reduced by 15% attaching the (5-SiFA)Ip moiety terminally and divided by a factor of 4.0 attaching a (5-SiFA)Ip moiety in a bridging construct instead of the classical (4-SiFA)Bz moiety, respectively.

Furthermore, there seemed to be a correlation of enhanced reactivity and decreased stability with a less negative ^{19}F NMR-shift (**Figure 55C)**, representing a lower electron density at the fluorine atom.

Although the *in vitro* data (**Figure 55A–C**) were determined for MPs, their data seemed to have a predictive value for the observed trend of *in vivo* stability in structurally-related PSMA ligands. The trend of *in vivo* stability of F–Si bonds within PSMA ligands was reflected by activity accumulation in bone, mainly due to dissociated [^{18}F]fluoride (**Figure 55D**). Again, the (5-SiFA)Ip moiety attached in a bridging way in [^{18}F]^{nat}Lu-MSM-6 possessed the highest instability 1 h p.i. with a bone uptake of 2.43 ± 0.58 %ID/g. The terminal use of the (5-SiFA)Ip moiety led to a bone uptake of 1.16 ± 0.22 %ID/g for [^{18}F]MSM-3. Comparatively, the (3-SiFA)Bz-bearing ligand [^{18}F]^{nat}Lu-MSM-5 revealed a similar bone uptake as the (4-SiFA)Bz moiety utilized in [^{18}F]^{nat}Ga-rhPSMA-7.3 (0.65 ± 0.11 %ID/g and 0.38 ± 0.32 %ID/g respectively) (*77*). To proof a bone uptake predominantly caused by cleaved [^{18}F]fluoride, MSM-6 was also examined as ^{177}Lu-labeled tracer leading to a clearly lower activity accumulation (0.11 ± 0.019 %ID/g).

However, clinical translation of a terminally or even a bridging (5-SiFA)Ip moiety seems feasible despite an increased [^{18}F]fluoride release in mice comparing the found bone uptake with results published about [^{18}F]SiFA*lin*-TATE (Femur: 1.9 ± 0.6 %ID/g at 60 min p.i. (estimated by figure); 1.31 ± 0.31 %ID/g at 90 min p.i.) (*141*). First clinical results about [^{18}F]SiFA*lin*-TATE in direct comparison with [^{68}Ga]Ga-DOTA-TOC in 13 patients lead to the conclusion of 'favorable characteristics' (*212*). In this study, a slightly higher bone uptake was found for [^{18}F]SiFA*lin*-TATE compared to the non-fluorinated [^{68}Ga]Ga-DOTA-TOC (SUV_{max}: 1.2 ± 0.5 vs. 0.7 ± 0.2; SUV_{mean}: 0.6 ± 0.3 vs. 0.4 ± 0.1). Thus, one can suppose that a certain instability of SiFA compounds is manageable in clinical translation of imaging agents. Noteworthy, while a sufficient imaging contrast might be maintained in spite of a present instability, the question of pharmacokinetic comparability between the ^{18}F- and ^{177}Lu-labeled twins is of concern for a truly theranostic application. Indeed, apart from the observed bone uptake, biodistribution data of [^{18}F]^{nat}Lu-MSM-6 and [^{177}Lu]Lu-MSM-6 revealed nearly the same uptake pattern indicating a theranostic potential.

Besides the determined stability exhibiting room for improvement, the concept of an additional carboxylic acid directly attached at the SiFA entity resulted in promising preclinical results. The beneficial application of the acid group itself efficiently boosting hydrophilicity or as a conjugation side for further modifiers to easily manipulate HSA binding as well as hydrophilicity over a broad range could be demonstrated in a set of model peptides as well as in some PSMA ligands. Thus, the strategy for modulating the *in vitro* properties of the SiFA entity can be judged as a valuable development step delivering a basis for the design of novel radiohybrid ligands.

IV. SUMMARY AND CONCLUSION

Previously, a novel class of radiohybrid compounds was introduced by *Wurzer et al.* suitable for the imaging of PSMA-positive lesions in prostate cancer. These PSMA ligands comprise of a silicon-based fluoride acceptor (SiFA) entity for ^{18}F-labeling and a chelator for radiometal complexation. This concept paves the way for a theranostic ligand pair of chemically identical twins either labeled with fluorine-18 or lutetium-177. On this basis, several approaches were investigated in this work to modify the lead structure, Lu-rhPSMA-7.3, aiming for an optimized pharmacokinetic profile that enables a therapeutic application with a reduced radiation exposure of the red bone marrow and the kidneys as dose-limiting organs.

In a first attempt to reduce kidney retention, the dipeptide fragments Gly-L-Tyr and Gly-L-Lys were incorporated in the lead structure to design a metabolically instable linker positioned in between the PSMA binding motif and the radionuclide-bearing entity. Their recognition by renal brush border enzymes should potentially decrease PSMA-mediated activity accumulation. *In vitro* results widely indicated a well toleration of the Gly-L-Lys modification with properties similar to the reference compounds and superior compared to the lipophilic Gly-L-Tyr ligand with extraordinarily high HSA binding. Not surprisingly, the Gly-L-Tyr ligand exhibited a remarkably slow blood clearance *in vivo*. In general, this concept led to no clear improvement of the tumor-to-kidney ratio in LNCaP tumor-bearing mice compared to the lead compound despite the proof of metabolic instability in a subset of the investigated ligands.

Soon, the binding strength towards HSA as most abundant plasma protein was assessed as a key parameter to maximize tumor-to-background ratios by fine-tuning pharmacokinetics to a fast whole-body clearance while preserving a reasonable tumor uptake. One concept assumed to accomplish this intent was the development of ligand constructs with a linker moiety branching off the main peptide chain to provide a distant terminal position for exchangeable entities with variable HSA binding strength. While a suitable anchoring position for a variety of additional linker moieties (Pro_9, Ser_9, $(Ser\text{-}Gly\text{-}Gly)_3$, PEG_8) was found to result in PSMA ligands with suitable target affinity (9–13 nM), the attachment of a strongly exposed, terminal, aromatic HSA binder led to quite lipophilic derivatives. Interestingly, HSA binding was dependent on the chosen linker with a remarkably decreased binding strength for derivatives with a rigid Pro_9-linker. However, the synthesis of such constructs was judged as overelaborated with low yields and the ligands were assessed to possess low potential for further optimizations.

Another project was focused on the reduction of the ligand's highly negative net charge as this was proposed to have an influence on renal tubular reabsorption and thus, kidney retention. For this purpose, three carboxylic acids in the linker of the lead structure were estimated as not essential for target affinity and were subsequently altered or omitted. The attempt to substitute the ornithine carboxylic acid by a shift of the 'orn-EuE' motif to the established structural 'Nal-KuE' motif was followed by a drastic drop in affinity and hydrophilicity in combination with the

radiohybrid unit (DOTAGA-dap(SiFA)). Furthermore, this additional aromatic entity strongly increased the HSA binding. The insertion of a physiologically uncharged, hydrophilic PEG_8-linker between the naphthyl residue and the SiFA entity in the ligand RNC-4 could at least partially compensate the negative influence in all these parameters. Though, the biodistribution study showed no improved tumor-to-kidney ratio but clearly revealed a decelerated blood/whole-body clearance probably as a consequence of the increased lipophilicity and HSA binding. Smaller structural changes by the omission of the carboxylic acid in proximity to the SiFA entity or even the substitution with a positively charged amino group were well tolerated regarding the target affinity. As similarly published for ibuprofen-modified PSMA ligands, this approach was also useful to decrease HSA binding at the cost of a certain loss of hydrophilicity as determined *in vitro*. Opposingly, *in vivo* results indicated no clear benefit for tumor-to-blood ratios. On the other hand, the change in net charge by the use of an amino group indeed significantly reduced the kidney retention, as hypothesized.

To face the generally high lipophilicity and HSA binding of SiFA-based compounds in a more universal and modular approach, the novel SiFA entity 5-SiFA-isophthalic acid [(5-SiFA)Ip] was developed with a divergent substituent pattern at the aromatic moiety and an additional carboxylic acid. The *in vitro* properties were evaluated in a set of model peptides as well as PSMA ligands. It was demonstrated that the simple addition of this charged group directly attached at the lipophilic prosthetic group could efficiently boost the hydrophilicity (decrease of logD by 1–3 orders of magnitude). Moreover, using the second acid group as conjugation site allows for a convenient, modular attachment of further modifiers to facilitate the adjustment of a ligand's pharmacokinetics to respective radiopharmaceutical requirements. This possibility was shown to enable the modulation of HSA binding over a broad range in two ways: 1) electrostatic repulsion by functional groups or 2) steric shielding by bulky groups with low HSA affinity.

Admittedly, the theranostic concept is restrained by the higher reactivity/limited stability of the Si–F bond within the novel prosthetic group, especially found for derivatives bearing the (5-SiFA)Ip moiety in a di-conjugated way. Compared to [^{18}F]^{nat}Ga-rhPSMA-7.3, *in vivo* experiments indicated a 3- and 6-fold higher bone uptake 1 h p.i. in a corresponding terminal or bridging embedding ([^{18}F]MSM-3 and [^{18}F]^{nat}Lu-MSM-6, respectively). Whether this impedes the clinical translation for a potential diagnostic application would have to be assessed by first-in-human studies. If necessary, an enhancement of the stability might be achieved by manipulating the electron density within the aromatic moiety, for example by substitution of the amide bonds by different functional groups for conjugation.

Nevertheless, the therapeutic twin [^{177}Lu]Lu-MSM-6 exhibited an outstanding tumor-to-blood ratio even surpassing the value of the FDA-approved, current clinical gold standard [^{177}Lu]Lu-PSMA-617 by a factor of two and a 6.5-fold improved tumor-to-kidney ratio compared to the lead compound [^{177}Lu]Lu-rhPSMA-7.3 at 24 h post injection. These findings render [^{177}Lu]Lu-MSM-6 as an interesting candidate for clinical investigation in a therapeutic context.

V. SUPPLEMENTAL INFORMATION

1. Overview of *In Vitro* Data

Table 4: Overview of *in vitro* data of PSMA ligands. All data of compounds bearing a chelating agent refer to the corresponding [$^{nat/177}$Lu]Lu-complexes; n.d. = not determined.

Compound	IC_{50} [nM] (n ≥ 3)	Internalization [% of Reference Ligand] (n ≥ 3)	$logD_{pH\ 7.4}$ (n ≥ 6)	HSA Binding (AMSEC, MW_{App}) [kDa]	HSA Binding (HPAC) [%]
Reference Ligands					
rhPSMA-7.3	3.3 ± 1.0	184 ± 12	–4.12 ± 0.11	21.6	98.6
rhPSMA-10.1	2.8 ± 0.51	177 ± 15	–3.78 ± 0.06	17.2	96.3
PSMA-617	3.3 ± 0.20	203 ± 10	–4.10 ± 0.10	9.4	84.9
PSMA I&T	4.2 ± 0.78	145 ± 14	–4.10 ± 0.10	1.9	71.9
Ligands Aiming for Metabolic Instability (MI)					
MI-1	5.6 ± 1.0	82 ± 3.0	–2.81 ± 0.03	39.9	92.7
MI-2	5.4 ± 1.2	151 ± 6.2	–3.12 ± 0.05	20.4	98.2
MI-3	3.1 ± 0.40	162 ± 5.9	–3.51 ± 0.07	11.6	90.2
MI-4	9.5 ± 1.3	98 ± 7.0	–2.88 ± 0.20	9.9	95.6
MI-5	5.1 ± 1.1	167 ± 2.3	–3.08 ± 0.22	10.2	88.8
Branched Linker Constructs (BLC) for HSA Binding Modulation					
BLC-1	>1000	n.d.	n.d.	n.d.	n.d.
BLC-2	70 ± 19	n.d.	n.d.	n.d.	n.d.
BLC-3	43 ± 13	n.d.	n.d.	n.d.	n.d.
BLC-4	7.8 ± 1.7	225 ± 8.4	–3.04 ± 0.04	3.6	76.7
BLC-5	9.3 ± 2.4	160 ± 11	–2.82 ± 0.10	4.4	87.9
BLC-6	11 ± 3.0	n.d.	–4.11 ± 0.06	n.d.	n.d.
BLC-7	9.9 ± 3.5	n.d.	–4.07 ± 0.16	n.d.	n.d.
BLC-8	9.2 ± 1.2	n.d.	–3.55 ± 0.05	n.d.	n.d.
BLC-9	9.2 ± 0.41	58 ± 3.6	–2.33 ± 0.09	21.3	98.5
BLC-10*	n.d.	n.d.	n.d.	n.d.	n.d.
BLC-11	13 ± 1.9	40 ± 2.9	–2.45 ± 0.09	38.3	97.5
BLC-12	9.6 ± 1.9	18 ± 0.76	–2.13 ± 0.17	41.9	92.9
Ligands with Reduced Net Charge (RNC)					
RNC-1	62 ± 8.3	n.d.	–0.89 ± 0.04	n.d.	n.d.
RNC-2	30 ± 12	20 ± 2.3	–0.83 ± 0.14	50.0	97.6
RNC-3	17 ± 2.7	34 ± 5.7	–2.31 ± 0.08	52.4	98.4
RNC-4	8.1 ± 0.90	44 ± 1.6	–1.97 ± 0.07	29.9	95.6
RNC-5	4.9 ± 0.67	232 ± 10	–3.38 ± 0.02	15.9	96.0
RNC-6	6.1 ± 0.25	163 ± 6.9	–2.88 ± 0.06	12.1	89.8
RNC-7	7.5 ± 0.70	121 ± 6.0	–2.90 ± 0.07	8.1	74.8
Ligands with Modified SiFA Moieties (MSM)					
MSM-1	327 ± 73	n.d.	n.d.	n.d.	98.7
MSM-2	14 ± 2.0	n.d.	n.d.	n.d.	98.2
MSM-3	6.5 ± 1.6	n.d.	n.d.	n.d.	98.7
MSM-4	4.1 ± 1.9	n.d.	n.d.	n.d.	96.7
MSM-5	5.6 ± 1.1	162 ± 8.1	–3.57 ± 0.10	9.1	94.0
MSM-6	4.9 ± 0.91	181 ± 2.5	–4.03 ± 0.04	2.7	78.9

*Ligand could not be isolated due to inseparable deletion peptides formed during the synthesis.

Table 5: Overview of *in vitro* data of model peptides (MPs) comprising of the GK-, GD- and GY-series with various SiFA entities attached; n.d. = not determined.

Compound	RCY [%] (n ≥ 3)	RCC [%] (n ≥ 3)	rRCC [%] (n = 3)	$^{19}F\{^{29}Si\}$NMR δ (ppm)	Half-Lives of ^{18}F-Defluorination [h] (n = 3)			$logD_{pH\ 7.4}$ (n = 10)	HSA Binding (HPAC) [%]
					pH 7.4, 37 °C	pH 5.5, 90 °C	NaF (1 mM), pH 6.5, rt		
MP-1GK	76 ± 14	77 ± 7.5	100	–187.17	2.0 ± 0.11	10 ± 1.7	0.90 ± 0.02	1.24 ± 0.10	93.3
MP-2GK	62 ± 2.6	74 ± 9.3	91 ± 0.40	–186.90	1.6 ± 0.03	9.0 ± 0.48	0.81 ± 0.03	1.12 ± 0.05	90.1
MP-3GK	75 ± 1.8	78 ± 3.0	134 ± 6.9	–186.66	1.7 ± 0.04	6.8 ± 1.7	1.4 ± 0.05	–1.66 ± 0.03	85.9
MP-K4GK	77 ± 1.7	81 ± 0.7	256 ± 32	–186.19	0.46 ± 0.07	2.4 ± 0.18	0.25 ± 0.004	–1.56 ± 0.03	42.0
MP-E4GK	77 ± 2.5	83 ± 2.9	238 ± 22	n.d.	0.81 ± 0.03	2.1 ± 0.12	0.64 ± 0.01	–1.19 ± 0.07	72.1
MP-3KG	75 ± 5.1	78 ± 5.1	106 ± 1.8	n.d.	11 ± 1.8	11 ± 0.30	1.1 ± 0.07	–1.68 ± 0.00	85.6
MP-(PEG8)4GK	78 ± 5.9	83 ± 5.5	165 ± 6.2	n.d.	0.56 ± 0.11	3.1 ± 0.33	0.45 ± 0.07	–0.64 ± 0.08	30.4
MP-Gal6N4GK	78 ± 2.0	84 ± 2.0	159 ± 9.4*	n.d.	0.38 ± 0.06	2.7 ± 0.43	0.32 ± 0.09	–1.08 ± 0.01	44.8
MP-1GD	73 ± 5.2	77 ± 4.8	100	–187.17	**	20 ± 4.8	2.2 ± 0.02	–0.72 ± 0.05	98.3
MP-2GD	58 ± 5.0	59 ± 3.4	71 ± 1.6	–186.90	**	12 ± 1.1	1.9 ± 0.07	–1.10 ± 0.02	97.6
MP-3GD	74 ± 10	73 ± 9.5	111 ± 1.8	–186.65	**	7.8 ± 1.4	3.3 ± 0.30	–3.17 ± 0.05	97.8
MP-K4GD	80 ± 13	82 ± 11	253 ± 46	–186.22	9.8 ± 1.5	2.5 ± 0.33	0.77 ± 0.07	–3.07 ± 0.07	63.0
MP-E4GD	75 ± 5.3	84 ± 2.1	228 ± 18	n.d.	n.d.	n.d.	n.d.	–2.02 ± 0.08	97.8
MP-1GY	72 ± 7.7	78 ± 11	100	–187.12	0.69 ± 0.01	5.4 ± 0.14	1.8 ± 0.29	1.20 ± 0.05	97.9
MP-2GY	62 ± 10	73 ± 4.1	69 ± 2.0	–186.86	0.82 ± 0.11	6.9 ± 1.1	1.74 ± 0.44	1.25 ± 0.06	96.8
MP-3GY	71 ± 11	72 ± 13	122 ± 0.73	–186.62	1.3 ± 0.21	8.3 ± 1.8	2.5 ± 0.16	–1.29 ± 0.03	97.1
MP-K4GY	79 ± 4.8	85 ± 5.4	256 ± 33	–186.28	0.29 ± 0.04	2.2 ± 0.2	0.56 ± 0.03	–1.18 ± 0.01	82.6
MP-E4GY	77 ± 1.4	84 ± 2.1	252 ± 27	n.d.	n.d.	n.d.	n.d.	–1.05 ± 0.07	96.6

*Quality controls via HPLC show the formation of two unidentified side products (approximately 5–10%) for the Gal6N-derivative which were added to the test compound integral and are estimated to occur by virtue of keto- and enol tautomerism at the sugar moiety.
**Half-lives not given because of unprecise regression (R^2<<90%) with stabilities of >95% intact MP after 2 h.

2. Overview of *In Vivo* Data

Table 6: *Ex vivo* biodistribution data of rhPSMA-7.3, rhPSMA-10.1 and PSMA-617 at 24 h p.i. in male LNCaP (I/II/III) tumor-bearing CB17-SCID mice; PG = parotid glands, SG = submandibular glands; data expressed as percentage of the injected dose per gram (%ID/g) and mean ± standard deviation; n.d. = not determined.

Organ	Activity Accumulation [%ID/g] of [^{177}Lu]Lu-Compounds, 24 h p.i.						
	rhPSMA-7.3* (n = 4, LNCaP I)	**rhPSMA-7.3** (n = 5, LNCaP III)	**rhPSMA-10.1*** (n = 5, LNCaP I)	**rhPSMA-10.1** (n = 4, LNCaP II)	**rhPSMA-10.1** (n = 4, LNCaP III)	**PSMA-617*** (n = 4, LNCaP I)	**PSMA-617** (n = 5, LNCaP III)
Blood	0.0032 ± 0.0007	0.0046 ± 0.0018	0.0009 ± 0.0001	0.0010 ± 0.0006	0.0023 ± 0.0008	0.0056 ± 0.0026	0.0007 ± 0.0003
Heart	0.0306 ± 0.0093	0.0333 ± 0.0027	0.0174 ± 0.0013	0.0175 ± 0.0031	0.0203 ± 0.0056	0.0119 ± 0.0043	0.0034 ± 0.0019
Lung	0.0491 ± 0.0114	0.0768 ± 0.0160	0.0317 ± 0.0040	0.0350 ± 0.0098	0.0352 ± 0.0162	0.0393 ± 0.0130	0.0134 ± 0.0043
Liver	0.2165 ± 0.0402	0.2352 ± 0.0342	0.1821 ± 0.0552	0.2302 ± 0.0811	0.1751 ± 0.0492	0.1167 ± 0.0567	0.0279 ± 0.0031
Spleen	0.7333 ± 0.2328	0.5817 ± 0.1595	0.1749 ± 0.0289	0.2410 ± 0.0411	0.1942 ± 0.0318	0.0812 ± 0.0063	0.0482 ± 0.0228
Pancreas	0.0247 ± 0.0049	0.0241 ± 0.0037	0.0132 ± 0.0022	0.0183 ± 0.0041	0.0160 ± 0.0066	0.0106 ± 0.0040	0.0055 ± 0.0020
Stomach	0.0592 ± 0.0281	0.0434 ± 0.0158	0.0556 ± 0.0135	0.0768 ± 0.0192	0.0441 ± 0.0211	0.0201 ± 0.0028	0.0500 ± 0.0192
Intestine	0.1325 ± 0.0814	0.1001 ± 0.0584	0.1147 ± 0.0523	0.6464 ± 0.2882	0.0744 ± 0.0483	0.1185 ± 0.0822	0.2252 ± 0.1785
Kidney	9.8160 ± 2.7388	11.3738 ± 1.2675	1.9737 ± 0.7770	1.5223 ± 0.3272	2.7754 ± 1.3387	1.4421 ± 0.4243	0.2867 ± 0.0760
Adrenals	0.5614 ± 0.2215	0.4233 ± 0.0765	0.0604 ± 0.0415	0.1275 ± 0.0614	0.1133 ± 0.0506	0.1910 ± 0.0711	0.0203 ± 0.0021
Muscle	0.0091 ± 0.0031	0.0094 ± 0.0029	0.0033 ± 0.0016	0.0046 ± 0.0011	0.0057 ± 0.0022	0.0092 ± 0.0018	0.0011 ± 0.0007
Bone	0.0475 ± 0.0097	0.0307 ± 0.0060	0.0218 ± 0.0078	0.0290 ± 0.0044	0.0317 ± 0.0050	0.0267 ± 0.0174	0.0052 ± 0.0034
Tumor	11.6274 ± 2.2372	18.1740 ± 3.9884	9.8244 ± 0.2982	16.1078 ± 3.0602	13.0021 ± 1.9868	7.4568 ± 0.8969	10.2172 ± 2.8471
PG	0.1314 ± 0.0424	0.1068 ± 0.0254	0.0413 ± 0.0087	0.0651 ± 0.0150	0.0582 ± 0.0080	n.d.	0.0164 ± 0.0073
SG	0.0564 ± 0.0103	0.0644 ± 0.0120	0.0368 ± 0.0066	0.0443 ± 0.0071	0.0349 ± 0.0079	n.d.	0.0070 ± 0.0024
T/Blood	3842.8 ± 1145.2	4255.6 ± 1030.2	11497.6 ± 1952.7	20145.6 ± 6997.8	6111.5 ± 1215.1	1423.8 ± 454.7	16323.0 ± 3998.5
T/Kidney	1.24 ± 0.29	1.64 ± 0.53	5.66 ± 1.99	10.81 ± 1.64	5.47 ± 1.91	5.85 ± 2.99	36.83 ± 10.5
T/Liver	53.68 ± 1.68	78.11 ± 16.65	57.46 ± 13.11	77.83 ± 27.10	78.09 ± 18.05	91.22 ± 73.46	361.86 ± 77.9

*Data were previously published by our group (*125*).

Table 7: *Ex vivo* biodistribution data of PSMA I&T and MI-1 to -5 at 24 h p.i. in male LNCaP (I/III) tumor-bearing CB17-SCID mice; PG = parotid glands, SG = submandibular glands; data expressed as percentage of the injected dose per gram (%ID/g) and mean ± standard deviation; n.d. = not determined.

Organ	Activity Accumulation [%ID/g] of [^{177}Lu]Lu-Compounds, 24 h p.i.						
	PSMA I&T* (n = 4, LNCaP I)	**PSMA I&T** (n = 5, LNCaP III)	**MI-1** (n = 1, LNCaP I)	**MI-2** (n = 5, LNCaP I)	**MI-3** (n = 3, LNCaP I)	**MI-4** (n = 4, LNCaP I)	**MI-5** (n = 4, LNCaP I)
Blood	0.0118 ± 0.0064	0.0061 ± 0.0024	0.0261	0.0058 ± 0.0041	0.0044 ± 0.0027	0.0014 ± 0.0012	0.0010 ± 0.0007
Heart	0.0486 ± 0.0339	0.0208 ± 0.0061	0.0192	0.0156 ± 0.0101	0.0062 ± 0.0012	0.0232 ± 0.0022	0.0118 ± 0.0022
Lung	0.1576 ± 0.0285	0.1138 ± 0.0204	0.0381	0.0348 ± 0.0101	0.0252 ± 0.0057	0.0715 ± 0.0760	0.0254 ± 0.0037
Liver	0.0485 ± 0.0109	0.0553 ± 0.0235	0.1643	0.0679 ± 0.0392	0.0331 ± 0.0018	0.2106 ± 0.0502	0.1082 ± 0.0099
Spleen	1.9416 ± 1.0077	1.2047 ± 0.9384	0.5508	0.1191 ± 0.0611	0.1261 ± 0.0219	0.2131 ± 0.1029	0.1329 ± 0.0220
Pancreas	0.0480 ± 0.0287	0.0295 ± 0.0229	0.3587	0.0068 ± 0.0036	0.0043 ± 0.0015	0.0177 ± 0.0039	0.0128 ± 0.0011
Stomach	0.0483 ± 0.0212	0.0326 ± 0.0112	0.0284	0.0571 ± 0.0291	0.0534 ± 0.0107	0.0362 ± 0.0200	0.0198 ± 0.0068
Intestine	0.1202 ± 0.0646	0.0507 ± 0.0259	0.3462	0.2554 ± 0.1980	0.2895 ± 0.0635	0.0779 ± 0.0667	0.0794 ± 0.0190
Kidney	34.66.19 ± 17.2004	15.8527 ± 10.6895	4.9682	6.0394 ± 6.2945	5.0987 ± 3.5129	8.2684 ± 1.9991	2.1049 ± 0.3451
Adrenals	1.0569 ±0.2398	1.3590 ± 0.4138	0.1712	0.2743 ± 0.2019	0.1489 ± 0.0653	0.0478 ± 0.0196	0.0827 ± 0.0137
Muscle	0.0097 ± 0.0037	0.0051 ± 0.0030	0.0052	0.0046 ± 0.0027	0.0021 ± 0.0012	0.0087 ± 0.0031	0.0025 ± 0.0011
Bone	0.0142 ± 0.0037	0.0209 ± 0.0053	0.0278	0.0596 ± 0.0352	0.0173 ± 0.0053	0.0193 ± 0.0045	0.0251 ± 0.0093
Tumor	4.0636 ± 1.1186	7.5780 ± 2.3957	3.7848	6.3378 ± 1.4994	6.4127 ± 1.0729	5.4203 ± 1.3463	9.1141 ± 0.9249
PG	n.d.	0.1346 ± 0.0728	0.0656	0.0505 ± 0.0296	0.0415 ± 0.0193	0.0645 ± 0.0058	0.0363 ± 0.0073
SG	n.d.	0.0581 ± 0.0247	0.0228	0.0162 ± 0.0094	0.0126 ± 0.0038	0.0437 ± 0.0035	0.0202 ± 0.0026
T/Blood	408.1 ± 209.3	1288.5 ± 121.9	144.8	1539.5 ± 725.2	1809.6 ± 829.7	7945.8 ± 6197.3	16325.2 ± 13579.1
T/Kidney	0.15 ± 0.08	0.61 ± 0.21	0.76	2.41 ± 1.54	1.92 ± 1.00	0.71 ± 0.26	4.47 ± 0.98
T/Liver	86.07 ± 30.84	155.09 ± 57.08	23.03	129.55 ± 76.72	196.19 ± 44.53	26.45 ± 6.13	84.67 ± 9.87

*Data were previously published by our group (*160*).

Table 8: *Ex vivo* biodistribution data of RNC-4 to -7 and MSM-5 and -6 at 24 h p.i. in male LNCaP (I/III) tumor-bearing CB17-SCID mice; PG = parotid glands, SG = submandibular glands; data expressed as percentage of the injected dose per gram (%ID/g) and mean ± standard deviation.

Organ	Activity Accumulation [%ID/g] of [^{177}Lu]Lu-Compounds, 24 h p.i.					
	RNC-4 (n = 5, LNCaP I)	**RNC-5 (n = 4, LNCaP II)**	**RNC-6 (n = 4, LNCaP I)**	**RNC-7 (n = 5, LNCaP III)**	**MSM-5 (n = 5, LNCaP III)**	**MSM-6 (n = 5, LNCaP III)**
Blood	0.5189 ± 0.1641	0.0026 ± 0.0014	0.0042 ± 0.0019	0.0007 ± 0.0001	0.0061 ± 0.0019	0.0004 ± 0.0003
Heart	0.2073 ± 0.0425	0.0339 ± 0.0061	0.0254 ± 0.0061	0.0139 ± 0.0013	0.0257 ± 0.0050	0.0100 ± 0.0027
Lung	0.5410 ± 0.0932	0.0498 ± 0.0181	0.0469 ± 0.0094	0.0235 ± 0.0033	0.0633 ± 0.0245	0.0170 ± 0.0030
Liver	0.7405 ± 0.1205	0.2504 ± 0.0196	0.2848 ± 0.0567	0.1971 ± 0.0106	0.1725 ± 0.0651	0.1135 ± 0.0136
Spleen	0.4902 ± 0.1251	0.6327 ± 0.1535	0.3218 ± 0.0557	0.5640 ± 0.1031	1.4191 ± 0.3867	0.1367 ± 0.0269
Pancreas	0.0919 ± 0.0224	0.0225 ± 0.0042	0.0264 ± 0.0070	0.0131 ± 0.0033	0.0403 ± 0.0132	0.0112 ± 0.0023
Stomach	0.2232 ± 0.1242	0.0414 ± 0.0097	0.0829 ± 0.0379	0.0461 ± 0.0262	0.0435 ± 0.0220	0.0332 ± 0.0215
Intestine	0.4061 ± 0.2690	0.0874 ± 0.0428	0.2229 ± 0.0932	0.0948 ± 0.0348	0.0703 ± 0.0384	0.1445 ± 0.1219
Kidney	6.3662 ± 3.1062	8.3965 ± 1.9839	2.0983 ± 0.4949	0.8923 ± 0.1145	35.2650 ± 12.7784	0.9725 ± 0.4269
Adrenals	0.4394 ± 0.2100	0.3678 ± 0.0410	0.1488 ± 0.0477	0.0693 ± 0.0230	0.9439 ± 0.1771	0.0275 ± 0.0168
Muscle	0.0595 ± 0.0217	0.0102 ± 0.0020	0.0067 ± 0.0033	0.0036 ± 0.0009	0.0134 ± 0.0044	0.0021 ± 0.0009
Bone	0.1490 ± 0.0201	0.0301 ± 0.0072	0.0363 ± 0.0061	0.0237 ± 0.0053	0.0330 ± 0.0074	0.0234 ± 0.0035
Tumor	6.9225 ± 1.6837	16.1749 ± 1.3241	11.8594 ± 0.7477	5.2228 ± 1.7612	12.0171 ± 2.3741	9.9269 ± 3.0591
PG	0.2933 ± 0.0777	0.1234 ± 0.0114	0.0857 ± 0.0181	0.0414 ± 0.0054	0.1695 ± 0.0424	0.0261 ± 0.0048
SG	0.1946 ± 0.0441	0.0690 ± 0.0068	0.0520 ± 0.0128	0.0311 ± 0.0042	0.0831 ± 0.0158	0.0195 ± 0.0049
T/Blood	13.83 ± 2.25	7775.7 ± 3335.3	2950.4 ± 682.5	8429.9 ± 4117.7	2064.7 ± 460.5	31658.5 ± 15690.7
T/Kidney	1.27 ± 0.44	2.03 ± 0.45	5.94 ± 1.27	6.00 ± 2.35	0.37 ± 0.11	10.71 ± 1.64
T/Liver	9.33 ± 1.30	64.70 ± 4.01	42.91 ± 6.70	26.36 ± 8.19	75.20 ± 16.21	91.52 ± 40.01

Table 9: *Ex vivo* biodistribution data of PSMA I&T and MI-1 to -5 at 1 h p.i. in male LNCaP (I/III) tumor-bearing CB17-SCID mice; PG = parotid glands, SG = submandibular glands; data expressed as percentage of the injected dose per gram (%ID/g) and mean ± standard deviation; n.d. = not determined.

Organ	Activity Accumulation [%ID/g] , 1 h p.i.				
	[^{18}F]^{nat}Ga-rhPSMA-7.3* **(n = 4, LNCaP I)**	**[^{18}F]MSM-3** **(n = 5, LNCaP III)**	**[^{18}F]^{nat}Lu-MSM-5** **(n = 5, LNCaP III)**	**[^{18}F]^{nat}Lu-MSM-6** **(n = 5, LNCaP III)**	**[^{177}Lu]Lu-MSM-6** **(n = 3, LNCaP III)**
Blood	0.96 ± 0.24	0.5509 ± 0.2409	0.4210 ± 0.0963	0.4157 ± 0.0909	0.3047 ± 0.175
Heart	0.87 ± 0.17	0.4233 ± 0.1313	0.4227 ± 0.1018	0.3620 ± 0.1681	0.1953 ± 0.0440
Lung	2.2 ± 0.35	0.9921 ± 0.3264	1.2022 ± 0.1399	0.6154 ± 0.1079	0.5119 ± 0.1394
Liver	0.69 ± 0.13	7.1993 ± 4.8286	0.4771 ± 0.1509	0.3340 ± 0.0572	0.2036 ± 0.0355
Spleen	16.6 ± 2.6	6.4396 ± 3.5988	31.703 ± 8.233	6.7052 ± 3.5854	6.3744 ± 0.4398
Pancreas	0.63 ± 0.44	0.8168 ± 0.6301	0.5955 ± 0.1146	0.2375 ± 0.0400	0.2026 ± 0.0500
Stomach	0.44 ± 0.23	0.5354 ± 0.4056	0.4781 ± 0.1721	0.3503 ± 0.1234	0.1963 ± 0.0338
Intestine	0.35 ± 0.07	17.702 ± 1.565	0.3490 ± 0.1130	0.5756 ± 0.3699	0.1579 ± 0.0342
Kidney	292 ± 45.1	67.113 ± 13.942	186.24 ± 23.37	114.71 ± 22.94	118.07 ± 4.05
Adrenals	2.2 ± 0.83	2.3128 ± 0.8259	6.0186 ± 1.0541	1.9899 ± 0.6469	1.6907 ± 0.3168
Muscle	0.33 ± 0.15	0.2021 ± 0.0866	0.1816 ± 0.0180	0.1278 ± 0.0325	0.0814 ± 0.0185
Bone	0.38 ± 0.32	1.1620 ± 0.2233	0.6496 ± 0.1074	2.4349 ± 0.5794	0.1100 ± 0.0190
Tumor	18.3 ± 7.2	8.4636 ± 2.9910	11.415 ± 2.419	10.996 ± 3.413	12.560 ± 3.194
PG	n.d.	0.8068 ± 0.2778	2.4481 ± 0.5265	0.7551 ± 0.1381	0.8472 ± 0.1335
SG	n.d.	0.5194 ± 0.2039	1.0298 ± 0.0863	0.3642 ± 0.1031	0.3189 ± 0.0487
T/Blood	n.d.	16.426 ± 4.417	27.303 ± 2.170	26.058 ± 3.957	43.867 ± 13.752
T/Kidney	n.d.	0.1238 ± 0.0238	0.0614 ± 0.0110	0.0953 ± 0.0208	0.1069 ± 0.0288
T/Liver	n.d.	1.412 ± 0.592	24.837 ± 3.816	32.201 ± 4.994	65.067 ± 23.777

*Data were previously published by our group (*77*).

3. Figure Index

4. Scheme and Table Index

Schemes

Tables

5. Abbreviations

%ID	percentage of injected dose
2-CTC	2-chlorotrityl chloride
2-PMPA	2-(phosphonomethyl)pentanedioic acid
AA	amino acid
ADT	androgen deprivation therapy
Alloc	allyloxycarbonyl
AMSEC	albumin-mediated size exclusion chromatography
AP-2	adaptor protein-2
ARPI	androgen receptor pathway inhibitor
ASIR	age-standardized incidence rate
ASMR	age-standardized mortality rate
AUC	area under the curve
BBE	brush border enzyme
BBM	brush border membrane
BLC	branched linker constructs
Boc	*tert*-butyloxycarbonyl
BSA	bovine serum albumin
BSoC	best standard of care
Bzl	benzyl
CB-17 SCID	mouse strain with severe combined immunodeficiency (SCID)
CDI	1,1'-carbonyldiimidazole
CPM	carboxypeptidase M
CT	computed tomography
DCE	1,2-dichloroethane
DCM	dichloromethane
Dde	1-(4,4-dimethyl-2,6-dioxocyclohex-1-ylidene)ethyl
DIPEA	*N*,*N*-diisopropylethylamine
DMAP	4-dimethylaminopyridine
DMSO	dimethyl sulfoxide
DNP	dinitrophenyl
DOTA	1,4,7,10-tetraazacyclododecane-1,4,7,10-tetraacetic acid
DOTAGA	1,4,7,10-tetraazacyclododececane,1-(glutaricacid)-4,7,10-triacetic acid
DRE	digital rectal examination
EAU	European Association of Urology
EBRT	external beam radiation
EDTA	ethylenediamine tetraacetic acid
ESI-MS	electrospray ionization mass spectrometry
Et_2O	diethyl ether
EtOAc	ethyl acetate
EtOH	ethanol
EuE	L-glutamate-urea-L-glutamate
FBS	fetal bovine serum
FDA	Food and Drug Administration
Fmoc	fluorenylmethoxycarbonyl
FOLH 1	folate hydrolase I
GCP II	glutamate carboxypeptidase II
GP	general procedure
H_3RESCA	restrained chelating agent
HBED-CC	*N*,*N*'-bis(2-hydroxy-5-(carboxyethyl) benzyl)ethylenediamine-*N*,*N*'-diacetic acid
HBSS	Hank's balanced salt solution
HDI	human development index
HEPES	4-(2-hydroxyethyl)-1-piperazineethanesulfonic acid
HLB	hydrophilic-lipophilic-balanced; reversed-phase sorbent
HOAt	1-hydroxy-7-azabenzotriazole
HPAC	high-performance affinity chromatography
HPFC	high-performance flash chromatography
HPLC	high-performance liquid chromatography
HSA	human serum albumin
IC_{50}	half-maximal inhibitory concentration
INEPT	insensitive nuclei enhancement by polarization transfer
IPB	4-(*para*-iodophenyl)butyric acid
ISUP	International Society of Urological Pathology
K'	capacity factor
KuE	L-lysine-urea-L-glutamate
LET	linear energy transfer
LNCaP	lymph node carcinoma of the prostate; a human PSMA-expressing cancer cell line
LUMO	lowest unoccupied molecular orbital

mCRPC	metastasized castration-resistant prostate cancer
MeCN	acetonitrile
mHSPC	metastasized hormon-sensitive prostate cancer
MI	metabolic instability
mpMRI	multiparametric magnetic resonance imaging
MSM	modified SiFA moieties
MW_{App}	apparent molecular weight [kDa], parameter representing HSA binding strength
NAAG	*N*-acetyl-L-aspartyl-L-glutamate
NAALADase	*N*-acetylated α-linked acidic dipeptidase
NaOAc	sodium acetate
NC	net charge
NEP	neutral endopeptidase
NMP	*N*-methyl-2-pyrrolidone
NMR	nuclear magnetic resonance
NOTA	1,4,7-triazacyclononane-1,4,7-triacetic acid
NPV	negative predictive value
PBS	phosphate buffered solution
PC3-PIP	PSMA-expressing cell line
PCa	prostate cancer
PEG	polyethylene glycol
PET	positron emission tomography
Ph	phenyl
PLND	pelvic lymph node dissection
PPV	positive predictive value
PRLT	PSMA-targeted radiologand therapy
PSA	prostate-specific antigen
PSMA	prostate-specific membrane antigen
QMA	quarternary methyl ammonium
RCC	radiochemical conversion
RCY	radiochemical yield
RNC	reduced net charge
RP	reversed-phase
rRCC	relative radiochemical conversion
rt	room temperature
SAX	strong anion exchange
SiFA	silicon-based fluoride acceptor
SPECT	single-photon emission computed tomography
t_0	dead time
TAT	targeted α-radiation therapy
TBDMSCl	*tert*-butyldimethylsilyl chloride
TBTU	2-(1*H*-benzotriazole-1-yl)-1,1,3,3-tetramethylaminium tetrafluoroborate
***t*Bu**	*tert*-butyl
TEA	triethylamine
TFA	trifluoroacetic acid
THF	tetrahydrofuran
TIPS	triisopropylsilane
TLC	thin-layer chromatography
TNM	tumor nodes metastases
t_R	retention time
UICC	Union for International Cancer Control
USPSTF	United Sates Preventive Services Task Force
UV/Vis	ultraviolet/visible light
WHO	World Health Organization

6. References

1. Sung H, Ferlay J, Siegel RL, et al. Global Cancer Statistics 2020: GLOBOCAN Estimates of Incidence and Mortality Worldwide for 36 Cancers in 185 Countries. *CA: Cancer J Clin.* 2021;71:209-249.

2. Bray F, Laversanne M, Weiderpass E, Soerjomataram I. The ever-increasing importance of cancer as a leading cause of premature death worldwide. *Cancer.* 2021;127:3029-3030.

3. Global Cancer Observatory: Cancer Today. 2020-12. Available online at: https://gco.iarc.fr/today/data/factsheets/cancers/39-All-cancers-fact-sheet.pdf. Accessed 14.07.2022.

4. Leitzmann M, Rohrmann S. Risk factors for the onset of prostatic cancer: age, location, and behavioral correlates. *Clin Epidemiol.* 2012;4:1-11.

5. Bostwick DG, Burke HB, Djakiew D, et al. Human prostate cancer risk factors. *Cancer.* 2004;101:2371-2490.

6. Allott EH, Masko EM, Freedland SJ. Obesity and Prostate Cancer: Weighing the Evidence. *Eur Urol.* 2013;63:800-809.

7. Wang L, Lu B, He M, Wang Y, Wang Z, Du L. Prostate Cancer Incidence and Mortality: Global Status and Temporal Trends in 89 Countries From 2000 to 2019. *Front Public Health.* 2022;10.

8. Lilja H, Cronin AM, Dahlin A, et al. Prediction of significant prostate cancer diagnosed 20 to 30 years later with a single measure of prostate-specific antigen at or before age 50. *Cancer.* 2011;117:1210-1219.

9. Leitlinienprogramm Onkologie: S3-Leitlinie Prostatakarzinom, Langversion 6.2, AWMF-Registernummer: 043/022OL. Available online at: https://www.leitlinienprogramm-onkologie.de/fileadmin/user_upload/Downloads/Leitlinien/Prostatatkarzinom/Version_6/LL_Prostatakarzinom_Langversion_6.2.pdf. Accessed 15.07.2022.

10. Ilic D, Neuberger MM, Djulbegovic M, Dahm P. Screening for prostate cancer. *Cochrane Database Syst Rev.* 2013;2013:Cd004720.

11. Hu JC, Nguyen P, Mao J, et al. Increase in Prostate Cancer Distant Metastases at Diagnosis in the United States. *JAMA Oncol.* 2017;3:705-707.

12. Kelly SP, Anderson WF, Rosenberg PS, Cook MB. Past, Current, and Future Incidence Rates and Burden of Metastatic Prostate Cancer in the United States. *Eur Urol Focus.* 2018;4:121-127.

13. Grossman DC, Curry SJ, Owens DK, et al. Screening for Prostate Cancer: US Preventive Services Task Force Recommendation Statement. *Jama.* 2018;319:1901-1913.

14. Mottet N, van den Bergh RCN, Briers E, et al. EAU-EANM-ESTRO-ESUR-SIOG Guidelines on Prostate Cancer—2020 Update. Part 1: Screening, Diagnosis, and Local Treatment with Curative Intent. *Eur Urol.* 2021;79:243-262.

15. Drost FH, Osses D, Nieboer D, et al. Prostate Magnetic Resonance Imaging, with or Without Magnetic Resonance Imaging-targeted Biopsy, and Systematic Biopsy for Detecting Prostate Cancer: A Cochrane Systematic Review and Meta-analysis. *Eur Urol.* 2020;77:78-94.

16. Gleason DF, Mellinger GT. Prediction of prognosis for prostatic adenocarcinoma by combined histological grading and clinical staging. *J Urol.* 1974;111:58-64.

17. Epstein JI, Egevad L, Amin MB, et al. The 2014 International Society of Urological Pathology (ISUP) Consensus Conference on Gleason Grading of Prostatic Carcinoma: Definition of Grading Patterns and Proposal for a New Grading System. *Am J Surg Pathol.* 2016;40:244-252.

18. Brierley JD, Gospodarowicz MK, Wittekind C. *TNM Classification of Malignant Tumours, 8th Edition*: John Wiley & Sons; 2017.

19. D'Amico AV, Whittington R, Malkowicz SB, et al. Biochemical outcome after radical prostatectomy, external beam radiation therapy, or interstitial radiation therapy for clinically localized prostate cancer. *Jama.* 1998;280:969-974.

20. Cooperberg MR, Pasta DJ, Elkin EP, et al. The University of California, San Francisco Cancer of the Prostate Risk Assessment score: a straightforward and reliable preoperative predictor of disease recurrence after radical prostatectomy. *J Urol.* 2005;173:1938-1942.

21. Cornford P, Bergh RCN, Briers E, et al. EAU-EANM-ESTRO-ESUR-SIOG Guidelines on Prostate Cancer 2020 published guidelines. 2020.

22. Jacklin C, Philippou Y, Brewster S, Bryant R. “More men die with prostate cancer than because of it” - an old adage that still holds true in the 21st century. *Cancer Treat Res Commun.* 2021;26:100225.

23. Klotz L, Vesprini D, Sethukavalan P, et al. Long-term follow-up of a large active surveillance cohort of patients with prostate cancer. *J Clin Oncol.* 2015;33:272-277.

24. Lu-Yao GL, Yao SL. Population-based study of long-term survival in patients with clinically localised prostate cancer. *Lancet.* 1997;349:906-910.

25. Hamdy FC, Donovan JL, Lane JA, et al. 10-Year Outcomes after Monitoring, Surgery, or Radiotherapy for Localized Prostate Cancer. *N Engl J Med.* 2016;375:1415-1424.

26. Klotz L. Active Surveillance, Quality of Life, and Cancer-related Anxiety. *Eur Urol.* 2013;64:37-39.

27. Kesch C, Heidegger I, Kasivisvanathan V, et al. Radical Prostatectomy: Sequelae in the Course of Time. *Front Surg.* 2021;8:684088.

28. Zelefsky MJ, Levin EJ, Hunt M, et al. Incidence of Late Rectal and Urinary Toxicities After Three-Dimensional Conformal Radiotherapy and Intensity-Modulated Radiotherapy for Localized Prostate Cancer. *Int J Radiat Oncol Biol Phys.* 2008;70:1124-1129.

29. Wallis CJ, Mahar AL, Choo R, et al. Second malignancies after radiotherapy for prostate cancer: systematic review and meta-analysis. *BMJ.* 2016;352:i851.

30. Huggins C, Hodges CV. Studies on prostatic cancer. I. The effect of castration, of estrogen and androgen injection on serum phosphatases in metastatic carcinoma of the prostate. *CA Cancer J Clin.* 1972;22:232-240.

31. Ng K, Smith S, Shamash J. Metastatic Hormone-Sensitive Prostate Cancer (mHSPC): Advances and Treatment Strategies in the First-Line Setting. *Oncol Ther.* 2020;8:209-230.

32. National Cancer Institute Surveillance, Epidemiology, and End Results (SEER) Program. Cancer Stat Facts Prostate Cancer. Available online at: https://seer.cancer.gov/statfacts/html/prost.html. Accessed 19.07.2022.

33. Yadav MP, Ballal S, Sahoo RK, Dwivedi SN, Bal C. Radioligand Therapy With ^{177}Lu-PSMA for Metastatic Castration-Resistant Prostate Cancer: A Systematic Review and Meta-Analysis. *AJR Am J Roentgenol.* 2019;213:275-285.

34. FDA approves Pluvicto for metastatic castration-resistant prostate cancer. Available online at: https://www.fda.gov/drugs/resources-information-approved-drugs/fda-approves-pluvicto-metastatic-castration-resistant-prostate-cancer. Accessed 19.07.2022.

35. Study of ^{177}Lu-PSMA-617 In Metastatic Castrate-Resistant Prostate Cancer (VISION). ClinicalTrials.gov Identifier: NCT03511664. Available online at: https://clinicaltrials.gov/ct2/show/NCT03511664. Accessed 19.07.2022.

36. Mesters JR, Barinka C, Li W, et al. Structure of glutamate carboxypeptidase II, a drug target in neuronal damage and prostate cancer. *EMBO J.* 2006;25:1375-1384.

37. Luthi-Carter R, Barczak AK, Speno H, Coyle JT. Molecular characterization of human brain N-acetylated alpha-linked acidic dipeptidase (NAALADase). *J Pharmacol Exp Ther.* 1998;286:1020-1025.

38. Tiffany CW, Lapidus RG, Merion A, Calvin DC, Slusher BS. Characterization of the enzymatic activity of PSM: comparison with brain NAALADase. *Prostate.* 1999;39:28-35.

39. Robinson MB, Blakely RD, Couto R, Coyle JT. Hydrolysis of the brain dipeptide N-acetyl-L-aspartyl-L-glutamate. Identification and characterization of a novel N-acetylated alpha-linked acidic dipeptidase activity from rat brain. *J Biol Chem.* 1987;262:14498-14506.

40. Pinto JT, Suffoletto BP, Berzin TM, et al. Prostate-specific membrane antigen: a novel folate hydrolase in human prostatic carcinoma cells. *Clin Cancer Res.* 1996;2:1445-1451.

41. Sácha P, Zámecník J, Barinka C, et al. Expression of glutamate carboxypeptidase II in human brain. *Neuroscience.* 2007;144:1361-1372.

42. Zhou J, Neale JH, Pomper MG, Kozikowski AP. NAAG peptidase inhibitors and their potential for diagnosis and therapy. *Nat Rev Drug Discov.* 2005;4:1015-1026.

43. Heston WD. Characterization and glutamyl preferring carboxypeptidase function of prostate specific membrane antigen: a novel folate hydrolase. *Urology.* 1997;49:104-112.

44. Silver DA, Pellicer I, Fair WR, Heston WD, Cordon-Cardo C. Prostate-specific membrane antigen expression in normal and malignant human tissues. *Clin Cancer Res.* 1997;3:81-85.

45. Ghosh A, Heston WD. Tumor target prostate specific membrane antigen (PSMA) and its regulation in prostate cancer. *J Cell Biochem.* 2004;91:528-539.

46. Kinoshita Y, Kuratsukuri K, Landas S, et al. Expression of prostate-specific membrane antigen in normal and malignant human tissues. *World J Surg.* 2006;30:628-636.

47. Pastorino S, Riondato M, Uccelli L, et al. Toward the Discovery and Development of PSMA Targeted Inhibitors for Nuclear Medicine Applications. *Curr Radiopharm.* 2020;13:63-79.

48. Yao V, Berkman CE, Choi JK, O'Keefe DS, Bacich DJ. Expression of prostate-specific membrane antigen (PSMA), increases cell folate uptake and proliferation and suggests a novel role for PSMA in the uptake of the non-polyglutamated folate, folic acid. *Prostate.* 2010;70:305-316.

49. Yao V, Parwani A, Maier C, Heston WD, Bacich DJ. Moderate Expression of Prostate-Specific Membrane Antigen, a Tissue Differentiation Antigen and Folate Hydrolase, Facilitates Prostate Carcinogenesis. *Cancer Res.* 2008;68:9070.

50. Barwe SP, Maul RS, Christiansen JJ, et al. Preferential association of prostate cancer cells expressing prostate specific membrane antigen to bone marrow matrix. *Int J Oncol.* 2007;30:899-904.

51. Sweat SD, Pacelli A, Murphy GP, Bostwick DG. Prostate-specific membrane antigen expression is greatest in prostate adenocarcinoma and lymph node metastases. *Urology.* 1998;52:637-640.

52. Ben Jemaa A, Bouraoui Y, Sallami S, et al. Co-expression and impact of prostate specific membrane antigen and prostate specific antigen in prostatic pathologies. *J Exp Clin Cancer Res.* 2010;29:171.

53. Wright GL, Jr., Haley C, Beckett ML, Schellhammer PF. Expression of prostate-specific membrane antigen in normal, benign, and malignant prostate tissues. *Urol Oncol.* 1995;1:18-28.

54. Rajasekaran AK, Anilkumar G, Christiansen JJ. Is prostate-specific membrane antigen a multifunctional protein? *Am J Physiol Cell Physiol.* 2005;288:C975-C981.

55. Bostwick DG, Pacelli A, Blute M, Roche P, Murphy GP. Prostate specific membrane antigen expression in prostatic intraepithelial neoplasia and adenocarcinoma: a study of 184 cases. *Cancer.* 1998;82:2256-2261.

56. Conway RE, Petrovic N, Li Z, Heston W, Wu D, Shapiro LH. Prostate-specific membrane antigen regulates angiogenesis by modulating integrin signal transduction. *Mol Cell Biol.* 2006;26:5310-5324.

57. Perner S, Hofer MD, Kim R, et al. Prostate-specific membrane antigen expression as a predictor of prostate cancer progression. *Hum Pathol.* 2007;38:696-701.

58. Minner S, Wittmer C, Graefen M, et al. High level PSMA expression is associated with early PSA recurrence in surgically treated prostate cancer. *Prostate.* 2011;71:281-288.

59. Israeli RS, Powell CT, Fair WR, Heston WD. Molecular cloning of a complementary DNA encoding a prostate-specific membrane antigen. *Cancer Res.* 1993;53:227-230.

60. Barinka C, Sácha P, Sklenár J, et al. Identification of the N-glycosylation sites on glutamate carboxypeptidase II necessary for proteolytic activity. *Protein Sci.* 2004;13:1627-1635.

61. Liu H, Rajasekaran AK, Moy P, et al. Constitutive and Antibody-induced Internalization of Prostate-specific Membrane Antigen. *Cancer Res.* 1998;58:4055.

62. Rajasekaran SA, Anilkumar G, Oshima E, et al. A novel cytoplasmic tail MXXXL motif mediates the internalization of prostate-specific membrane antigen. *Mol Biol Cell.* 2003;14:4835-4845.

63. Anilkumar G, Rajasekaran SA, Wang S, Hankinson O, Bander NH, Rajasekaran AK. Prostate-specific Membrane Antigen Association with Filamin A Modulates Its Internalization and NAALADase Activity. *Cancer Res.* 2003;63:2645.

64. Davis MI, Bennett MJ, Thomas LM, Bjorkman PJ. Crystal structure of prostate-specific membrane antigen, a tumor marker and peptidase. *Proc Natl Acad Sci.* 2005;102:5981-5986.

65. Barinka C, Byun Y, Dusich CL, et al. Interactions between Human Glutamate Carboxypeptidase II and Urea-Based Inhibitors: Structural Characterization. *J Med Chem.* 2008;51:7737-7743.

66. Majer P, Jackson PF, Delahanty G, et al. Synthesis and biological evaluation of thiol-based inhibitors of glutamate carboxypeptidase II: discovery of an orally active GCP II inhibitor. *J Med Chem.* 2003;46:1989-1996.

67. Stoermer D, Liu Q, Hall MR, et al. Synthesis and biological evaluation of hydroxamate-Based inhibitors of glutamate carboxypeptidase II. *Bioorg Med Chem Lett.* 2003;13:2097-2100.

68. Novakova Z, Wozniak K, Jancarik A, et al. Unprecedented Binding Mode of Hydroxamate-Based Inhibitors of Glutamate Carboxypeptidase II: Structural Characterization and Biological Activity. *J Med Chem.* 2016;59:4539-4550.

69. Zhang AX, Murelli RP, Barinka C, et al. A remote arene-binding site on prostate specific membrane antigen revealed by antibody-recruiting small molecules. *J Am Chem Soc.* 2010;132:12711-12716.

70. Babich JW, Zimmerman CN, Maresca KP. HETERODIMERS OF GLUTAMIC ACID. *PCT/US2007/083934.* 2008.

71. Kopka K, Benesova M, Barinka C, Haberkorn U, Babich J. Glu-Ureido-Based Inhibitors of Prostate-Specific Membrane Antigen: Lessons Learned During the Development of a Novel Class of Low-Molecular-Weight Theranostic Radiotracers. *J Nucl Med.* 2017;58:17S-26S.

72. HIGHLIGHTS OF PRESCRIBING INFORMATION. PYLARIFY® (piflufolastat F 18) injection. Available online at: https://www.accessdata.fda.gov/drugsatfda_docs/label/2021/214793s000lbl.pdf. Accessed 26.07.2022.

73. HIGHLIGHTS OF PRESCRIBING INFORMATION. Gallium Ga 68 PSMA-11 Injection. Available online at: https://www.accessdata.fda.gov/drugsatfda_docs/nda/2020/212642Orig1s000lbl.pdf. Accessed 26.07.2022.

74. Pan MH, Gao DW, Feng J, et al. Biodistributions of ^{177}Lu- and ^{111}In-labeled 7E11 antibodies to prostate-specific membrane antigen in xenograft model of prostate cancer and potential use of ^{111}In-7E11 as a pre-therapeutic agent for ^{177}Lu-7E11 radioimmunotherapy. *Mol Imaging Biol.* 2009;11:159-166.

75. ProstaScint® Kit (capromab pendetide). Kit for the Preparation of Indium In 111 Capromab Pendetide. . Available online at: https://www.accessdata.fda.gov/drugsatfda_docs/label/2012/103608s5043lbl.pdf. Accessed 26.07.2022.

76. Piron S, Verhoeven J, Vanhove C, De Vos F. Recent advancements in ^{18}F-labeled PSMA targeting PET radiopharmaceuticals. *Nucl Med Biol.* 2022;106-107:29-51.

77. Wurzer A, Parzinger M, Konrad M, et al. Preclinical comparison of four [^{18}F, ^{nat}Ga]rhPSMA-7 isomers: influence of the stereoconfiguration on pharmacokinetics. *EJNMMI Res.* 2020;10:149.

78. Vallabhajosula S, Nikolopoulou A, Babich JW, et al. ^{99m}Tc-Labeled Small-Molecule Inhibitors of Prostate-Specific Membrane Antigen: Pharmacokinetics and Biodistribution Studies in Healthy Subjects and Patients with Metastatic Prostate Cancer. *J Nucl Med.* 2014;55:1791.

79. Duan H, Iagaru A, Aparici CM. Radiotheranostics - Precision Medicine in Nuclear Medicine and Molecular Imaging. *Nanotheranostics.* 2022;6:103-117.

80. Troyer JK, Feng Q, Beckett ML, Wright GL, Jr. Biochemical characterization and mapping of the 7E11-C5.3 epitope of the prostate-specific membrane antigen. *Urol Oncol.* 1995;1:29-37.

81. Troyer JK, Beckett ML, Wright GL, Jr. Location of prostate-specific membrane antigen in the LNCaP prostate carcinoma cell line. *Prostate.* 1997;30:232-242.

82. Product Approval Information - Licensing Action. Available online at: https://www.accessdata.fda.gov/drugsatfda_docs/appletter/1996/capcyt102896L.htm. Accessed 27.07.2022.

83. FDA Approves First PSMA-Targeted PET Imaging Drug for Men with Prostate Cancer. Available online at: https://www.fda.gov/news-events/press-announcements/fda-approves-first-psma-targeted-pet-imaging-drug-men-prostate-cancer. Accessed 26.07.2022.

84. Hope TA, Eiber M, Armstrong WR, et al. Diagnostic Accuracy of ^{68}Ga-PSMA-11 PET for Pelvic Nodal Metastasis Detection Prior to Radical Prostatectomy and Pelvic Lymph Node Dissection: A Multicenter Prospective Phase 3 Imaging Trial. *JAMA Oncol.* 2021;7:1635-1642.

85. Fendler WP, Calais J, Eiber M, et al. Assessment of ^{68}Ga-PSMA-11 PET Accuracy in Localizing Recurrent Prostate Cancer: A Prospective Single-Arm Clinical Trial. *JAMA Oncol.* 2019;5:856-863.

86. Calais J, Ceci F, Eiber M, et al. ^{18}F-fluciclovine PET-CT and ^{68}Ga-PSMA-11 PET-CT in patients with early biochemical recurrence after prostatectomy: a prospective, single-centre, single-arm, comparative imaging trial. *Lancet Oncol.* 2019;20:1286-1294.

87. HIGHLIGHTS OF PRESCRIBING INFORMATION. LOCAMETZ® (kit for the preparation of gallium Ga 68 gozetotide injection). Available online at: https://www.accessdata.fda.gov/drugsatfda_docs/label/2022/215841s000lbl.pdf. Accessed 26.07.2022.

88. HIGHLIGHTS OF PRESCRIBING INFORMATION. PLUVICTO™ (lutetium Lu 177 vipivotide tetraxetan) injection. Available online at: https://www.accessdata.fda.gov/drugsatfda_docs/label/2022/215833s000lbl.pdf. . Accessed 26.07.2022.

89. FDA approves second PSMA-targeted PET imaging drug for men with prostate cancer. Available online at: https://www.fda.gov/drugs/news-events-human-drugs/fda-approves-second-psma-targeted-pet-imaging-drug-men-prostate-cancer. Accessed 26.07.2022.

90. Cal-Gonzalez J, Herraiz JL, España S, Desco M, Vaquero JJ, Udias JM. Positron range effects in high resolution 3D PET imaging. *2009 IEEE Nuclear Science Symposium Conference Record (NSS/MIC).* 2009:2788-2791.

91. Pienta KJ, Gorin MA, Rowe SP, et al. A Phase 2/3 Prospective Multicenter Study of the Diagnostic Accuracy of Prostate Specific Membrane Antigen PET/CT with ^{18}F-DCFPyL in Prostate Cancer Patients (OSPREY). *J Urol.* 2021;206:52-61.

92. Morris MJ, Rowe SP, Gorin MA, et al. Diagnostic Performance of ^{18}F-DCFPyL-PET/CT in Men with Biochemically Recurrent Prostate Cancer: Results from the CONDOR Phase III, Multicenter Study. *Clin Cancer Res.* 2021;27:3674-3682.

93. Sprute K, Kramer V, Koerber SA, et al. Diagnostic Accuracy of ^{18}F-PSMA-1007 PET/CT Imaging for Lymph Node Staging of Prostate Carcinoma in Primary and Biochemical Recurrence. *J Nucl Med.* 2021;62:208-213.

94. Giesel FL, Knorr K, Spohn F, et al. Detection Efficacy of ^{18}F-PSMA-1007 PET/CT in 251 Patients with Biochemical Recurrence of Prostate Cancer After Radical Prostatectomy. *J Nucl Med.* 2019;60:362-368.

95. Liu T, Toriyabe Y, Kazak M, Berkman CE. Pseudoirreversible Inhibition of Prostate-Specific Membrane Antigen by Phosphoramidate Peptidomimetics. *Biochemistry.* 2008;47:12658-12660.

96. Schuster DM. Detection rate of ^{18}F-rhPSMA-7.3 PET in patients with suspected prostate cancer recurrence: Results from a phase 3, prospective, multicenter study (SPOTLIGHT). *J Clin Oncol.* 2022;40:9-9.

97. Goffin KE, Joniau S, Tenke P, et al. Phase 2 Study of ^{99m}Tc-Trofolastat SPECT/CT to Identify and Localize Prostate Cancer in Intermediate- and High-Risk Patients Undergoing Radical Prostatectomy and Extended Pelvic LN Dissection. *J Nucl Med.* 2017;58:1408-1413.

98. Benešová M, Schäfer M, Bauder-Wüst U, et al. Preclinical Evaluation of a Tailor-Made DOTA-Conjugated PSMA Inhibitor with Optimized Linker Moiety for Imaging and Endoradiotherapy of Prostate Cancer. *J Nucl Med.* 2015;56:914-920.

99. Weineisen M, Schottelius M, Simecek J, et al. ^{68}Ga- and ^{177}Lu-Labeled PSMA I&T: Optimization of a PSMA-Targeted Theranostic Concept and First Proof-of-Concept Human Studies. *J Nucl Med.* 2015;56:1169-1176.

100. Sartor O, de Bono J, Chi KN, et al. Lutetium-177-PSMA-617 for Metastatic Castration-Resistant Prostate Cancer. *N Engl J Med.* 2021;385:1091-1103.

101. Sartor AO, Morris MJ, Chi KN, et al. PSMAfore: A phase 3 study to compare ^{177}Lu-PSMA-617 treatment with a change in androgen receptor pathway inhibitor in taxane-naïve patients with metastatic castration-resistant prostate cancer. *J Clin Oncol.* 2022;40:TPS211-TPS211.

102. Sartor AO, Tagawa ST, Saad F, et al. PSMAddition: A phase 3 trial to compare treatment with ^{177}Lu-PSMA-617 plus standard of care (SOC) versus SOC alone in patients with metastatic hormone-sensitive prostate cancer. *J Clin Oncol.* 2022;40:TPS210-TPS210.

103. Privé BM, Janssen MJR, van Oort IM, et al. Update to a randomized controlled trial of lutetium-177-PSMA in Oligo-metastatic hormone-sensitive prostate cancer: the BULLSEYE trial. *Trials.* 2021;22:768.

104. Keam SJ. Lutetium Lu 177 Vipivotide Tetraxetan: First Approval. *Mol Diagn Ther.* 2022;26:467-475.

105. Dash A, Pillai MRA, Knapp FF. Production of 177Lu for Targeted Radionuclide Therapy: Available Options. *Nuclear Medicine and Molecular Imaging.* 2015;49:85-107.

106. Morgenstern A, Apostolidis C, Kratochwil C, Sathekge M, Krolicki L, Bruchertseifer F. An Overview of Targeted Alpha Therapy with (225)Actinium and (213)Bismuth. *Curr Radiopharm.* 2018;11:200-208.

107. Haberkorn U, Giesel F, Morgenstern A, Kratochwil C. The Future of Radioligand Therapy: α, β, or Both? *J Nucl Med.* 2017;58:1017.

108. Sgouros G, Roeske JC, McDevitt MR, et al. MIRD Pamphlet No. 22 (abridged): radiobiology and dosimetry of alpha-particle emitters for targeted radionuclide therapy. *J Nucl Med.* 2010;51:311-328.

109. Delker A, Fendler WP, Kratochwil C, et al. Dosimetry for ^{177}Lu-DKFZ-PSMA-617: a new radiopharmaceutical for the treatment of metastatic prostate cancer. *Eur J Nucl Med Mol Imaging.* 2016;43:42-51.

110. Kratochwil C, Bruchertseifer F, Giesel FL, et al. ^{225}Ac-PSMA-617 for PSMA-Targeted α-Radiation Therapy of Metastatic Castration-Resistant Prostate Cancer. *J Nucl Med.* 2016;57:1941.

111. Ballal S, Yadav MP, Sahoo RK, Tripathi M, Dwivedi SN, Bal C. ^{225}Ac-PSMA-617-targeted alpha therapy for the treatment of metastatic castration-resistant prostate cancer: A systematic review and meta-analysis. *Prostate.* 2021;81:580-591.

112. Kratochwil C, Bruchertseifer F, Rathke H, et al. Targeted α-Therapy of Metastatic Castration-Resistant Prostate Cancer with ^{225}Ac-PSMA-617: Swimmer-Plot Analysis Suggests Efficacy Regarding Duration of Tumor Control. *J Nucl Med.* 2018;59:795.

113. Sathekge M, Bruchertseifer F, Vorster M, et al. Predictors of Overall and Disease-Free Survival in Metastatic Castration-Resistant Prostate Cancer Patients Receiving ^{225}Ac-PSMA-617 Radioligand Therapy. *J Nucl Med.* 2020;61:62.

114. Yadav MP, Ballal S, Sahoo RK, Tripathi M, Seth A, Bal C. Efficacy and safety of ^{225}Ac-PSMA-617 targeted alpha therapy in metastatic castration-resistant Prostate Cancer patients. *Theranostics.* 2020;10:9364-9377.

115. Wirtz M. Development of biomarkers for molecular imaging and endoradiotherapy of prostate cancer. PhD thesis, Technical University Munich. 2015.

116. Schuchardt C, Zhang J, Kulkarni HR, Chen X, Müller D, Baum RP. Prostate-Specific Membrane Antigen Radioligand Therapy Using ^{177}Lu-PSMA I&T and ^{177}Lu-PSMA-617 in Patients with Metastatic Castration-Resistant Prostate Cancer: Comparison of Safety, Biodistribution, and Dosimetry. *J Nucl Med.* 2022;63:1199.

117. Zacherl MJ, Gildehaus FJ, Mittlmeier L, et al. First Clinical Results for PSMA-Targeted α-Therapy Using ^{225}Ac-PSMA-I&T in Advanced-mCRPC Patients. *J Nucl Med.* 2021;62:669-674.

118. Liu H, Moy P, Kim S, et al. Monoclonal antibodies to the extracellular domain of prostate-specific membrane antigen also react with tumor vascular endothelium. *Cancer Res.* 1997;57:3629-3634.

119. Tagawa ST, Vallabhajosula S, Christos PJ, et al. Phase 1/2 study of fractionated dose lutetium-177–labeled anti–prostate-specific membrane antigen monoclonal antibody J591 (^{177}Lu-J591) for metastatic castration-resistant prostate cancer. *Cancer.* 2019;125:2561-2569.

120. Emmett L. Side effects of therapy with radiolabelled prostate specific membrane antigen (PSMA). *Nucl Med Mol Imaging.* 2022:214-219.

121. Wang Z, Tian R, Niu G, et al. Single Low-Dose Injection of Evans Blue Modified PSMA-617 Radioligand Therapy Eliminates Prostate-Specific Membrane Antigen Positive Tumors. *Bioconjug Chem.* 2018;29:3213-3221.

122. Choy CJ, Ling X, Geruntho JJ, et al. ^{177}Lu-Labeled Phosphoramidate-Based PSMA Inhibitors: The Effect of an Albumin Binder on Biodistribution and Therapeutic Efficacy in Prostate Tumor-Bearing Mice. *Theranostics.* 2017;7:1928-1939.

123. Dumelin CE, Trussel S, Buller F, et al. A portable albumin binder from a DNA-encoded chemical library. *Angew Chem Int Ed Engl.* 2008;47:3196-3201.

124. Smith-Jones PM, Vallabahajosula S, Goldsmith SJ, et al. In Vitro Characterization of Radiolabeled Monoclonal Antibodies Specific for the Extracellular Domain of Prostate-specific Membrane Antigen1. *Cancer Res.* 2000;60:5237-5243.

125. Wurzer A, Kunert J-P, Fischer S, et al. Synthesis and Preclinical Evaluation of ^{177}Lu-labeled Radiohybrid PSMA Ligands (rhPSMAs) for Endoradiotherapy of Prostate Cancer. *J Nucl Med.* 2022:jnumed.121.263371.

126. Wurzer A, Di Carlo D, Schmidt A, et al. Radiohybrid Ligands: A Novel Tracer Concept Exemplified by ^{18}F- or ^{68}Ga-Labeled rhPSMA Inhibitors. *J Nucl Med.* 2020;61:735-742.

127. Pretze M, Grosse-Gehling P, Mamat C. Cross-coupling reactions as valuable tool for the preparation of PET radiotracers. *Molecules.* 2011;16:1129-1165.

128. Jacobson O, Kiesewetter DO, Chen X. Fluorine-18 radiochemistry, labeling strategies and synthetic routes. *Bioconjug chem.* 2015;26:1-18.

129. Kesch C, Kratochwil C, Mier W, Kopka K, Giesel FL. ^{68}Ga or ^{18}F for Prostate Cancer Imaging? *J Nucl Med.* 2017;58:687.

130. Dornan MH, Simard J-M, Leblond A, et al. Simplified and robust one-step radiosynthesis of [^{18}F]DCFPyL via direct radiofluorination and cartridge-based purification. *J Label Compd Radiopharm.* 2018;61:757-763.

131. Jivan S, Neumann K, Villeret G, et al. Fully automated preparation of [^{18}F]CTT1057, a new prostate cancer imaging agent, prepared using the ORA Neptis® Perform Synthesizer. *J Labelled Compd Radiopharm.* 2017;60:S297-S297.

132. Bouvet V, Wuest M, Jans H-S, et al. Automated synthesis of [^{18}F]DCFPyL via direct radiofluorination and validation in preclinical prostate cancer models. *EJNMMI Res.* 2016;6:40.

133. Cardinale J, Martin R, Remde Y, et al. Procedures for the GMP-Compliant Production and Quality Control of [^{18}F]PSMA-1007: A Next Generation Radiofluorinated Tracer for the Detection of Prostate Cancer. *Pharmaceuticals.* 2017;10:77.

134. Archibald SJ, Allott L. The aluminium-[^{18}F]fluoride revolution: simple radiochemistry with a big impact for radiolabelled biomolecules. *EJNMMI Radiopharm Chem.* 2021;6:30.

135. Lütje S, Franssen GM, Herrmann K, et al. In Vitro and In Vivo Characterization of an ^{18}F-AlF-Labeled PSMA Ligand for Imaging of PSMA-Expressing Xenografts. *J Nucl Med.* 2019;60:1017-1022.

136. Cleeren F, Lecina J, Ahamed M, et al. Al^{18}F-Labeling Of Heat-Sensitive Biomolecules for Positron Emission Tomography Imaging. *Theranostics.* 2017;7:2924-2939.

137. Huang Y, Li H, Ye S, Tang G, Liang Y, Hu K. Synthesis and preclinical evaluation of an Al^{18}F radiofluorinated bivalent PSMA ligand. *Eur J Med Chem.* 2021;221:113502.

138. Rosenthal MS, Bosch AL, Nickles RJ, Gatley SJ. Synthesis and some characteristics of no-carrier added [^{18}F]fluorotrimethylsilane. *Int J Appl Radiat Isot.* 1985;36:318-319.

139. Schirrmacher R, Bradtmöller G, Schirrmacher E, et al. ^{18}F-labeling of peptides by means of an organosilicon-based fluoride acceptor. *Angew Chem Int Ed Engl.* 2006;45:6047-6050.

140. Höhne A, Yu L, Mu L, et al. Organofluorosilanes as model compounds for ^{18}F-labeled silicon-based PET tracers and their hydrolytic stability: experimental data and theoretical calculations (PET = positron emission tomography). *Chem Eur J.* 2009;15:3736-3743.

141. Niedermoser S, Chin J, Wängler C, et al. In Vivo Evaluation of ^{18}F-SiFA*lin*–Modified TATE: A Potential Challenge for ^{68}Ga-DOTATATE, the Clinical Gold Standard for Somatostatin Receptor Imaging with PET. *J Nucl Med.* 2015;56:1100.

142. Kostikov AP, Iovkova L, Chin J, et al. N-(4-(di-tert-butyl[^{18}F]fluorosilyl)benzyl)-2-hydroxy-N,N-dimethylethylammonium bromide ([^{18}F]SiFAN+Br–): A novel lead compound for the development of hydrophilic SiFA-based prosthetic groups for ^{18}F-labeling. *J Fluor Chem.* 2011;132:27-34.

143. Wurzer A, Di Carlo D, Herz M, et al. Automated synthesis of [^{18}F]Ga-rhPSMA-7/ -7.3: results, quality control and experience from more than 200 routine productions. *EJNMMI Radiopharm Chem.* 2021;6:4.

144. Kelly JM, Amor-Coarasa A, Ponnala S, et al. Albumin-Binding PSMA Ligands: Implications for Expanding the Therapeutic Window. *J Nucl Med.* 2019;60:656-663.

145. Benesova M, Umbricht CA, Schibli R, Muller C. Albumin-Binding PSMA Ligands: Optimization of the Tissue Distribution Profile. *Mol Pharm.* 2018;15:934-946.

146. Deberle LM, Benešová M, Umbricht CA, et al. Development of a new class of PSMA radioligands comprising ibuprofen as an albumin-binding entity. *Theranostics.* 2020;10:1678-1693.

147. Umbricht CA, Benešová M, Schibli R, Müller C. Preclinical Development of Novel PSMA-Targeting Radioligands: Modulation of Albumin-Binding Properties To Improve Prostate Cancer Therapy. *Mol Pharm.* 2018;15:2297-2306.

148. Vegt E, Melis M, Eek A, et al. Renal uptake of different radiolabelled peptides is mediated by megalin: SPECT and biodistribution studies in megalin-deficient mice. *Eur J Nucl Med Mol Imaging.* 2011;38:623-632.

149. de Jong M, Barone R, Krenning E, et al. Megalin is essential for renal proximal tubule reabsorption of ^{111}In-DTPA-octreotide. *J Nucl Med.* 2005;46:1696-1700.

150. Pomper MG, Mease RC, Kumar V, Banerjee SR, Zalutsky MR, Vaidyanathan G. PSMA TARGETED RADIOHALOGENATED UREA-POLYAMINOCARBOXYLATES FOR CANCER RADIOTHERAPY. *PCT/US2019/016821.* 2019.

151. Weineisen M, Simecek J, Schottelius M, Schwaiger M, Wester H-J. Synthesis and preclinical evaluation of DOTAGA-conjugated PSMA ligands for functional imaging and endoradiotherapy of prostate cancer. *EJNMMI Res.* 2014;4:63.

152. Wurzer A. Novel Structural Concepts for the Development of complex-based Radiopharmaceuticals and Ligand Systems, PhD thesis, Technical University Munich. 2020.

153. Lim DS, Lin J-H, Welch JT. The Synthesis and Characterization of a Pentafluorosulfanylated Peptide. *Eur J Org Chem.* 2012;2012:3946-3954.

154. Iovkova L, Wängler B, Schirrmacher E, et al. para-Functionalized Aryl-di-tert-butylfluorosilanes as Potential Labeling Synthons for ^{18}F Radiopharmaceuticals. *Chem Eur J.* 2009;15:2140-2147.

155. Vaidyanathan G, Zalutsky MR. Preparation of N-succinimidyl 3-[*I]iodobenzoate: an agent for the indirect radioiodination of proteins. *Nat Protoc.* 2006;1:707-713.

156. Sosabowski JK, Mather SJ. Conjugation of DOTA-like chelating agents to peptides and radiolabeling with trivalent metallic isotopes. *Nat Protoc.* 2006;1:972-976.

157. Valko K, Nunhuck S, Bevan C, Abraham MH, Reynolds DP. Fast gradient HPLC method to determine compounds binding to human serum albumin. Relationships with octanol/water and immobilized artificial membrane lipophilicity. *J Pharm Sci.* 2003;92:2236-2248.

158. Yamazaki K, Kanaoka M. Computational prediction of the plasma protein-binding percent of diverse pharmaceutical compounds. *J Pharm Sci.* 2004;93:1480-1494.

159. Kunert J-P, Fischer S, Wurzer A, Wester H-J. Albumin-Mediated Size Exclusion Chromatography: The Apparent Molecular Weight of PSMA Radioligands as Novel Parameter to Estimate Their Blood Clearance Kinetics. *Pharmaceuticals.* 2022;15:1161.

160. Wirtz M, Schmidt A, Schottelius M, et al. Synthesis and in vitro and in vivo evaluation of urea-based PSMA inhibitors with increased lipophilicity. *EJNMMI Res.* 2018;8:84.

161. Gallyamov M, Meyrick D, Barley J, Lenzo N. Renal outcomes of radioligand therapy: experience of ^{177}lutetium—prostate-specific membrane antigen ligand therapy in metastatic castrate-resistant prostate cancer. *Clin Kidney J.* 2019;13:1049-1055.

162. Yordanova A, Becker A, Eppard E, et al. The impact of repeated cycles of radioligand therapy using [^{177}Lu]Lu-PSMA-617 on renal function in patients with hormone refractory metastatic prostate cancer. *Eur J Nucl Med Mol Imaging.* 2017;44:1473-1479.

163. O'Donoghue J. Relevance of external beam dose-response relationships to kidney toxicity associated with radionuclide therapy. *Cancer Biother Radiopharm.* 2004;19:378-387.

164. Fujioka Y, Satake S, Uehara T, et al. In Vitro System To Estimate Renal Brush Border Enzyme-Mediated Cleavage of Peptide Linkages for Designing Radiolabeled Antibody Fragments of Low Renal Radioactivity Levels. *Bioconjug Chem.* 2005;16:1610-1616.

165. Uehara T, Koike M, Nakata H, et al. Design, Synthesis, and Evaluation of [^{188}Re]Organorhenium-Labeled Antibody Fragments with Renal Enzyme-Cleavable Linkage for Low Renal Radioactivity Levels. *Bioconjug Chem.* 2007;18:190-198.

166. Uehara T, Yokoyama M, Suzuki H, Hanaoka H, Arano Y. A Gallium-67/68–Labeled Antibody Fragment for Immuno-SPECT/PET Shows Low Renal Radioactivity Without Loss of Tumor Uptake. *Clin Cancer Res.* 2018;24:3309-3316.

167. Akizawa H, Imajima M, Hanaoka H, Uehara T, Satake S, Arano Y. Renal Brush Border Enzyme-Cleavable Linkages for Low Renal Radioactivity Levels of Radiolabeled Antibody Fragments. *Bioconjug Chem.* 2013;24:291-299.

168. Spungin-Bialik A, Ben-Meir D, Fudim E, Carmeli S, Blumberg S. Sensitive substrates for neprilysin (neutral endopeptidase) and thermolysin that are highly resistant to serine proteases. *FEBS Lett.* 1996;380:79-82.

169. Watanabe Y, Nakajima K, Shimamori Y, Fujimoto Y. Comparison of the hydrolysis of the three types of natriuretic peptides by human kidney neutral endopeptidase 24.11. *Biochem Mol Med.* 1997;61:47-51.

170. Barros NM, Campos M, Bersanetti PA, et al. Neprilysin carboxydipeptidase specificity studies and improvement in its detection with fluorescence energy transfer peptides. *Biol Chem.* 2007;388:447-455.

171. Zhang M, Jacobson O, Kiesewetter DO, et al. Improving the Theranostic Potential of Exendin 4 by Reducing the Renal Radioactivity through Brush Border Membrane Enzyme-Mediated Degradation. *Bioconjug Chem.* 2019;30:1745-1753.

172. Bendre S, Zhang Z, Kuo HT, et al. Evaluation of Met-Val-Lys as a Renal Brush Border Enzyme-Cleavable Linker to Reduce Kidney Uptake of ^{68}Ga-Labeled DOTA-Conjugated Peptides and Peptidomimetics. *Molecules.* 2020;25.

173. Coker JA, Brenchley JE. Protein engineering of a cold-active beta-galactosidase from Arthrobacter sp. SB to increase lactose hydrolysis reveals new sites affecting low temperature activity. *Extremophiles.* 2006;10.

174. Skidgel RA, Davis RM, Tan F. Human carboxypeptidase M. Purification and characterization of a membrane-bound carboxypeptidase that cleaves peptide hormones. *J Biol Chem.* 1989;264:2236-2241.

175. Vaidyanathan G, Kang CM, McDougald D, et al. Brush border enzyme-cleavable linkers: Evaluation for reducing renal uptake of radiolabeled prostate-specific membrane antigen inhibitors. *Nucl Med Biol.* 2018;62-63:18-30.

176. Bond JS, Shannon JD, Beynon RJ. Certain mouse strains are deficient in a kidney brush-border metallo-endopeptidase activity. *Biochem J.* 1983;209:251-255.

177. Schmidt A. Structural modifications of PSMA ligands to optimize their pharmacokinetics. PhD thesis, Technical University Munich. 2017.

178. Ghuman J, Zunszain PA, Petitpas I, Bhattacharya AA, Otagiri M, Curry S. Structural basis of the drug-binding specificity of human serum albumin. *J Mol Biol.* 2005;353:38-52.

179. Fasano M, Curry S, Terreno E, et al. The extraordinary ligand binding properties of human serum albumin. *IUBMB Life.* 2005;57:787-796.

180. Kelly JM, Amor-Coarasa A, Nikolopoulou A, et al. Dual-Target Binding Ligands with Modulated Pharmacokinetics for Endoradiotherapy of Prostate Cancer. *J Nucl Med.* 2017;58:1442.

181. Kuo H-T, Lin K-S, Zhang Z, et al. ^{177}Lu-Labeled Albumin-Binder–Conjugated PSMA-Targeting Agents with Extremely High Tumor Uptake and Enhanced Tumor-to-Kidney Absorbed Dose Ratio. *J Nucl Med.* 2021;62:521.

182. Kelly J, Amor-Coarasa A, Ponnala S, et al. Trifunctional PSMA-targeting constructs for prostate cancer with unprecedented localization to LNCaP tumors. *Eur J Nucl Med Mol Imaging.* 2018;45:1841-1851.

183. Stryer L, Haugland RP. Energy transfer: a spectroscopic ruler. *Proc Natl Acad Sci.* 1967;58:719-726.

184. Adzhubei AA, Sternberg MJ, Makarov AA. Polyproline-II helix in proteins: structure and function. *J Mol Biol.* 2013;425:2100-2132.

185. Ma Z, LeBard DN, Loverde SM, et al. TCR Triggering by pMHC Ligands Tethered on Surfaces via Poly(Ethylene Glycol) Depends on Polymer Length. *PLOS ONE.* 2014;9:e112292.

186. Evers TH, van Dongen EMWM, Faesen AC, Meijer EW, Merkx M. Quantitative Understanding of the Energy Transfer between Fluorescent Proteins Connected via Flexible Peptide Linkers. *Biochemistry.* 2006;45:13183-13192.

187. Rathke H, Giesel FL, Flechsig P, et al. Repeated ^{177}Lu-Labeled PSMA-617 Radioligand Therapy Using Treatment Activities of Up to 9.3 GBq. *J Nucl Med.* 2018;59:459-465.

188. Behr TM, Becker WS, Sharkey RM, et al. Reduction of renal uptake of monoclonal antibody fragments by amino acid infusion. *J Nucl Med.* 1996;37:829-833.

189. Behr TM, Sharkey RM, Juweid ME, et al. Reduction of the renal uptake of radiolabeled monoclonal antibody fragments by cationic amino acids and their derivatives. *Cancer Res.* 1995;55:3825-3834.

190. Pimm MV, Gribben SJ. Prevention of renal tubule re-absorption of radiometal (indium-111) labelled Fab fragment of a monoclonal antibody in mice by systemic administration of lysine. *Eur J Nucl Med.* 1994;21:663-665.

191. Bodei L, Cremonesi M, Zoboli S, et al. Receptor-mediated radionuclide therapy with ^{90}Y-DOTATOC in association with amino acid infusion: a phase I study. *Eur J Nucl Med Mol Imaging.* 2003;30:207-216.

192. Rolleman EJ, Valkema R, de Jong M, Kooij PP, Krenning EP. Safe and effective inhibition of renal uptake of radiolabelled octreotide by a combination of lysine and arginine. *Eur J Nucl Med Mol Imaging.* 2003;30:9-15.

193. Hennrich U, Kopka K. Lutathera®: The First FDA- and EMA-Approved Radiopharmaceutical for Peptide Receptor Radionuclide Therapy. *Pharmaceuticals.* 2019;12.

194. Béhé M, Kluge G, Becker W, Gotthardt M, Behr TM. Use of polyglutamic acids to reduce uptake of radiometal-labeled minigastrin in the kidneys. *J Nucl Med.* 2005;46:1012-1015.

195. Christensen EI, Verroust PJ. Megalin and cubilin, role in proximal tubule function and during development. *Pediatr Nephrol.* 2002;17:993-999.

196. Verroust PJ, Christensen EI. Megalin and cubilin—the story of two multipurpose receptors unfolds. *Nephrol Dial Transplant.* 2002;17:1867-1871.

197. Borgna F, Deberle LM, Cohrs S, Schibli R, Müller C. Combined Application of Albumin-Binding [^{177}Lu]Lu-PSMA-ALB-56 and Fast-Cleared PSMA Inhibitors: Optimization of the Pharmacokinetics. *Mol Pharm.* 2020;17:2044-2053.

198. Harsini S, Saprunoff H, Alden TM, Mohammadi B, Wilson D, Benard F. The effects of monosodium glutamate on PSMA radiotracer uptake in men with recurrent prostate cancer: a prospective, randomized, double-blind, placebo-controlled intra-individual imaging study. *J Nucl Med.* 2020:jnumed.120.246983.

199. Ekblad T, Tran T, Orlova A, et al. Development and preclinical characterisation of ^{99m}Tc-labelled Affibody molecules with reduced renal uptake. *Eur J Nucl Med Mol Imaging.* 2008;35:2245-2255.

200. Bapst J-P, Eberle AN. Receptor-Mediated Melanoma Targeting with Radiolabeled α-Melanocyte-Stimulating Hormone: Relevance of the Net Charge of the Ligand. *Front Endocrinol.* 2017;8.

201. Baranski AC, Schäfer M, Bauder-Wüst U, et al. Improving the Imaging Contrast of ^{68}Ga-PSMA-11 by Targeted Linker Design: Charged Spacer Moieties Enhance the Pharmacokinetic Properties. *Bioconjug Chem.* 2017;28:2485-2492.

202. Hillier SM, Maresca KP, Lu G, et al. ^{99m}Tc-Labeled Small-Molecule Inhibitors of Prostate-Specific Membrane Antigen for Molecular Imaging of Prostate Cancer. *J Nucl Med.* 2013;54:1369-1376.

203. Eder M, Kopka K, Schäfer M, Bauder-Wüst U, Haberkorn U. LABELED INHIBITORS OF PROSTATE SPECIFIC MEMBRANE ANTIGEN (PSMA), THEIR USE AS IMAGING AGENTS AND PHARMACEUTICAL AGENTS FOR THE TREATMENT OF PROSTATE CANCER. *PCT/EP2014/002808.* 2015.

204. Schuchardt C, Zhang J, Kulkarni HR, Chen X, Mueller D, Baum RP. Prostate-specific membrane antigen radioligand therapy using ^{177}Lu-PSMA I&T and ^{177}Lu-PSMA-617 in patients with metastatic castration-resistant prostate cancer: comparison of safety, biodistribution and dosimetry. *J Nucl Med.* 2021:jnumed.121.262713.

205. Kostikov AP, Chin J, Orchowski K, et al. Oxalic acid supported Si-^{18}F-radiofluorination: one-step radiosynthesis of N-succinimidyl 3-(di-tert-butyl[^{18}F]fluorosilyl)benzoate ([^{18}F]SiFB) for protein labeling. *Bioconjug Chem.* 2012;23:106-114.

206. Blau M, Ganatra R, Bender MA. ^{18}F-fluoride for bone imaging. *Semin Nucl Med.* 1972;2:31-37.

207. Idrees M, Mohammad AR, Karodia N, Rahman A. Multimodal Role of Amino Acids in Microbial Control and Drug Development. *Antibiotics.* 2020;9:330.

208. Haynes WM, Lide DR, Bruno TJ. CRC Handbook of Chemistry and Physics (97th ed.). *CRC Press.* 2016.

209. Kulkarni HR, Singh A, Schuchardt C, et al. PSMA-Based Radioligand Therapy for Metastatic Castration-Resistant Prostate Cancer: The Bad Berka Experience Since 2013. *J Nucl Med.* 2016;57:97S-104S.

210. Banerjee SR, Kumar V, Lisok A, et al. ^{177}Lu-labeled low-molecular-weight agents for PSMA-targeted radiopharmaceutical therapy. *Eur J Nucl Med Mol Imaging.* 2019;46:2545-2557.

211. Gotthardt M, van Eerd-Vismale J, Oyen WJ, et al. Indication for different mechanisms of kidney uptake of radiolabeled peptides. *J Nucl Med.* 2007;48:596-601.

212. Ilhan H, Lindner S, Todica A, et al. Biodistribution and first clinical results of ^{18}F-SiFAlin-TATE PET: a novel ^{18}F-labeled somatostatin analog for imaging of neuroendocrine tumors. *Eur J Nucl Med Mol Imaging.* 2020;47:870-880.

7. Publications

Previously Published Contents of this Work

Peer-Reviewed Journal Articles

- Wurzer A, Kunert J-P, **Fischer S**, Felber V, Beck R, Rose F, D'Alessandria C, Weber W, Wester HJ. Synthesis and Preclinical Evaluation of ^{177}Lu-Labeled Radiohybrid PSMA Ligands for Endoradiotherapy of Prostate Cancer. *J Nucl Med*. 2022;63:1489.

- Kunert J-P, **Fischer S**, Wurzer A, Wester HJ. Albumin-Mediated Size Exclusion Chromatography: The Apparent Molecular Weight of PSMA Radioligands as Novel Parameter to Estimate Their Blood Clearance Kinetics. *Pharmaceuticals*. 2022;15:1161.

Patent Application

- **Fischer S**, Beck R, Deiser SM, Fahnauer MF, Fenzl SA, Guenther T, Holzleitner N, Kunert J-P, Stopper L, Urtz-Urban N, Wester HJ. SILICON BASED-FLUORIDE ACCEPTOR GROUPS FOR RADIOPHARMACEUTICALS. *EP22187845.7*. 2022.

Further Publications Beyond the Scope of this Work

Peer-Reviewed Journal Article

- Günther T, Konrad M, Stopper L, Kunert J-P, **Fischer S**, Beck R, Casini A, Wester HJ. Optimization of the Pharmacokinetic Profile of [^{99m}Tc]Tc-N_4-Bombesin Derivatives by Modification of the Pharmacophoric Gln-Trp Sequence. *Pharmaceuticals*. 2022;15:1133.

Patent Applications

- **Fischer S**, Kunert J-P, Wester HJ, Wurzer A. DUAL MODE RADIOTRACER AND -THERAPEUTICS. *EP21157154.2*. 2021.

- **Fischer S**, Kunert J-P, Wester HJ, Wurzer A. SILICON-CONTAINING LIGAND COMPOUNDS. *PCT/EP2021/070686*. 2021.

Conference Abstracts

- Guenther T, **Fischer S**, Beck R, Wester HJ. Preclinical results of novel GRPR-targeted antagonists with modified binding sequences. *J Nucl Med*. 2020;61:1054.

- Guenther T, **Fischer S**, Casini A, Lapa C, Wester HJ. Attempts to improve the pharmacokinetic Profile of Pharmacophore-modified ^{99m}Tc-N_4-conjugated GRPR-targeted Compounds via Addition of a Ga-DOTA moiety. *J Nucl Med*. 2022;63:4057.

8. Acknowledgements

First of all, I want to thank Prof. Dr. Hans-Jürgen Wester for giving me the opportunity to graduate at his chair and handing this interesting as well as challenging research topic to me. Moreover, I highly appreciated the passionate lectures of the master courses held by Prof. Wester and Prof. Dr. Margret Schottelius. Their inspiring fascination and motivation for radiopharmacy confirmed my plan to graduate at this department.

Subsequent to the retirement of Prof. Wester, Prof. Dr. Angela Casini took the responsibility for the chair in addition to the management of her own group. I am very thankfull for her strong comittment and support to all PhD students and especially for being my mentor in the final phase of my graduation.

During the writing process of my PhD thesis, Prof. Dr. Susanne Kossatz readily agreed to become my new supervisor. I highly appreciate her kind help and motivating feedback as well as the fact that she invested her time despite of her tough schedule.

Thinking about time management, Christine Winkler is the person that comes to my mind. Thank you for handling the bureaucreatic stuff with this carefulness while staying calm and open for all sorts of questions.

One substantial part of my PhD studies included animal experiments. Thanks to the training by our veterinarians, Dr. Roswitha Beck and Dr. Nicole Urtz-Urban, I now feel confident in conducting such demanding experiments by myself.

Special thanks belong to all my colleagues and friends in the laboratory with some of you even sharing my whole way at the TUM since the beginning of our Bachelor's studies a decade ago: Dr. Markus Fahnauer, Jan-Philip Kunert, Dr. Martina Wirtz, Dr. Stephanie Robu, Dr. Alexander Schmidt, Dr. Theresa Osl, Dr. Alexander Wurzer, Dr. Thomas Günther, Dr. Veronika Felber, Dr. Matthias Konrad, Mara Parzinger, Daniel Di Carlo, Stefanie Färber, León Stopper, Nadine Holzleitner, Sandra Deiser, Sebastian Fenzl, Franziska Schuderer, Sven Hintze, Jana Herbst and Tanja Reichhart. You all created a warm, inviting and familiar atmosphere. It was a pleasure for me to spend time with you during this exciting period, no matter if it were inspiring scientific or non-work-related discussions, refreshing coffee breaks or thrilling table soccer games.

Of course, I acknowledge the support by my students regarding several research projects. Sebastian Fenzl, I thank you once again for your help – also as my loyal, former student. Furthermore, I thank you, Viktorija Kozina, Johannes Mayr, Aron Baierlein and Robin Kretschmer.

Finally, I want to express the gratitude I feel for my family and in particular my wonderfull, lovable wife Patricia Fischer and both our parents Renate & Andreas Fischer and Hannelore & Werner Reichart. You don't only have the patience to endure my scientific monologues. But you truly care and I can count on you whatever life holds for us. Thank you so much!